Imperial College
London

The Blue-Detuned Magneto-Optical Trap

A Thesis Submitted to the Department of Physics,
Imperial College London
by

Kyle N. Jarvis

In Partial Fulfilment of the Requirements for the Degree of
Doctor of Philosophy

2018

Abstract

It has been more than 30 years since the first demonstration of a magneto-optical trap (MOT) using sodium atoms. Since then the MOT has revolutionised the field of atomic physics by facilitating the emergence of a broad range of productive avenues of research using atoms prepared at low temperatures and high densities. This thesis describes the development of a novel kind of magneto-optical trap: the blue-detuned MOT. Unlike in all previous MOTs the light is blue detuned from atomic resonances and drives "type-II" transitions that have dark ground-state sub-levels. A discussion of the position-dependent and velocity-dependent forces experienced by an atom or molecule in a MOT is first used to consolidate recent theoretical work and, in particular, to introduce the concept of a blue-detuned MOT. The design and construction of an experiment that has been built to demonstrate a blue-detuned MOT using ^{87}Rb is described. A thorough characterisation of this novel MOT has been performed. At high magnetic field gradients, radiation-pressure-limited densities exceeding 10^{11} cm^{-3} have been reached whilst temperatures are cooled below 30 μK by the efficient and robust sub-Doppler cooling mechanisms. The maximum phase-space density measured is 6×10^{-6}, which is higher than in most normal atomic MOTs, comparable to the best dark SPOTs, and a million times higher than that reported for red-detuned type-II MOTs. This makes the blue-detuned MOT particularly attractive for molecules where laser cooling and trapping always uses type-II transitions. For the first time, a study of trap loss due to ultra-cold collisions between atoms occurring in the presence of near-resonant blue-detuned light is undertaken. Finally, the experiment is used to demonstrate many new and unreported configurations of MOT for ^{87}Rb, showing that a comprehensive understanding of complicated MOTs is now possible, and presenting a clear direction for further research.

Declaration of Originality

I declare that the work presented in this thesis is my own. Where data has been reproduced from existing sources, those sources have been appropriately referenced. The experiment was constructed by myself, with the help of T. E. Wall.

Copyright Declaration

Contents

List of Figures

List of Tables

1 Introduction

Laser cooling and trapping is the manipulation of the external degrees of freedom of a particle, such as an atom, ion, or molecule, by the mechanical effects of light in order to bring about a reduction in temperature, and achieve spatial confinement. The first experimental demonstrations of the mechanical effects of light on macroscopic objects were reported in a pair of papers published in 1901 [1] and 1903 [2], where the minute deflection of a torsion balance demonstrates the existence of a radiation pressure. Later, in 1933, a sodium lamp was used to deflect a beam of individual atoms [3]. It was, however, the advent of commercially available laser systems that allowed the field of laser-cooling and trapping to emerge as a productive and revolutionary field of research. The earliest experiments recognisable as belonging to the field were the atomic-beam-deceleration experiments of the late 1970s [4] and early 1980s [5]. The realisation of the magneto-optical trap for neutral atoms in 1987 [6] allowed researchers to prepare large samples of atoms at unprecedentedly low temperatures and high densities. A multitude of productive avenues of research that rely on the MOT have since emerged. There have been three Nobel prizes awarded in the field. These were to S. Chu, C. Cohen-Tannoudji, and W. Phillips for "the development of methods to cool and trap atoms with laser light" in 1997, to E. A. Cornell, W. Ketterle, and C. E. Wieman "for the achievement of Bose-Einstein condensation in dilute gases of alkali atoms, and for early fundamental studies of the properties of the condensates" in 2001, and, most recently, to S. Haroche and D. J. Wienland "for ground-breaking experimental methods that enable measuring and manipulation of individual quantum systems" in 2012. In addition to the study of quantum phenomena and cold chemistry, applications of laser-cooled atoms span tests of fundamental physics [7], precision metrology [8] and frequency standards [9], matter-wave interferometry for inertial sensing [10], and searches for additional forces [11, 12].

In recent years a number of groups have succeeded in applying the magneto-optical trapping technique to diatomic molecules [13, 14]. There are numerous proposed applications of cold molecules that could soon be demonstrable thanks to this exciting development. Some of the most ambitious of these proposals involve the loading of single molecules into optical tweezer traps, as has been done with atoms [15], and the deterministic assembly of arrays of strongly interacting dipolar molecules for quantum computation [16]. Similar systems have previously been demonstrated using atoms confined in microscopic optical traps and excited to Rydberg states. In these states, strong dipole-dipole interactions can lead to entangle-

ment [17] and the realisation of elementary quantum computation protocols [18]. All examples of magneto-optical traps of diatomic molecules demonstrated to date have the unfavourable properties of high temperature and low density, which is likely to hamper the efforts to realise many of the most exciting proposals.

In this thesis a novel kind of magneto-optical trap is demonstrated, which could lead to a dramatic improvement in the performance of magneto-optical traps of diatomic molecules, as well as to new applications of ultra-cold atoms. The MOT uses light that is blue detuned from so-called "type-II" transitions in ^{87}Rb. Laser cooling and trapping schemes for diatomic molecules necessarily use type-II transitions to avoid rotational branching. It is therefore hoped that the new techniques demonstrated in this thesis will be applicable molecular MOTs, with similarly impressive results.

1.1 Structure of this thesis

Below, a brief outline of the content of each of the subsequent chapters of this thesis is given.

Chapter 2. This chapter provides an overview of the emergence and progression of laser cooling and trapping techniques. To begin, a brief account of the early demonstrations of the deflection, deceleration, cooling and confinement of atoms by radiation pressure is given. The basic physical principles underpinning these techniques are introduced. The chapter culminates in a discussion of recent experimental demonstrations of the successful application of these techniques to diatomic molecules.

Chapter 3. Experimental demonstrations of the laser cooling and trapping of diatomic molecules have stimulated a renewed interest in the theoretical understanding of how these traps operate. This chapter provides a more detailed analysis of the nature of the position-dependent and velocity-dependent forces experienced by an atom or molecule confined in a magneto-optical trap. Various angular momentum cases are investigated quantitatively by solving the optical Bloch equations. The concept of a blue-detuned MOT is introduced and a trapping scheme is proposed that could demonstrate the idea using ^{87}Rb.

Chapter 4. In this chapter the construction of an experiment to demonstrate and investigate the properties of a blue-detuned MOT of ^{87}Rb is described.

Chapter 5. The experimental realisation and detailed characterisation of the blue-detuned MOT is described. Data obtained from a number of experiments are presented alongside a discussion of the methods used. Throughout this chapter comparisons are made to other MOTs, and the similarity and differences are discussed with reference to the theoretical considerations of earlier chapters.

Chapter 6. In this section a number of new magneto-optical trapping schemes are presented. These are in addition to the blue-detuned MOT discussed in chapter 5, and have not been previously reported. Included are schemes in which both hyperfine ground-states are coupled to a single excited state, and a long-lived, stable MOT operating on the $F = 1 \rightarrow F' = 0$ transition, for which the usual magneto-optical force in non-existent.

Chapter 7. Finally, a summary of the outcomes of the investigation is given. The work presented in this thesis is considered in the context of the field more generally. Prospective avenues for further research, which could be achieved with the existing set-up, are proposed.

2 Laser cooling and trapping

The subject of laser cooling and trapping is well established, and there exists an enormous wealth of literature devoted to the subject which now spans over four decades. This chapter begins by unambiguously describing the convention that is used throughout this thesis for laser polarisations and the associated atomic transitions which they drive. Then, a review of the basic principles of laser cooling is given along with a concise discussion of the operating principles of a conventional MOT for a simple atom. The derivation of simple analytical expressions for key quantities, such as the damping coefficient and Doppler temperature, serves as an introduction to a more rigorous treatment of the MOT physics that will be presented in later chapters. The content presented in those chapters is necessary for a good understanding of the key experimental observations presented in this thesis and also of recent experimental observations made by a number of groups. The material presented in this chapter follows chronologically the development of the methods that are now routinely used to capture, cool, and manipulate atoms using laser light in laboratories worldwide.

2.1 Laser polarisations and atomic transitions

When considering laser polarisations and the associated atomic transitions they couple to, it is convenient to work in the spherical basis. In this basis each polarisation component of the light couples to at most a single atomic transition. The handedness of a circularly-polarised laser beam can be inferred from the observation of the temporal evolution of the electric-field vector of the light as the beam propagates through a plane normal to its direction of propagation. However, such an exercise can be defined from the point of view of the source of the beam, or of the receiver of the beam. Both conventions are used within different sub-fields and this can lead to ambiguity. Such ambiguity is especially prevalent in the discussion of magneto-optical traps. This ambiguity is often exacerbated when the multi-level nature of an atom in a MOT is considered, because light of a given polarisation, from the point of view of the experimenter, can drive different transitions at different points in the quadrupole magnetic field. For these reasons a brief discussion of the nomenclature used in this thesis to describe the laser polarisations, and the transitions they couple to in atoms or molecules, is given. The convention used here follows that established in the Optical Society of America's *Handbook of Optics* [19].

Laser polarisations

Eqs. 2.1 describe two travelling plane waves, each of which is polarised along one of the three spherical basis vectors. The polarisation is described by a Cartesian column vector. The fields are written in complex notation, and so the physical electric field is represented by the real part of the expression.

$$\mathcal{E}_R = \frac{E_0}{\sqrt{2}} \begin{pmatrix} 1 \\ -i \\ 0 \end{pmatrix} e^{i(kz-\omega t)} \tag{2.1a}$$

$$\mathcal{E}_L = \frac{E_0}{\sqrt{2}} \begin{pmatrix} 1 \\ i \\ 0 \end{pmatrix} e^{i(kz-\omega t)} \tag{2.1b}$$

The waves propagate in the $+\hat{z}$ direction. The two circular polarisations describe an electric field that rotates in the xy-plane in both time and position along z. A right handed circularly-polarised (RCP) plane wave is described by $\mathcal{E}_R$, and a left handed circularly-polarised (LCP) plane wave by $\mathcal{E}_L$. When the quantisation axis of an atom or molecule is aligned along z, circularly-polarised light drives $\Delta m_F = \pm 1$ transitions, also called $\sigma^{\pm}$ transitions. The exact transition depends on both the polarisation of the light and whether the quantisation axis is parallel or anti-parallel to $\vec{k}$. Any linear polarisation in the xy-plane can be formed from a superposition of the two circular polarisations. When the quantisation axis is not aligned parallel or anti-parallel to the direction of propagation of a circularly-polarised beam, transitions with $\Delta m_F = 0$ can also be induced. These $\Delta m_F = 0$ transitions are also referred to as π transitions, and are driven by the component of the electric-field vector of the light aligned along the quantisation axis, typically defined by an external magnetic field.

The selection rules for transitions driven by laser light of a given polarisation are the result of the conservation of angular momentum of the photon/particle system. A single photon posses a spin angular momentum that is directly related to its polarisation. Using the convention adopted in this thesis, the projections of a photon's spin on its direction of propagation for two possible circular polarisations given in Eqs. 2.1 are

$$\langle R|\hat{S}_z|R\rangle = -\hbar, \tag{2.2a}$$

and

$$\langle L|\hat{S}_z|L\rangle = +\hbar. \tag{2.2b}$$

In Eqs. 2.2, $|L\rangle$ denotes a photon prepared with a left hand circular polarisation, and $|R\rangle$ a right hand circular polarisation.

Atomic transitions

The actual atomic transition driven by a laser depends upon the polarisation of the laser light with respect to the quantisation axis defining the orientation of the atom. A quantisation axis can be readily defined in an experiment by applying a weak magnetic field along some direction. A right handed circularly-polarised photon can drive any of the $\sigma^{\pm}$ or π transitions in an atom or molecule depending on the projection of the photon's spin on the quantisation axis of the particle. If the quantisation axis is parallel to the direction of propagation, $\vec{k}$, of the RCP photon, σ^{-} transitions are driven. On the other hand, if the quantisation axis is anti-parallel to $\vec{k}$, σ^{+} transitions are driven. Finally, if the quantisation axis is neither parallel nor anti-parallel to $\vec{k}$, so that some component of the electric-field vector is aligned along the quantisation axis, π transitions can be driven.

Example: polarisations in the MOT

For concreteness consider a conventional MOT of ^{87}Rb, where the cooling and trapping is due to transitions driven from $F = 2 \rightarrow F' = 3$. The upper state g-factor is $g'_F = +\frac{2}{3}$, and the light is red detuned. At all points in the MOT the restoring MOT beams, which propagate inwards towards the trap centre, should drive σ^{-} transitions, because these are shifted closer to resonance by the magnetic field. The quadrupole fields can be driven so the magnetic field vector points inwards to the trap centre axially and outwards from the trap centre radially, which is referred to as 'configuration A'. Reversing the direction of the current in the coils gives 'configuration B'.

Beams	Configuration A	Configuration B
Axial	RCP	LCP
Radial	LCP	RCP

Table 2.1: MOT beam polarisations required for correct MOT operation in a conventional type-I MOT of ^{87}Rb.

Summary

Fig. 2.1 summarises the statements made in this section. The figure shows how the electric-field vector varies in space at a fixed moment in time, and how the electric-field rotates in a fixed plane in space as a function of time, for both LCP and RCP wave packets. Also shown are the transitions driven by each of the polarisations for the cases where the quantisation axis of the atom or molecule is parallel or anti-parallel to the direction of propagation. The conventions described in this section will be used throughout the remaining content of this thesis.

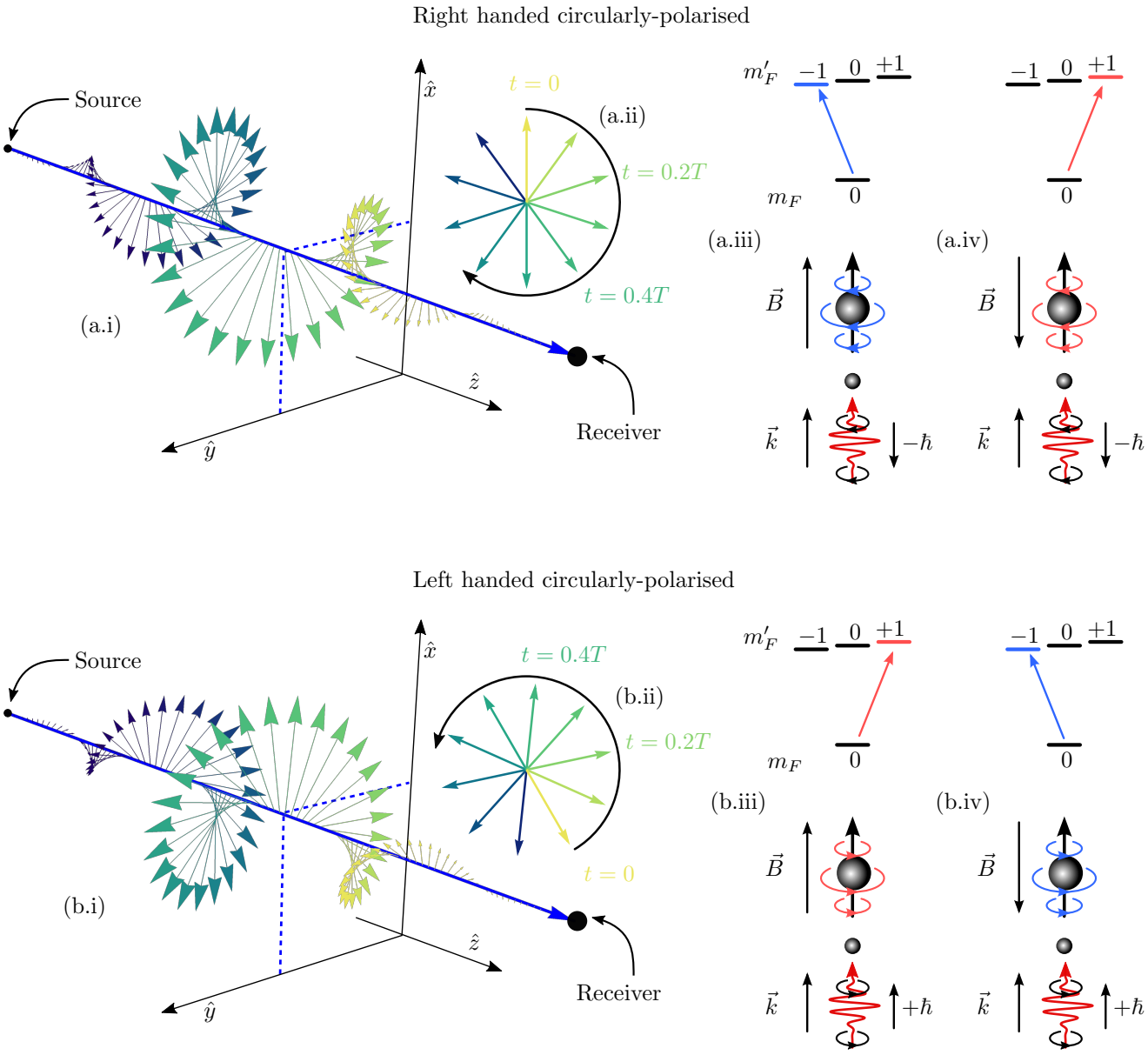

Figure 2.1: Understanding circularly-polarised light and the associated transitions driven in an atom or molecule. The top part of the image depicts a RCP wave packet. Part (a.i) shows the electric-field vector along the axis of propagation for a fixed instant in time. Part (a.ii) shows how the electric-field vector rotates in the xy-plane as a function of time as observed by the receiver looking into the source. Parts (a.iii) and (a.iv) show the transitions driven by a RCP photon for two orientations of the quantisation axis, which is defined through an external magnetic field as illustrated. The lower part of the image depicts the same information but for a LCP wave packet.

2.2 The radiation-pressure force

An atom irradiated by laser light of angular frequency ω_L can exchange energy with the light by stimulated absorption and emission of photons, providing that the photon energy is close to the difference in energy between two states of the atom $E = \hbar\omega_L = E_b - E_a$. The excited state of the atom can also couple to vacuum fluctuations, spontaneously emitting a photon in a random direction and returning to its ground state. The direction of spontaneous emission is random, whereas the photons in a collimated beam of laser light have a well-defined momentum $\vec{p} = \hbar\vec{k}$. Repeated absorption of photons from a laser, followed by randomly orientated spontaneous emission, can lead to a significant transfer of momentum to an atom. The idea of using the mechanical effects of light to alter the trajectory of an atom was first proposed by A. Ashkin in 1970 [20], who recognised that the development of intense, spectrally narrow laser light sources made this experimentally achievable. It was initially proposed that such a technique could be used to reduce or eliminate motional effects in high-resolution spectroscopy or precision measurements, and to extend the interrogation time of atomic beams. For an atom with a radiative lifetime τ_R, and associated line-width $\Gamma = 1/\tau_R$, the maximum acceleration of the atom due to the scattering process is $a_{\max} = \frac{\hbar k\Gamma}{2m}$. For sodium atoms emerging from an oven with a velocity $v = 2 \times 10^4$ cm/s, which is the case considered in [20], the maximum acceleration gives a stopping distance $d = v^2/(2a_{\max})$ of ~2 cm. This change in velocity corresponds to the scattering of approximately 10^4 photons from a counter-propagating laser.

There were initially two obstacles to achieving a sufficiently high number of photon scattering events to realise efficient slowing. The first was optical pumping of the atoms into uncoupled states, which prevents any further interaction with the light. The second is the change in the apparent frequency of the laser light in the frame of reference of the atom due to the Doppler effect [21, 22].

The first definitive demonstration of the laser deceleration of an atomic beam was made by J. V. Proden et al. in 1982 [23]. In their experiment a tapered solenoid compensated for the Doppler shift of the atoms via the differential Zeeman shift of the two states involved in the optical cycling. This technique would later come to be known as Zeeman deceleration. Additionally, the Zeeman shift of the allowed transitions to $F' = 2$ is so large in this set up that optical pumping to the lower hyperfine ground state is effectively inhibited [24]. Soon after, atoms were brought completely to rest using the same apparatus [25], and the first demonstration of trapped neutral atoms was made using laser-cooled sodium in a magnetic trap by A. L. Migdall et al. [26] in 1985. Only shallow trap depths are feasible using magnetic traps. For the arrangement in [26] the depth is 17 mK for sodium atoms. The

successful loading of such a shallow trap from a high-velocity source demonstrates the capability of the laser-cooling and slowing technique, and the rapid progress that had been made in the field.

2.3 Optical molasses and the Doppler-cooling limit

At about the same time, the first observation was made, by S. Chu et al. [27], of the three-dimensional viscous confinement of neutral atoms by laser light. There are a number of advantages to this set-up over that used to demonstrate the magnetic trap. In this experiment a beam of sodium atoms are slowed by an intense, frequency-chirped laser before being confined in a 3D 'optical-molasses'. The optical molasses is formed from three pairs of counter-propagating beams, red detuned from the resonant frequency of the atomic transition. Two lasers are used, each addressing different hyperfine ground states, which prevents optical pumping into an uncoupled state. Atomic motion along the axis of propagation of the molasses causes a Doppler-shift of the two lasers in the atom's frame of reference, so that the counter-propagating laser is closer to resonance. The scattering rate of photons from the counter-propagating beam is therefore higher than from the co-propagating beam and a net transfer of momentum to the atom is achieved, reducing its velocity. By arranging three pairs of counter-propagating beams along the three spatial axes, damping of the atomic velocity is achieved in all three dimensions. Once captured by the optical molasses, atoms move diffusively due to the random walk caused by spontaneous emission and fluctuations in the numbers of photons absorbed from each of the beams. Over a long period of time, atoms can diffuse out of the optical molasses. A time-of-flight method was used to determine the temperature of the atoms, which was found to be ~240 μK, far lower than obtained in the conservative magnetic trap in [25]. This is also the theoretical value of the Doppler-cooling limit for sodium, which at the time was the only known mechanism by which laser light can be used to cool atoms.

The finite limit to which atoms can be cooled by Doppler processes [28, 29] is established by a competition between the heating and cooling rates of the atom. In the following sections expressions are derived for these rates for the case of a two-level atom in an optical molasses. By equating these rates an equation describing the equilibrium temperature of atoms cooled by Doppler processes in an optical molasses is obtained. The minimum value of this equilibrium temperature is the Doppler-cooling limit.

Doppler cooling rate

The velocity-dependent force exerted on an atom in motion with velocity v through an optical molasses due to Doppler processes can be quantified in terms of a damping coefficient α, $F_{\text{Mol}} = -\alpha v$. To evaluate the cooling rate the damping coefficient must be computed. For a two-level atom the scattering force is calculated by solving the optical Bloch equations to obtain the steady-state excited-state population ρ_{ee}. The result is

$$\rho_{ee} = \frac{1}{2}\frac{s}{1+s+\frac{4\Delta^2}{\Gamma^2}}, \tag{2.3}$$

where $s = I/I_{\text{sat}}$ is the saturation parameter, I_{sat} is the saturation intensity, Δ is the detuning of the laser from the resonant frequency of the atomic transition, and $\Gamma = 1/\tau$ is the natural linewidth of the transition. For a single laser beam the force is then simply $\vec{F}_{\text{Scatt}} = \hbar\vec{k}\Gamma\rho_{ee}$. An atom in motion through an optical molasses sees an additional velocity-dependent detuning of the two beams due to the Doppler effect. At low intensities, where $s \ll 1$, the total force experienced by an atom moving through a 1D optical molasses is simply the sum of the two individual forces exerted by each of the laser beams,

$$F_{\text{Mol}} = F_{\text{Scatt}}(\Delta - kv) - F_{\text{Scatt}}(\Delta + kv). \tag{2.4}$$

To calculate the damping coefficient, which describes the frictional force valid at small atomic velocities ($kv \ll \Delta$), the scatting force is written as a Taylor expansion in kv. Then, $F_{\text{Mol}} = -2kv\frac{\partial}{\partial\Delta}F_{\text{Scatt}}$, and the result is

$$F_{\text{Mol}} = \frac{8\hbar k^2 s\Delta v}{\Gamma(1+s+\frac{4\Delta^2}{\Gamma^2})^2} \equiv -\alpha v \qquad ; \qquad \alpha = \frac{-8\hbar k^2 s\Delta}{\Gamma(1+s+\frac{4\Delta^2}{\Gamma^2})^2}. \tag{2.5}$$

Hence, the force is a damping force when $\Delta < 0$. The maximum value of α is obtained when $s = 1+\frac{4\Delta^2}{\Gamma^2}$ and $\Delta = -\Gamma/2$, so that $\alpha_{\text{max}} = -\hbar k^2/2$. The force in 3D is simply $\vec{F}_{\text{Mol}} = -\alpha(v_x\hat{x} + v_y\hat{y} + v_z\hat{z})$, which assumes the three pairs of beams are identical and aligned along orthogonal axes. The cooling rate is the rate at which kinetic energy is removed from the atom by its motion through the optical molasses.

$$\frac{d}{dt}E_{\text{Kin}} = \frac{d}{dt}\frac{p^2}{2m} = \frac{p\dot{p}}{m} = |\vec{F}_{\text{Mol}}|v = -\alpha v^2, \tag{2.6}$$

where $p = \sqrt{p_x^2 + p_y^2 + p_z^2}$, and $v = \sqrt{v_x^2 + v_y^2 + v_z^2}$. The average rate of cooling is $\langle\dot{E}_{\text{Kin}}\rangle = -\alpha\langle v^2\rangle$. The rate of change of $\langle\Delta p^2\rangle$ is given by

$$\frac{d}{dt}\langle\Delta p^2\rangle = -2m\alpha\langle v^2\rangle. \tag{2.7}$$

Heating rate

There are two contributions to the heating rate. The first is due to the random walk of the atom in its momentum space caused by the recoil from spontaneously emitted photons. In three dimensions, the average displacement of a random walk consisting of N steps, each of length $\hbar k$, is $\sqrt{N}\hbar k$. The mean number of photons scattered from a single beam in an interval Δt is $N = \Gamma\rho_{ee}\Delta t$. After a time Δt the magnitude of the momentum vector has increased by an amount Δp, where the mean value of Δp^2 is $\langle\Delta p^2\rangle = \hbar^2k^2\Gamma\rho_{ee}\Delta t$. The average rate of increase of Δp^2 from spontaneous emission due to all 6 beams in a low intensity 3D optical molasses is

$$\frac{d}{dt}\langle\Delta p^2\rangle = 6\hbar^2k^2\Gamma\rho_{ee}. \tag{2.8}$$

The second contribution to the heating rate is due to fluctuations in the number of photons absorbed from the molasses beams. First consider the number of photons N absorbed from a single beam, which has a Poissonian probability distribution $P(N)$. The variance of a Poissonian distribution is equal to its mean. For sufficiently large N the resulting distribution is approximately normal. It is given by

$$P(N) = \frac{1}{2\pi\overline{N}}\exp\left[-\frac{(N-\overline{N})^2}{2\overline{N}}\right], \tag{2.9}$$

where $\langle N\rangle = \overline{N} = \Gamma\rho_{ee}\Delta t$. Consider now the addition of a second counter-propagating beam, and for definiteness let the beams be aligned along $\hat{x}$. Let the number of photons absorbed from the beam with $\vec{k} = +k\hat{x}$ be N_+, and the number of photons absorbed from the beam with $\vec{k} = -k\hat{x}$ be N_-. The difference in the numbers of photons absorbed from the two beams is obtained from a convolution of $P(N_+)$ and $P(N_-)$, and is also given by a normal distribution with variance $\mathrm{Var}(N_+ - N_-) = 2\overline{N}$, so that

$$P(N_+ - N_-) = \frac{1}{4\pi\overline{N}}\exp\left[-\frac{N^2}{4\overline{N}}\right]. \tag{2.10}$$

The corresponding probability distribution for the momentum imparted to the atoms by fluctuations in the scattering force, $P(p_x)$, can be obtained by making the substitutions $\overline{p_x} = \hbar k\overline{N}$, and $p_x = \hbar kN$. The probability density for the momentum vector in 3D, when all three pairs of beams are included, is simply $P(p_x, p_y, p_z) = P(p_x)P(p_y)P(p_z)$,

$$P(p_x, p_y, p_z) \propto \exp\left[-\frac{p_x^2}{4\hbar k\overline{p_x}}\right]\exp\left[-\frac{p_y^2}{4\hbar k\overline{p_y}}\right]\exp\left[-\frac{p_z^2}{4\hbar k\overline{p_z}}\right]. \tag{2.11}$$

The three pairs of molasses beams are assumed to be identical. This implies that the probability distribution for the momentum vector has spherical symmetry, $\overline{p_x} = \overline{p_y} = \overline{p_z} = \overline{p}$, and so its magnitude is distributed according to

$$P(p, p+dp) = \frac{1}{8}(\hbar k \pi \overline{p})^{-3/2} \exp\left[-\frac{p^2}{4\hbar k \overline{p}}\right] 4\pi p^2 dp. \tag{2.12}$$

The average value of $\langle \Delta p^2 \rangle$ can be calculated using Eq. 2.12,

$$\langle \Delta p^2 \rangle = \int P(p, p+dp) p^2 = 6\hbar k \overline{p} = 6\hbar k \Gamma \rho_{ee} \Delta t. \tag{2.13}$$

It follows that the rate of increase of $\langle \Delta p^2 \rangle$ due to fluctuations in the numbers of photons absorbed from the molasses beams is given by

$$\frac{d}{dt}\langle \Delta p^2 \rangle = 6\hbar^2 k^2 \Gamma \rho_{ee}. \tag{2.14}$$

Doppler-cooling limit

An equilibrium temperature is reached when $\frac{d}{dt}\langle p^2 \rangle_{\text{cooling}} = -\frac{d}{dt}\langle p^2 \rangle_{\text{heating}}$. There are two contributions to the heating rate, given by Eq. 2.8, and Eq. 2.14. The result is $\frac{d}{dt}\langle p^2 \rangle_{\text{heating}} = 12\hbar^2 k^2 \Gamma \rho_{ee}$. The effect of the cooling on the average magnitude squared of the momentum vector is given by Eq. 2.6. At the equilibrium temperature $2m\alpha\langle v^2 \rangle = 12\hbar^2 k^2 \Gamma \rho_{ee}$. Using the expressions for ρ_{ee} and α, given by Eq. 2.3 and Eq. 2.5 respectively, the following expression is obtained:

$$\langle v^2 \rangle = -\frac{3\hbar\Gamma^2}{8m\Delta}(1 + s + \frac{4\Delta^2}{\Gamma^2}). \tag{2.15}$$

For an ensemble of atoms in 3D, $\frac{1}{2}m\langle v^2 \rangle = \frac{3}{2}k_{\text{B}}T$. Substituting this expression into Eq. 2.15, and taking the low-intensity limit ($s \ll 1$), the equilibrium temperature T_{eq} is found to be,

$$k_{\text{B}}T_{\text{eq}} = \frac{\hbar\Gamma}{4}\left(\frac{2|\Delta|}{\Gamma} + \frac{\Gamma}{2|\Delta|}\right). \tag{2.16}$$

The Doppler temperature T_{D} is the minimum value of the equilibrium temperature within this model, and is obtained for $\Delta = -\Gamma/2$,

$$T_{\text{D}} = \frac{\hbar\Gamma}{2k_{\text{B}}}. \tag{2.17}$$

Initially, the Doppler theory of laser cooling did seem adequate to describe the heating and cooling processes an atom undergoes in an optical molasses. In the first experiment to demonstrate optical molasses in 3D the lowest temperature obtained was reported to be 240^{+200}_{-60} µK. For sodium, which was the element used, $T_{\text{D}} =$

235 µK. The experimental value was therefore in good agreement with that predicted by the Doppler theory, albeit with quite a large uncertainty.

2.4 Sub-Doppler cooling

The demonstration of atoms cooled to very low temperatures in optical molasses prompted the development of more sophisticated methods to determine the temperature of the atoms. Being able to precisely measure these temperatures would allow the predictions of the Doppler theory of laser cooling to be rigorously tested. One such example, known as the time-of-flight method, was developed by P. D. Lett et al. and was used to provide the first experimental evidence [30] that the Doppler theory of laser cooling was incomplete.

In their experiment, a number of complimentary techniques were used to measure various characteristics of the velocity distribution of atoms cooled in an optical molasses. When combined, these techniques allowed for a precise determination of the temperature, and demonstrated that the Doppler limit was dramatically violated over a broad range of experimental parameters.

These observations demanded a new theory of laser cooling. It was immediately suggested that the theoretical exploration of the new cooling mechanisms should take into consideration the multi-state nature of an atom. This was based upon the observation that the equilibrium temperature of atoms in the optical molasses strongly depended upon the relative polarisation of the molasses beams. Another observation was that the additional cooling mechanisms were strongly suppressed by weak magnetic fields. As a consequence of this it was further stipulated that the cooling mechanism might involve narrow Raman resonances or two-photon transitions between pairs of ground-state Zeeman sub-levels.

This new theory of sub-Doppler laser cooling was provided soon after, both by J. Dalibard and C. Cohen-Tannoudji in [31] and by P. J. Ungar et al. in [32]. In [31] two new cooling mechanisms are explored. The first is referred to as the Sisyphus cooling mechanism and can occur when the energies of the ground states of the system are modulated in space due to the AC Stark effect. Fig. 2.2 illustrates the mechanism for an atom with $F = 1/2$ and $F' = 3/2$. The molasses configuration most commonly associated with the Sisyphus effect is that where the counter-propagating beams have orthogonal linear polarisations. This produces a standing wave in which the ellipticity of the polarisation alternates in space, varying between linear and circular polarisations. The light-shifts of the ground states are proportional to the strength of the coupling between the ground and excited-states by the local laser polarisation. At the point where the standing wave is polarised to σ^- transitions, population is optically pumped into $m_F = -1/2$, which has the

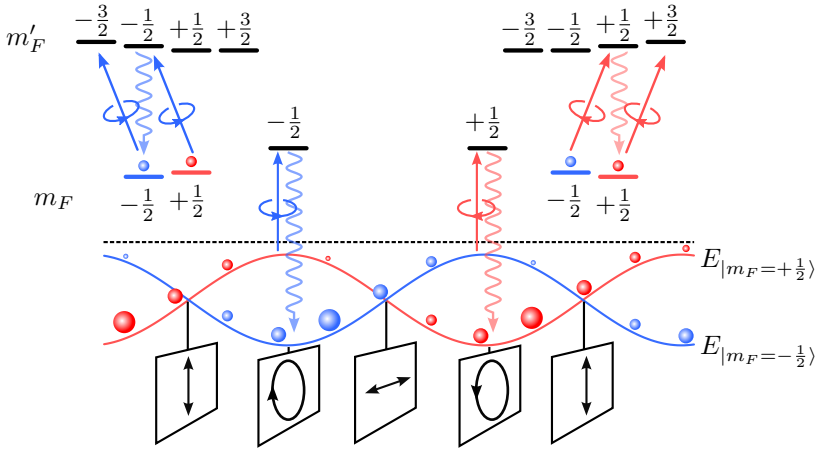

Figure 2.2: Understanding the Sisyphus mechanism in type-I systems. Here, the effect is illustrated for a system with $F = \frac{1}{2}$ and $F' = \frac{3}{2}$. An atom moves through a lin⊥lin optical molasses. The resulting polarisation of the standing wave varies between circular and linear as indicated in the panels, which causes the ground-state energy levels to vary due to the light-shift. Optical pumping concentrates atoms in the lowest-energy state, but this takes a finite amount of time. The net effect of the optical pumping and light-shifts is that, on average, atoms climb a potential hill, which converts kinetic energy into potential energy. This energy is dissipated by blue-shifted spontaneous emission, as indicated by the wavy lines. Linear polarisations are formed from equal superpositions of the two circularly polarised components, and at these points $\sigma^{\pm}$ transitions are equally likely.

lowest energy because it couples more strongly to the σ^- light than $m_F = +1/2$. To move away from this position, atoms must climb a potential hill, which reduces their kinetic energy. As the polarisation changes the atom can be optically pumped into the other ground state, which is most likely to occur when its energy is lowest. The net effect is a cooling mechanism whereby the kinetic energy of the atoms is transformed into potential energy via the spatial modulation of the light-shift. The accumulated potential energy is then dissipated through blue-shifted spontaneous emission, cooling the atoms. The process can also be effective at cooling atoms in a MOT, where the polarisation gradients are more complicated.

In Chap. 3 the velocity-dependent forces that arise as a result of these effects are studied more quantitatively by solving the optical Bloch equations.

2.5 Trapping atoms with laser light

The majority of early proposals for neutral-atom light-force traps were based upon the conservative potential due to the interaction between the induced atomic dipole and electric field of the laser light [4, 33, 34]. The depths of these traps are shallow and the laser-cooling and slowing techniques were, for a long time, insufficient to realize these traps experimentally. This was despite the rapid progress that had being made in cooling and decelerating atomic beams and magnetic trapping of the

cooled atoms.

The development optical molasses technique allowed atoms to be cooled to far lower temperatures than had previously been demonstrated, close to what was then thought to be the "quantum limit" for the temperature of atoms cooled by laser light. Very soon after reporting the realisation of optical molasses, the same group made the first demonstration of optical trapping of atoms. By overlapping a tightly-focussed beam from a separate laser with the optical molasses, atoms were efficiently loaded into the dipole trap and accumulated at high densities. The first demonstration of the dipole trap is reported in [35]. It was estimated that the trap had a depth of ~5 mK, and contained about 500 atoms at densities of $10^{11} - 10^{12}$ cm^{-3}.

Some proposals also existed for optical traps based upon the spontaneous scattering force. One example is described in [36], where it is proposed a tetrahedral arrangement of diverging beams could form a trap for neutral dielectric particles such as atoms. However, in 1983 Ashkin and Gordon published a letter in which they prove an Earnshaw theorem for optical radiation: it is not possible to achieve a stable trap using only the spontaneous force [37]. It was later pointed out that the optical Earnshaw theorem did not generally apply to atoms with an internal structure [38]. Instead, the atom's structure could lead to a position-dependent proportionality between the Poynting vector of a laser and the force exerted due to the spontaneous force, induced via an external field for example. The first demonstration of the trapping of atoms by the spontaneous force was made in 1987 and is described in [6], wherein the authors credit the seminal idea for the trap to J. Dalibard. In their experiment a pulsed atomic beam of sodium atoms was first slowed using a frequency-chirped laser and then confined and cooled in three-dimensions using an arrangement combining optical molasses and an inhomogeneous magnetic field that would come to be referred to as a magneto-optical trap (MOT). The trap relied on the manipulation of the internal structure of the atom by a quadrupole magnetic field to induce an anisotropy in the radiation pressure exerted on the atom by the optical molasses. A relatively modest magnetic field induces Zeeman shifts in the frequencies of the atomic transitions that are comparable to the natural linewidth. This is sufficient to obtain a very large imbalance in the scattering rates from two counter-propagating beams. The arrangement used for obtaining confinement is illustrated in Fig. 2.3, for a single dimension. The trap depths and capture volumes obtained using the spontaneous force trap far exceeded those obtained for traps operating using the conservative dipole potential. Additionally, because the trap is dissipative, its capture velocity is far higher than the dipole trap, which greatly simplifies its loading. For these reasons MOTs are robust and able to load very large numbers of atoms.

The technique was quickly adopted by many groups and permitted entirely new

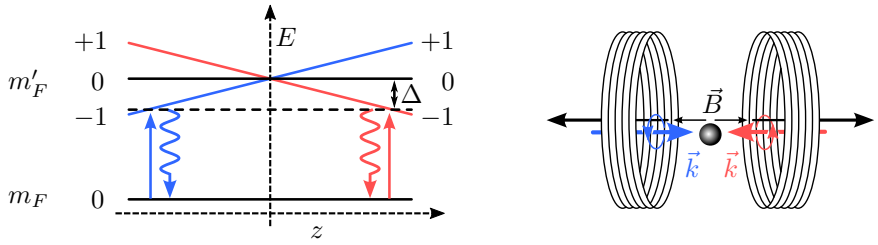

Figure 2.3: Understanding a simple MOT. Here, a ground-state with $F = 0$ is coupled to an excited-state with $F' = 1$, and $g'_F > 0$. Two counter-propagating circularly-polarised beams drive $\Delta m_F = \pm 1$ transitions, and are detuned by an amount Δ. The excited-state Zeeman sub-levels are coloured according to which of the two lasers excites them. For example, the beam propagating along $+\hat{z}$ drives σ^- transitions for $z < 0$ and σ^+ transitions for $z > 0$. The Zeeman shift of the excited state is $V_Z = g'_F m'_F \mu_B |B|$. The atom scatters photons at a higher rate from the beam with $\vec{k}$ opposite to its displacement, which tends to return the atom to the centre of the trap.

and productive fields of research to emerge, such as the study of ultra-cold collisions between atoms [39], and collective effects [40] between atoms confined at high densities. The observation that the capture velocity of MOTs was sufficiently high to permit loading from a background thermal vapour [41], for some species of atoms, and subsequent simplification of the experimental design aided the proliferation of the technique. The efficient cooling and large trap-depths in a MOT allowed unprecedented phase-space densities to be achieved. The focus of a number of groups soon became an exploration of the limits in performance of the MOT, motivated in part by the tantalising notion of observing Bose-Einstein condensation in an atomic vapour. As first observed experimentally in [40] the high densities of atoms in a MOT can lead to repulsive effects mediated by multiple photon scattering in the optically thick cloud. This radiation trapping limits the ultimate phase-space density achievable, and further increases can only be obtained by transferring to a conservative potential such as a magnetic or dipole trap. Despite this inherent limitation MOTs are simple to construct and are able to trap large numbers of atoms at high densities and low temperatures. The MOT is nowadays ubiquitous in modern atomic physics experiments and has directly led to many of the most significant developments in the field.

Spring constant of the magneto-optical trap

It is straightforward to calculate analytically the restoring force experienced by a simple atom in a magneto-optical trap. Consider an atom with $F = 0$ and $F' = 1$, and upper-state g-factor g'_F, which is displaced from the trap centre in the axial direction. The Zeeman interaction shifts the energies of the excited-state sub-levels by an amount

$$V_Z = m'_F g'_F \mu_B |B|, \tag{2.18}$$

where μ_{B} is the Bohr magneton and $|B|$ is the magnetic-field strength. The magnetic-field strength at a displacement z is $|B| = |zB'|$, where B' is the magnetic-field gradient at the trap centre in the axial direction. The Zeeman interaction shifts the frequencies of transitions to the excited-state sub-levels by an amount $\delta_Z = V_Z/\hbar$. In the low-intensity limit, where the forces exerted by each of the MOT beams are independent, the total force experienced by the atom is

$$F_{\mathrm{MOT}} = F_{\mathrm{Scatt}}(\Delta - \delta_Z) - F_{\mathrm{Scatt}}(\Delta + \delta_Z), \tag{2.19}$$

where Δ is the frequency detuning of the lasers from the atomic transition. For small displacements, such that $\delta_Z \ll \Delta$, the expression can be written as a Taylor expansion. Following a very similar method to that used to obtain Eq. 2.5 for the damping coefficient, one obtains

$$F_{\mathrm{MOT}} = -\kappa z \quad ; \quad \kappa = -\frac{8 g'_F \mu_{\mathrm{B}} B' k s \Delta}{\Gamma} \frac{1}{(1 + s + \frac{4\Delta^2}{\Gamma^2})^2}, \tag{2.20}$$

where the symbols have their usual meanings. For ^{87}Rb, $g'_F = 2/3$, and using the values $\Delta = -\Gamma$, $s = 0.1$, and $B' = 12$ G/cm, a value of $\kappa = 1.8 \times 10^{-19}$ N/m is obtained.

2.6 Type-I and type-II MOTs

The first experimental realisation of the magneto-optical trap is reported in [6]. The authors note that there are two situations in which a MOT of Na is formed. The first is when the lasers are tuned to the red side of the $F = 2 \rightarrow F' = 3$ and $F = 1 \rightarrow F' = 2$ transitions, and the second occurs when the lasers are tuned to the red of the $F = 2 \rightarrow F' = 2$ and $F = 1 \rightarrow F' = 0$ transitions. The properties of the MOTs formed for each of the two trapping configurations are very different. In the first configuration, where one laser is tuned close to the stronger $F = 2 \rightarrow F' = 3$ transition, 3×10^6 atoms are confined to a cloud with a Gaussian full-width at half-maximum (FWHM) of 320 µm, reaching peak densities of 2×10^{11} cm^{-3} at temperatures of ~600 µK. The cloud produced by the second trapping configuration contained up to 1.2×10^7 atoms but had a FWHM diameter of ~1 mm, implying the densities were only ~2×10^{10} cm^{-3}. Additionally, the temperature in the second trapping configuration was 2-3 orders of magnitude higher. In a subsequent investigation into the atom-density-dependent loss rates of the traps, the authors define the following nomenclature to distinguish between various trapping conditions: 'Type-I' behaviour is observed when the lowest-frequency laser is tuned close to the $F = 2 \rightarrow F' = 3$ transition and the repumper is tuned to the $F = 1 \rightarrow$

$F' = 2$ transition. 'Type-II' behaviour is observed when the lasers are tuned close to $F = 2 \rightarrow F' = 2$ and $F = 1 \rightarrow F' = 0$. It is now known that the weak confinement and high temperatures observed in the type-II trapping configuration reported in [6] are characteristic to any MOT where type-II transitions contribute significantly to the cooling or confinement, and that this is a consequence of the presence of dark ground-state Zeeman sub-levels.

Any transition with $F' \leq F$ has one or more dark ground-state sub-levels for a given laser polarisation, whereas for a transition with $F' = F + 1$, all the Zeeman sub-levels interact with light of any polarisation. This, then, is the definition of type-I and type-II transitions.

$$\text{Type-I:} \quad F' = F + 1 \tag{2.21a}$$

$$\text{Type-II:} \quad F' \leq F \tag{2.21b}$$

Virtually all subsequent experiments that have used MOTs of alkali-metal atoms have used the type-I trap. A common application of the MOT is to prepare atoms at high densities as the initial stage in more complicated experiments, such as making Bose-Einstein condensates (BEC), and studying cavity quantum-electrodynamics (QED). In these cases the type-I configuration is exclusively used, for obvious reasons. For a long period of time the type-II trapping scheme was largely overlooked and considered to be a curiosity rather than being deserving of a more focussed and concerted effort to understand its properties, despite the trapping and cooling mechanisms being poorly understood. There is one area of research that is an exception to this, which is the study of cold collisions between atoms.

The earliest experiments to measure the intra-trap collisional loss rate studied both the type-I and type-II configurations, observing a high intra-trap collisional loss rate in both cases [42]. The authors also note in the same study that the loss rates observed in the MOT are far higher than those observed previously in the far-off-resonance dipole trap, and thus infer the existence of additional loss mechanisms. Additional theoretical work recognised the importance of exoergic processes in trap loss rates when atoms are confined at ultra-cold temperatures, where collision times become comparable to the excited-state lifetime of the atom. These collisions are discussed in more detail in later chapters, where they are relevant to experimental measurements made for this thesis. Many subsequent investigations sought to understand these light-assisted collisions in more detail, while others recognised that in some cases type-II trapping schemes could be used to provide complementary measurements of the loss rates for atoms prepared in different hyperfine states. In [43] the authors compare the trap-loss rate coefficient for sodium atoms prepared in the $F = 2$ state by using a type-I MOT to that for atoms prepared predominantly in

the $F = 1$ state by using a type-II configuration. Notably in the type-II trap, where atoms are mainly in the lower hyperfine ground state, there are far fewer inelastic collisions between ground-state atoms. These collisions lead to trap loss at low laser intensity and are evident in the case of the type-I trapping scheme by a loss-rate coefficient that rapidly decreases as the intensity is increased from its lowest values. In a later investigation, reported in [44], type-II transitions in the D1 line of sodium are used to make a MOT. As the authors point out, in such a configuration collisions between ground and excited-state atoms in which the fine-structure quantum number J of the excited-state atom changes are non-existent. Trap loss resulting from collisions between ground and excited-state atoms is therefore primarily due to the radiative-escape mechanism and information on the loss rate coefficient due to this process can be obtained using this arrangement.

Other alkali-metal atoms have also been confined using type-II schemes. In [45] ^{85}Rb atoms are confined in the lower hyperfine ground state using a type-II MOT operating on the $F = 2 \rightarrow F' = 1$ transition. The type-II ^{85}Rb MOT exhibits the characteristically low density ($\sim 3 \times 10^8$ cm^{-3}) and high temperature (4.4 mK) common to all previously demonstrated comparable traps.

In conclusion, for a long period of time since the first demonstration of the MOT, type-II trapping schemes have been largely dismissed due to their low densities and high temperatures. There are few examples of investigations using these schemes, with most being for the purposes of measuring various loss rate coefficients. More recently, however, rapid progress has been made in the development of laser cooling and trapping techniques for molecules, where type-II transitions must be used. As a result of this there has been a renewed interest in obtaining a good understanding of the properties of type-II MOTs.

2.7 Sub-Doppler cooling in type-II systems

Following the demonstration of sub-Doppler cooling in an optical molasses, rapid progress was made on developing a comprehensive theoretical understanding of the new cooling mechanisms. A complex interplay between the energy level shifts due to the AC Stark effect and optical pumping between ground-state sub-levels can lead to an efficient cooling mechanism at low velocities. When this takes place in a magnetic field the dynamics of the system are further complicated by Zeeman shifts and Larmor precession of population between ground-state sub-levels. Competition between the processes can lead to a rich variety of effects and the manifestation of entirely new behaviour. In a MOT, for example, it is well known that magnetic fields can suppress sub-Doppler cooling, as explained in [46]. Under different conditions magnetic fields can actually facilitate laser cooling. In [47] a magnetic field applied

perpendicularly to a 1D optical molasses is shown to collimate the transverse velocity distribution of an atomic beam to sub-Doppler widths centred on non-zero velocities, a technique termed velocity-selective magnetic-resonance laser cooling. A separate cooling mechanism, magnetic-field-induced laser cooling, is demonstrated in [48] wherein a 1D optical molasses drives σ^+ transitions at all points, i.e. there are no gradients in intensity or ellipticity, yet sub-Doppler cooling is facilitated by a weak magnetic field that induces Larmor precession between the ground states at the nodes of the standing wave. These observations are explained in terms of velocity-selective Raman resonances between pairs of Zeeman-shifted ground states in [49].

Similar experiments were later conducted for a variety of different alkali-metal atoms. In [50], 1D sub-Doppler cooling on the caesium D2 line is investigated. Sub-Doppler cooling on both the $F = 4 \rightarrow F' = 5$ and $F = 3 \rightarrow F' = 2$ cycling transitions is studied for a number of molasses configurations and magnetic fields. While many of the results shared similarities with earlier experiments, one remarkable observation was made: sub-Doppler laser cooling on the $F = 3 \rightarrow F' = 2$ transition required blue-detuned light.

The observation that efficient sub-Doppler cooling could be performed on transitions with $F' \neq F+1$ prompted a number of proposals to cool atoms to low temperatures using a variety of schemes. In [51], the authors explore, both experimentally and theoretically, the magnetically-assisted Sisyphus effect for a $F = 1 \rightarrow F' = 1$ transition in a 1D molasses. The molasses is polarised to drive σ^+ transitions at all points in space, so that the $m_F = +1$ state is dark. The light-shifts of the other two states, which are both bright, are identical and modulated in space with the periodicity of the standing wave. At the nodes of the standing wave atoms are optically pumped into the dark state. At the anti-nodes of the molasses, mixing between the ground states is facilitated by a weak, transverse magnetic field. Crucially, in order to obtain cooling, the light must be blue-detuned from resonance. This cooling mechanism is illustrated in Fig. 2.4(a).

By a judicious arrangement of the relative polarisations of the molasses beams a closely related cooling effect can be obtained, which does not require a magnetic field. This 'non-adiabatic' cooling, described in [52], relies on motion-induced non-adiabatic transitions between bright and dark states, and requires the two beams to be linearly polarised and orientated with an angle $\phi \neq 0, \pi/2$. Sub-Doppler cooling via the non-adiabatic force is illustrated in Fig. 2.4(b).

A multidimensional optical molasses has a spatial periodicity in the intensity and ellipticity of the resulting light field, and the requirements for the relative polarisations of the beams are less stringent to realise an efficient non-adiabatic sub-Doppler cooling force. A number of experimental demonstrations of sub-Doppler laser cooling with blue-detuned light have been made. In [53], the authors cool caesium in three

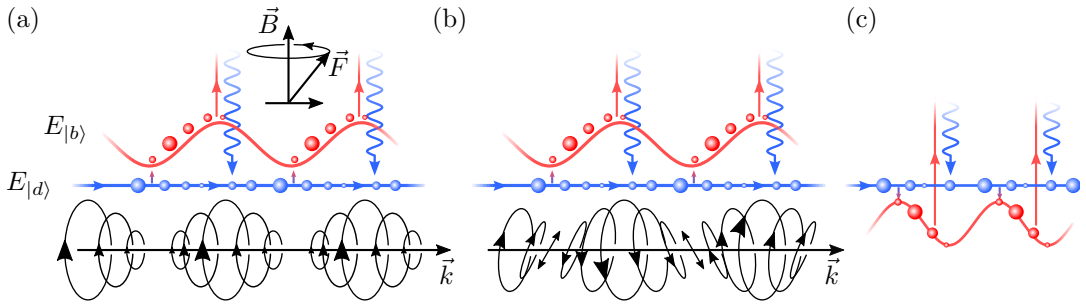

Figure 2.4: Sub-Doppler laser cooling schemes for $F = 1 \rightarrow F' = 1$ in 1D molasses using blue-detuned light. The solid black lines show the laser polarisation. (a) Magnetic-field-induced laser cooling. A weak magnetic field is applied transverse to the optical axis of the standing wave, which is circularly-polarised. Optical pumping to the dark state occurs at the anti-nodes where the light shift exceeds the Zeeman shift. Close to the nodes of the standing wave the Zeeman shift can exceed the light shift and the magnetic field mixes the bright and dark states. A particle in the bright state then climbs a potential hill due to the light shift before again being pumped to the dark state, which results in cooling. (b) Non-adiabatic force that leads to sub-Doppler cooling for a blue-detuning. Each beam is linearly polarised and there is an angle ϕ between the two polarisations. The resulting standing wave has a spatial variation in both intensity and ellipticity. The instantaneous dark state $|d\rangle$ depends upon the local laser polarisation. As the dark state evolves due to the motion through the molasses, a non-adiabatic transition can occur to the bright state $|b\rangle$. These non-adiabatic transitions are most likely to occur where the electric field amplitude is smallest, and as a result the energy separation between bright and dark states is minimal. (c) For red detuning the light shift of the bright ground states is negative, leading to heating effects.

dimensions using a four-beam molasses where the cooling light is tuned to the blue side of the $F = 3 \rightarrow F' = 2$ transition, and, in a subsequent study, temperatures as low as 1.1 µK were obtained using a 6-beam molasses [54]. In these studies the authors refer to the technique as 'gray-molasses' cooling. The key difference to the usual case of 'bright' molasses on a type-I transition is that most of the atoms are in dark states, hence the fluoresence rate of atoms in the gray molasses is far lower. It was stipulated that such a scheme might lead to higher phase-space-densities being obtainable in an optical molasses, where radiation trapping can inhibit efficient cooling [55]. A similar technique, whereby atoms are shelved in dark states to reduce the effects of radiation trapping, allows higher densities and longer lifetimes to be obtained than in a bright MOT and is known as the dark spontaneous-force optical trap, or dark-SPOT [56].

The gray-molasses technique has been successfully applied to other atomic species, such as Rb [57] and ^{40}K [58]. Recently, more exotic cooling schemes have been demonstrated using 'Λ-enhanced' gray-molasses, achieving efficient sub-Doppler cooling of the light alkali-metal atoms ^{40}K [59] and ^{7}Li [60].

In Chap. 3 these ideas are discussed in more detail and quantitative results are obtained by solving the optical Bloch equations for a variety of different cases relevant to the experimental investigation presented in later chapters.

2.8 Laser cooling and magneto-optical trapping of molecules

There are a vast number of proposed applications of ultra-cold molecules. These include precision tests of fundamental physics [61], platforms for quantum information processing [16, 62], controlled chemistry and the study of ultra-cold collisions, the study of new quantum phases and phase transitions, and many more [63]. The availability of additional internal degrees of freedom, tuneable interactions and existence of a permanent electric dipole moment offer the experimenter a variety of handles with which to interact and manipulate samples that are not present in cold atomic gases. A cold, dense source of molecules would provide an ideal, universally applicable starting point from which to investigate many proposed applications. Just as the atomic MOT revolutionised the field of atomic physics, so it is hoped similarly productive fields of new research might be facilitated by an analogous technique for molecules.

There are two routes to obtaining cold molecules. The first is via the manipulation and cohesion of cold atoms. For example, in [64] weakly-bound Feshbach molecules of ^{87}Rb^{133}Cs are formed by magnetoassociation in a levitated dipole

trap and then transferred to the deeply-bound ro-vibrational ground state using stimulated-Raman-adiabatic-passage (STIRAP). The second route is via the direct cooling and trapping of thermal molecules. Falling into the latter category, laser cooling and trapping has recently emerged as a promising technique to obtain large, dense samples of cold molecules.

Many of the proposed applications of cold molecules make use of the extra degrees of freedom a molecule possesses. While this large internal state-space is appealing for many reasons, it is also the reason why, for many years, direct laser cooling and trapping of molecules has seemed implausible. In general, the vibrational and rotational degrees of freedom possessed by a molecule prohibit any feasible optical-cycling scheme from being realised. Hence, laser slowing and cooling remained elusive for some time.

2.8.1 Slowing molecules with laser light

In 2009 E. S. Shuman et al. demonstrated the first deflection of a beam of strontium monofluoride molecules by resonance radiation pressure [65]. A year later Doppler and sub-Doppler transverse cooling of the beam were demonstrated [66]. The key to these breakthroughs was in the devising of an optical cycling scheme that was sufficiently closed as to require an experimentally plausible number of cooling and re-pumping lasers.

Diatomic molecules, in addition to having nuclear, electronic orbital, and intrinsic spin angular momentum are able to rotate and vibrate. These degrees of freedom are labelled by the quantum numbers N and ν when writing the wavefunction. In an electronic transition there are no selection rules for the vibrational quantum number. Instead, the likelihood of ν changing following the spontaneous emission of a photon from the excited state is given by the Franck-Condon factors. These numerical factors are found by evaluating the overlap in the vibrational wave function of the excited-state with the wavefunctions of ground states corresponding to different vibrational quantum numbers. Each of the electronic states of a molecule consists of a manifold of vibrational states, and each vibrational state contains a manifold of rotational states. The energy separation between states with different rotational and vibrational quantum numbers is sufficiently large that separate lasers are needed to address states of different ν. When there is a net nuclear spin each of the ro-vibrational states is further split by the hyperfine interaction, giving rise to the kind of energy level structure illustrated in Fig. 2.5. Herein lies the difficulty in laser cooling and slowing molecules.

The number of ground states populated by spontaneous decay can be greatly reduced by a careful choice of the ro-vibrational ground state used in the cooling

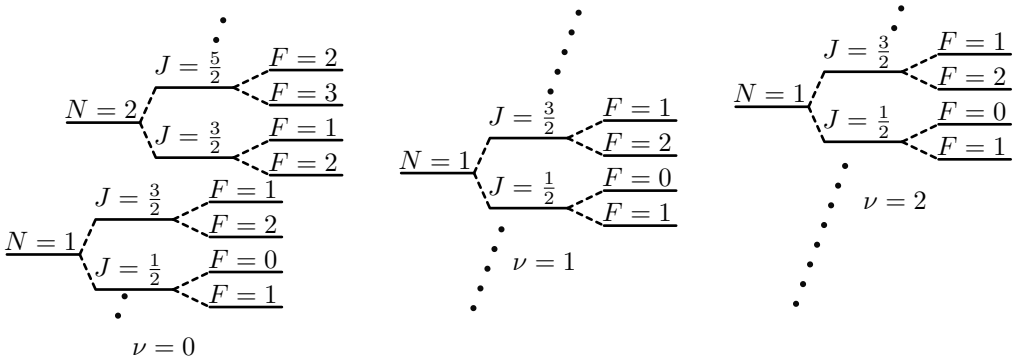

Figure 2.5: Typical hyperfine structure of a molecule in its ground electronic state. The spin-rotation interaction couples the intrinsic electron spin S to the rotational angular momentum N giving a total angular momentum labelled by the quantum number $J = N \pm S$. The nuclear spin I couples to J to give the hyperfine splitting. Here, $I = \frac{1}{2}$. The ground state has multiple vibrational states $\nu = 0, 1, 2 \ldots$ and each vibrational state has multiple rotational states.

scheme. In [67] the authors propose a laser-cooling and magneto-optical trapping scheme for the dipolar molecule TiO. By exploiting the selection rules for dipole-allowed transitions a rotationally-closed cycling scheme is possible. Additionally, using a molecule with a highly diagonal Frack-Condon factor reduces the likelihood of the excited state decaying to higher-energy vibrational states, further closing the optical cycling scheme. These principles have been applied by a number of separate groups to demonstrate laser slowing and cooling of SrF in 2009 [65], YO in 2013 [68] and CaF in 2014 [69].

The use of a rotationally-closed laser-cooling scheme has a very important implication for the hyperfine angular momentum quantum number and, in turn, the physics of laser cooling. Dipole-allowed transitions between hyperfine states of these molecules in a rotationally closed scheme necessarily include type-II transitions. This means that some of the Zeeman sub-levels in each of the ground states are dark, and molecules will be optically pumped into those states and undergo no further cooling. This is in contrast to the schemes for alkali-metal atoms, where $F' = F + 1$, and all of the ground-state sub-levels are bright. The solution to the dark-state problem is straightforward when considering laser slowing of a fast-moving molecular beam, where the slowing and cooling is along a single well-defined axis. Consider the case illustrated in Fig. 2.6, where a linearly polarised beam couples a ground state with $F = 1$ to an excited state with $F' = 1$. The light is linearly polarised and its electric-field vector lies in the same plane as the magnetic-field vector generated by some external source. The two vectors are separated by an angle θ. In the absence of the magnetic field, and for any static polarisation of the light, there is a time-independent dark ground state into which atoms are eventually pumped. In general, this dark state is a superposition of different m_F states. The theory of dark-state destabilisation is discussed in [70], where two methods are

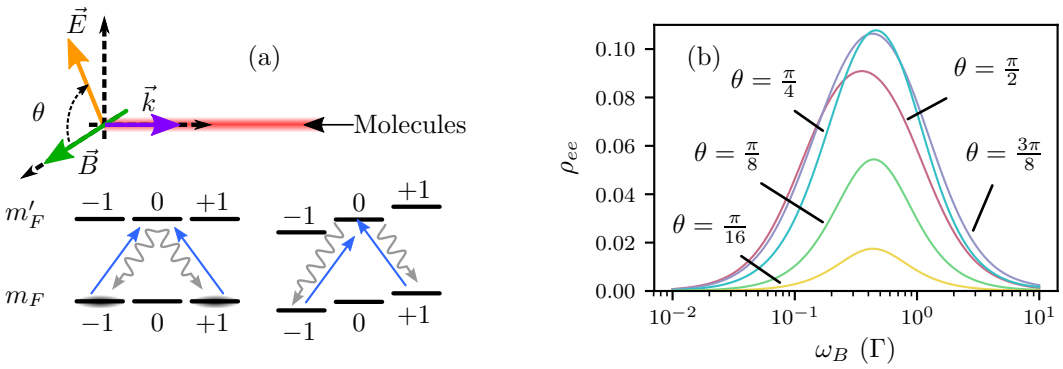

Figure 2.6: Brightening of dark states in a molecular-beam-slowing experiment where $F' = F = 1$. A magnetic field is used to destabilise the dark state. (a) The light has a linear polarisation and subtends an angle θ with the magnetic field direction. For $\theta = \pi/2$, and quantisation axis along $\vec{B}$ the light drives $\sigma^{\pm}$ transitions, leading to a three-level lambda scheme. A dark state exists that is a coherent superposition of ground states. The magnetic field shifts the energies of these states so that the dark state evolves in time. (b) Excited-state population of a system with $F = 1 \rightarrow F' = 1$ calculated by numerically solving the OBEs, using the model described in Chap. 3, with $\Delta = 0$, and $I = I_{\text{sat}}$. The population shown is obtained after a time $t = 500\ \Gamma^{-1}$. The light is linearly polarised and there is an angle θ between the polarisation and the external magnetic field. The magnitude of the magnetic field is expressed in terms of $\hbar\omega_B = \mu_{\text{B}} B$ and the g-factors of the ground and excited states are $\frac{1}{2}$ and $\frac{2}{3}$, respectively. The Zeeman shift of the $m_F = +1$ state is $\frac{1}{2}\hbar\omega_B$.

considered: destabilisation via application of a magnetic field, and destabilisation via modulation of the polarisation of the light. Both of these techniques impart a time-dependence to the dark state. If the dark state evolves at a rate comparable to the optical pumping time, then it is never significantly populated. Fig. 2.6(b) shows the results of some simulations that illustrate the effect of the magnetic field on the dark-state fraction. The results are obtained by solving the optical Bloch equations, using the model described in Chap. 3, for the system illustrated in the figure. The excited-state population is calculated after an optical pumping duration $t = 500\ \Gamma$ for a variety of magnetic-field amplitudes and orientations. When $\theta = 0$ the light drives π transitions and the dark state is simply $|m_F = 0\rangle$. Since the dark state consists of a single Zeeman sub-level the presence of the magnetic field does not induce a time dependence. Hence, for small values of θ this method is ineffective. For $\theta = \pi/2$ the light drives $\sigma^{\pm}$ transitions and the dark, non-coupled state is $|\text{NC}\rangle = \frac{1}{\sqrt{2}}(|m_F = -1\rangle + |m_F = +1\rangle)$. The magnetic field shifts the energies of the $m_F = \pm 1$ states in opposite directions so that the dark state evolves in time, as indicated in the figure. When $\omega_B \gg \Gamma$ transitions are Zeeman shifted out of resonance, and the excited-state fraction decreases.

2.8.2 Molecular MOT

Brightening dark molecular ground states in laser slowing experiments is straightforward. However, to achieve any confinement using a type-II transition via a conventional magneto-optical force requires a more complicated method. In a MOT there is a fixed geometry between the direction of the magnetic field, which is used to induce an anisotropic radiation pressure, and the electric-field vector of the MOT light. For an atom or molecule displaced from the magnetic-field zero of the MOT the restoring beam is Zeeman-shifted closer to resonance than the anti-restoring beam. However, the particle can only scatter a few photons before it is pumped into the state that is dark to the restoring beam. From there it can only absorb from the anti-restoring beam and, over many cycles, the net force averages to zero. For a static magnetic-field direction and 1D circularly-polarised light there is no steady-state magneto-optical trapping force for a type-II system. To obtain a restoring force the polarisation of the trapping light and the direction of the magnetic field can be synchronously reversed as illustrated in Fig. 2.7, brightening the ground state. The synchronised reversal of both the polarisation handedness of the light and the magnetic-field direction ensures the sign of the force does not vary between cycles. This idea was initially used to compress a beam of YO molecules in one transverse dimension [68]. Later, it was applied to a 3D MOT [71], which resulted in improved confinement and lower temperatures.

Magneto-optical trapping of a diatomic molecule in three dimensions was first achieved by J. Barry et al. in 2014 [13] using SrF. The authors report the observation of a MOT with axial spring constant $5.9(4) \times 10^{-21}$ N m^{-1} and axial temperature 2.1(1) mK. As noted in that article the measured temperature is an order of magnitude higher than the Doppler temperature for SrF and the spring constant is 2-3 orders of magnitude smaller than for atomic type-I MOTs. The authors refer to similar observations made for type-II atomic MOTs and note the lack of a widely accepted understanding of the mechanisms of the confining force in type-II MOTs in the literature at that time.

2.8.3 Improving the properties of molecular MOTs

The lack of a comprehensive understanding of the properties of type-II MOTs, coupled with the rapid experimental progression and first observation of trapping in three dimensions motivated additional theoretical work. One of the most glaring disparities between the first MOT of SrF and existing atomic MOTs was the relatively weak confinement. In an early study of the properties of a MOT of Rb spring constants up to $\kappa_{\mathrm{Rb}} \sim 3 \times 10^{-18}$ N m^{-1} are reported, whereas for the molecule MOT $\kappa_{\mathrm{SrF}} = 5.9(4) \times 10^{-21}$ N m^{-1}. The disparity is attributable to the presence of the

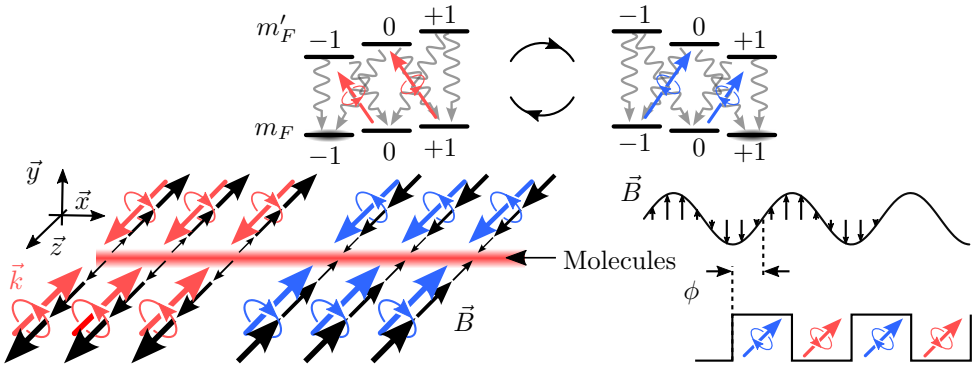

Figure 2.7: Illustrations of the method used for transverse magneto-optical compression of YO in [68]. Here, the g-factors of the upper and lower states are positive. The magnetic-field is indicated by the black arrows, which are aligned along $\vec{z}$ and define the quantisation axis. The coloured arrows indicate the k-vector and polarisation of the laser light. A Pockels cell is used to periodically modulate the handedness of the polarisation. The magnetic-field amplitude is driven at the same frequency, and with a constant phase difference, to the Pockels cell driving signal. The magneto-optical force is observed to be greatest when $\phi = 0$.

dark ground-state sub-levels mentioned previously. In fact, for any restoring force to exist at all there must be some mechanism to mix dark and bright states. In the 3D static MOT, molecules are prevented from accumulating in dark states due to their motion through the complex gradients of polarisation, and due to Larmor precession induced by the quadrupole field. The essential physics required to qualitatively model the properties of the confining force in the SrF MOT is contained within a rate-equation model where the whole set of excited and ground state Zeeman sub-levels are considered as well as all three pairs of counter-propagating laser beams. In such a model, the action of the orthogonal laser beams can lead to a net restoring force. This rate-equation approach was used by M. R. Tarbutt [72] to propose a set of general rules to consider when choosing the polarisation of light to be used in a magneto optical trap. An illustration of these rules for a transition with $F' = F = 1$ is given in Fig. 2.8 and a discussion of those rules is given in the caption of the figure. The findings presented in [72] assert that the choice of polarisation for the restoring beam should be determined solely by the sign of the g-factor of the excited state. This is in contrast to the methodology used for the SrF MOT, where the authors state that the optimal polarisation is determined by the sign of the difference in g-factors between the upper and lower states. This insight led to the suggestion of an improved trapping scheme for the SrF MOT and subsequent increase of the spring constant by about a factor of 20, as reported in [71]. Additionally, the lifetime of the trap and trapped molecule number was observed to be significantly higher using the revised polarisations.

One further observation following the implementation of the revised polarisation scheme was that the temperature increased by almost a factor of 6, rising to ~11 mK.

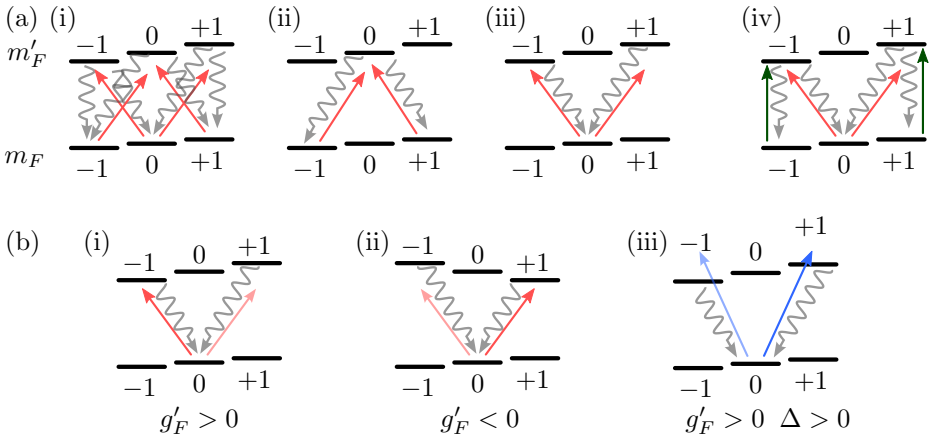

Figure 2.8: Understanding MOT forces in an $F = 1 \rightarrow F' = 1$ system in 3D. An atom is displaced from the magnetic zero at the trap centre along one of the principal axes and interacts with six circularly-polarised beams in the usual way, which is described in Sec. 2.1 and Fig. 2.3. The radiation pressure from one of the beams pushes the atom back towards the centre—this is called the restoring beam. The counter-propagating beam is called the anti-restoring beam. The other four beams are referred to as orthogonal beams. (a)(i) Spontaneous decay of the excited state sub-levels and $\sigma^{\pm}$ transitions from the ground-state. All line strength factors are equal for $F' = F = 1$. (ii) $m'_F = 0$ decays with equal probability to $m_F = \pm 1$, where atoms are dark to either the restoring or anti-restoring beam. Atoms in these states always decay back to $m_F = \pm 1$ following excitation to $m_F = 0$ and so do not contribute to the confining force. (iii) Atoms in $m_F = 0$ can absorb photons from either the restoring or anti-restoring beam and the rates are different due to the Zeeman shift of the excited states. When the excited state g-factor is positive, as shown here, the instantaneous rate of transitions with $\Delta m_F = -1$ is faster. In the absence of the orthogonal beams the average force is still zero because the population in $m_F = 0$ falls to zero. (iv) π transitions are driven by orthogonal laser beams in the MOT, which return atoms from $m_F = \pm 1$ to $m_F = 0$. When the restoring beam is polarised to drive σ^- transitions, a small confining force is recovered due to the steady-state population in $m_F = 0$. (b)(i) Relevant transitions contributing to the MOT force. The restoring beam should be polarised to drive the transitions shown in bold. (ii) The polarisation of the restoring beam should be reversed if the sign of the upper-state g-factor is changed or if the sign of the detuning is changed (iii).

This is despite the authors measuring an increase in the motional damping coefficient of the trap by over a factor of two. A large discrepancy also existed between the theoretical damping coefficient of the trap, as predicted by the rate equation model, and the observed value. The situation is reminiscent of the first experimental observation of sub-Doppler temperatures in an atomic MOT. In both cases a rate-equation approach had failed to accurately model the velocity-dependent forces in the MOT, and the observed temperature of the trapped atoms was at odds with the theory. The striking difference between these two situations is that, for the atomic case, temperatures far lower than the Doppler limit were observed, suggesting additional cooling mechanisms, whereas for the improved SrF MOT the temperature was almost 70 times higher than the Doppler theory predicts.

Substantial theoretical progress was made on understanding the properties of type-II MOTs by J. A. Devlin and M. R. Tarbutt in [73]. In that paper the authors present a comprehensive theoretical model which considers the force exerted on an atom or molecule in a MOT due to the magneto-optical, Doppler, and polarisation-gradient forces for a variety of different angular momentum cases. In order to calculate the polarisation-gradient forces the optical Bloch equations are solved. These forces arise due to modifications to the ground-state energy levels or populations caused by stimulated processes between pairs of ground states. The authors are able to show that, for the angular momentum structure relevant to a type-II MOT, sub-Doppler processes lead to strong heating effects at small velocities when the light is red detuned. These effects persist over the whole range of magnetic field amplitudes an atom or molecule would explore in a typical MOT, and help to explain the observed behaviour of the temperature and damping coefficients in type-II MOTs.

The experimental realisation of an RF MOT for SrF was reported by E. B. Norrgard et al. in [74], 2016. In that experiment dark Zeeman sub-levels are actively destabilised at a rate comparable to the optical-pumping time using a synchronous reversal of the magnetic-field and polarisation handedness. The method is identical in principle to that which had earlier been used to transversely compress a beam of YO molecules, illustrated in Fig. 2.7. By applying this technique to destabilising dark states the scattering rate from the restoring beam can be dramatically increased. In addition to increasing the confinement this has the effect of allowing the Doppler cooling to be far more efficient in the MOT. Using this technique temperatures as low as 400 µK have been observed, far closer to the Doppler-cooling limit. The phase-space density was observed to be up to 3 orders of magnitude higher using this method but it is technically challenging to implement due to the use of high-power, RF magnetic-field coils and polarisation-modulation optics.

Using the insight that recent theoretical work has provided, magneto-optical

trapping and sub-Doppler cooling of the CaF molecule has been demonstrated by S. Truppe et al. [14]. Sub-Doppler temperatures are obtained using a technique similar to the gray-molasses cooling demonstrated in the alkali-metal atoms.

Impressive progress has been made in the laser cooling and trapping of molecules in recent years. Still, the phase-space densities obtained for laser-cooled molecules remains many orders of magnitude below that routinely achieved with type-I atomic MOTs, and below what is needed to realise many proposed applications. This is in part due to the difficulty in obtaining a high flux of slow molecules suitable for loading into a MOT, but also due to the very low temperature-limited-density obtainable using molecules confined in a conventional MOT. Great increases in the phase-space density of type-II MOTs might be obtainable if the strong sub-Doppler cooling demonstrated using the gray-molasses technique could be reconciled with the confinement obtainable in a MOT. The feasibility of this proposal will be explored in more detail in the following chapter.

3 Theories and models of laser cooling and magneto-optical trapping

The Doppler theory of laser cooling fails to correctly predict the lowest temperatures that are routinely observed when atoms are cooled in an optical molasses or magneto optical trap. New cooling mechanisms facilitated by the multi-level structure of the atom were first proposed by J. Dalibard and C. Cohen-Tannoudji in [31] and P. J. Ungar et al. [32].

Experimental observations of red-detuned type-II MOTs have revealed properties that are very different to those of their type-I counterparts. Typically, the temperatures reported for red-detuned type-II MOTs far exceed the Doppler-cooling limit for the atom or molecule being trapped. This is despite the many existing, highly successful laser cooling techniques in which atoms are cooled to sub-Doppler temperatures using type-II transitions. Clearly, the type-II nature of an atom or molecule is not an inherent obstacle to performing efficient laser cooling. If the low temperatures demonstrated using, for example, the gray molasses technique could be reconciled with the spatial confinement of atoms in a MOT then a great increase in the performance of type-II MOTs could be obtained.

In this section an overview of the theory of sub-Doppler laser cooling is provided. Using a density-matrix approach the velocity and position-dependent forces experienced by an atom in a magneto-optical trap are quantitatively investigated for a variety of angular momentum cases relevant to the investigation presented in this thesis. In particular, subtle differences in the mechanisms that lead to sub-Doppler cooling in type-I and type-II systems are highlighted. It is shown that even small magnetic fields disrupt sub-Doppler cooling in type-I systems. For type-II systems, however, sub-Doppler cooling is facilitated by transitions between a bright state and a velocity-selective dark state. The dark state can be destabilised by an external magnetic field, but is still most efficiently populated when the velocity-selective resonance condition is met. This effect is robust, persisting for magnetic-field amplitudes where the type-I mechanism is inhibited, and implies that efficient cooling should be possible in a MOT, even when the magnetic-field gradient is large.

3.1 The atom-field interaction Hamiltonian for a multi-level system

In this section the atom-field interaction Hamiltonian is written for a multi-level atom, and a method of obtaining a matrix representation of the Hamiltonian in terms of a reduced dipole matrix element is described. The atom is multi-level because the ground-state, excited-state, or both ground and excited-states posses non-zero angular momentum. Only a single hyperfine level of the ground and excited states are considered, so the atom remains fictional. The non-zero angular momentum is sufficient to allow insight to be gained into the sub-Doppler processes, whilst remaining more computationally tractable than if the entire hyperfine structure were to be considered. This approach is especially suitable for studying a type-II MOT of rubidium, where the separation between different excited-state hyperfine levels is much larger than a typical laser detuning used in a MOT. Atoms in either ground state can then be considered to be coupled to a single excited state and the two ground states can be considered individually.

3.1.1 Basis

The basis used is the set of simultaneous eigenstates of a general angular momentum operator $\hat{F}^2$, and the operator that projects the angular momentum onto the z axis, $\hat{F}_z$. The angular momentum and magnetic quantum numbers are written as F and m_F for the electronic ground state and F' and m'_F for the electronic excited state. The basis of states is therefore $\{|F, m_F\rangle, |F', m'_F\rangle\}$, where

$$\hat{F}^2|F, m_F\rangle = F(F+1)\hbar^2|F, m_F\rangle, \tag{3.1a}$$

$$\hat{F}_z|F, m_F\rangle = m_F\hbar|F, m_F\rangle, \tag{3.1b}$$

and similarly for the primed quantities. Allowed values of m_F are $-F \leq m_F \leq F$. Having defined a representation by setting $|F, m_F = -F\rangle = (100\ldots)^\intercal$, $|F, m_F = -F+1\rangle = (010\ldots)^\intercal$ etc., the matrix-elements of the atom-field Hamiltonian can be evaluated in this basis.

3.1.2 Saturation intensity

There are a number of conventions for the reduction of the dipole-moment operator in use in the literature: in some cases the matrix elements of the atom-field Hamiltonian are written in terms of the reduced matrix element $\langle F'||d^{(1)}||F\rangle$, elsewhere the conjugate value $\langle F||d^{(1)}||F'\rangle$ is used. $d^{(1)}$ is the atomic dipole-moment operator

written in spherical tensor notation. A spherical tensor operator of rank k is written $T^{(k)}$ and has $2k+1$ components labelled by q, $T^{(k)}_q$. There are also different conventions for how the normalisation of the reduced matrix element of the dipole-moment operator is defined. To begin this section, the linewidth of a transition is related to the reduced matrix element for that transition. This allows a saturation intensity to be defined for a given F and F', and the elements of the atom-field interaction Hamiltonian to be specified in terms of this.

It is a result from the quantisation of the electromagnetic field in quantum optics that the decay rate from a state $|F', m'_F\rangle$ to a state $|F, m_F\rangle$ is given by,

$$\Gamma_{F',m'_F,F,m_F} = \frac{\omega_0^3}{3\pi\epsilon_0\hbar c^3}|\langle F, m_F|d^{(1)}|F', m'_F\rangle|^2, \tag{3.2}$$

where $\hbar\omega_0 = E_{F'} - E_F$ is the energy separation between the ground and excited states, and the other symbols have their usual meaning. A single excited state F', and single ground state F are considered. There are $2F+1$ Zeeman sub-levels in the ground state and $2F'+1$ Zeeman sub-levels in the excited state. The total decay rate of an excited state sub-level is obtained by summing over the different possible decay channels, $\Gamma_{F',m'_F} = \sum_{m_F}\Gamma_{F',m'_F,F,m_F}$,

$$\Gamma_{F',m'_F} = \frac{\omega_0^3}{3\pi\epsilon_0\hbar c^3}\sum_{m_F}|\langle F, m_F|d^{(1)}|F', m'_F\rangle|^2. \tag{3.3}$$

Decays from the excited state caused by spontaneous emission are independent of the orientation of the excited-state atom, each of the sub-levels decays at the same rate $\Gamma_{F',m'_F} \equiv \Gamma$ and $\sum_{m'_F}\Gamma = (2F'+1)\Gamma$. Therefore,

$$\Gamma = \frac{\omega_0^3}{3\pi\epsilon_0\hbar c^3}\frac{1}{2F'+1}\sum_{m_F,m'_F}|\langle F, m_F|d^{(1)}|F', m'_F\rangle|^2. \tag{3.4}$$

Following the normalisation convention for the reduced matrix element used by Brink and Satchler[1] one can write

$$|\langle F||d^{(1)}||F'\rangle|^2 = \sum_{m'_F}|\langle F m_F|d^{(1)}|F', m'_F\rangle|^2. \tag{3.5}$$

Substitution of Eq. 3.5 into Eq. 3.4, and by once again noting the resulting summand does not depend on m_F, the following expression is obtained

$$\Gamma = \frac{\omega_0^3}{3\pi\epsilon_0\hbar c^3}\frac{2F+1}{2F'+1}|\langle F||d^{(1)}||F'\rangle|^2. \tag{3.6}$$

[1]D. M. Brink and G. R. Satchler, Angular Momentum, 2nd ed. (Oxford, 1968), Section 4.7, p. 56.

This expression can now be used to define a saturation parameter $p = I/I_s$ in terms of the reduced matrix element of the dipole-moment operator for a given F', F. The electric-field amplitude E of an electromagnetic wave is related to the intensity of the light by $I = \frac{1}{2}c\epsilon_0 E^2$, and the saturation intensity for a two-level atom is $I_s = \pi hc\Gamma/3\lambda^3$ [75]. Using these expressions the saturation parameter p can be defined,

$$p = \frac{I}{I_s} = \frac{3c\epsilon_0 E^2 \lambda^3}{2\pi hc\Gamma}. \tag{3.7}$$

Multiplying this expression by Γ/Γ and substitution of Eq. 3.6 results in the expression,

$$p = \frac{I}{I_s} = \frac{2E^2}{\hbar^2\Gamma^2}\frac{2F+1}{2F'+1}|\langle F||d^{(1)}||F'\rangle|^2. \tag{3.8}$$

Eq. 3.8 allows the electric field amplitude of the light to be written in terms of a reduced matrix element, the dimensionless saturation parameter p, the multiplicity of the state, and the excited state lifetime. A similar expression is used in [73].

3.1.3 The atom-field interaction

In order to explicitly write the rotating wave approximation in a concise expression, it is convenient to temporarily introduce the notation $\mathbf{d} \equiv d^{(1)}$. By definition, the components of the spherical tensor operator $d^{(1)}$ transform under rotations like the components of a Cartesian three-vector, so this notation is suitable. The Hamiltonian describing the interaction between the atom and the laser field is,

$$H_{\mathrm{AF}} = -\mathbf{d} \cdot \mathbf{E}(z,t), \tag{3.9}$$

where $\mathbf{d}$ is the atomic dipole-moment operator, and $\mathbf{E}(z,t)$ is the electric-field operator of the laser field. As usual, the dipole approximation is used, and the rotating-wave approximation will now be made.

To make the rotating-wave approximation, the atomic dipole-moment operator is expanded into its raising and lowering components by left-multiplying and right-multiplying by the identity operator, which is constructed from the basis states like

$$\mathcal{I} = \sum_{m_F, m'_F} |F, m_F\rangle\langle F, m_F| \; + \; |F', m'_F\rangle\langle F', m'_F|. \tag{3.10}$$

Only matrix elements of the dipole-moment operator taken between states of oppo-

site parity are non-zero, the result is

$$\mathbf{d} = \sum_{m_F, m'_F} |F, m_F\rangle\langle F', m'_F|\langle F, m_F|\mathbf{d}|F', m'_F\rangle + |F', m'_F\rangle\langle F, m_F|\langle F', m'_F|\mathbf{d}|F, m_F\rangle \tag{3.11}$$

$$= \sum_{m_F, m'_F} \sigma_{m_F, m'_F}\langle F, m_F|\mathbf{d}|F', m'_F\rangle + \sigma^{\dagger}_{m_F, m'_F}\langle F', m'_F|\mathbf{d}|F, m_F\rangle, \tag{3.12}$$

where the atomic lowering operator σ_{m,m'_F} and raising operator $\sigma^{\dagger}_{m,m'_F}$ have been defined for brevity. The state $|F, m_F\rangle$ has time-dependence $e^{-iE_g t/\hbar}$, and the state $|F', m'_F\rangle$ has time-dependence $e^{-iE_e t/\hbar}$, and so the expectation value of σ_{m_F,m'_F} has the time-dependence $e^{-i(E_e-E_g)t/\hbar} = e^{-i\omega_0 t}$. Similarly, the expectation value of $\sigma^{\dagger}_{m_F,m'_F}$ has time dependence $e^{i\omega_0 t}$. In accordance with the time dependence of the expectation values of the raising and lowering operators, the dipole-moment operator is written in terms of the positive and negative-frequency components, $\mathbf{d} = \mathbf{d}^{(+)} + \mathbf{d}^{(-)}$, where $\mathbf{d}^{(+)} \propto e^{-i\omega_o t}$ is the component that rotates with a positive frequency. The electric-field operator is similarly expanded in terms of its positive and negative-frequency components, $\mathbf{E}(z,t) = \mathbf{E}^{(+)}(z)e^{-i\omega_L t} + \mathbf{E}^{(-)}(z)e^{i\omega_L t}$. The interaction between the atomic dipole moment and the electric field is,

$$-\mathbf{d}\cdot\mathbf{E} = \left(\mathbf{d}^{(+)} + \mathbf{d}^{(-)}\right)\cdot\left(\mathbf{E}^{(+)}(z)e^{-i\omega_L t} + \mathbf{E}^{(-)}(z)e^{i\omega_L t}\right). \tag{3.13}$$

When the laser light is close to resonance with only a single excited-state, so that $\omega_L \approx \omega_0$, then the rotating wave approximation (RWA) can be made. Within the RWA the components of $-\mathbf{d}\cdot\mathbf{E}$ whose expectation values evolve at optical frequencies $\propto \omega_0 + \omega_L$ are replaced by their zero-value average, whilst the components that evolve at the much slower rate $\propto \omega_0 - \omega_L$ are retained. The atom-field interaction Hamiltonian in the rotating wave approximation is therefore,

$$-\mathbf{d}\cdot\mathbf{E} = -\mathbf{d}^{(+)}\cdot\mathbf{E}^{(-)}(z)e^{i\omega_L t} - \mathbf{d}^{(-)}\cdot\mathbf{E}^{(+)}(z)e^{-i\omega_L t}. \tag{3.14}$$

The dot-product in Eq. 3.14 can now be written as a sum over the components of the vector operators. It is now convenient to return to spherical basis notation, so that the following expression is obtained,

$$-\mathbf{d}\cdot\mathbf{E} = -\sum_q (-1)^q (d^{(+)}_q E^{(-)}_{-q}(z)e^{i\omega_L t} + d^{(-)}_q E^{(+)}_{-q}(z)e^{-i\omega_L t}). \tag{3.15}$$

This is a convenient basis to use because each of the components of the electric field couples a ground-state sub-level to, at most, one sub-level in the excited state. The

components of the dipole-moment operator are given by

$$d_q^{(+)} = \sum_{m_F, m'_F} |F, m_F\rangle\langle F', m'_F|\langle F, m_F|d_q|F', m'_F\rangle, \tag{3.16a}$$

and

$$d_q^{(-)} = \sum_{m_F, m'_F} |F', m'_F\rangle\langle F, m_F|\langle F', m'_F|d_q|F, m_F\rangle. \tag{3.16b}$$

The matrix elements of the dipole moment operator can be evaluated using the Wigner-Eckart theorem. The key assertion of the Wigner-Eckart theorem is that these matrix elements can be written as a product of a reduced matrix element, which does not depend on the magnetic quantum number, and a Clebsch-Gordon coefficient. The reduced matrix element is written $\langle \alpha F||d^{(1)}||\alpha' F'\rangle$, and depends on the quantum numbers I, S, L, J, n, summarised by α. The components of a spherical tensor operator $T_q^{(k)}$, transform among themselves in an identical way to an angular momentum eigenstate $|k, q\rangle$. Therefore the object $d_q^{(k)}|F', m'_F\rangle$ transforms like the composite state $|k, q\rangle|F', m'_F\rangle$, which is written more compactly as $|F', m'_F; k, q\rangle$. The Clebsch-Gordon coefficient to be evaluated is $\langle F, m_F|F', m'_F; k, q\rangle$. The dipole-moment operator is a rank-1 tensor, and so $k = 1$. Eqs. 3.16, written in terms of reduced matrix elements and Clebsch-Gordon coefficients, are given by

$$d_q^{(+)} = \langle \alpha F||d^{(1)}||\alpha' F'\rangle \sum_{m_F, m'_F} |F, m_F\rangle\langle F', m'_F|\langle F, m_F|F', m'_F; 1, q\rangle, \tag{3.17a}$$

and

$$d_q^{(-)} = \langle \alpha' F'||d^{(1)}||\alpha F\rangle \sum_{m_F, m'_F} |F', m'_F\rangle\langle F, m_F|\langle F', m'_F|F, m_F; 1, q\rangle. \tag{3.17b}$$

To make the expressions more symmetrical the following relationship can be used,

$$\begin{aligned}\langle \alpha' F'||d^{(1)}||\alpha F\rangle\langle F', m'_F|F, m_F; 1, q\rangle \\ = \langle \alpha F||d^{(1)}||\alpha' F'\rangle\langle F, m_F|F', m'_F; 1, -q\rangle(-1)^{m_F - m'_F}.\end{aligned} \tag{3.18}$$

Denoting the reduced matrix element of the dipole moment operator taken between the ground and excited states by the scalar quantity $d_{FF'} = \langle \alpha F||d^{(1)}||\alpha' F'\rangle$, the atom-field Hamiltonian is written in its final form,

$$\begin{aligned}-\mathbf{d}\cdot\mathbf{E} = &- d_{FF'} \sum_{m, m'_F, q} (-1)^q |F, m_F\rangle\langle F', m'_F|\langle F, m_F|F', m'_F; 1q\rangle E_{-q}^{(-)}(z) e^{i\omega_L t} \\ &+ (-1)^{q+m-m'_F} |F', m'_F\rangle\langle F, m_F|\langle F, m_F|F', m'_F; 1, -q\rangle E_{-q}^{(+)}(z) e^{-i\omega_L t}.\end{aligned} \tag{3.19}$$

Although Eq. 3.19 appears quite verbose, the expression is straightforwardly evaluated given a specific form for the electric-field vector. Expressing the electric field amplitudes in terms of the saturation parameter given in Eq. 3.6 leads to the cancellation of the reduced dipole matrix element and allows a comparison to be made between different angular momentum cases.

3.1.4 Electric fields

The electric fields used in the simulations are defined so that the time-averaged intensity transmitted by each of the beams is $I = \frac{1}{2}c\epsilon_0 E^2$. For simulations of a 1D molasses, two electric-field configurations are considered. The first is where the counter-propagating beams have linear polarisations and the planes of polarisation have an angle ϕ between them,

$$\mathcal{E}_{\mathrm{1D}}^{\mathrm{lin}\phi\mathrm{lin}}(z,t) = E_0\boldsymbol{\epsilon}_x\cos(kz-\omega t) + E_0(\cos(\phi)\boldsymbol{\epsilon}_x + \sin(\phi)\boldsymbol{\epsilon}_y)\cos(kz+\omega t). \quad (3.20a)$$

It can be shown that a physically equivalent expression [73] is given by,

$$\mathcal{E}_{\mathrm{1D}}^{\mathrm{lin}\phi\mathrm{lin}}(z,t) = E_0\sqrt{2}(\boldsymbol{\epsilon}_{-1}\cos(kz-\phi/2) - \boldsymbol{\epsilon}_{+1}\cos(kz+\phi/2))\cos(\omega t). \quad (3.20b)$$

In the second expression the electric field has been written in terms of the spherical basis vectors, which are defined by $\boldsymbol{\epsilon}_{\pm1} = \mp\frac{1}{\sqrt{2}}(\boldsymbol{\epsilon}_x \pm i\boldsymbol{\epsilon}_y)$ and $\boldsymbol{\epsilon}_0 = \boldsymbol{\epsilon}_z$. In the spherical basis each of the components of the electric field couple each ground state sub-level to at most one excited state sub-level. From the second expression, when $\phi = \pi/2$, the polarisation varies between $\boldsymbol{\epsilon}_x$ at $kz = 0$, $\boldsymbol{\epsilon}_{-1}$ at $kz = \pi/4$, $\boldsymbol{\epsilon}_y$ at $kz = \pi/2$, $\boldsymbol{\epsilon}_{+1}$ at $kz = 3\pi/4$ and returns to $\boldsymbol{\epsilon}_x$ at $kz = \pi$. For $\phi \neq \pi/2$, there is some amplitude modulation of the standing wave, and for $\phi = 0$ there is a complete amplitude modulation of the electric field, which varies between $|\mathcal{E}| = 2E_0$ at the anti-nodes and $|\mathcal{E}| = 0$ at the nodes of the standing wave. When $\phi = 0$, the polarisation is the same at all points along the standing wave.

The second configuration is formed by counter-propagating circularly-polarised light. Each beam carries the same handedness of polarisation relative to its direction of propagation, but drives opposite Δm_F transitions when the quantisation axis is chosen along one of the beams. This configuration is used in three dimensions in a magneto-optical trap. In 1D it is sometimes referred to as a 'corkscrew' configuration because the resulting polarisation is linear at all points in space but rotates about the optical axis, making one full rotation every wavelength. More commonly it is referred to as a $\sigma^+\sigma^-$ configuration. This is because each individual beam drives pure σ^+ or σ^- transitions when the quantisation axis is fixed, which is the case in an optical molasses. In an optical molasses external magnetic fields are commonly

nulled, and the axis of propagation of the light defines the quantisation axis in 1D. The resulting electric field can be written as a sum of two right hand circularly-polarised waves, propagating in opposite directions:

$$\begin{aligned}\mathcal{E}_{\mathrm{1D}}^{\sigma^+\sigma^-}(z,t) = &\frac{1}{\sqrt{2}}E(\boldsymbol{\epsilon}_x\cos(kz+\omega t)+\boldsymbol{\epsilon}_y\sin(kz+\omega t)) \\ &+\frac{1}{\sqrt{2}}E(\boldsymbol{\epsilon}_x\cos(kz-\omega t)+\boldsymbol{\epsilon}_y\sin(kz-\omega t)),\end{aligned} \tag{3.21}$$

which is equivalent to

$$\mathcal{E}_{\mathrm{1D}}^{\sigma^+\sigma^-}(z,t) = E\sqrt{2}(\boldsymbol{\epsilon}_x\cos(kz)+\boldsymbol{\epsilon}_y\sin(kz))\cos(\omega t). \tag{3.22}$$

Note that the constituent electric fields in Eq. 3.21 are defined such that the time-averaged intensity transmitted in each beam is the same as for a linearly-polarised electric field with amplitude E_0.

3.1.5 Optical Bloch equations

An atom in an excited electronic state does not remain in this state indefinitely, instead there is a finite probability per unit time that the atom will decay to its ground state and randomly emit a photon. This spontaneous emission arises due to coupling between the atom and the modes of the vacuum state of the quantised electric field. Fermi's golden rule states that the transition rate between two states $a \rightarrow b$ is proportional to both the square of the matrix element of the interaction Hamiltonian causing the transition and the density of states in the vicinity of the final state. For spontaneous emission the initial state consists of an excited state atom and the set of modes of the vacuum state of the electric field. The final state consists of the ground state atoms plus a single photon in one of the modes. In free space the density of states into which a photon can be emitted leads to a rate of decay of the excited state given by Eq. 3.2.

The resulting system is described as being 'open' because an experimenter typically is not aware of the state of the entire system and instead makes measurements of the state of a reduced sub-system, which is the atoms. This uncertainty in the state of the entire system leads to the sub-system existing as a statistical mixture of possible states. It is therefore described using a density-matrix operator $\rho(t)$. The evolution of the sub-system is, in general, non-Hermitian because of the probabilistic nature of spontaneous emission. Nevertheless, there are strict requirements that the density matrix operator must adhere to. The trace of the density matrix operator for the sub-system must sum to unity, $\mathrm{Tr}[\rho] = 1$ and, by its definition, the density matrix is Hermitian. It can also be shown that the density matrix has the property

of positivity. In the limit where the coupling between the atoms and reservoir is weak, the equation of motion for the density matrix is linear in ρ and is known as the Lindblad equation. A derivation of this master equation is given in [76]. When the dissipation is due to spontaneous emission, the set of equations describing the time evolution of the elements of the density matrix are referred to as the optical Bloch equations. The equation of motion is

$$i\hbar\frac{\partial}{\partial t}\rho(t) = [H, \rho(t)] - \frac{1}{2}\Gamma\sum_q \left[\Sigma_q^\dagger\Sigma_q\rho(t) + \rho(t)\Sigma_q^\dagger\Sigma_q - 2\Sigma_q\rho(t)\Sigma_q^\dagger\right], \tag{3.23}$$

where

$$\begin{aligned}\Sigma_q &= \sum_{m_F, m'_F} |F, m_F\rangle\langle F', m'_F|\langle Fm_F|F'm'_F; 1q\rangle \\ &= \sum_{m_F} |F, m_F\rangle\langle F', m'_F|\langle Fm_F|F'(m_F - q); 1q\rangle.\end{aligned} \tag{3.24}$$

In order to calculate the populations, coherences, and force experienced by an atom due to its interaction with the light the equation of motion for the density matrix, Eq. 3.23, is numerically integrated. The semi-classical expression for the force exerted on an atom as it is dragged along the z axis is $f = \langle -\partial\tilde{H}_{\rm AF}/\partial z\rangle$. $\tilde{H}_{\rm AF}$ is the atom-field Hamiltonian, after a transformation to the interaction picture has been made. The atom is dragged with a fixed speed v, so that $z(t) = vt$. Then, Eq. 3.23 is numerically integrated to obtain $\rho(t)$, which requires an exact form of the electric-field of the laser light to be specified, as well as its detuning and intensity. The instantaneous force can then be calculated by evaluating $f(t) = -\mathrm{Tr}[\rho(t).\partial\tilde{H}_{\rm AF}/\partial z]$. When the polarisation of the electric field depends upon the position of the atom, such as in the Sisyphus cooling mechanism, then the solution for $\rho(t)$ is periodic, and has the same periodicity as the polarisation. In these cases the force is averaged over one full spatial period, once the quasi-steady-state behaviour has been reached.

In the following sections the optical Bloch equations are solved for a variety of different angular momentum cases and electric-field configurations. To begin, the familiar type-I system is investigated. The force-velocity curves for an atom dragged through a lin$\perp$lin and $\sigma^+\sigma^-$ optical molasses are calculated. Afterwards, the type-II systems that are relevant to the experiments presented in later chapters are investigated.

3.2 Sub-Doppler laser cooling when $F' = F + 1$

As a first example of how the multi-level structure of atoms can lead to an enhanced coefficient of friction at low velocities, the familiar type-I level structure is considered. For an atom in motion through a one-dimensional optical molasses, two

physically distinct cooling mechanisms can arise. The first occurs in the linϕlin configuration, and is known as Sisyphus cooling. The second cooling mechanism occurs in the $\sigma^+\sigma^-$ configuration and is the result of a motion-induced-orientation of the ground state. Both stimulated and spontaneous processes are important to each of the cooling effects, but their precise roles are quite different. In the sections that follow quantitative results are obtained by numerically integrating the equation of motion for the density matrix, which is given by the optical Bloch equations.

3.2.1 Sisyphus cooling

Sisyphus cooling can occur in a range of optical molasses configurations. Most commonly it is associated with the configuration where the counter-propagating waves have orthogonal linear polarisations. The simplest type-I atomic system in which Sisyphus cooling can proceed has $F = \frac{1}{2}$ and $F' = \frac{3}{2}$. The coupling between internal states of the atom and the electric field in this configurations gives rise to a pair of light-shifted ground-state energy levels that vary in space with a periodicity of $\lambda/2$ along the axis of propagation of the lasers.

Fig. 3.1 illustrates how this mechanism removes kinetic energy from an atom that is in motion along the standing wave. Shown in the figure are the energy levels of the two lowest-energy eigenstates, a decomposition of the total electric field into its two circularly-polarised components, the populations of the two ground states, and the instantaneous force experienced by the atom. The force and populations are calculated using the OBEs, the energy levels and field components are included to elucidate the cooling mechanism. The electric field being considered is given by Eq. 3.20(a). The beams each have an intensity $I = 0.25\ I_{\rm sat}$ and detuning $\Delta = -\Gamma$. The atom is dragged through the molasses at a speed $v = 0.004\ \Gamma/k$. The coupling between ground and excited states by the laser light leads to a perturbation of the energy levels known as the light shift, or AC Stark shift. When the detuning of the light is negative, the energy shift of the ground state sub-levels ΔE_g is also negative. When the laser polarisation drives a single transition, $m_F \rightarrow m'_F$ the magnitude of the ground-state light-shift is proportional to the amplitude-squared of the Rabi frequency of the transition, and inversely proportional to the detuning, $\Delta E_g \propto |\Omega_{m_F,m'_F}|^2/\Delta$. Fig. 3.1(b) shows how the populations in each of the two ground states varies as the atom moves along the standing wave. The laser light tends to optically pump atoms into the ground state where the light shift is most negative, but this takes a finite time. When the optical pumping time is comparable to the time it takes an atom to travel one period of the standing wave, the population can lag behind the laser polarisation. This effect is clearly seen by comparing the top two panels of Fig. 3.1. A consequence of this effect is that, on average, the

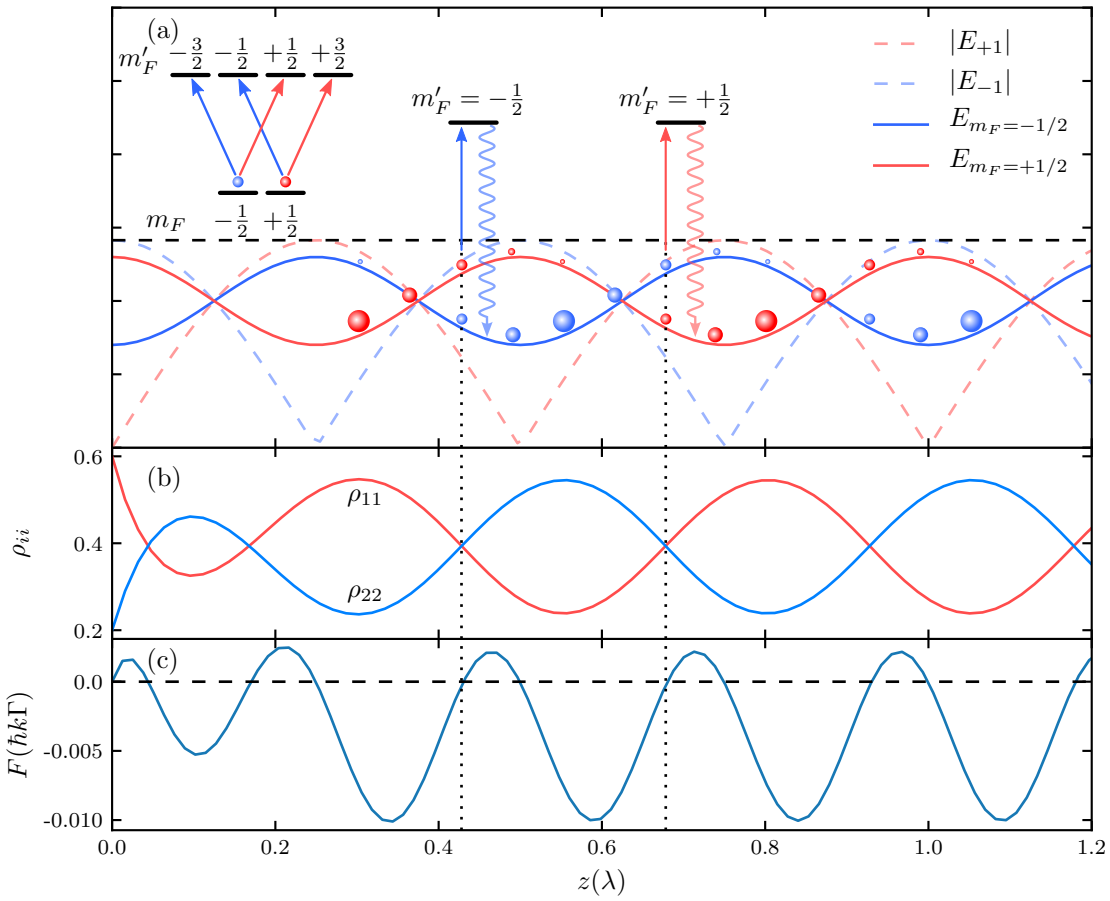

Figure 3.1: The Sisyphus cooling mechanism for a $F = \frac{1}{2} \rightarrow F' = \frac{3}{2}$ transition. The atom starts at $z = 0$, and is dragged in the positive z-direction. (a) The decomposition of the total electric field into the σ^+ component, with amplitude $|E_{+1}|$, and the σ^- component, with amplitude $|E_{-1}|$. Also shown is the variation in the ground-state energy levels as a function of position along the standing wave. The atomic populations, for which numerical data are shown in (b), are indicated by the coloured spheres. Optical pumping tends to accumulate population in the lowest-energy state. Motion along the standing wave converts the kinetic energy of the atom into potential energy through AC Stark shift of the ground states. Accumulated potential energy is dissipated through blue-shifted spontaneous emission. (b) Atomic population in each of the two ground states, $\rho_{11} = \langle m_F = -\frac{1}{2}|\rho|m_F = -\frac{1}{2}\rangle$ and $\rho_{22} = \langle m_F = \frac{1}{2}|\rho|m_F = \frac{1}{2}\rangle$, calculated by solving the optical-Bloch-equations where each beam has $I = 0.25\ I_{\text{sat}}$, $\Delta = -\Gamma$, $v = 0.004\ \Gamma/k$. (c) Force exerted on an atom in motion through the molasses as a function of position, on average the force is negative for positive velocities, indicating a frictional force. After an initial period of transient behaviour the populations and instantaneous force settle to a periodic steady-state.

majority of the atoms are climbing a potential hill. The energy accumulated by a ground state atom near the potential maxima is dissipated by spontaneous emission, indicated by the wavy lines, that is blue-shifted relative to the frequency of the light absorbed by the atom in the optical pumping. The force exerted on the atom due to motion through the standing wave is shown in Fig. 3.1(c), the force is, on average,

negative when the velocity is positive, and so acts to dampen the atomic motion. The average force is calculated over one spatial period of the standing wave, once the quasi-steady-state populations have been reached.

Similar calculations are performed for a range of atomic velocities in order to obtain the velocity-dependent force curves shown in Fig. 3.2. The parameters used are given in the caption. The Sisyphus effect is responsible for the sharp sub-Doppler cooling features in the linϕlin curves. Fig. 3.2(b) shows an enlarged version of these sub-Doppler features. In addition to the lin$\perp$lin case, which is obtained for $\phi = \pi/2$, force-velocity curves are calculated for $\phi = \pi/4$ and $\phi = 0$. When $\phi = 0$ there are no gradients in the polarisation of the optical molasses, and so only Doppler cooling occurs. When $\phi \neq 0$ Sisyphus cooling dominates the cooling force for small velocities, $kv \lesssim 0.1\Gamma$. The damping coefficient is the gradient of the force with respect to the velocity evaluated at the locking velocity, where $F(v) = 0$. If the damping coefficient is large, the rate at which the kinetic energy of an ensemble is dissipated by the molasses is higher, and the final temperature can be lower. The damping coefficient due to the sub-Doppler cooling is many times larger than that due to Doppler cooling. At larger velocities, Doppler cooling is the main contribution to the cooling force. Doppler cooling does not depend on the angle ϕ between the counter propagating waves because it is a one-photon process and the net force is just the sum of the two individual forces from the separate beams. On the other hand, sub-Doppler cooling is most efficient when $\phi = \pi/2$ and non-existent for $\phi = 0$.

3.2.2 Motion along a rotating polarisation

There is a second mechanism that gives rise to enhanced frictional forces at low velocities, which occurs when the optical molasses is formed from circularly-polarised counter-propagating beams. In this configuration the electric field is linearly polarised at all points in space, but the direction of the polarisation rotates about the axis of propagation of the beams with a period λ. A transformation can be made to a frame that co-rotates with the laser polarisation. In this frame, since the electric field vector is linearly polarised, has the same magnitude at all points, and is static, there is no spatial variation in the AC Stark shift of the ground-states of the atom. In a one-dimensional picture the mechanism by which the atom is slowed is now very different to the Sisyphus mechanism, since there is no exchange between the potential energy of the ground state and the kinetic energy of the atom. In fact, as explained in [31], the enhanced friction is a result of the atom acquiring a non-zero orientation of its ground state when in motion. A non-zero orientation, in this sense, means that the expectation value of the angular momentum projection operator taken along the quantisation axis of the atom is non-zero,

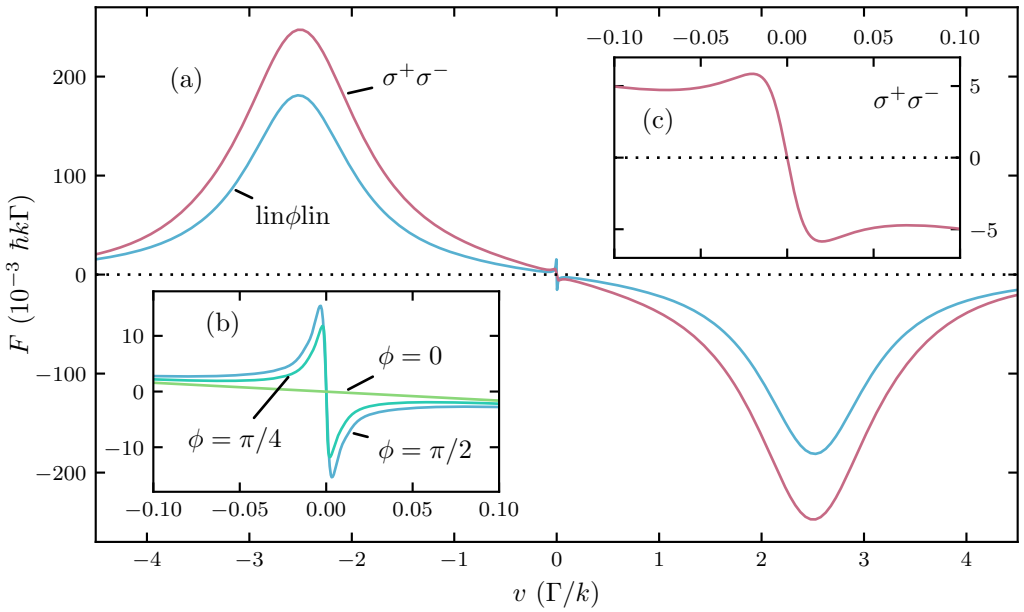

Figure 3.2: Force experienced by an atom dragged at a fixed speed through a number of 1D optical molasses configurations. The atom has $F = 1$ and $F' = 2$. For all curves the parameters are $\Delta = -2.5\ \Gamma$ and each of the beams has $I = I_{\rm sat}$. The main feature seen in (a) is due to Doppler cooling. The polarisation-gradient forces act over a narrow range of velocities, centred on zero, and the two insets show these features more clearly. For the linϕlin configuration three values of ϕ are simulated. When $\phi = 0$ there are no gradients in the polarisation and only a Doppler force exists. The Doppler force is strongest for the $\sigma^+\sigma^-$ configuration, and when an atom is moving with a speed $kv = -\Delta$.

i.e. $\langle\psi|\hat{J}_z|\psi\rangle \neq 0$, as a result of the perturbation caused by the rotating laser polarisation in the frame co-moving with the atom [31]. For a type-I system where the laser light is red detuned this orientation is such that an atom is more likely to absorb a counter-propagating photon than a co-propagating photon. The simplest type-I system exhibiting such a 'motion-induced orientation' of its ground state is that with $F = 1$, $F' = 2$. Again, the steady-state solution for the density-matrix operator is obtained by solving the optical Bloch equations, and the force experienced by an atom in motion is calculated from this. The results are shown in Fig. 3.2. Fig. 3.2(c) shows clearly the sub-Doppler cooling feature resulting from this motion-induced orientation. Both the coefficient of friction and the maximum force at low velocities are less than for the linϕlin configuration. The Doppler contribution to the force is larger than for the linϕlin configuration because the orientation of the atoms is more strongly polarised by the $\sigma^\pm$ light. When the atom is on-resonance with one of the beams, $kv = \pm\Delta$, the behaviour is well-described by a two-level atom. In this case, when $I = I_{\rm sat}$, the force is very close to the nominal two-level value, $F_{\rm scatt} = \hbar k\Gamma\rho_{ee}(I = I_{\rm sat}) = 0.25\ \hbar k\Gamma$.

For both linϕlin and $\sigma^+\sigma^-$ optical molasses a type-I atom in motion experiences a

vastly enhanced coefficient of friction at low velocities due to its multi-level structure. It is due to these polarisation-gradient forces that atoms are routinely observed at temperatures much lower than would be obtained due solely to Doppler cooling. Using the data in Fig. 3.2 the coefficient of friction can be extracted. For the linϕlin configuration the coefficient of friction is about 15 times larger than in the $\sigma^+\sigma^-$ configuration. The equilibrium temperature, however, also depends on the coefficient of diffusion. Similar calculations to those presented here are performed in [77]. In addition, the coefficient of diffusion is calculated, and shown to be much larger for the linϕlin case. The net result is that similar equilibrium temperatures are obtained in both cases.

3.3 Sub-Doppler laser cooling when $F' \neq F + 1$

The principle of sub-Doppler cooling for systems with $F' \neq F + 1$ has already been briefly introduced in Sec. 2.7. The cooling mechanism is closely related to the Sisyphus effect, but there are some subtleties introduced by the presence of dark ground-state sub-levels.

As mentioned earlier, sub-Doppler cooling on a type-II transition can be achieved without the use of a magnetic field, for certain configurations of optical molasses. In [52] the authors propose using a novel kind of sub-Doppler force, which they term the 'non-adiabatic force', to efficiently cool atoms to low-velocities on a $F = 1 \rightarrow F' = 1$ transition. They consider a 1D optical molasses formed from counter-propagating linearly polarised light with an angle ϕ between the planes of polarisation of the two waves. $\phi = \pi/2$ corresponds to the usual lin$\perp$lin configuration. Providing $\phi \neq 0$ or $\pi/2$, the resulting standing wave has a spatial variation in both its intensity and the ellipticity of its polarisation. In the 1D molasses the selection rules for dipole-allowed transitions lead to an effective three-level lambda-system, in which the two states $|1, \pm 1\rangle$ are coupled to $|F' = 1, m'_F = 0\rangle$. As described in [78], a basis can be chosen so that the ground-states of the atom consist of a coupled, or bright, state and a non-coupled, or dark, state. For $\phi \neq \pi/2$, the energy of the coupled state varies in space and is proportional to the local intensity of the standing wave. A steady-state sub-Doppler force is facilitated by non-adiabatic transitions between the coupled and non-coupled states, which are most likely to take place when the energy splitting between the two states is smallest[1]. Fig. 3.3 illustrates the mechanism. Optical pumping to the dark state is most likely to occur at the potential maxima, where the intensity, and hence optical pumping rate, is largest. In order for the force to cool the atom, the light-shift of the bright state must

[1]See for example Sec. 9.4, p. 447 of [79] for a discussion of the adiabatic approximation in time-dependent perturbation theory.

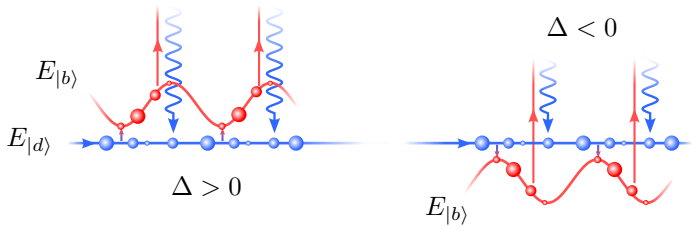

Figure 3.3: Laser cooling via the non-adiabatic force. The energy of the bright state, $|b\rangle$, varies in space, whereas that of the dark state, $|d\rangle$, does not. Optical pumping to the dark state is most likely to occur at the intensity maxima, where the AC Stark shift of the coupled state is largest. Non-adiabatic transitions occur where the energy difference between the ground-states is smallest, and mix population between the bright and dark states. The result is a cooling force when the light is blue-detuned from the resonance, and a heating force for red-detuning.

be positive, which requires a positive detuning. Thus, a blue-detuning results in a Sisyphus-like cooling mechanism. The motional coupling between the dark and bright states is velocity dependent, with the probability of a transition occurring falling to zero for an atom at rest [52]. For this reason the dark state is said to be velocity-selective and can, in theory, lead to sub-recoil temperatures.

This cooling mechanism can be investigated more quantitatively by again solving the OBEs, now for a system with $F = F' = 1$. The methods followed here are similar to those presented in [31, 73]. Those investigations provide data against which the predictions of the code used here can be tested and verified. Fig. 3.4 shows the velocity-dependent force and excited-state population calculated for two different angular momentum cases. The results are obtained for a 1D linϕlin molasses, defined through the electric field in Eq. 3.20, for a range of different angles ϕ. Parts (a) and (b) of the figure show, respectively, the velocity-dependent force and excited-state population obtained for a system with $F' = F = 1$. The results of the simulations indicate that the Doppler cooling force is about 100 times smaller than for a type-I system, and is not visible in these plots. By contrast, the cooling feature resulting from the non-adiabatic force is similar in size to that of the sub-Doppler feature of the type-I case, and operates over a similar range of velocities. The non-adiabatic force becomes inefficient as $\phi \to 0$ or $\phi \to \pi/2$, which is clearly visible from the figure. When the first of these two conditions is fulfilled, there is no motion-induced mixing between the coupled and non-coupled states and so the probability of an atom making a non-adiabatic transition to a bright state is zero. When the second condition is fulfilled there is no spatial modulation of the light-shift of the bright state and so there is no Sisyphus mechanism to remove energy from an atom in motion. The excited-state population, which is the sum over the populations of all excited-state sub-levels $\rho_{ee} = \sum_{m'_F} \langle F', m'_F|\rho(t)|F', m'_F\rangle$, shows clearly the velocity-

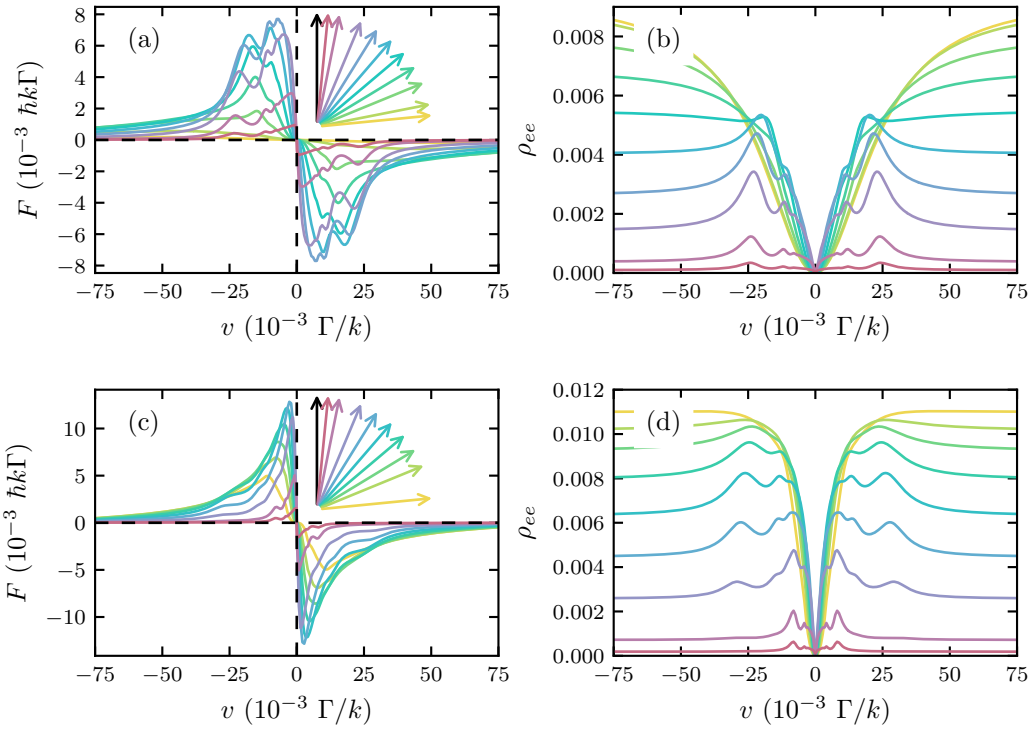

Figure 3.4: Velocity-dependent force and excited-state population, ρ_{ee}, for an atom with $F' = F = 1$, (a) & (b) and $F' = F = 2$, (c) & (d). The atom is in motion through a linϕlin 1D optical molasses. The cooling force is due to a Sisyphus-like mechanism facilitated by non-adiabatic motion-induced transitions between dark and bright ground-states. In these simulations the angle, ϕ, between the plane of polarisation of the two counter-propagating laser fields is varied. The arrows in the top-right part of (a) and (c) serve as a legend, where the black arrow indicates the orientation of $\vec{E}_1$ and the angle of $\vec{E}_2$, represented by the coloured arrow, is varied. In both sets of simulations each beam has $I = I_{\text{sat}}$ and $\Delta = +2.5\ \Gamma$.

selective nature of the dark-state. As $v \to 0$ the velocity-selective non-adiabatic transitions become inefficient at remixing the populations of bright and dark-state sub-levels, and the population of the dark state approaches 100%.

A second type-II transition relevant to the experimental investigation presented in later chapters is that with $F' = F = 2$. The OBEs have also been solved for this system and the results are given in parts (c) and (d) of Fig. 3.4. Despite the increased multiplicity of the sub-levels, the characteristics of the sub-Doppler forces calculated for these angular momenta are very similar to those calculated for $F' = F = 1$. Again there is a velocity-selective dark-state, although in this system it is narrower. Similar to the $F' = F = 1$ case, the sub-Doppler force is also smaller as $\phi \to 0$ or $\phi \to \pi/2$, so that the description of the non-adiabatic cooling force provided earlier appears to be generally applicable.

The excited-state population and velocity-dependent force are shown for a variety of detunings in Fig. 3.5. As is typical for type-II transitions, the velocity-dependent sub-Doppler force is a cooling force for a positive detuning of the laser light. When

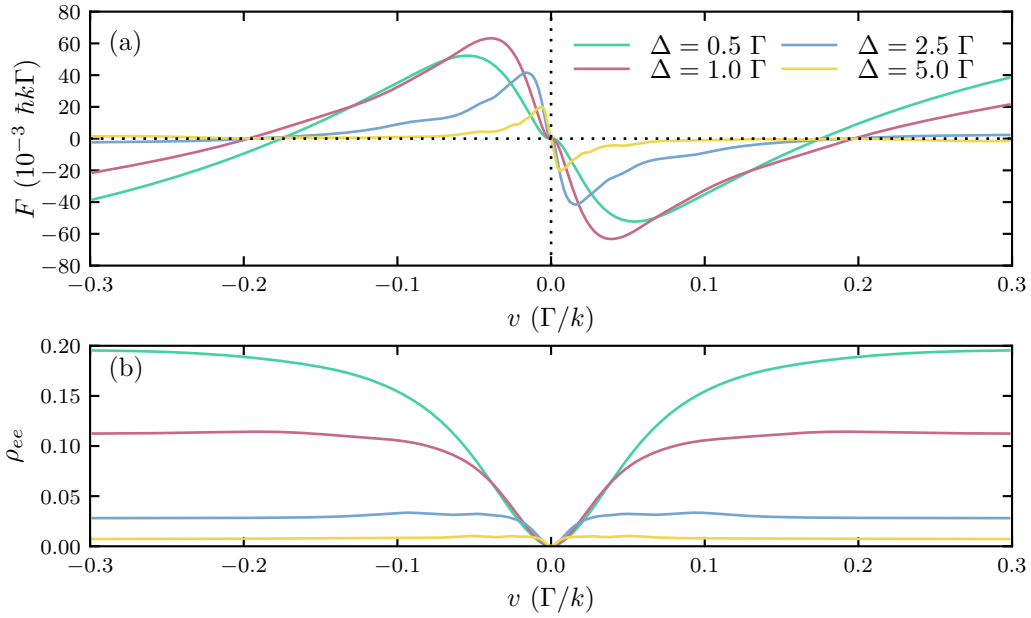

Figure 3.5: (a) Sub-Doppler force curves for a range of detunings for an atom with $F' = F = 2$ in motion through a 1D linϕlin optical molasses, with $\phi = \pi/4$. (b) Excited-state population for the same parameters, showing the effect of the velocity-selective dark ground-state, which is present for all detunings. The force is qualitatively similar to the case where $F' = F = 1$.

the atom is moving sufficiently fast for the non-adiabatic transitions at the minima of the optical potential to efficiently re-mix the dark and bright ground states then the excited-state fraction increases as $|\Delta|$ is reduced. For the lowest velocities the non-adiabatic motion-induced transitions are inefficient and atoms populate the dark state. This leads to the non-linear shape of the force-velocity curve near $v = 0$.

It follows from the above discussion that, although the presence of dark ground-state sub-levels subtly changes the nature of the sub-Doppler cooling processes, efficient cooling forces do exist for most arrangements of laser polarisation in 1D optical molasses. The gradients in the polarisation and intensity in a 1D optical molasses are quite different to those in a 3D configuration. In the subsequent sections the calculations presented previously are generalised and extended to consider a 3D optical molasses and the effect of a magnetic field on the cooling, such as is encountered by an atom in a magneto-optical trap.

3.4 Sub-Doppler cooling in a magneto-optical trap

A 3D optical molasses has additional spatial variations in its intensity and polarisation when compared to the 1D case. In general, in a 3D configuration, there are regions where atoms are optically pumped by light polarised to drive both π and $\sigma^{\pm}$ transitions. This has important implications for the velocity-dependent forces.

In type-II systems, for instance, motion through a 3D configuration leads to the recovery of a Doppler force, similar in magnitude to that obtained in type-I systems.

As has been noted in many experimental studies, external magnetic fields can profoundly alter the sub-Doppler velocity-dependent forces, inhibiting or even facilitating cooling. While these effects have been studied in 1D in a number of atomic-beam experiments, the effect of a magnetic field on gray-molasses cooling has not, to the author's knowledge, been studied in three-dimensions. The theoretical investigation presented in [73] considers the effect of the Zeeman interaction on the position-dependent and velocity-dependent forces experienced by an atom with a type-II nature in a 3D optical molasses. The main conclusion relevant to this investigation is that, while magnetic fields strongly inhibit sub-Doppler cooling in type-I systems, in type-II systems the cooling is more robust, and is more efficient over a wider range of magnetic-field gradients.

3.4.1 Extension to 3D optical molasses

The simulations presented in previous sections are readily extended to the case of a 3D optical molasses. The electric field in the 1D $\sigma^+\sigma^-$ molasses is defined in Eq. 3.21. The electric field in the 3D configuration can be obtained by using the rotation operators, where $\mathcal{R}_i(\theta)$ represents a rotation about the i axis by an amount θ,

$$\mathcal{E}_{3\mathrm{D}}(z,t) = \mathcal{E}_{1\mathrm{D}}(z,t) + \mathcal{R}_x(\frac{\pi}{2}).\mathcal{E}_{1\mathrm{D}}(0,t) + \mathcal{R}_y(\frac{\pi}{2}).\mathcal{E}_{1\mathrm{D}}(0,t). \tag{3.25}$$

In these 3D simulations, the motion of the atom is constrained to be along the z axis for simplicity. Therefore, these simulations might be more accurately described as quasi-3D, since they represent a 1D trajectory in a 3D electric field. In [73] similar simulations are performed in which the trajectory of an atom is varied, but the magnitude of the velocity is constant. The resulting force is shown to be quite insensitive to the specific trajectory, and as such there appears to be no 'special axis' along which markedly different results are obtained. Therefore, it is reasonable to conclude that the quasi-3D approach used here does capture all of the physics contained within a more general consideration.

There are a number of noteworthy differences between the force-velocity curves in the 1D and 3D optical molasses configurations. The polarisation-gradient force for type-II systems relies on the motion-induced non-adiabatic coupling between light and dark states. There is no efficient polarisation-gradient force in either a lin$\perp$lin or $\sigma^\pm$ 1D optical molasses. In 3D, however, a significant low-velocity force is recovered for both of these configurations. This is because, in 3D, there are always gradients of both intensity and polarisation, for all polarisation configurations. Additionally, at higher velocities, a Doppler force is recovered in the type-II systems. The recovery

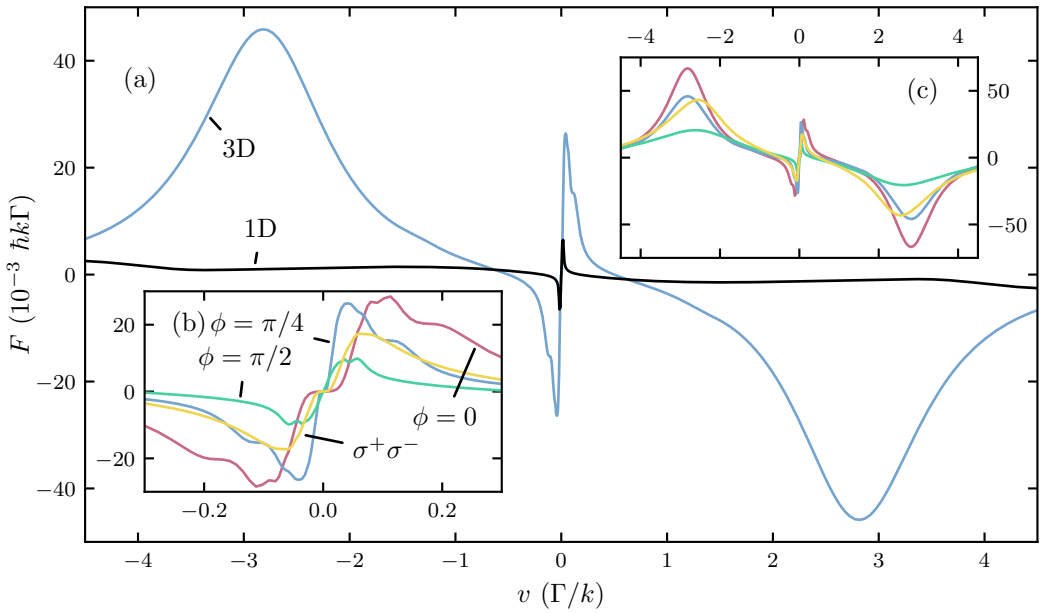

Figure 3.6: Force-velocity curves calculated for $F' = F = 1$ in a number of molasses configurations. For all the simulations the beams have $I = I_{\text{sat}}$ and $\Delta = -2.5$ Γ. (a) 1D and 3D versions of linϕlin with $\phi = \pi/4$. In both 1D and 3D there is a sub-Doppler feature, which heats the atoms at low velocities. In 3D there is a Doppler cooling feature, which is absent for the 1D case. (b) Force-velocity curves at small velocities for a variety of 3D molasses configurations. In 1D there is no force for this system when $\phi = 0, \pi/2$ or for the $\sigma^+\sigma^-$ case. In 3D all these give both sub-Doppler and Doppler features. (c) The full force-velocity curves for the same molasses configurations as in (b).

of Doppler and sub-Doppler contributions to the force-velocity curve for arbitrary laser polarisations implies that sub-Doppler cooling should proceed in a blue-detuned MOT, providing the cooling is not severely inhibited by the magnetic field.

Fig. 3.6 shows the force-velocity curves for a system with $F' = F = 1$ in a number of different molasses configurations. The Doppler and sub-Doppler contributions to the force have opposite signs. The detuning used in these simulations is negative, and so the Doppler force leads to a cooling effect for all molasses configurations. Part (a) of the figure shows the force-velocity curve for the 1D and 3D linϕlin configurations, with $\phi = \pi/4$. The velocity where the force crosses zero and has a negative slope is referred to as the locking velocity, because atoms are driven towards this velocity. When the laser is red-detuned, as in the figure, the locking-velocity is far from $v = 0$. For the $\sigma^+\sigma^-$ configuration, like that used in the MOT, the locking velocity is ~0.47 Γ/k when each beam has $I = I_{\text{sat}}$ and $\Delta = -2.5$ Γ. Using $\frac{1}{2}m\langle v^2\rangle = \frac{3}{2}k_BT$, the corresponding temperature is 17 mK for ^{87}Rb. Actually extracting a temperature for an ensemble of atoms or molecules subject to the force-velocity curve in Fig. 3.6 is more challenging, and requires a Fockker-Plank equation to be solved. Nonetheless, the results shown in Fig. 3.6 illustrate why

atoms or molecules confined in a red-detuned type-II MOT are routinely observed at temperatures far exceeding the Doppler-cooling limit.

By making $\Delta \rightarrow -\Delta$ in the simulations presented in Fig. 3.6, the curves are exactly reflected about $F = 0$. It follows that when the light is blue-detuned, and the magnetic field is zero, the locking velocity is $v = 0$, and atoms are cooled to low temperatures.

3.4.2 Zeeman interaction

Now the effects of an external magnetic field on the cooling mechanisms will be included in the simulations. The Hamiltonian describing the Zeeman interaction for weak magnetic fields[1] is,

$$\hat{H}_B = \hbar\omega_B(g_F \sum_{m_F} m_F|F, m_F\rangle\langle F, m_F| + g_{F'} \sum_{m'_F} m'_F|F', m'_F\rangle\langle F', m'_F|), \qquad (3.26)$$

where $\hbar\omega_B = \mu_B B$, and $g_F, g_{F'}$ are the g-factors of the ground and excited-state, respectively.

Fig. 3.7 shows the effect of applying an external magnetic field on the force-velocity curve calculated for a $F = 1 \rightarrow F' = 2$ system. A magnetic-field gradient B' of ~12 G/cm^2 is typical for a Rb MOT. A characteristic length scale σ_z for the atom cloud might be of the order 1 mm. From these quantities a typical magnetic field strength can be calculated: $B_0 = B'\sigma_z = 1.2$ G, which corresponds to $\omega_B \approx 0.28\ \Gamma$ for ^{87}Rb. These simulations are similar to those performed in [46], and illustrate the cause of the disruption of SDLC by a magnetic field. As the magnetic-field is increased, the locking velocities due to both the Doppler and sub-Doppler features are translated along the horizontal axis, in proportion to the magnetic-field gradient. The narrow sub-Doppler feature is no longer centred on the locking velocity of the Doppler force, and efficient cooling is inhibited. This is visible in the inset of the figure. Furthermore, since the magnetic field depends on the position of the atom, different atoms will be driven towards different, non-zero, velocities, which is a heating effect.

Fig. 3.8 shows similar data obtained for both $F = 1 \rightarrow F' = 1$ and $F = 1 \rightarrow F' = 2$. Now the optical molasses is in three dimensions, and the magnetic field is applied along the direction of motion of the atom, which in turn is along one of the optical axes. There are similarities and differences between the force-velocity curves in parts (a) and (b) of the figure. In both cases as the magnetic field increases,

[1] This is valid for weak fields, where F is a good quantum number, and describes the anomalous Zeeman interaction.

[2] It is common within the atomic physics community to quote magnetic-field strengths in units of gauss, rather than the SI-derived tesla, where 1 G $= 10^{-4}$ T.

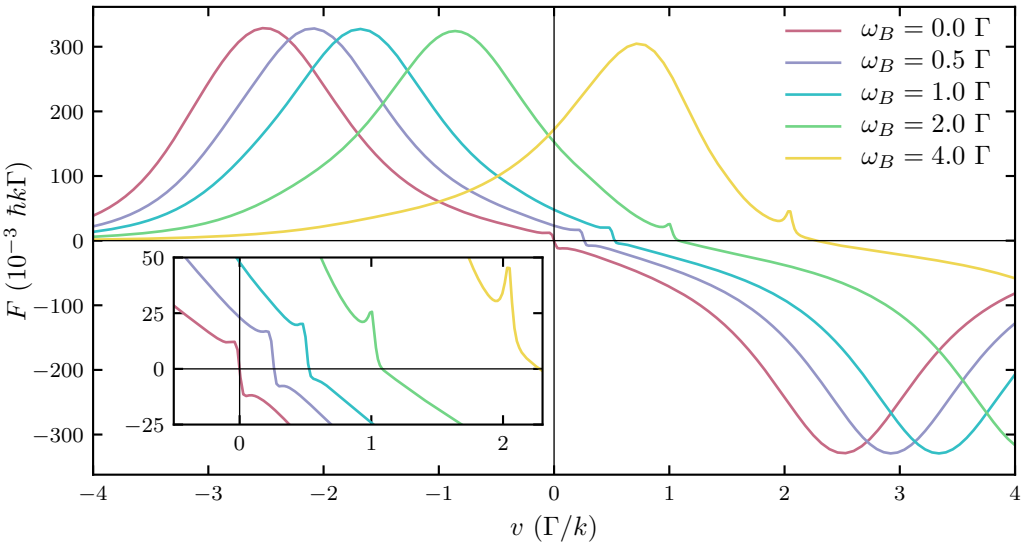

Figure 3.7: Force-velocity curve calculated for a $F = 1 \rightarrow F' = 2$ system in a variety of magnetic fields. The lower-state g-factor $g = 1/2$ and the upper-state g-factor $g' = 2/3$. At sufficiently high values of ω_B the SDLC feature does not contribute to the gradient of the force curve at the locking velocity. For ^{87}Rb, a value of $\omega_B = 4.0\ \Gamma$ corresponds to $B = 17$ G. The calculations are performed for a 1D $\sigma^+\sigma^-$ molasses where each beam has $I = 2\ I_{\text{sat}}$ and $\Delta = -2.5\ \Gamma$.

the sub-Doppler feature separates out into many smaller features, each centred on different velocities. This helps to illustrate that the sub-Doppler forces are facilitated by multi-photon processes between different ground states. At zero magnetic field, all multi-photon transitions between ground states are degenerate in energy. At non-zero magnetic fields the degeneracy is lifted and a given multi-photon transition is resonant at a specific velocity. The main difference between the two sets of curves is that the sub-Doppler feature closest to $v = 0$ in the type-II system gives a well defined zero-crossing over the whole range of magnetic fields simulated. For the type-I system this is not the case. Here, even very small magnetic field gradients shift the locking velocity quickly away from $v = 0$. As mentioned previously, sub-Doppler cooling of type-II systems relies on transitions between bright and dark states. In general, the dark state is a superposition of ground-state sub-levels that depends on the local polarisation of the light. As the magnetic-field is increased, the dark state is destabilised, which diminishes the sub-Doppler feature in Fig. 3.8(a). However, the dark state is always most efficiently populated close to $v = 0$, and so the locking velocity does not change.

The simulations support the conclusions made in [73], that sub-Doppler cooling in type-II systems should be robust to the magnetic fields encountered by an atom in a typical MOT. Indeed, in later chapters experimental data is obtained that illustrates that atoms can be efficiently cooled to sub-Doppler temperatures even in very high magnetic-field gradients.

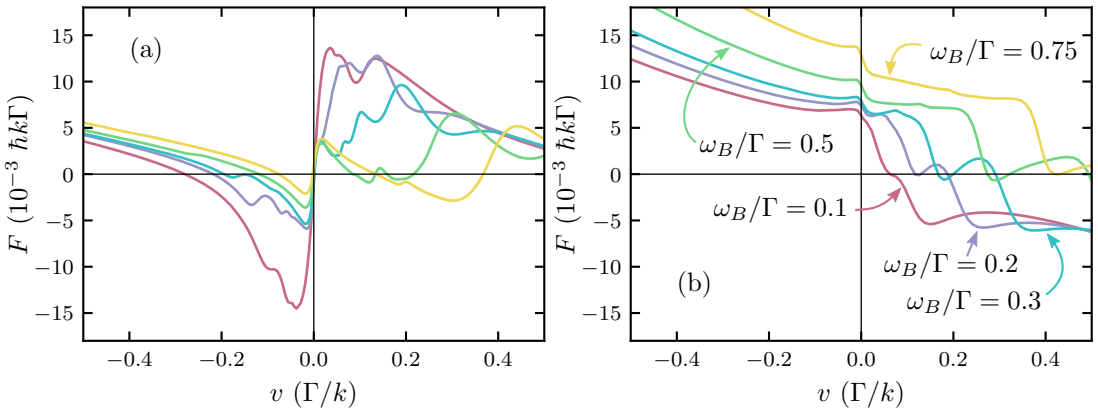

Figure 3.8: Sub-Doppler laser cooling of type-I and type-II systems in a 3D $\sigma^+\sigma^-$ optical molasses with an external magnetic field. (a) shows the force-velocity curves for a system with $F = 1$ and $F' = 1$. (b) shows the same simulations when $F = 1$ and $F' = 2$. The labels shown in (b) also apply to the curves in (a). In both cases the beams have $I = I_{\text{sat}}$ and $\Delta = -2.5\ \Gamma$.

3.5 Concept of the blue-detuned type-II MOT

The velocity-dependent force experienced by an atom or molecule in a 3D molasses in the presence of a magnetic field has been discussed. Although in 3D the gradients of polarisation and intensity are complicated, and the role of the magnetic field is subtle, the sections above have elucidated the main mechanisms leading to the form of the velocity-dependent force. The numerical simulations presented in this chapter, along with those presented in [73], confirm that many of the characteristics of the sub-Doppler force obtained for a type-II system in 1D also apply to the 3D case, but that both Doppler and sub-Doppler features tend to be significantly larger in 3D and far less sensitive to the choice of polarization configuration.

Doppler-cooling requires light that is red-detuned from the atomic transition, irrespective of the angular momentum of the ground and excited states. Conversely, for a given detuning, sub-Doppler processes can either cool or heat an atom or molecule, depending on its angular momentum structure. For type-I systems, with $F' = F + 1$ or $F' = F - 1$, sub-Doppler cooling requires the light to be red-detuned from the transition. For type-II systems with $F' = F$, sub-Doppler cooling requires the light to be blue-detuned.

Consider an atom (or molecule) with a type-II nature moving through a blue-detuned molasses. At a sufficiently high velocity, Doppler forces dominate, which causes its velocity to increase. The light may also be red-detuned, so that Doppler cooling remains effective, but sub-Doppler heating dominates at low velocities. This raises the temperature of the atoms confined in a MOT, but increases the overall capture velocity of the damping forces. Importantly, as discussed in [73], sub-Doppler

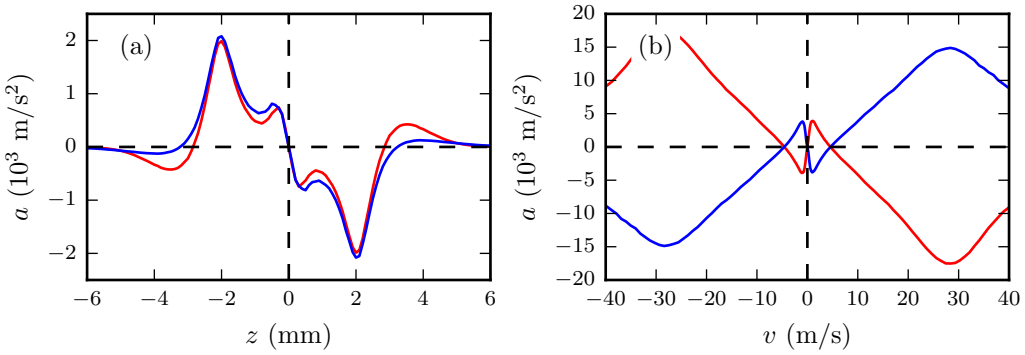

Figure 3.9: Simulation of the position-dependent and velocity dependent forces for ^{87}Rb in a type-II MOT. (a) Shows the position-dependent force for an atom moving with $v = 9$ cm/s, the most-probable velocity at 40 µK. (b) Shows the velocity-dependent force at the centre of the trap. The simulation takes into account the full level-structure of the atom. There are two lasers, one addressing each ground-state. The first is detuned from $F = 1 \rightarrow F' = 1$ by an amount $\Delta_{11}/(2\pi) = \pm 26$ MHz, and the second is detuned from $F = 2 \rightarrow F' = 2$ by an amount $\Delta_{22}/(2\pi) = \pm 11.5$ MHz. The red-coloured curves correspond to the red-detuning. The total intensity at the trap centre is $I_t = 113$ mW/cm^2, which is divided equally between the two frequencies and again between the six beams of the MOT. The polarisation of the light in the red and blue cases is opposite. The figure was calculated by J. A. Devlin and is reproduced from [80].

cooling in type-II systems remains efficient over the whole range of magnetic fields typically encountered by an atom in a MOT.

A position-dependent confining force can be obtained for a stationary atom for either red-detuned or blue-detuned light, providing the polarisation of the light is chosen correctly. Assuming that the laser detuning is significantly smaller than the excited-state hyperfine intervals, the confining forces obtained in the red-detuned and blue-detuned cases are near-identical in magnitude and differ only by their sign. There appears to be no discussion of this important point in the literature, but it is pivotal to the conjecture that a type-II blue-detuned MOT should be feasible and out-perform its red-detuned equivalent.

In Fig. 3.9 the velocity-dependent and position-dependent forces are shown for a ^{87}Rb atom in a magneto-optical trap. The lasers are blue-detuned from the $F = 1 \rightarrow F' = 2$ and $F = 2 \rightarrow F' = 2$ transitions and the detuning and intensities of the beams are representative of typical values used in the experiments presented in later chapters. The force-curves are obtained by solving the OBEs for a variety of atomic trajectories through a 3D molasses in the presence of a magnetic field. The full hyperfine-level-structure of the atom is taken into account. A stable MOT can be obtained with either red-detuned or blue-detuned light, but atoms confined in the blue-detuned MOT are cooled to far lower temperatures because of the strong sub-Doppler cooling feature present in this case.

3.5.1 Loading atoms or molecules into a blue-detuned MOT

In the experiments presented in this thesis, ^{87}Rb atoms are first captured and cooled in a normal type-I MOT. These cold atoms are then loaded into a blue-detuned MOT, whose character is then investigated. This method works well for Rb atoms, where a type-I MOT exists, but would not work for molecules, where all MOTs are type-II MOTs. In this case, there is an alternative procedure that can be followed. This procedure exploits the fact that there is an intensity dependence to the locking-velocity v_c to which atoms are cooled in a red-detuned type-II MOT. According to [73], $v_c \propto I_t^{1/2}$. If the intensity is initially $I_t = I_0$, then the velocity distribution will be centred on v_{c0}. Then, the intensity can be lowered, cooling the atoms so that the majority have a velocity $v < v_{c0}$. If the detuning is quickly shifted to the blue-side of the transition and intensity increased, without heating the atoms, then a blue-detuned MOT can be efficiently loaded. If any atoms have $v > v_{c0}$ when the blue-detuned MOT is switched on, these atoms are heated by Doppler processes and evaporate from the trap.

4 Constructing the experiment

In the previous chapters an introduction to the field of laser cooling and trapping was given, with particular attention being paid to the properties of so-called type-II MOTs. Historical observations have been discussed in the context of recent theoretical work, and a good understanding of many of the properties of these MOTs is now possible. The concept of a blue-detuned MOT was then suggested as a method to improve the characteristics of the type-II MOT. This chapter describes the construction of an experiment to investigate such a MOT, using the D2 line in ^{87}Rb.

4.1 Introduction

To provide some context for the experiment, this section begins by stating the objectives of the research group, and giving a brief review of recent progress towards realising some of its ambitions. A summary of the remaining content of this chapter is then provided.

4.1.1 Context

One of the current research goals of the Centre for Cold Matter at Imperial College London is to be able to cool, capture, and manipulate ultracold molecules with broad-ranging applications that include quantum simulation, and precision tests of fundamental physics. The initial motivation for the investigation presented in this thesis was to obtain a good understanding of the physics of type-II MOTs using a readily available source of cold atoms. This was in anticipation of realising a MOT of CaF, which had been successfully slowed but not yet captured. Rb belongs to the group of atoms most amenable to laser cooling and trapping—it is relatively straightforward to assemble a set-up which allows ^{87}Rb to be cooled and captured in a MOT from a thermal vapour obtained from a dispenser. The choice to use Rb was based upon the availability of existing equipment, much of which was repurposed from a previous Rb BEC experiment.

During the early stages of the investigation it had been intended to demonstrate an RF type-II MOT in Rb, as the technique had been applied to a MOT of SrF in [74] with promising results. Although a substantial amount of time was dedicated to understanding and overcoming some of the technical difficulties with implementing an RF MOT scheme, it later emerged that an alternative route to obtaining a better performance might be via the blue-detuned MOT. These two approaches share some

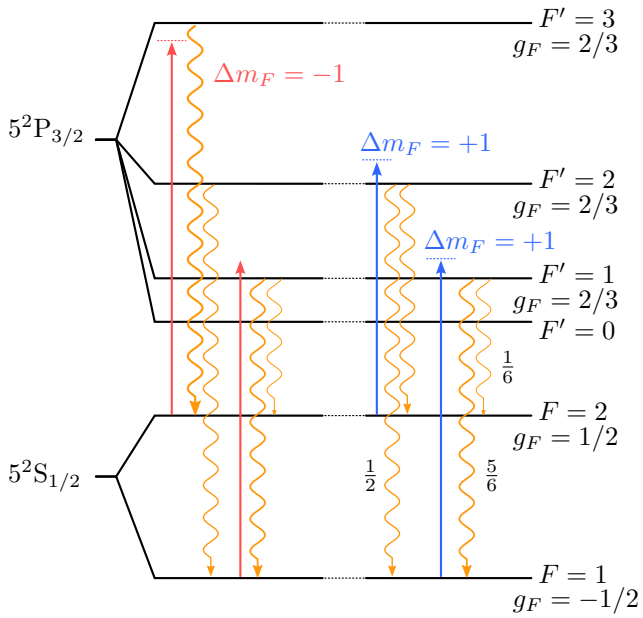

Figure 4.1: Trapping scheme for the red-detuned type-I MOT, and possible trapping scheme for a blue-detuned type-II MOT, in ^{87}Rb. The g-factors of the upper states used for both schemes are all positive but the blue detuning requires the polarisations of the trapping light to be reversed.

similarity in their experimental implementation as both require fast control of the polarisation of the MOT light. It was decided that the investigation should prioritise the pursuit of a blue-detuned MOT, which was a novel idea and had not been demonstrated or discussed by any other group. The ability to quickly switch between two trapping schemes was very useful in diagnosing the performance of the blue-detuned MOT and certainly reduced the time to its first successful demonstration. This approach allowed dense clouds of ultra-cold atoms to be prepared in a type-I MOT before being released into the type-II scheme. Optimisation could then be performed by eye by observing the motion of the cloud of cold atoms following a rapid switch to the blue-detuned MOT. In hindsight this approach was not only convenient but absolutely necessary because the small capture velocity of the blue-detuned MOT is insufficient to load atoms from a thermal vapour.

The experiment also offers a unique system within which to test the predictions of recent theoretical models developed within the group. To the credit of this theoretical work, and the flexibility of the experiment, a number of new trapping schemes have been realised for ^{87}Rb, which have not been reported before. These are the subject of Chap. 6.

4.1.2 Content of this chapter

The purpose of the experiment is to investigate laser cooling and magneto-optical trapping operating on transitions between pairs of levels with a variety of different

angular momentum quantum numbers. The key requirements of the experiment are a flexible locking scheme that can be tuned over a wide range, the ability to use either handedness of polarisation for the trapping light and to be able to quickly switch the polarisation if desired.

Most of the results presented in Chap. 5 were obtained using the basic method illustrated in Fig. 4.1. Atoms are captured and cooled in a red-detuned type-I MOT before being loaded into the blue-detuned type-II trapping scheme shown on the right-hand side of the figure.

The remainder of this chapter provides a discussion of each of the key components of the experiment. Firstly, the optical set-up used to stabilise the lasers is described along with the associated monitoring and control systems. Next the opto-mechanical set up used to obtain the MOT light and to switch between the two polarisations is described with the associated control system. The vacuum chamber layout, assembly, and preparation are discussed, along with the collection of coils and drivers used for the magnetic-field control. The optical set-up used to record absorption images, and methods used to calculate atom numbers and densities from these images, are discussed next. In the penultimate section a brief description of the computer interface and software suite used to control the hardware and run experiments is given. Finally, a thorough discussion is given of the potential sources of systematic uncertainty in making an absolute atom-number measurement, and a quantitative estimate of the magnitude of the uncertainty is given.

4.2 Laser spectroscopy and frequency stabilization

All of the laser frequencies that have been used in this investigation are illustrated in Fig. 4.2. The dashed segments are indicative of the range over which each of the frequencies are routinely locked. This section provides a description of the optical set-up and associated electronics used to obtain, control, and monitor the various frequencies shown in Fig. 4.2. Two Toptica TA-Pro tapered-amplifier lasers provide the cooling and trapping light used during the course of the investigations presented in this thesis. It is convenient to refer to these lasers according to which hyperfine-ground state of ^{87}Rb each of the lasers addresses. This nomenclature is more suitable when discussing the type-II trapping schemes as the labelling of a given transition as 'cooling' or 'repumping' is often less obvious than in the type-I case. Instead, transitions from either ground-state have a similar role, and are equally important to the trapping scheme. Equal consideration must be given to the intensity, polarisation, and alignment of the beams driving each of the transitions.

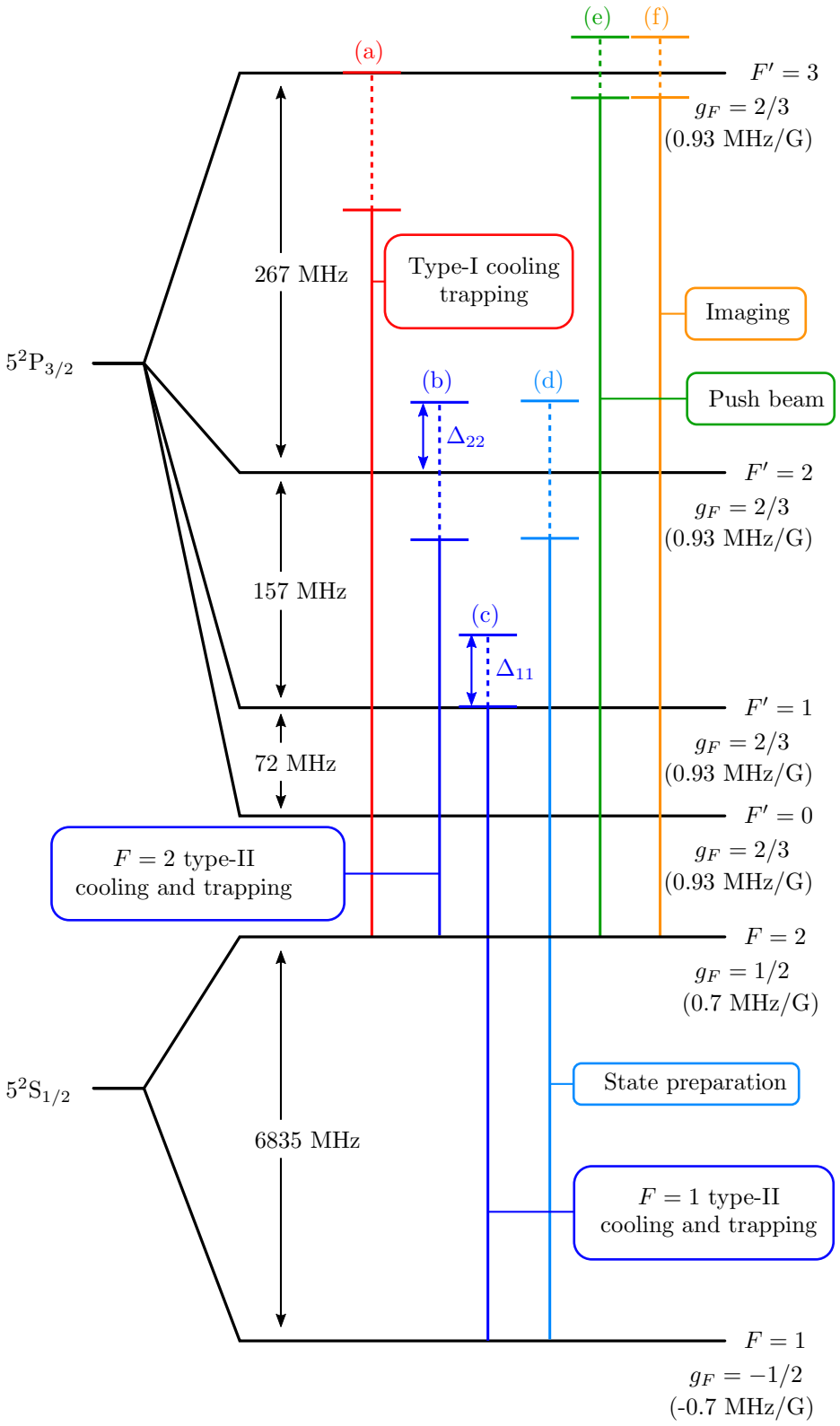

Figure 4.2: Key laser frequencies in use at the time of writing. The experiment uses two Toptica TA-Pros and a Toptica DL-Pro. (a) and (b) are derived from the first TA-Pro, (c) and (d) from the second. (e) and (f) are derived from the DL-Pro. Each of their roles are discussed in the text and will be referred to in later chapters.

The first TA-Pro, with a nominal output power of 1.5 W, primarily drives transitions from the $F = 2$ ground state and is therefore referred to as the '$F = 2$ laser'. The $F = 2$ laser serves two main functions. The first is to provide the cooling and trapping light used to load the type-I MOT from the rubidium vapour in the experiment chamber and to cool the atoms in an optical molasses. For this purpose the light is red detuned from the $F = 2 \rightarrow F' = 3$ transition. The second main purpose is to serve as a cooling and trapping laser in the type-II MOT, where it is most commonly detuned from the $F = 2 \rightarrow F' = 2$ transition. The frequencies used in each of these two roles are labelled (a) and (b) in Fig. 4.2, respectively. A specialised, home-made controller allows the laser to be quickly unlocked from (a) and relocked to (b), and vice versa, during the experimental sequence and is the subject of Sec. 4.3.1.

A second Toptica TA-Pro has a nominal output power of 3 W. This is referred to as the $F = 1$ laser. It serves two main purposes. The first is to provide the repumping light for the type-I MOT. The role of the laser in this situation is to remove atoms from $F = 1$, which can be populated by decays following off-resonant excitation to $F' = 2$ by the trapping laser. Ordinarily, the re-pumping laser would be resonant with the $F = 1 \rightarrow F' = 2$ transition, since $F' = 2$ is the accessible excited-state most likely to decay to $F = 2$. In this experiment the laser is instead locked close to $F = 1 \rightarrow F' = 1$, which is in anticipation of the fast switch to the type-II MOT scheme. This is a less effective repumping transition for the type-I scheme, as atoms decay from $F' = 1$ to $F = 2$ only $\frac{1}{6}$ of the time. Nonetheless, so few atoms decay to $F = 1$ in the type-I scheme that this serves perfectly well to enable the trap to function. The intensity of the repumping light is far higher than would be typically used in a type-I MOT, which compensates for the reduced efficiency of the scheme. The second purpose of this laser is to provide the cooling and trapping light for atoms in the lower hyperfine ground-state in the type-II scheme. This is labelled (c) in Fig. 4.2. In the type-II scheme, due to the branching ratios of decays from the $F' = 1$ and $F' = 2$ states, the $F = 1$ laser provides the majority of the confinement. A small amount of light from this laser is also used to prepare the state of the atoms by optical pumping from $F = 1$ to $F = 2$. This can allow, for example, the ground-state distribution of atoms to be measured by absorption imaging. This optical pumping beam is tuned by varying the frequency of an acousto-optical modulator (AOM), which the beam is aligned through in a double-pass configuration. The light, now resonant with $F = 1 \rightarrow F' = 2$, is coupled into the same optical fibre as the imaging light (see Fig. 4.22), and is labelled (d) in Fig. 4.2.

Lastly, a DL-Pro is used as the reference laser, to which the two TA-Pros are frequency-offset locked. Light used for absorption imaging, and as a 'push beam', is derived from this laser. The push beam is used in the study of MOT dynamics

presented in later chapters. The imaging beam is labelled by (e), and the push beam by (f) in Fig. 4.2.

All of the lasers used in this experiment are extended-cavity semiconductor diode lasers and can be stabilised by modulation of the semiconductor junction current and modulation of the length of the external cavity, formed at one end by a diffraction grating mounted on a piezo actuator.

Each of the lasers has a saturated-absorption spectroscopy set-up using a room-temperature atomic-vapour cell. The associated transmission spectrum provides a set of identifiable features corresponding to the hyperfine structure of the atomic species. This enables the experimenter to determine the precise frequency of operation, and perform diagnostics. Spectroscopic techniques can be used to generate error signals, which in turn can be used to 'lock' a laser to a very precise frequency. Servo-mechanisms then stabilize the laser against fluctuations in its frequency caused by, for example, temperature changes, acoustic noise and vibrations. In the following sections, the systems constructed to stabilise the frequencies of the lasers are discussed.

4.2.1 Reference laser

A number of reference lasers have been used during the course of the experiment. For the majority of the results presented in later chapters, the reference laser used was a Toptica DL-Pro. The reference laser is locked to the $F = 2 \rightarrow F' = 1, 3$ crossover resonance in a rubidium vapour cell using a sub-Doppler dichroic atomic vapour laser locking (DAVLL) technique. This lock point, being some 211 MHz below the $F = 2 \rightarrow F' = 3$ transition, is well positioned for loading of the type-I MOT and sub-Doppler cooling of the atoms, which is most effective at large detuning, and is especially convenient for the fast frequency-switching used when loading atoms into the type-II MOT. The sub-Doppler DAVLL technique [81] provides a sharp, well defined spectroscopic signal for frequency stabilisation to the $F = 2 \rightarrow F' = 1, 3$ crossover resonance in ^{87}Rb. The optical set up for this technique is illustrated in Fig. 4.3 (see also [82]) along with the error signal obtained. Both the strong pump beam and weak probe beam are linearly polarised. A solenoid around the vapour cell induces a dichroism in the atomic vapour, such that the frequencies of the $\sigma^{\pm}$ transitions driven by the circularly-polarised components of the probe beam are shifted in opposite directions. After propagating through the vapour cell the weak, linearly-polarised probe beam is decomposed into its circularly-polarised components by a quarter-wave plate (QWP), which is aligned so that these components are projected onto orthogonal linear polarisations. A polarising beamsplitter cube (PBS) is used to separate the two linear polarisations and the transmission

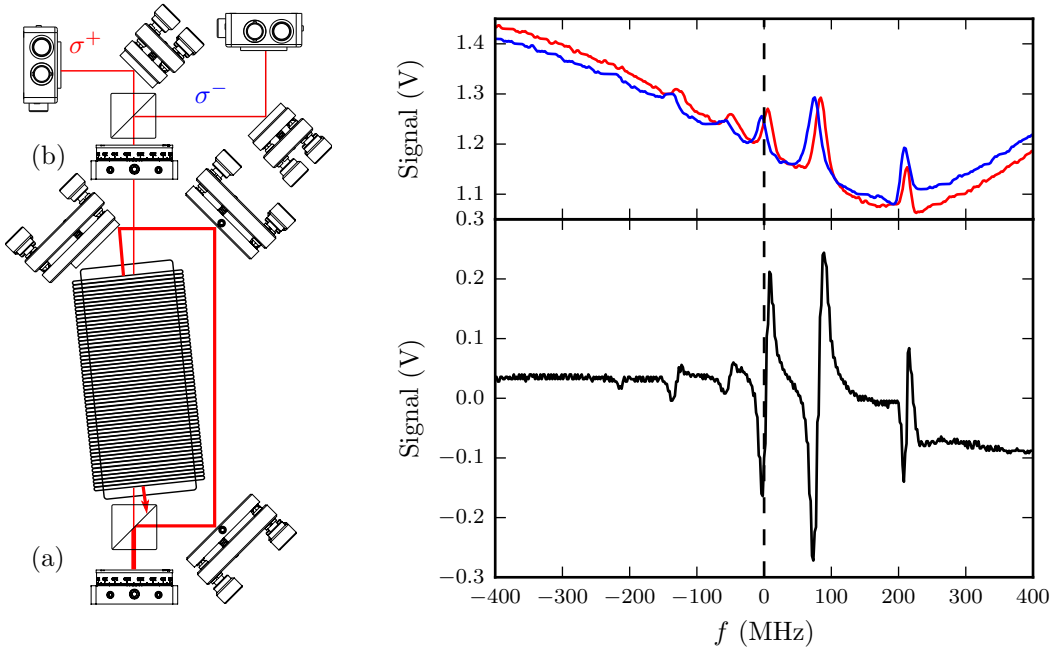

Figure 4.3: Left: Optical arrangement used to obtain DAVLL spectra used for frequency stabilisation of the reference laser. The half-wave-plate at (a) divides the input beam into a weak probe and stronger pump, both of which are linearly polarised. The quarter-wave plate at (b) separates the weak probe into its circularly-polarised components. Right: Transmission spectra and error signal as a function of laser frequency, which is measured relative to the lock point of the reference laser, which is the $F = 2 \rightarrow F' = 1, 3$ crossover resonance. The solenoid induces a dichroism in the transmission of the $\sigma^{\pm}$ components in the vapour, which is clearly visible in the top-right panel. The resultant error signal obtained from the difference in the photodiode signals is shown in the bottom-right panel.

of the circularly-polarised components through the atomic vapour is recorded by analysing the resulting beams with a pair of photodiodes. An error signal suitable for frequency stabilisation is obtained by taking the difference in voltages obtained for the transmission spectra of the two probe polarisations.

To see why this is the case consider the transmission of the probe beam in the vicinity of the $F = 2 \rightarrow F' = 3$ transition. The strong pump beam optically pumps most atoms into the extremal-m_F ground states. The pump beam also most strongly saturates these transitions, so that at this frequency the transmission of the probe beam is highest. As the magnetic field is increased the differential Zeeman shift of the $m_F = 2 \rightarrow m'_F = 3$ transition is about +1.4 MHz/G, whereas the shift of the $m_F = -2 \rightarrow m'_F = -3$ transition is the opposite, -1.4 MHz/G. The peaks in transmission of the $\sigma^{\pm}$ probe light therefore separate by approximately 2.8 MHz/G.

Fig. 4.3 shows the signals recorded by each of the photodiodes. The transmission spectrum of the σ^- component of the pump beam is shown in blue, and is shifted to lower frequencies. The transmission spectrum of the component driving σ^+ transitions is shown in red, and is shifted to higher frequencies. The spacing of

the features in the transmission spectrum can by used to calibrate the frequency axis. By doing this, an estimate is obtained of the frequency separation between the peaks in the $\sigma^{\pm}$ spectra that correspond to the $F = 2 \rightarrow F' = 3$ transition. This separation is estimated to be about 5.5 MHz/A, from which it follows the solenoid surrounding the vapour cell generates a magnetic field of about 2 G/A. The solenoid is wound directly around the atomic-vapour cell and the current in the solenoid is provided by a bench-top power supply. Further detail on the sub-Doppler DAVLL technique is given in [83].

In order to stabilise the frequency of the reference laser the DAVLL error signal is used as the input to a frequency controller with proportional and integral gain, a 'PI-controller'. The output of the PI-controller is used to modulate the length of the external cavity of the diode laser via the external modulation input of the piezo-stack driver module on the laser control unit (Toptica DLC-110). The proportional gain bandwidth has a frequency-dependent roll-off that helps to prevent acoustic resonances in the piezo actuator from being driven by the PI-controller. The proportional and integral gains of the controller are adjusted to give quick settling times without inducing oscillations.

4.2.2 Frequency-offset locking

Both cooling lasers used in the type-II MOT experiments are locked to the reference laser via a frequency-offset lock. The offset lock for the laser addressing atoms in the $F = 1$ ground state is the simpler of the two to construct. This is due to the fact that a convenient bandwidth, of perhaps a few hundred MHz, is decades narrower than the ~6.6 GHz frequency offset from the desired bandwidth centre, which simplifies the choice of components.

Both frequency offset locks are similar in design, and based upon that found in [84]. Laser light from the laser to be locked is overlapped with light from a stabilised reference laser using a non-polarising beam-splitter cube. The light passes through a linear polariser, ensuring that the electric field vectors of the two beams are well aligned to give a strong beat signal, and is coupled into a single-mode optical fibre. The low-frequency optical beat-note between the two lasers is detected by a fast photo-diode. An error signal suitable for frequency stabilisation is obtained from the beat note using the frequency-discriminator circuit illustrated in Fig. 4.4.

The optical beat note is detected on a fast photodiode, which is connected to a bias tee, and amplified. The amplified signal is mixed with the output of a voltage-controlled oscillator (VCO) so that the resulting signal contains components at the sum and difference of the two frequencies. At this point it may be convenient to filter out one of the two components in order to increase the spectral purity of the

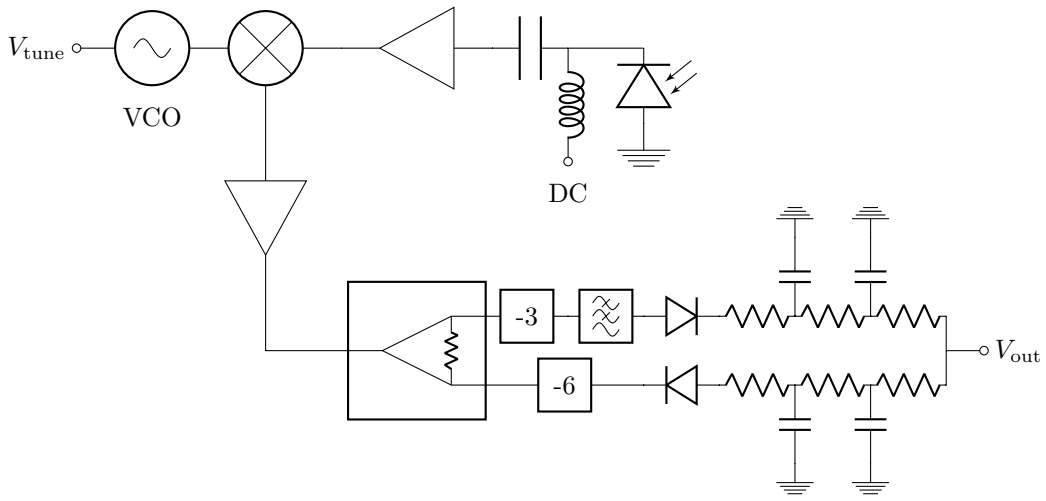

Figure 4.4: Simplified schematic of the frequency discriminator used in the frequency-offset locks described in the text. The optical beat note between two lasers is detected on a fast photo-diode connected to a bias-tee. The beat note is amplified and mixed with the output of a VCO, which can be tuned to vary position of the zero crossing as a function of frequency in V_{out}. The lock point, $V_{\text{out}} = 0$ V, is obtained when the difference in frequencies between the VCO and optical beat note coincides with the -3 dB point of the filter.

signal, which can otherwise result in multiple lock points being obtained from the frequency discriminator. The signal is again amplified and passes through a power splitter, with the first output connected to a -3 dB attenuator followed by a low-pass filter and the second output connected to a -6 dB attenuator. The two signals are at this point rectified by a pair of oppositely-orientated high-speed diodes, each in a half-wave configuration, resulting in two high-frequency rectified signals of opposite polarity. Each of the signals passes through a second-order low-pass filter and the resulting voltages are summed across a resistive divider. When the frequency of the mixed-down beat note coincides with the -3 dB point of the filter the RF powers at each of the two inputs to the rectifying circuit are nominally equal, in which case $V_{\text{out}} = 0$ V. It is the roll-off of the electronic filter around the -3 dB point that results in a zero crossing feature being obtained. The lower the cut-off frequency of the filter the sharper the roll-off, and hence the narrower the zero crossing feature will be in frequency. The rectifying and filtering circuit is assembled using surface-mount components soldered to a circuit board manufactured on a milling machine. The rest of the components are purchased as SMA-connectorized packages. The entire assembly is mounted on an upright steel sheet, which gives a conveniently small footprint.

The error signal obtained from the frequency discriminator circuit described above is used as the input to a home made PI-controller. For optimum performance the PI-controller is tuned to eliminate or minimise undesirable effects such as oscillatory behaviour and overshoot, and to reduce the settling time of the system.

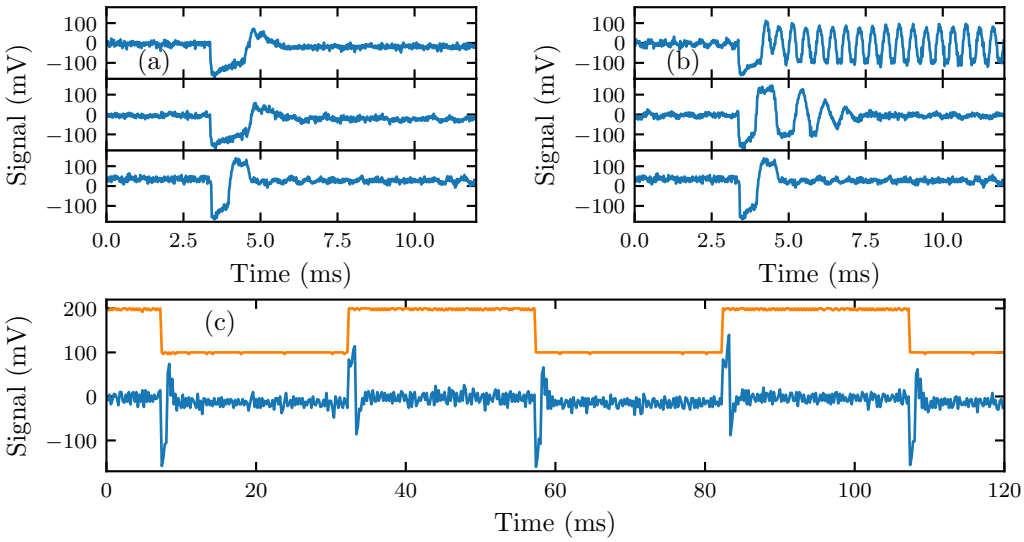

Figure 4.5: Tuning of the laser recapture lock. (a) Integral gain is tuned to reduce settling time at the expense of over-shoot. (b) Proportional gain is tuned to suppress acoustic oscillations of the laser cavity, whilst giving a reasonable response time. (c) The frequency offset lock set point is modulated and the error signal monitored with the laser locked. The settling time is < 2 ms.

To tune the controller the offset-lock set-point is modulated by applying a square-wave voltage to V_{tune}. When the feedback loop is enabled the PI controller attempts to compensate for any sudden change, which is visible as an abrupt deviation in the error signal from close to 0 V, followed by a more gradual relaxation back towards 0 V. Fig. 4.5 shows this tuning procedure as applied to a separate, but functionally-identical arrangement. The response of the control loop can be seen to improve as the individual gains of the proportional and integral feedback are varied.

F = 2 laser

Laser light used to obtain an error signal is taken from the master-oscillator output of the TA-Pro, prior to the injection of the TA. The laser light is overlapped with light from the reference laser, coupled into a fibre and sent to the frequency discriminator. The error signal obtained from the frequency discriminator constructed to lock the laser to transitions from the $F = 2$ ground state is shown in Fig. 4.6. The lock point can be varied from ~38 MHz to ~309 MHz red-detuned or blue-detuned from the reference laser frequency by tuning the VCO frequency, as indicated in the figure. The laser-frequency controller allows the frequency to be locked to either a positive-going or negative-going zero crossing by switching the sign of the feedback. A useful frequency discriminator should allow the zero crossing to be tuned with a bandwidth comparable to the frequency-span of the excited-state hyperfine structure. In this case however, since the reference laser is itself locked to a transition from the $F = 2$

ground state, the mixed-up and mixed-down beat-notes are separated by at most a few octaves and both are visible down-stream of the mixer. This can lead to a complication of the error signal and multiple zero crossings, which may be partially mitigated by a careful choice of components. The error signal obtained contains two well-defined zero crossings that are higher in frequency, and two lower in frequency, than the reference laser. The zero crossings are well separated and the zero crossing closest in frequency to the reference laser is used as a lock point. As can be seen in the figure, the gradient of the zero crossing is steep and the range of frequencies captured by the lock-point is very large, which gives a robust and flexible lock. A full list of components used in the construction of the $F = 2$ frequency discriminator Fig. 4.6 is provided in Table A.2.

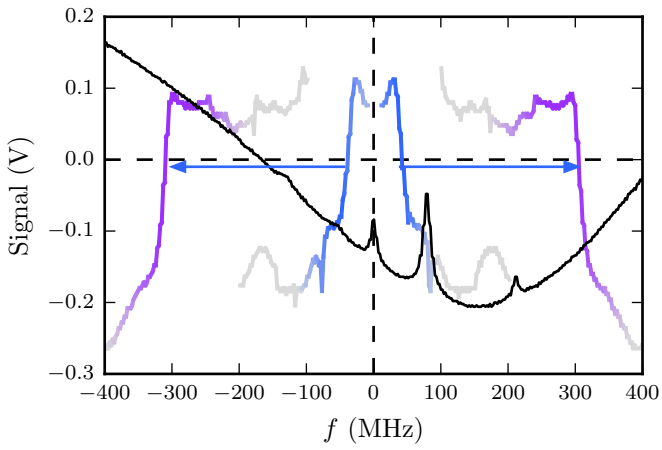

Figure 4.6: Sub-Doppler spectroscopy of transitions from the $F = 2$ ground state in a Rb vapour cell. The x-axis is centred on the $F = 2 \rightarrow F' = 1, 3$ crossover transition. Also shown are the error signals obtained from the frequency discriminator described in the text, for two different set points. The zero crossings that can be used to lock the feedback loop is highlighted for both set points. The range of lock points extends from approximately 38 MHz to 309 MHz above the reference laser lock point, and the same range below. The arrows indicates how the error signal varies as the VCO tuning voltage in the frequency discriminator circuit is varied.

F = 1 laser

The offset lock for the laser addressing the $F = 1$ ground state allows the lock point to be tuned across the entire excited-state hyperfine manifold as shown in Fig. 4.7. This is achieved by using a frequency-doubled VCO (MiniCircuits ZX95-3450+) with a nominal centre frequency of 3350 MHz and 200 MHz of bandwidth. Some 400 MHz of tuning bandwidth is obtained by the frequency discriminator circuit, conveniently centred between the $F = 1 \rightarrow F' = 2$ and $F = 1 \rightarrow F' = 2$ transitions. A complete parts list of components used is provided in Table A.3.

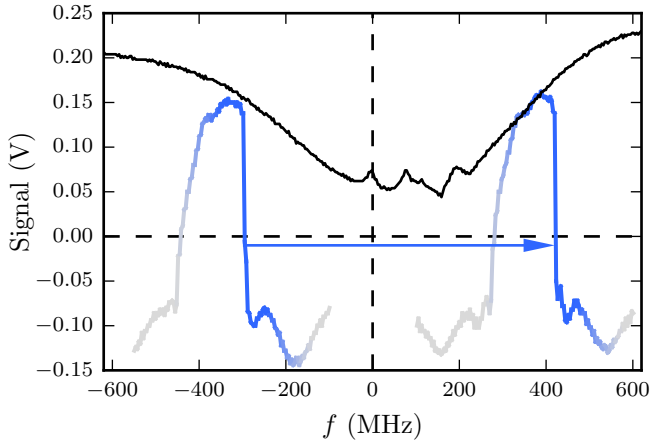

Figure 4.7: Sub-Doppler spectroscopy of transitions from the $F = 1$ ground state in a rubidium vapour cell. The x-axis is centred on the $F = 1 \rightarrow F' = 0$ transition. Also shown are the error signals obtained from the frequency discriminator described in the text, for two different set points. The zero crossing used to lock the feedback loop is highlighted for both set points. The frequency offset lock can be set to address any of the transitions from the $F = 1$ ground state. The arrow indicates how the error signal varies as the VCO tuning voltage in the frequency discriminator circuit is varied.

4.2.3 Laser frequency monitoring

While the offset lock is very robust and versatile, it does not itself provide a direct readout of the laser frequency. To obtain this the frequency of the optical beat note is measured directly using a frequency counter. Laser light from the experiment laser and reference laser is mixed on a non-polarising beam-splitter cube. One output of this is used to derive the error signal, as has been described above. The other output is used to monitor the precise frequency of the locked laser, relative to the reference laser. The mixed light is focussed onto a fast photodiode and amplified. A MiniCircuits UFC-6000 frequency counter is used to monitor the beat note from both locked lasers. An RF-switch is used to select the input to the frequency counter, alternating between the beat-notes of each of the TA-Pros with the reference laser. The UFC-6000 is a compact, low-cost frequency counter with a USB-interface and API allowing it to be integrated into the experiment control software described in section Sec. 4.8.2. The frequency counter has an upper-limit cut-off of 6 GHz, which is too low to detect the beat note between the reference laser and the $F = 1$ laser. Therefore, it is necessary to reduce the frequency of the beat-note, which is achieved by mixing-down with the output of a VCO running at a fixed frequency.

To calibrate the absolute frequency offset between the $F = 1$ laser and the reference laser we simultaneously monitor the steady-state MOT fluorescence and the beat-note frequency measured by the counter. The intensity of re-pump light is reduced until a MOT is only formed when the $F = 1$ laser is tuned close to either

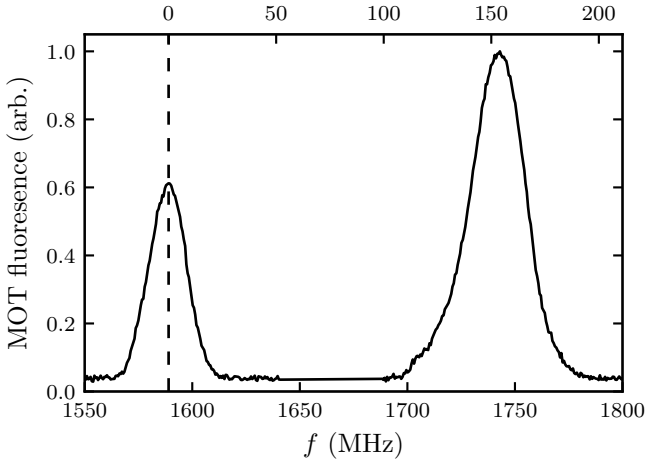

Figure 4.8: MOT fluorescence as the frequency of the $F = 1$ laser is scanned with low intensity. The lower-frequency peak occurs when the repump laser is tuned close to the $F = 1 \rightarrow F' = 1$ transition. The larger, higher-frequency peak is obtained when the repump laser is tuned close to the $F = 1 \rightarrow F' = 2$ transition, which is a more effective repumping transition. The peaks are used to calibrate the frequency of the mixed-down beat signal between the reference laser and the $F = 1$ laser, as measured by the frequency counter. The fluorescence data is plotted as a function of the frequency-counter readout on the lower axis. The upper axis is centred on the $F = 1 \rightarrow F' = 1$ transition and the frequency splitting between the two peaks is 157 MHz, as expected.

the $F = 1 \rightarrow F' = 1$ or $F = 1 \rightarrow F' = 2$ transitions. As the frequency of the $F = 1$ laser is scanned two clear peaks are visible, shown in Fig. 4.8. The centres of these peaks are used to calibrate the frequency of the $F = 1$ laser. The frequency of the beat-note between the $F = 2$ laser and the reference laser is well below the cut-off frequency of the counter and is monitored directly.

4.3 Capturing a blue-detuned MOT

For reasons that are discussed in previous chapters a blue-detuned MOT cannot be loaded from a thermal vapour, as in type-I atomic MOTs. Instead, atoms are first captured in a type-I MOT (using transitions (a) and (c) of Fig. 4.2). Once a sufficient number of atoms have been loaded the type-I MOT light is extinguished and the type-II MOT light is switched on (transitions (b) and (c) of Fig. 4.2). This involves stepping the frequency of the MOT light to a new lock point, which is done using the offset lock via the procedure described in Sec. 4.3.1, and simultaneously reversing the handedness of the light, which is done by switching between two sets of beams using AOMs, as will be described in Sec. 4.3.2. The recapturing process involves the following steps: Initially the type-I MOT is loaded from the background vapour for a period of time. Often atoms are further cooled by lowering the intensity of the type-I MOT for a few milliseconds after the loading phase. This process somewhat relaxes

the timing constraints in recapturing the atoms in the blue-detuned MOT. The light is then quickly extinguished using an AOM in combination with an RF-switch. At this point the type-I MOT cooling laser is unlocked from the red side of the $F = 2 \rightarrow F' = 3$ transition and relocked to the blue side of the $F = 2 \rightarrow F' = 2$ transition, (a)→(b) in Fig. 4.2. A brief period of time elapses to allow the laser frequency to settle before the blue-detuned MOT light, which has the opposite-handedness polarisation, is quickly switched back on using a second AOM. The experimental sequence is quite complicated and a significant effort was made in developing a robust solution that would enable a thorough investigation of the properties of the blue-detuned MOT. The content of the following two sub-sections is dedicated to the particulars of the techniques and experimental set-up developed to achieve this polarisation and frequency switching. First the method used to quickly unlock the laser from one transition and relock to a second, which can be hundreds of MHz away, is discussed. Then, the means by which the handedness of the polarisation is reversed is described.

4.3.1 Automatic laser relocking

One of the most technically challenging demands of the experiment is having the ability to quickly switch between two lock points separated by up to ~300 MHz, during the course of an experimental sequence. Such large frequency separations are difficult to account for quickly by using a modulation of the cavity length, due to the limited bandwidth of the feedback loop to the piezo-mounted grating. Such bandwidths are typically sub-kHz to prevent acoustic resonances being driven in the piezo stack. Instead, the frequency step is achieved by a modulation of the laser-diode current, which changes the optical path-length inside the diode. The current can be modulated much more quickly than the ECDL grating without adverse effects.

A controller has been designed which allows the feedback to the piezo during the diode current modulation to be disabled, permitting a fast step-change in the lock-point of the laser. However, long-term frequency drifts of the laser due to, for example, small variations in ambient temperature are compensated for using an integral feedback to the piezo. Therefore, at any given time there is a non-zero voltage on the piezo modulation input that must be held constant during the fast current modulation. When the feedback is re-enabled, close to the new lock point, then the output of the feedback circuit should be summed with the existing voltage, which allows the laser frequency to be 'jumped' between lock points in a reliable fashion.

The PI-controller has been designed with a 'track' and 'hold' functionality. A

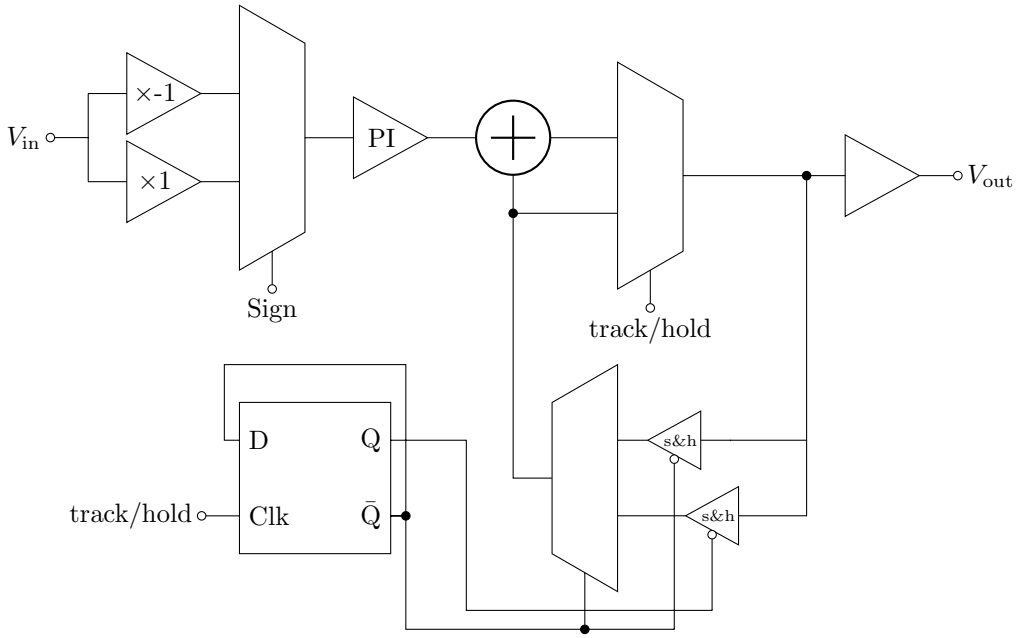

Figure 4.9: Simplified schematic of the circuit used to lock and relock the $F = 2$ laser. The circuit consist a pair of unity-gain differential-input instrumentation amplifiers. The laser can be locked to negative-going or positive-going zero crossings in the error signal using the input multiplexer to switch the sign of the error signal input to the PI-stage. Upon a transition from track→hold one of the sample and hold amplifiers samples the output voltage and is then connected to the output buffer using the two multiplexers shown.

simplified schematic illustrating the key components of the circuit is given in Fig. 4.9. When operated in 'track' mode the PI controller behaves in the usual way. Upon a change of state of the digital input signal defining the mode of operation the instantaneous output voltage accumulated on the piezo modulation input is recorded by of a pair of sample-and-hold (s&h) amplifiers. A multiplexer routes the output of the s&h amplifier to the output and the feedback loop is opened, which resets the integrator. At this point the set-point of the frequency-discriminator circuit is changed to the desired frequency and a calibrated feed-forward is applied to the laser current modulation input such that the operating frequency of the laser is close to the new locking point. When the controller is returned to its track mode the feedback loop is closed and the output summed with the initial voltage to ensure well behaved and predictable operation without any unintentional frequency jumps. The circuit allows the blue-detuned MOT to be efficiently loaded with high numbers of atoms that have been captured and cooled in the type-I MOT. Similarly, atoms in the blue-detuned MOT, which are mostly found in the $F = 1$ ground state, can be re-loaded into a type-I MOT or illuminated in an optical molasses on the $F = 2 \rightarrow F' = 3$ transition, where instead atoms are almost exclusively found in $F = 2$, using the same method in reverse. This technique has been used during some of the characterisation of the blue-detuned MOT to repump atoms into the $F = 2$

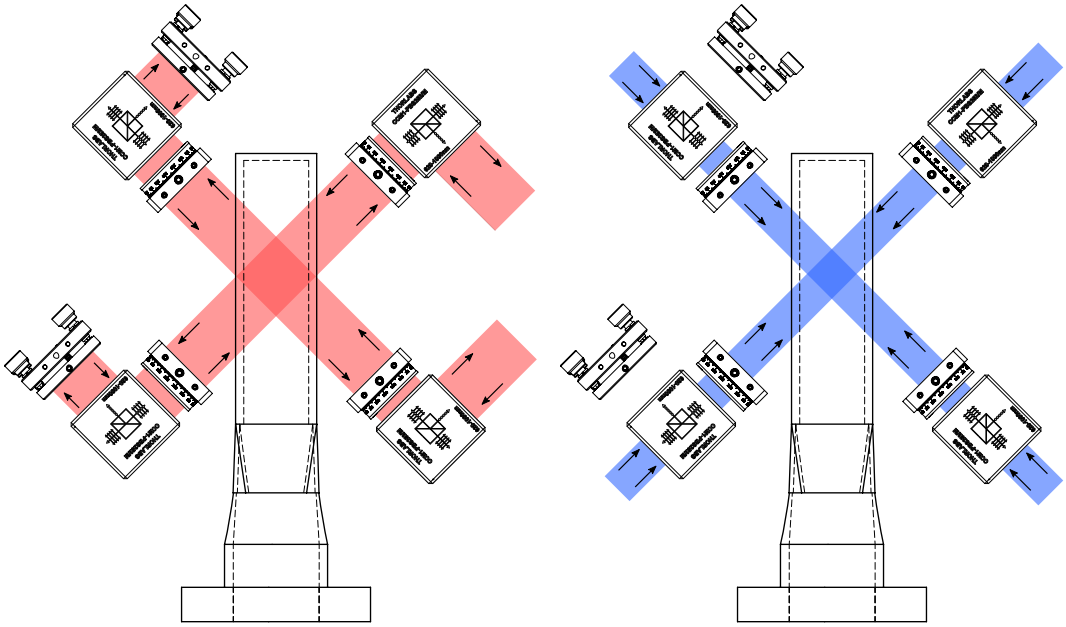

Figure 4.10: An illustration of some of the MOT optics used in the experiment. The radial MOT beams are shown. The x, y, z components of two independent sets of MOT beams (red, blue) have orthogonal linear polarisations and are mixed on PBS cubes. The quarter-wave-plates impart circular polarisations of opposite handedness onto the two sets of beams. For simplicity the beams used to load the type-I MOT are retro-reflected, as shown on the left. The type-II MOT is weaker and more sensitive to intensity imbalances between counter-propagating components. For this reason the beams are not retro-reflected and instead a 6-beam MOT is used, as indicated by the illustration on the right.

state, which is sensitive to the imaging light, to explore a larger parameter space that would otherwise be constrained by the visibility of the atoms. At a later stage in the investigation a dedicated optical pumping beam was set up, which rendered this technique obsolete.

The circuit schematic and PCB layout was designed using EAGLE. A PCB was manufactured by PCBway, on which the circuit was assembled. The design allows the laser to be quickly unlocked, tuned to address a different transition, and relocked in a time < 2 ms. Atoms can consequently be cooled in a type-I MOT and recaptured in a blue-detuned type-II MOT with ease.

4.3.2 Switching the polarisation of the MOT light

The polarisation of MOT light required to provide confinement in the red-detuned type-I MOT is opposite to that required in the blue-detuned type-II MOT. This is true for the hyperfine quantum numbers and g-factors of the states used for the schemes shown in Fig. 4.1. The method used in the course of this investigation is to have two independent sets of MOT beams, each of which is circularly polarised but with opposite handedness.

The optical arrangement used to obtain two independent sets of fast-switching

MOT beams is shown in Fig. 4.11. Light from each of the two TA-Pro lasers first passes through a half-wave plate and then a high-power PBS cube, which discards some of the power into a beam dump. The two beams are then mixed on a non-polarising beam-splitter cube and coupled into a pair of single-mode polarisation-maintaining optical fibres. The beams from both lasers have an identical linear polarisation and, after being mixed on the 50:50 beamsplitter cube, a HWP is used to make fine adjustments relative to the optical axes of the fibre. The output of one of these fibres is used to derive the cooling and trapping light for the type-I MOT and the other is used for the type-II MOT. In both arrangements the output of each of the optical fibres passes through an AOM, and the alignment is adjusted to maximise the power in the +1-order mode. The AOMs are driven by MiniCircuits VCOs mounted on a control board that provides an output with a voltage-variable frequency and attenuation. The output from the control board is used as one input to an RF-switch and the other input is terminated. The output of the RF switch is amplified by a power-amplifier (API Technologies QBH-2832 or MiniCircuits ZHL-2W+) and connected to the AOM. Light emerging from the +1-order mode of the AOM then passes through an iris, which blocks stray light in the other modes, and a mechanical shutter. The mechanical shutters are driven by a bipolar current-pulse generating circuit with TTL inputs. Using a mechanical shutter allows the AOM to be on most of the time, even when the light is not desired, because the mechanical shutter can be closed and the AOM switched back on. The experiment control sequences are programmed to synchronise the action of the AOM and mechanical switch in such a way as to exploit the fast rise and fall-time of the AOMs, whilst also having an AOM duty-cycle of close to 100%. Having a high duty-cycle minimises transient effects, which can alter the power and polarisation of the light down-stream, as the AOM heats up.

One benefit of using separate sets of beams is that different sized beams can be used in each set. The type-I MOT beams are made larger, in order to maximise the loading rate and number of trapped atoms [85]. The type-II MOT beams are smaller, in order to be able to investigate a greater range of intensities. A disadvantage of this technique is that care must be taken to overlap the centres of the traps formed by each set of beams in order to ensure efficient transferral of atoms. In practice, coarse alignment of the two sets of beams is achieved by loading a type-I MOT and observing the perturbation of the trapped atoms by the second set of beams, which are apertured down to a small size. The large capture volume defined by the intersection of these beams at the chamber is beneficial to loading high numbers of atoms. By contrast, the type-II MOT capture volume need not be large, as this is loaded directly from atoms previously cooled in the type-I MOT.

Following the mechanical shutter the beam path for the type-I MOT light and the

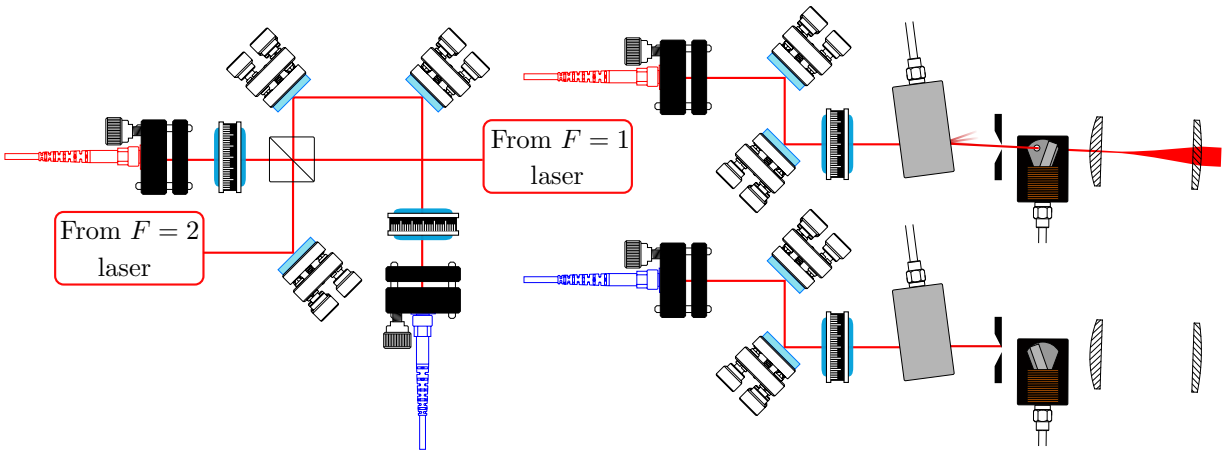

Figure 4.11: Optical switches used to reverse the polarisation of the MOT light. Light from the $F = 1$ and $F = 2$ lasers is mixed on a non-polarising beamsplitter cube and coupled into a pair of optical fibres. Laser light from each of the outputs of the fibres is aligned to maximise the +1-order mode of an AOM. The light then passes through an iris and mechanical shutter before being telescoped up to a larger size for use in the MOT. The purpose of the mechanical shutters is described in the text.

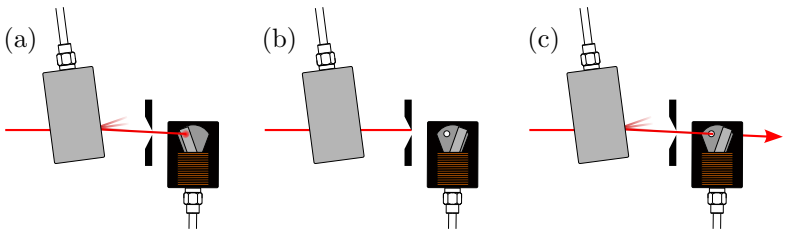

Figure 4.12: AOM switching sequence. The images illustrate switching one set of beams on. (a) When the MOT light is off the AOM is running and the mechanical shutter blocks the light. (b) The AOM is switched off using an RF switch and the mechanical shutter is opened. This happens a few milliseconds before the MOT light is switched on. (c) The AOM is switched back on, using the RF switch, and the light passes through the mechanical shutter, which is already open. The combination allows the AOM to be on, even when the MOT light is required to be off—the AOM need only be switched off for the few milliseconds it takes for the mechanical shutter to open or close.

type-II MOT light differ slightly. Both beam paths pass through a telescope but the type-I MOT light is expanded to a greater degree, approximately filling a one-inch aperture. This light is then divided into four beams; two of these form the radial MOT beams, which are retro-reflected back on themselves, and the remaining two form the axial MOT beams. A six-beam arrangement is unnecessary for the type-I MOT as the confinement is more robust to small imbalances in intensity and polarisation. Small adjustments of the two independent axial beams can help to improve the overlap of the centres of the type-I and type-II MOTs, and so this arrangement is designed with four independently controllable beams. The type-II MOT is found to be sensitive to any intensity imbalance between counter-propagating beams and a 6-beam MOT is required for robust operation, which allows the powers in counter-propagating pairs to be balanced more precisely. Expanding these beams to a lesser degree allows high intensities of light to be achieved, despite the six-beam configuration. Due to the sensitivity of the type-II MOT to the balance of intensities between counter-propagating beams it is important to eliminate any variations in the polarisation of the light. A linear polariser is therefore placed between the AOM and the first PBS used to divide the light. The linear polariser fixes the plane of polarisation of the MOT light prior to it being divided up to obtain the separate beams. This makes the relative intensities between beams insensitive to small changes in the polarisation of the light upstream. Instead, small changes of the incoming polarisation result in small changes of the total power of the MOT light. Additionally, the total power is also actively monitored by focussing a small fraction of the light, obtained using a beam-sampling plate after the linear polariser, onto a photodiode.

The four beams of the type-I MOT and the six of the type-II MOT share a common set of optical axes at the MOT position. To achieve this, PBS cubes are used to mix light from the two sets, as shown in Fig. 4.13 and previously, in Fig. 4.10. The mixed light emerges with the same $\vec{k}$ but two orthogonal linear polarisations. Finally, a quarter-wave-plate is used to map the the two linear polarisations onto circular polarisations with opposite handedness. The light enters the MOT chamber and intersects the other trapping beams at the geometric centre of the quadrupole magnetic-field coils. The polarisation of the MOT beams is quickly reversed by switching the states of the two AOMs/shutters.

4.4 Experiment chamber

In this section the vacuum chamber arrangement, assembly, and preparation is described. A description of the magnetic field coils, mounted around the chamber to control the ambient field, and associated control systems is also provided.

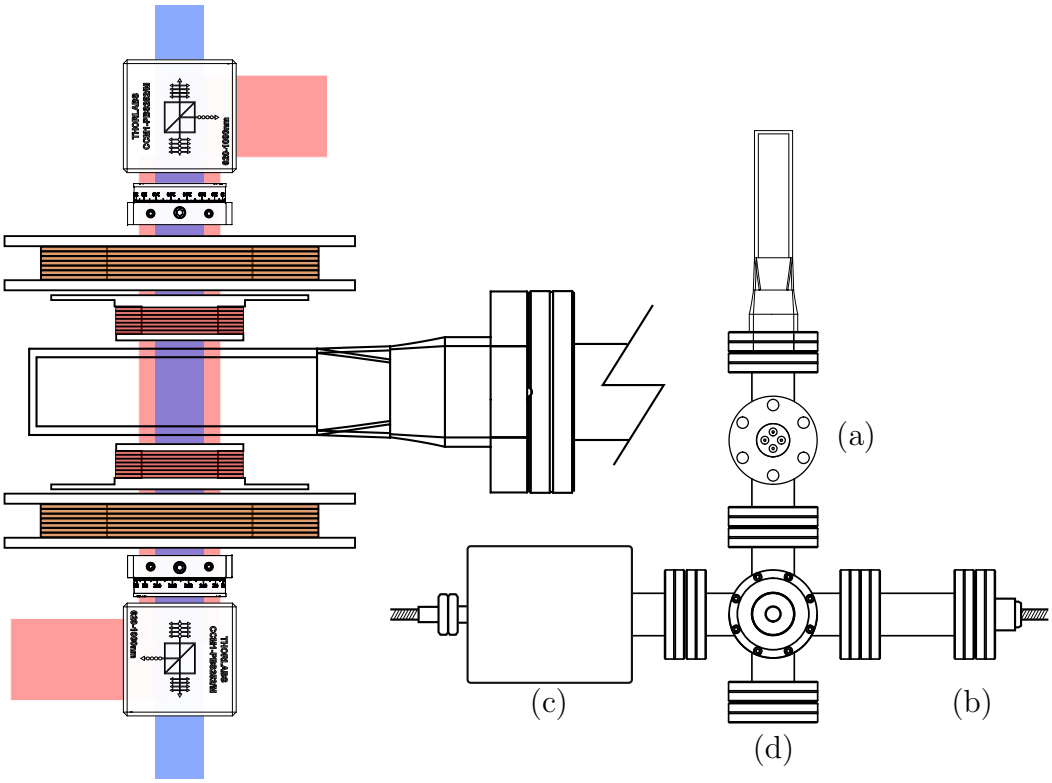

Figure 4.13: Left: the axial MOT optics and magnetic-field coils are shown in relation to the cell. The MOT beams for the type-I and type-II MOTs are overlapped on a PBS and have circular polarisations of opposite handedness after passing through the quarter-wave plate. The larger-diameter magnetic field coils are arranged in a Helmholtz configuration and provide a bias field along the MOT axis. The smaller-diameter coils provide the quadrupole field for the MOT. Right: the vacuum chamber assembly. The dispensers are located at (a), and are mounted in a tee. A 6-way cross connects the remaining components. An ion-gauge is located at (b). An angle-valve is connected to the cross and is in the plane of the illustration. An ion pump is connected at (c). (d) is a viewport, which is used to monitor the MOT using a CCTV camera and also provide optical access for a push beam.

4.4.1 Vacuum chamber layout

The vacuum chamber assembly consists of an ion-pump, ion-gauge, Rb dispensers attached to electrical feed-throughs, and an all-metal angle valve. A fused-silica UHV glass cell serves as the main experiment chamber in which the MOT is formed. The assembly is illustrated in Fig. 4.13. The ion pump, all-metal valve and ion gauge are mounted on a 6-way cross. The dispensers are mounted in a tee which connects the 6-way cross to the glass cell. A window is installed on the opposite port of the cross to the cell, through which the MOT can be imaged. This window also provides optical access for the push beam, as described later.

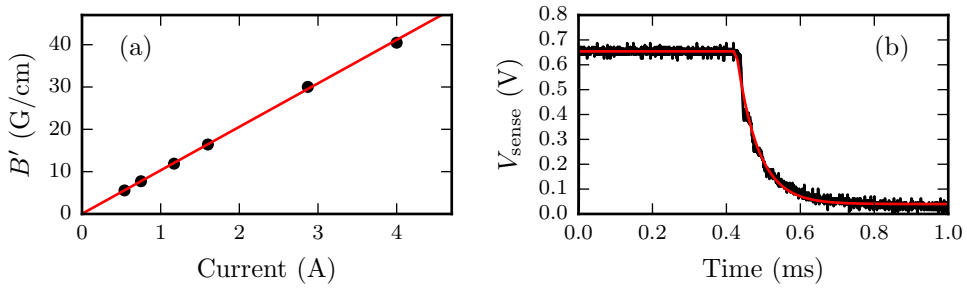

Figure 4.14: (a) The magnetic field gradient B' is measured, for a number of different currents, by translating a Gaussmeter along the axis of the MOT coils. The pair of coils produce a field gradient of 10.3(1) (G/cm)/A at their geometric centre when mounted around the glass cell. (b) The decay of current in the coils following a sudden change of the set-point of the coil driver, which closes the MOSFET. Part of the data is fit to an exponential decay, which yields a best-fit decay time of $\tau = 58.1(4)$ µs.

4.4.2 Magnetic-field control

The quadrupole MOT field is generated by a pair of anti-Helmholtz magnetic field coils wound from 100 turns of 0.8 mm diameter, enamelled, circular-cross-section wire. Coil forms have been designed to be mounted directly on the Thorlabs cage assembly surrounding the cell. The forms have inner and outer diameters of 25 mm and 45 mm, respectively, and the inside faces of the coil forms are separated by 35 mm once mounted. The coil pairs generate a magnetic field gradient at their geometric centre of 10.3(1) (G/cm)/A, which is measured by translating a gaussmeter along the axis of the coils, Fig. 4.14(a). The current flowing in the MOT coils is controlled using a high-power MOSFET (IXYS IXFN180N15P), and a high-power sense resistor, with an op-amp in a simple voltage-feedback circuit driving the gate of the MOSFET. A simplified schematic is shown in Fig. 4.15. To measure the switching time of the coils the gate voltage of the MOSFET is changed suddenly to 0 V, and the decay of current in the coils is monitored using the sense resistor voltage. This data is recorded and fitted to an exponential decay which gives a characteristic decay time of 58.1(4) µs, Fig. 4.14(b). Low inductance, and hence fast switching times, are achieved by mounting the coils as close to the face of the glass cell as is possible. Magnetic-field gradients of up to 90 G/cm are obtained using a 10 A power supply. The out-of-vacuum coils are tolerant of the currents required to generate these high field gradients.

Three pairs of magnetic-field biasing coils, each in a Helmholtz arrangement, are used to compensate for the background magnetic field at the centre of the trap, and also to manipulate the position of the magnetic zero in the MOT. Each of the coils has 100 turns and is wound around a form that has been designed to be mounted on a Thorlabs 60 mm cage assembly. Each of the three pairs of coils are driven by a high-voltage, high-current operational amplifier (OPA549), with a high-power sense

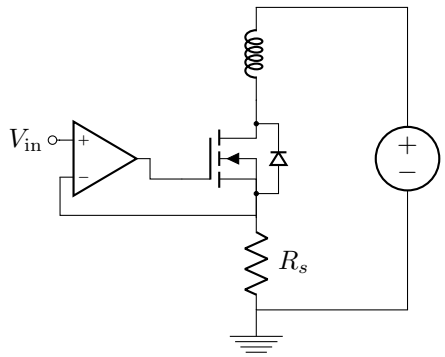

Figure 4.15: Current driver used for the magnetic-field coils in the magneto-optical trap. The current is controlled by a high-power MOSFET switch. The gate of the transistor is driven by an op-amp in a feedback circuit with proportional and integral gains. Feedback is provided by a sense-resistor in series with the coils.

resistor providing voltage feedback to the op-amp.

The temperature of atoms cooled in an optical molasses is a sensitive probe to the presence of a magnetic field [46]. A non-zero magnetic field disrupts the sub-Doppler cooling mechanisms and limits the temperature to which atoms can be cooled. In order to determine the operating current at which the background magnetic field is most effectively cancelled, the temperature of atoms cooled in a molasses is measured as the current through each pair of bias coils is varied iteratively. Some data from the process is shown in Fig. 4.16, where the current in two different pairs of bias coils (pair A and pair B) is scanned sequentially. The field due to bias pair A is varied first, then fixed at the value that minimises the temperature of the atoms. Next, the field due to bias pair B is varied, and a lower minimum temperature is reached indicating the background field has components along the axes of both pairs of bias coils.

Also mounted on the cage assembly are a pair of bias coils providing the quantisation axis for the imaging light, as discussed in Sec. 4.5. The axis of the coils is aligned with the axis of propagation of the imaging light through the cell. The coils are driven with a MOSFET current driver using an arrangement like that shown in Fig. 4.15.

4.4.3 Preparing the chamber

Prior to assembly, the vacuum chamber components were cleaned with isopropanol, and new rubidium dispensers were attached to the electrical feed-throughs. During the assembly annealed copper gaskets were used between flanges attached to delicate components such as the rear window and UHV glass cell. Elsewhere, standard copper gaskets have been used. A torque wrench was used to achieve the recommended bolt torque when connecting the components, as per the manufacturers' specifications.

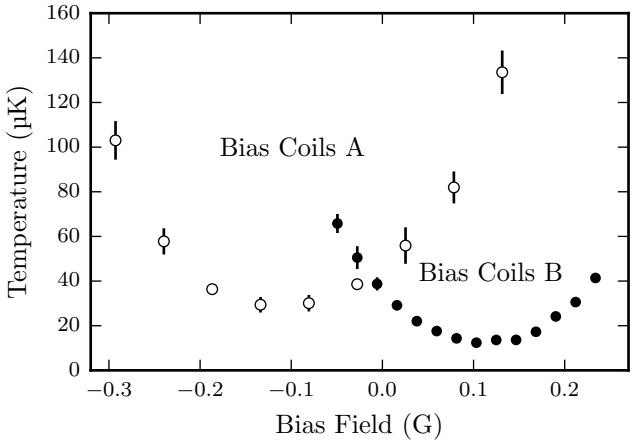

Figure 4.16: The temperature of atoms cooled in an optical molasses is used to probe the background magnetic field in the experiment chamber. The magnetic field produced by two pairs of bias coils is varied, in turn, and the resulting temperature of the atoms is recorded. Bias coil pair A (unfilled markers) is varied first and is then fixed at the value that minimises the temperature. Bias coil pair B (filled markers) is subsequently varied, and a lower temperature is seen to be reached.

Once assembled, the gate valve exhaust was attached via a bellows to a turbo-pump, which was in turn backed by a roughing line. The chamber was evacuated through the roughing line and the turbo-pump was switched on. Once the base pressure of the vacuum chamber pumped by the turbo-pump had been reached the vacuum assembly was wrapped in heater tape and aluminium foil, and baked over the course of a week or so. The temperature was increased up to about 190 °C, which removes water vapour and other contaminants from the chamber. For the duration of the baking the ion-pump magnet assembly was removed. Particular care was taken around the glass cell, where the heater tape does not make direct contact with the surfaces. Instead, a number of layers of aluminium foil were first wrapped tightly around the cell and the heater tape was then wrapped around this. The heater tape was fixed in place in a manner that attempted to stress the cell as little as possible. After baking, the temperature of the chamber was gradually reduced, and the heater tape and foil removed. The ion-pump magnets were reattached and the ion pump was switched on, with the turbo pump still running.

The rubidium dispensers were activated in a controlled way by using a high-current op-amp current driver with a high power sense resistor providing voltage feedback to the op-amp. The set-point voltage of the current driver was increased gradually over time using a simple console program to control an analog output voltage from the hardware interface described in Sec. 4.8.1. The current drawn by the ion-pump was monitored and provided a measure of the pressure inside the vacuum chamber during the activation procedure. The current was increased at a rate of about 2 A/hour. As the protective layers of the rubidium dispenser boiled

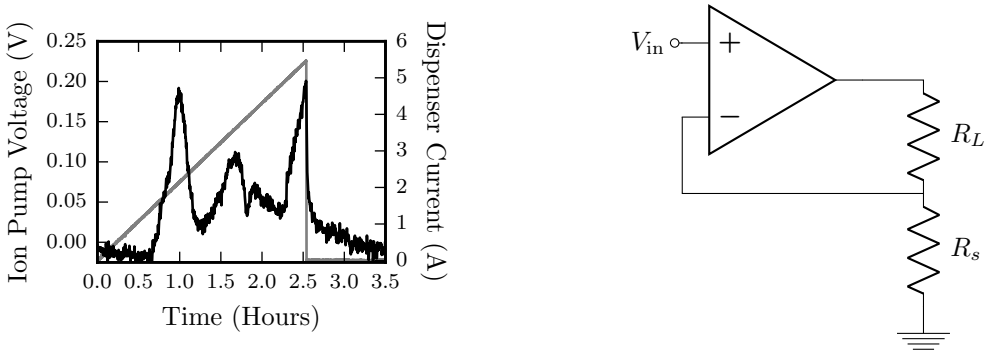

Figure 4.17: Left: The ion pump current monitor output voltage (black) as the dispenser current is gradually increased. A high-power op-amp serves as a current driver for the dispenser, R_L and is controlled through the computer interface. The pressure begins to increase sharply as the dispenser current reaches about 5A, which is close to the nominal activation current provided by the manufacturer. At this point the current driver is switched off and the pressure can be seen to fall sharply.

off a number of features were observed in the current drawn by the ion pump, which are visible in Fig. 4.17. Once properly activated the vacuum pressure should rise steadily with increasing current. As can be seen from the figure, this occurred at a current of ~5 A, at which point the dispenser was disconnected from the current driver and the pressure was observed to fall very quickly. The activation process was then applied to each remaining dispenser in turn, and each of them was observed to have a very similar profile to that shown in Fig. 4.17. The presence of rubidium in the chamber was verified by observing the absorption profile of a weak laser on a photodiode as the laser frequency was scanned.

For the majority of the measurements presented in the results section of this thesis the base pressure inside the chamber is about 8×10^{-8} mbar, as indicated by the ion gauge. This is not as low as would be required in some experiments, when evaporating to BEC for example, but it is more than sufficient for this investigation. Trap lifetimes exceeding 10 s are routinely observed.

4.5 Imaging the MOT

In this section the methods used to record absorption images of the MOT are discussed, and the calculations used to obtain an atom-number from the absorption images are also detailed.

4.5.1 Imaging optics

The optics used in the imaging system are illustrated in Fig. 4.18. Laser-light used for absorption imaging is derived from the reference laser, which is locked to the $F = 2 \rightarrow F' = 1, 3$ crossover resonance in a Rb vapour cell. The detuning of the

reference laser lock-point is some 212 MHz from the transition that maximises the optical cross-section of the atoms (either $|F = 2,\ m_F = +2\rangle \rightarrow |F' = 3, m'_F = +3\rangle$ or $|F = 2,\ m_F = -2\rangle \rightarrow |F' = 3, m'_F = -3\rangle$). The light is double-passed through an acousto-optical modulator (AA Optoelectrics MT110-B50A1-IR), which has a nominal centre-frequency of 110 MHz, using the arrangement shown in Fig. 4.19, similar to that described in [86]. The double-passed first-order mode is coupled into a single-mode, polarisation-maintaining optical fibre and sent to the experiment chamber.

At the experiment chamber the output of the fibre is collimated and passes through a 1:2 telescope to give a beam with a $1/e^2$ radius of 6.3 mm, which is measured by recording the total power remaining as a knife-edge is translated through the beam. The beam is circularly polarised by a quarter-wave plate and passes through the cell at 90° to the cell wall. A 4-f lens system using two two-inch achromatic doublet lenses (Thorlabs AC508-150-B-M) is used to form an image of the absorption of the probe beam by the MOT. The detector of an AVT Pike F-145B CCD camera is placed at the focal plane of the imaging system and is used to record absorption images. The imaging system allows both fluorescence images and absorption images to be recorded by the camera at a magnification of 1:1. A set of magnetic field coils in a Helmholtz configuration provides a homogeneous bias field aligned along the imaging axis, defining a quantisation axis for the atoms during the imaging sequence. By observing the shift in the centre of the absorption profile of the probe beam as its frequency is scanned (Fig. 4.21 c) it is estimated that the bias coils generate a magnetic field of ~1.4 G/A along the imaging axis. The circularly polarised probe light optically pumps atoms into the ground $m_F = +2$ or $m_F = -2$ state, depending on the relative orientation of the polarisation of the probe beam and the magnetic field vector defining the quantisation axis. Once in this state, atoms are coupled to only a single excited state by the probe light and are well described by a two-level system. The duration for which atoms are imaged depends upon the circumstances of the measurement. When the temperatures are low the ballistic expansion of the atoms is slow and longer exposure times can be used. This allows a lower-intensity probe beam to be used, which reduces any systematic effects arising from atoms being in the excited state. At low temperatures, atoms are typically imaged for a period of up to 325 µs, with a probe beam power of 20 µW corresponding to a peak intensity of 32 µW/cm^2, equivalent to less than 1% of the saturation intensity of the cycling transition. This corresponds to approximately 60 photon scattering events per atom in the imaging duration, when the probe light is on resonance. The associated Doppler shift, following the absorption of N photons

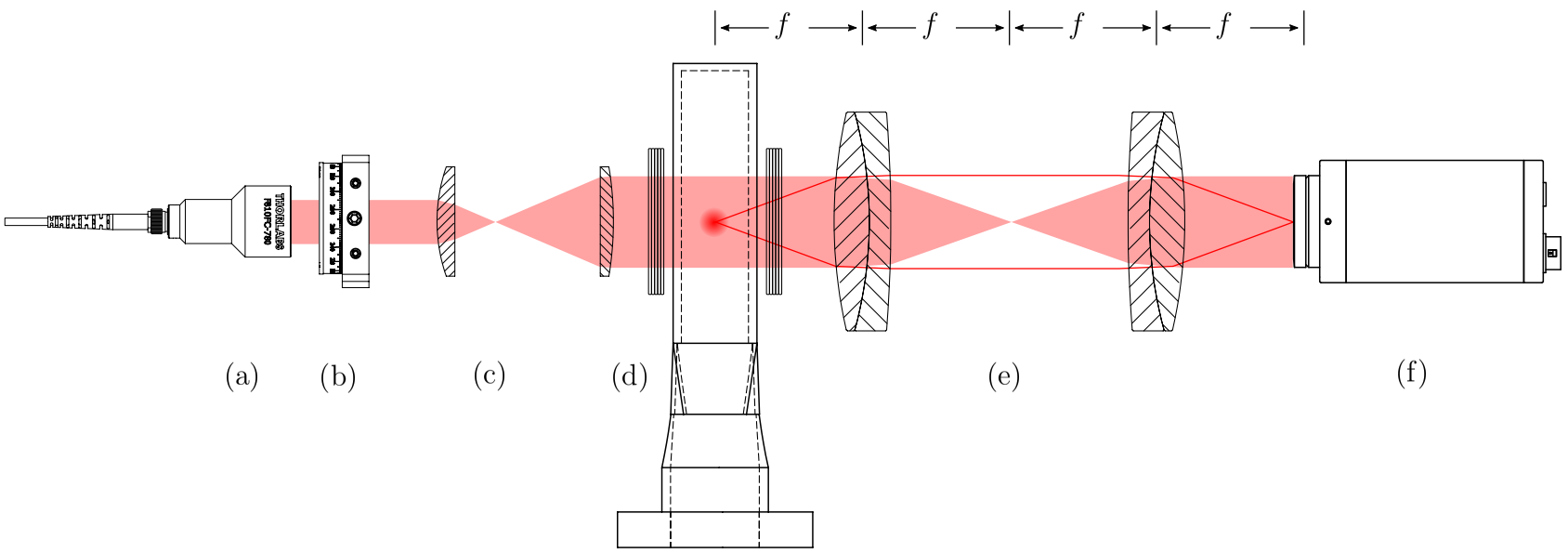

Figure 4.18: Optical arrangement for absorption imaging. (a) Light, taken from the reference laser and tuned using the arrangement in Fig. 4.19, emerges from a polarisation-maintaining optical fibre and is collimated. (b) The imaging beam is circularly polarised by a quarter wave plate. (c) The beam diameter is doubled and the beam re-collimated by a telescope. (d) A pair of Helmholtz magnetic field coils provides a quantisation axis for the atoms along the $\vec{k}$ of the light. At the position of the MOT the beam is profiled used a knife-edge and is found to have a $1/e^2$ radius of 6.3 mm. (e) 4-f imaging system comprising two achromatic doublet lenses. An image of the absorption profile of the MOT is formed on the detector of the camera at (f).

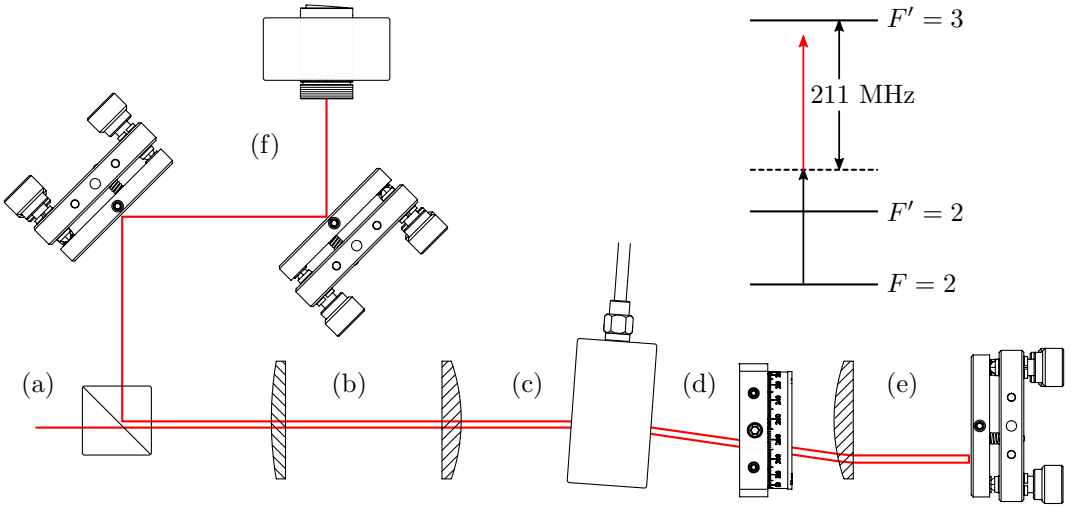

Figure 4.19: The AOM configuration used to obtain imaging light from the reference laser. The reference laser is locked to the $F = 2 \rightarrow F' = 1, 3$ crossover resonance, indicated by the dashed line on the inset energy-level diagram, some 211 MHz from the $F = 2 \rightarrow F' = 3$ imaging transition. Linearly polarised light enters the PBS at (a), the input mode is reduced in size by the telescope at (b) and enters the AOM (c). The orientation of the AOM is adjusted to maximise the power in the +1-order beam. The beam path is collimated and reflected by the 'cat's-eye' arrangement at (e) and re-enters the AOM with an orthogonal linear polarisation having made two passes through the quater-wave plate at (d). The beam, with a frequency increase of $+2\ f_{\mathrm{AOM}}$ is now reflected by the PBS at (a) and is collimated into a single-mode polarisation-maintaining fibre at (f). The cat's-eye arrangement at (e) minimises beam walk as f_{AOM}, which is necessary to ensure good coupling at (f).

from the imaging beam, Γ_d is

$$\Gamma_d = k v_d = N \frac{\hbar k^2}{m_{\mathrm{Rb}}}, \tag{4.1}$$

where k is the wavevector of the light and m_{Rb} is the mass of a rubidium atom. When $N = 60$, $\Gamma_d/\Gamma \approx 0.074$, so that the imaging process does not significantly affect the apparent detuning of the probe beams to the atoms. The systematic effect on the cross section of the atoms due to the Doppler shift from the imaging beam is calculated quantitatively in Sec. 4.9.1. When the atoms are at higher temperatures, the exposure time is reduced and the intensity of the probe light increased accordingly to ensure the cloud does not expand significantly in the duration of the exposure.

4.5.2 Measuring the number of atoms

For the case of a two-level atom interacting with near-resonant light, the optical absorption cross section of the atom $\sigma(\omega)$ has a particularly simple form given by

$$\sigma(\omega) = \frac{\sigma_0}{1 + 4(\omega - \omega_0)^2/\Gamma^2}\ , \tag{4.2}$$

where ω is the angular frequency of the laser light, $E = \hbar\omega_0$ is the energy difference between the two atomic states, Γ is the linewidth of the transition, and σ_0 is the resonant optical absorption cross-section, which is given by

$$\sigma_0 = \frac{3\lambda^2}{2\pi}. \tag{4.3}$$

A sample of atoms prepared in the stretched ground state, $m_F = F$, and coupled only to the excited state $m'_F = F'$ will present an optical absorption cross section equal to that for the two-level case, given in Eq. 4.2. The absorption and consequent attenuation of a near-resonant probe beam as it passes through a gas of atoms of density $n(x, y, z)$ is governed by the equation,

$$\frac{dI(x, y, z)}{dz} = -\sigma(\omega)n(x, y, z)I(x, y, z). \tag{4.4}$$

This expression is valid only when the intensity of the imaging light is significantly less than the saturation intensity of the transition being driven. The implication of this is that the light does not alter the ground-state population of the atoms (and therefore $n(x, y, z)$ is independent of the intensity), which is taken to be 100%. The solution to Eq. 4.4 for the intensity of the probe laser at coordinates x, y, z is

$$\begin{aligned} I(x, y, z) &= I_0(x, y) \exp\left(-\sigma(\omega) \int_{-\infty}^{z} n(x, y, z')dz'\right) \\ &= I_0(x, y)e^{-\sigma(\omega)n_{\mathrm{cl}}(x,y,z)}, \end{aligned} \tag{4.5}$$

where $I_0(x, y)$ is the initial intensity of the probe beam at coordinates x, y and the column density, $n_{\mathrm{cl}}(x, y, z)$, has been defined. If the coordinate z encompasses the whole extent of the distribution of the atoms then the column density of atoms at position x, y is simply,

$$n_{\mathrm{cl}}(x, y) = \frac{1}{\sigma(\omega)} \ln\left(\frac{I_0(x, y)}{I(x, y)}\right), \tag{4.6}$$

where $I_0(x, y)$ and $I(x, y)$ are the intensities of the probe beam at the position of the detector in the absence and presence of the atoms, respectively. The distribution $n_{\mathrm{cl}}(x, y)$ is sampled by the pixels of the CCD camera, whose response is verified to be proportional to the incident intensity distribution on the detector and the exposure time. In this case the column density function $n_{\mathrm{cl}}(x, y)$ is readily computed in terms of the ratio of the pixel values, $p(x_i, y_i)$, recorded in the set of images since

$$\frac{I_0(x_i, y_i)}{I(x_i, y_i)} \equiv \frac{p_0(x_i, y_i)}{p(x_i, y_i)}, \tag{4.7a}$$

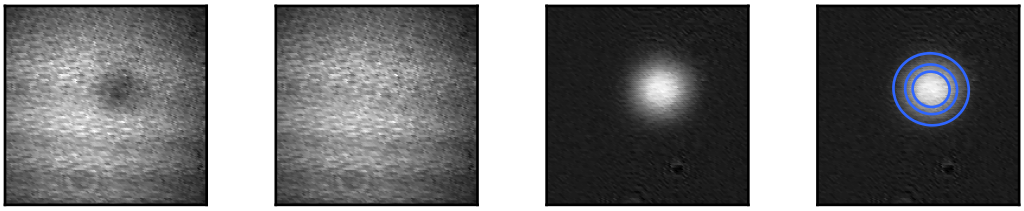

Figure 4.20: From left: An absorption image is recorded in the presence of an atom cloud, which is visible as a region of diminished intensity in the probe beam. A reference image is recorded in the absence of the atoms. The third image is obtained by taking the logarithm of the ratios of the first two images and is proportional to Eq. 4.7b. The distribution can then be fit to a two-dimensional Gaussian function (Eq. 4.10), as shown in the final image where contours of constant $n_{\rm cl}$ are plotted. All of the above images represent a 7.5 mm $\times$ 7.5 mm region of the CCD detector.

so that,

$$n_{\rm cl}(x_i, y_i) = \frac{1}{\sigma(\omega)} \ln\left(\frac{p_0(x_i, y_i)}{p(x_i, y_i)}\right), \tag{4.7b}$$

where the subscripts on the coordinate labels indicate the discretised nature of the detector pixels. The full distribution $n_{\rm cl}(x, y)$ is approximated by fitting the $n_{\rm cl}(x_i, y_i)$ to an analytic function. The total number of atoms imaged by the probe beam, N, is simply,

$$N = \int\int n_{\rm cl}(x, y)\ dx\ dy. \tag{4.8}$$

When atoms with a thermal distribution of energies are confined to a harmonic potential - as is the case near the centre of a MOT - the atoms adopt a Gaussian spatial distribution,

$$n(x, y, z) = n_0 \exp\left[-\frac{(x - x_0)^2}{2\sigma_x^2}\right] \exp\left[-\frac{(y - y_0)^2}{2\sigma_y^2}\right] \exp\left[-\frac{(z - z_0)^2}{2\sigma_z^2}\right]. \tag{4.9}$$

The corresponding column density distribution $n_{\rm cl}(x, y) = \int n(x, y, z)\ dz$ is,

$$n_{\rm cl}(x, y) = n_0 (2\pi)^{1/2} \sigma_z \exp\left[-\frac{(x - x_0)^2}{2\sigma_x^2}\right] \exp\left[-\frac{(y - y_0)^2}{2\sigma_y^2}\right], \tag{4.10}$$

from which it follows, using Eq. 4.8,

$$N = n_0 (2\pi)^{3/2} \sigma_x \sigma_y \sigma_z. \tag{4.11}$$

The imaging axis forms an angle of 45° with the radial MOT beams and lies in the same plane. To calculate the peak density of atoms at the trap centre the assumption is made that the MOT is axially symmetric, $\sigma_x = \sigma_y \equiv \sigma_r$. Providing the MOT beams are well aligned and well balanced, and given that the extent of

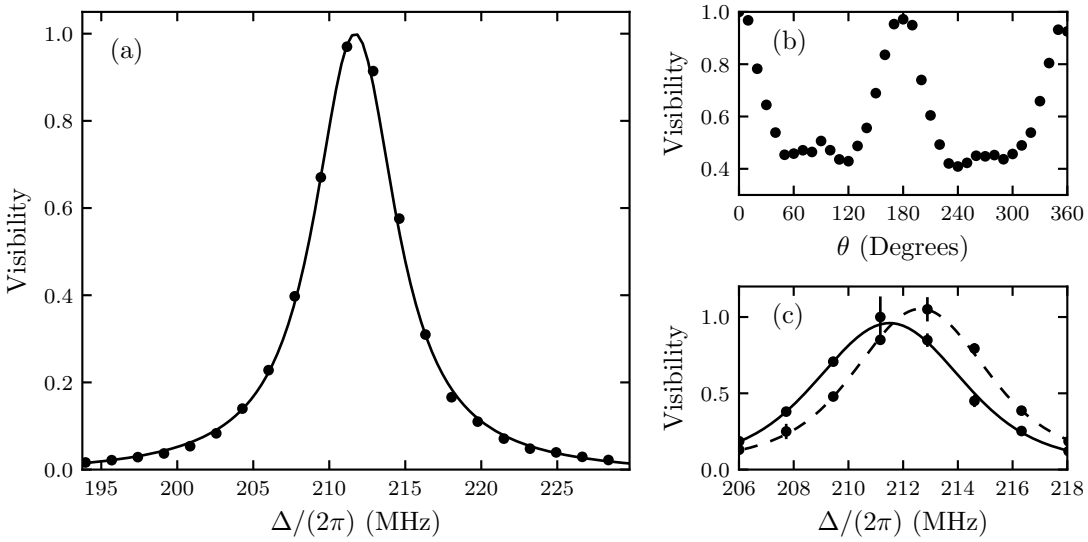

Figure 4.21: Preparing light for absorption imaging. (a) Visibility of atoms as imaged by the probe beam as the frequency is varied across the $F = 2 \rightarrow F' = 3$ transition resonance. The frequency is relative to the lock-point of the reference laser and is varied by tuning an AOM. The fit is to a Voigt lineshape and has $\Gamma = 2\pi \times 6.065$ MHz, a central frequency $f_0 = 211.7$ MHz. (b) Dependence of the visibility of the atoms as the probe laser polarisation is varied by adjusting the angle θ of a QWP. (c) Absorption profile of the probe beam with the imaging bias field switched off (solid) and with the imaging bias coils running at 3.2 A (dashed). The differential Zeeman shift of the cycling transition is 1.4 MHz/G, from which we estimate the bias coils produce a magnetic field of about 0.3 G/A at the position of the MOT. The centre of the absorption profile is shifted to higher frequencies, so the imaging light drives σ^+ transitions.

the cloud of atoms confined in the MOT is typically much smaller than the MOT beams, this is a reasonable assumption to make. Additionally, two CCTV cameras image the MOT from different angles to the absorption imaging axis, so that up to three different views of the MOT can be made simultaneously, which helps to ensure a good alignment. Fig. 4.20 shows how an absorption image is recorded, processed, and fitted to an analytical function. The parameters extracted from the fit can be used to make a measurement of the number of atoms, or their density, using the equations above.

Fig. 4.21 shows how the visibility of the atoms depends on a number of different parameters of the probe light. A MOT is loaded and the atoms are cooled in an optical molasses before being imaged by the probe light onto the CCD. The number of atoms is extracted by fitting a 2D Gaussian function to the absorption images. The visibility of the atoms as a function of probe laser detuning is plotted in Fig. 4.21(a). The data is fitted to a Voigt profile, which is a convolution of the Lorentzian lineshape of the transition with a Gaussian function. The Gaussian function accounts for broadening due to the velocity distribution of the atoms as

well as the finite linewidth of the laser and the goodness of the laser lock. The width of the Lorentzian distribution is constrained to be $\Gamma = 2\pi \times 6.065$ MHz, the linewidth of the ^{87}Rb D2 transitions. The standard deviation of the contribution to the resulting lineshape from the Gaussian distribution is found to be 0.73(8) MHz from the fit, suggesting that the laser linewidth and locking scheme, in combination, have sub-MHz precision, which is sufficiently precise for the investigations presented in later chapters. The fitted lineshape has a central frequency $f_0 = 211.7$ MHz, corresponding to the frequency separation between the $F = 2 \rightarrow F' = 1, 3$ crossover resonance and $F = 2 \rightarrow F' = 3$ resonance in a thermal vapour of ^{87}Rb. To obtain these best fit parameters a Levenberg-Marquardt least squares minimisation is performed. The errors in the data points are assumed to be equal and given by $\sigma_i^2 = \frac{1}{N-n}\sum_i R_i^2$, where R_i is the residual of the i^{th} data point from the best-fit model, N is the number of data points, and n is the number of parameters in the fit. The uncertainty in the fit parameters are generated using the procedure described in Sec. 4.9.2. Also shown is the dependence of the visibility of the atoms to the polarisation of the probe beam, which is altered by varying the angle of the QWP shown in Fig. 4.18. The optical cross section of the atoms is maximal when the probe beam is purely polarised to drive σ^+ or σ^- transitions, which optically pumps atoms into one of the two cycling transitions, as described earlier. As can be seen from Fig. 4.21(b), the optical cross section of the atoms is maximised when the wave-plate angle is either $\approx 0°$ or $180°$, these angles correspond to the two possible choices for the handedness of circular polarisation.

4.5.3 Visibility of the atoms

In the blue-detuned type-II MOT the populations in each of the two ground-states are comparable. Absorption imaging uses light resonant with the $F = 2 \rightarrow F' = 3$ transition, and so many of the atoms do not interact with the imaging light. Two methods to increase the visibility have been used and are discussed in more detail in Chap. 5. Briefly, the first method uses an optical molasses to pump atoms into $F = 2$ prior to imaging, and the second uses a dedicated 'state-preparation' beam. The state preparation beam is obtained from the $F = 1$ laser and is tuned to the $F = 1 \rightarrow F' = 2$ transition, as depicted by (e) in Fig. 4.2, using a double-passed AOM configuration. The laser light is coupled into the same optical fibre as the imaging light, as is shown in Fig. 4.22.

4.6 Launching the atoms into the MOT

One of the most important properties of a magneto-optical trap is its capture velocity. Measurements of the capture velocity provide information on the velocity-dependent forces in the MOT. The capture velocity also affects what kind of collisions can lead to trap loss from a MOT. In this investigation measurements of the capture velocity are performed by launching atoms into the MOT using a push beam. The push beam is derived from the reference laser, and tuned to the $F = 2 \rightarrow F' = 3$ resonance using a double-passed AOM configuration, which is identical to that illustrated in Fig. 4.19. The optical arrangement and method is described in more detail in Sec. 5.7. The layout of the push beam, in relation to the vacuum chamber and MOT, is illustrated in Fig. 4.22.

4.7 Overview of the experiment chamber

Fig. 4.22 shows the vacuum chamber assembly, radial MOT optics, imaging optics, radial magnetic-field bias coils, fluorescence collection optics, push beam, and CCTV camera for monitoring the MOT. The figure illustrates how the MOT optics are mounted around the cell using a Thorlabs optical cage system, and the geometrical relationship between the imaging beams, MOT beams, and push beam. Fluorescence from atoms trapped in the main chamber is collected at the front face of the cell and focussed onto a photodiode. A CCTV camera, attached to a long-focal-length objective, is focused on the plane of the MOT through the rear of the glass cell and through the length of the chamber, providing a visual diagnostic of the state of the MOT.

4.8 Experiment control and data acquisition

This section describes the interface between the computer and the experiment hardware, and the software used to control the hardware through the interface. The general data acquisition and procession procedures are also described.

4.8.1 Hardware

The computer interface to the experiment's hardware is provided by a National-Instruments PXI-6733 mounted in an external PXI chassis, and a National-Instruments PCI-6251 mounted in the lab computer. The PXI-6733 provides 8 high-speed analog output channels, with 16-bits of precision, as well as 8 digital input/output lines. The NI PCI-6251 provides a further 8 digital outputs, 2 16-bit analog outputs and

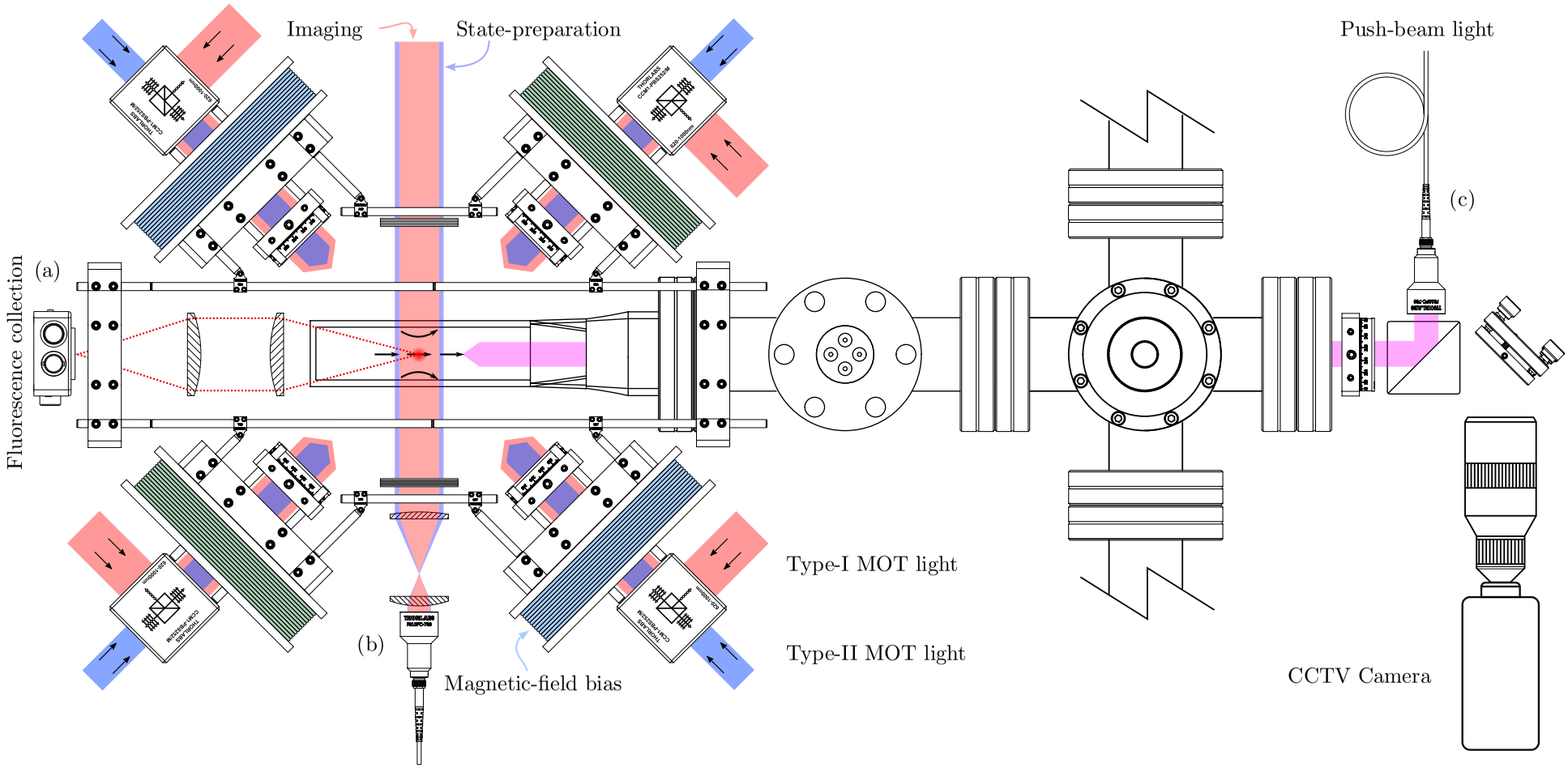

Figure 4.22: An overview of the experimental apparatus and assembly. The MOT optics and magnetic-field bias coils are mounted around the UHV glass cell using a Thorlabs optical cage system. Fluorescence from the MOT is collect at (a) and monitored on a photodiode. The state preparation and absorption-imaging light emerge from the optical fibre at (b). The rear window, at the opposite end of the chamber, is used for the push-beam light, at (c), and by a CCTV camera to monitor the MOT.

8 16-bit analog inputs for data acquisition. Fig. 4.23 shows an illustration of the data acquisition and experiment control system, with the origin and destination of various timing and synchronisation signals across the pair. The sample-clock signal for the digital and analog output tasks programmed into the PXI-6733 is generated from the on-board 20 MHz timebase using one of the two counting channels on the card. The sample-clock of the analog output task is also routed externally to one of the programmable function input pins of the PCI-6251, where it is used as the sample-clock input of the digital output task. All of the output tasks are therefore synchronised to the master timebase of the PXI card.

In preparation for an experimental sequence the various waveforms to be output by the cards are written to 'tasks' configured using the National-Instruments API, the analog output task of the PXI-6733 and digital output task of the PCI-6251 are configured to await a start trigger, which is output by one of the lines of the digital output task of the PXI-6733. This task is configured last, and software-triggered upon verification of the task, thus synchronously triggering the other outputs.

4.8.2 Software

The software used to control the experiment is built around the National-Instruments NI-DAQmx API. The API can be used to configure the various hardware-timing and synchronisation signals, and to specify waveforms to be output or acquired by the various channels. The user-interface built around the NI API is part of a suite of software used across many experiments within the CCM, to which many people have contributed over time. The part of the software suite used to run an experimental sequence is called 'MOTMaster'. An experimental sequence is defined as an instance of a C# class, which allows various values, pulses and ramps to be defined for each of the channels. MOTMaster compiles the class, extracting from the sequence various waveforms to be output and input channels to monitored, configures the data-acquisition boards, and finally writes the sequence to a set of fist-in-first-out (FIFO) buffers on the cards. A dictionary of key/value pairs can be defined in the script, parametrising the sequence to be output. This dictionary is extracted by MOTMaster after the compilation of the class, but before the waveforms are written to the FIFO buffers, and can be modified by methods that allow new values for each of the dictionary entries to be specified. These methods can be accessed remotely, and are routinely done so using an IronPython console session. This allows the various parameters of the sequence to be scanned across a range of values in an automated way, repeating the experiment for each one. Some modifications to MOTMaster have been made in order to expand its functionality. One limitation of the hardware interface used here is that tasks—outputting a series of analog

waveforms across multiple channels, for instance—cannot be defined across multiple isolated devices with different data bus standards, i.e. PXI, PCI, and PCIe. Methods have therefore been added to manage a sequence that contains tasks to be written to multiple devices.

In addition to MOTMaster there is a HardwareController program, which allows the state of the experiment to be updated on demand, and monitored, via a graphical user interface (GUI) that provides a convenient way to interact with the data acquisition hardware. The HardwareController also controls and receives data from the MiniCircuits frequency counter.

The CCD camera used to record absorption images of the MOT is controlled by a separate program, built around libraries provided by National Instruments Vision Acquisition Software, which allows individual images to be recorded or footage to be streamed from the camera. Camera control is integrated into the HardwareController via a TCP channel. MiniCircuits also provide drivers and a library of classes that allow the frequency counter, used to monitor the laser frequencies, to be integrated into the HardwareController.

The console used to interact remotely with MOTMaster is an Iron Python interpreter. Iron Python is a .NET-compatible implementation of Python, which allows python scripts and programs to be tightly integrated with the other software. The console interface allows a dictionary of parameters to be defined and iterated over by remote calling the MOTMaster compiler. To summarise, the following example is provided. An experiment to measure the temperature of the atoms proceeds in the following way. First, the sequence is described in a human-readable form within a C# class through a sequence of commands that adds voltage waveforms to each of the output channels. The waveforms are parametrised through a dictionary of key/value pairs. For example, there is a key corresponding to the camera trigger and corresponding value for the time at which a rising edge should be applied to this channel. To obtain a sequence of ballistic expansion images, the experimenter uses the Iron Python console to define a list of camera trigger times. MOTMaster is then instructed to compile the script and replace the camera trigger time with the current element from this list. The script is then executed and the process is repeated for each element in the list.

4.9 Data analysis

Images recorded during an experiment are saved along with a copy of the dictionary of parameters used to define various parts of the sequence. Images are analysed using a fitting routine written in Python, which makes use of the NumPy library for image manipulation, and SciPy library for model fitting. The functions in these

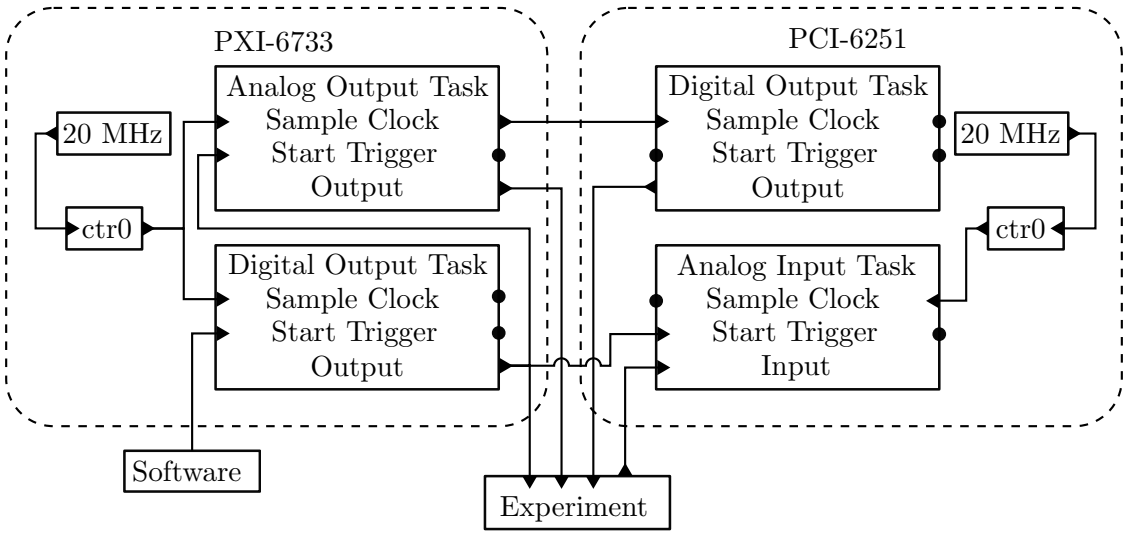

Figure 4.23: Routing of various signals between the PXI/PCI cards used to control and monitor the experiment. The output tasks are synchronised to the 10 MHz timebase of the PXI-6733.

libraries call compiled-C code to efficiently perform calculations involving arrays, such as fitting an analytical function to a 2D image.

Unless otherwise stated the error bars presented on data points in this thesis are obtained using the following method. Each point is an average of 5 realisations of the same experiment. The profile of the atom cloud is extracted from the images for each realisation of the experiment. Each of these profiles is fitted to a Gaussian distribution, which gives a set of best-fit parameters for the cloud size, position, and number of atoms. For each of these parameters the mean and standard deviation of the set of 5 is taken, giving the best estimate and uncertainty on that parameter. These estimates and their uncertainties can then be used to fit more complicated models, in order to extract the temperature from a ballistic expansion for example, which are fit using Wolfram Mathematica.

4.9.1 Systematic uncertainties in atom number measurements

There are a number of potential sources of uncertainty in the calculation of an atom number or density from an absorption image. Sources of uncertainty can broadly be divided into those arising from experimental imperfections, such as impure polarisation, and those arising due to the use of a number of simplifications and approximations. For example, there are uncertainties in the actual value of the optical cross section of the atoms, uncertainties in the actual value of the scattering rate due to the polarisation of the light and saturation effects, and uncertainties in the magnification of the imaging system. Many of these effects are complicated by the intensity profile of the imaging laser across the size of the cloud, and the change in intensity of the light as it propagates through the cloud of atoms.

The value of the optical absorption cross section used to calculate atom numbers is given by Eq. 4.2, and is valid for a two level atom. In this experiment the imaging light is resonant with the $F = 2 \rightarrow F' = 3$ transition. A weak magnetic field defines a quantisation axis along the direction of propagation of the beam, which is circularly polarised to drive pure σ^+ transitions. The imaging light optically pumps atoms into $m_F = 2$ and drives the closed transition to $m'_F = 3$. Therefore, the optical absorption cross-section these atoms present to the circularly-polarised light is indeed equal to that of a two level atom.

However, the validity of this statement depends upon what fraction of the total number of photons scattered by the atoms during the imaging occur on the cycling transition. If the light is not purely polarised to drive only σ^+ transitions then the effective optical absorption cross-section will be reduced from that of a two-level atom. Even if the polarisation is pure, the distribution of atoms among the different m_F sub-levels at the start of the imaging exposure introduces a transient effect to the cross-section, the instantaneous value of which only becomes equal to the two-level case when 100% of the population is pumped to the stretched state. The value of the actual cross section depends on the distribution of the ground-state population because atoms in different m_F sub-levels couple with different strengths to the circularly polarised light. In order for the average value of the cross section to be close to the two-level value, the total number of photons scattered during the imaging process should be large compared to the mean number of photons required to optically pump atoms into the stretched state. If the total number of photons becomes too large, however, then sufficient momentum can be imparted to the atoms by the imaging beam to Doppler-shift the atoms away from resonance. Again, this leads to an underestimate of the atom number when the resonant cross section is assumed. All of these effects are complicated by the intensity profile of the imaging beam across the atom cloud, and by the attenuation of the light as it propagates through the cloud.

First, the question of the polarisation purity of the imaging light is addressed. Prior to passing through the chamber the probe light used in the absorption imaging is polarised using a PBS cube and coupled into a polarisation-maintaining optical fibre. Care is taken to align the plane of polarisation of the light with the principal optical axis of the fibre. The output of the fibre is collimated and passes through a QWP, which circularly polarises the light. The light passes through the cell wall at 90° so that the transmitted light only contains polarisation components parallel to the air-glass-vacuum interfaces. The purity of the polarisation therefore should not be affected by the glass cell. A set of absorption images are taken of atoms released from a MOT as the QWP angle is varied, and the angle is subsequently fixed at the value that maximises the absorption as shown in Fig. 4.21(b). Fig. 4.24

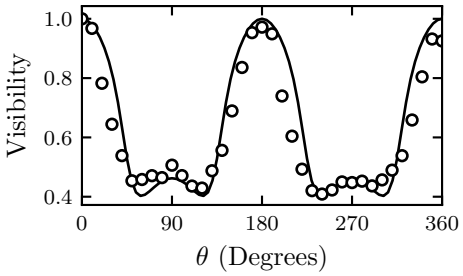

Figure 4.24: Estimating the polarisation purity of the imaging light using the optical Bloch equations. The circles represent the same experimental data as is presented in Fig. 4.21(b). The solid line is the excited-state population for an atom with $F = 2$ and $F' = 3$, illuminated by a beam with $I = 0.05\ I_{\rm sat}$. In the simulation the light is linearly polarised then passes through a QWP at an angle θ, when $\theta = 0$ the light drives σ^+ transitions. A small magnetic field is included, $\omega_B = 0.35\ \Gamma$, to simulate the effects of the magnetic-bias field used in the imaging. The detuning is $\Delta = 0.25\ \Gamma$, so the maximum visibility is obtained when the light drives σ^+ transitions, and when the light is polarised to drive σ^- transitions the scattering rate is lower.

shows the same data plotted with the results of a simulation performed using the OBEs. The simulation calculates the steady-state excited-state population for an atom with $F = 2$ and $F' = 3$. The atom is illuminated by a beam that is initially linearly polarised and then passes through a QWP at an angle θ, which is the same arrangement as is used in the experiment. For an angle $\theta = 0°$ the light drives σ^+ transitions, which implies σ^- transitions are driven when $\theta = 90°$. The simulation assumes that the initial linear polarisation is pure. The contrast in visibility of the atoms as the QWP angle is comparable between the data and simulations, indicating that the polarisation of the probe light is of a high enough purity that it should not contribute significantly to the systematic error in an atom number measurement.

A typical estimate for the number of photons scattered by an atom during the imaging sequence is 60, as discussed above. Fig. 4.25 shows the probability distributions for the number of photons scattered by an atom, starting in state m_F, before it reaches the stretched state. Atoms that are initially in the adjacent sub-level to that coupled by the cycling transition absorb 3 photons, on average, before reaching the cycling transition. Assuming the population is initially uniform across the ground states then the average value is $\langle \bar{N} \rangle = 4.65$. This probabilistic model is limited in its usefulness since it contains no information about the optical pumping rates. It does, however, give a rough indication of the magnitude of the systematic error to anticipate and provide insight into the sources of systematic uncertainty in an atom-number measurement.

To make a quantitative estimate of the systematic uncertainty in the cross section of the atoms, the OBEs can be used. Following the procedure outlined in the previous chapter, the Hamiltonian is constructed for $F' = 3$ and $F = 2$. The electric field is purely circularly polarised $\vec{E}(t) = \frac{E_0}{\sqrt{2}}(\cos(\omega t)\hat{\epsilon_x} - \sin(\omega t)\hat{\epsilon_y})$ so that only σ^+

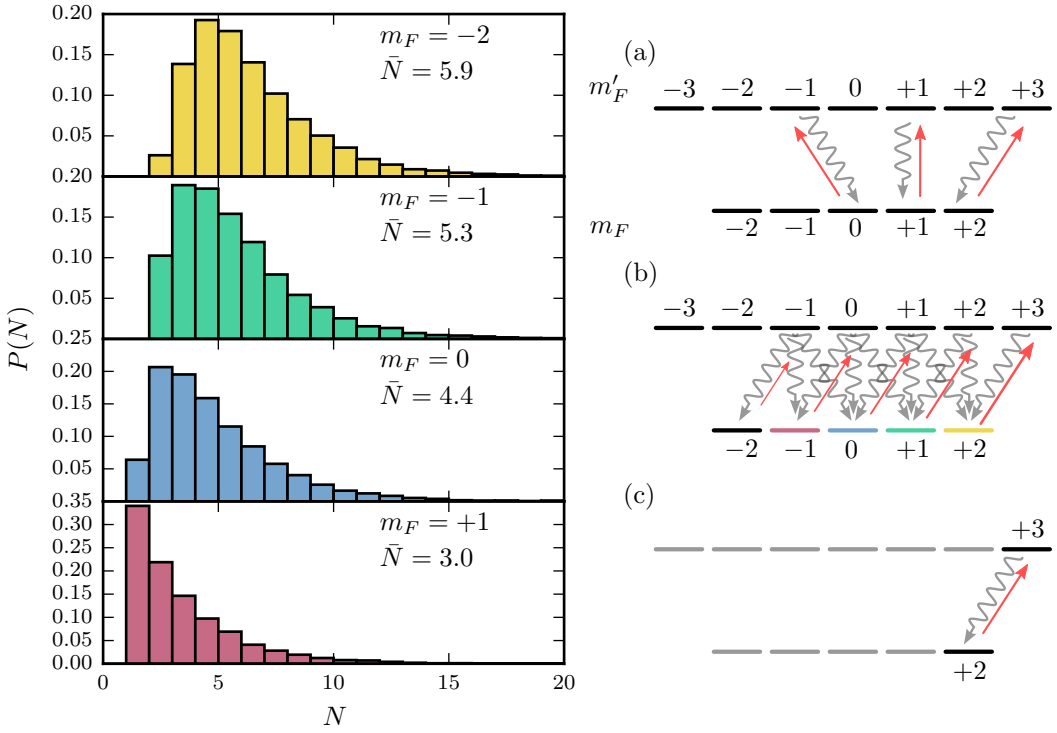

Figure 4.25: Left: Probability distributions for N, the number of photons scattered before the atom reaches the stretched state, for various initial m_F states. The atom is pumped by circularly-polarised light that drives σ^+ transitions. Results are obtained using a simple probabilistic model. Right: The optical absorption cross section is reduced from the two-level value by impure polarisation (a), and the distribution of population across the ground-state sub-levels (b). The ground-state sub-levels in (b) are coloured to match the corresponding distribution of the number of photons scattered to reach the stretched state. (c) Only when all the population is in the stretched state, and the polarisation is pure, is the cross section equal to σ_0.

transitions are driven. The velocity of the atom is taken into account by adding a velocity-dependent detuning that is coupled to the excited-state populations. Again the units of time are Γ^{-1}. If δ_d is the Doppler shift due to the recoil velocity expressed as a fraction of the linewidth, then $\dot{\Delta}/\Gamma = \delta_d \sum_{m'_F} \rho^{F'F'}_{m'_F m'_F}$. $\delta_d = 0.00124$ for ^{87}Rb. Fig. 4.26 shows the results of such a simulation for the level structure used for the absorption imaging in this experiment. The saturation parameter is $s = 0.2$. The effects of the optical pumping time, and the Doppler effect, are clearly visible as upward-going and downward-going trends in the excited-state population, respectively.

These simulations can be used to obtain a quantitative measure of the systematic 'correction factor', denoted by c, which should be applied to measurements of the atom number because of a reduction in the effective cross section of the atoms from the resonant two-level value. The quantity of interest is the value of the excited-state population averaged over some exposure time and compared to the nominal

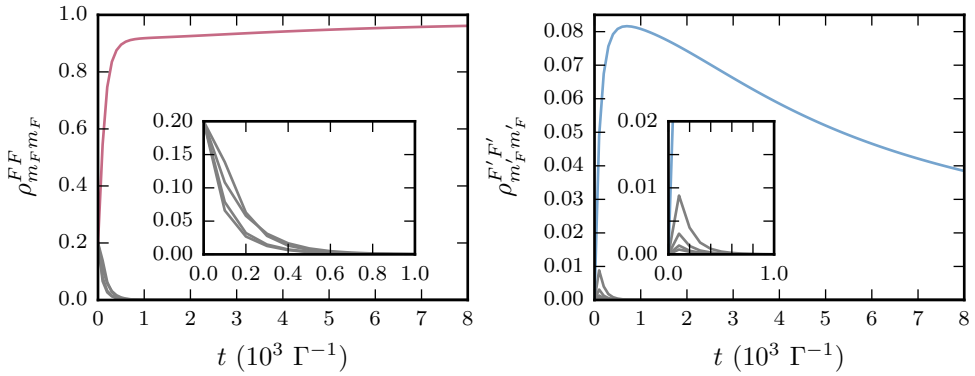

Figure 4.26: Populations of ground states (left), and excited states (right), obtained by solving the OBE for $F = 2 \rightarrow F' = 3$. The Doppler shift is taken into account and the light is polarised to drive σ^+ transitions. The population is initially distributed evenly among the ground states. The sharp rise in the excited state population at early times is due to optical pumping to the ground $m_F = F$ state, which couples most strongly to the light. The slow decrease is due to the atom being Doppler-shifted out of resonance. These effects can reduce the optical absorption cross section of the atom from the nominal 2-level value. The saturation parameter is $s = 0.2$ and the laser is on resonance, $\Delta = 0$. The Doppler shift due to absorption of a photon is set to be that of ^{87}Rb. The insets show a magnified view of the behaviour at short times.

resonant value for a two-level atom, ρ_{ee}, for the same saturation parameter.

$$c = \frac{1}{\rho_{ee}} \times \frac{1}{t} \int_0^t \sum_{m'_F} \rho^{F'F'}_{m'_F,m'_F}(t')dt', \tag{4.12a}$$

where

$$\rho_{ee} = \frac{1}{2}\frac{s}{1+s}. \tag{4.12b}$$

Fig. 4.27(a) shows the total excited-state population as a function of time, compared to the steady-state value for the same atom held in a fixed position. A number of different saturation parameters are shown. In all cases the excited-state population initially increases as more atoms are pumped into the stretched state, and then slowly decreases as the atoms are Doppler-shifted out of resonance. Fig. 4.27(b) shows the correction factor as a function of simulation/exposure time for the same set of saturation parameters. With $s = 0.10$ the correction factor is closest to one when $t \approx 2 \times 10^3$ Γ^{-1}, which is about 52 µs. If the saturation parameter is higher then a shorter exposure time should be used, else the systematic effect of the Doppler shift on the cross section becomes significant. On the other hand, if the saturation parameter is too low than a long exposure time is needed to ensure that the majority of the scattering still occurs on the stretched state. Both of these effects are clearly visible in Fig. 4.27.

Coincidentally, the response of the CCD camera used to record absorption images is such that the exposure time required to give a good signal to noise ratio coincides

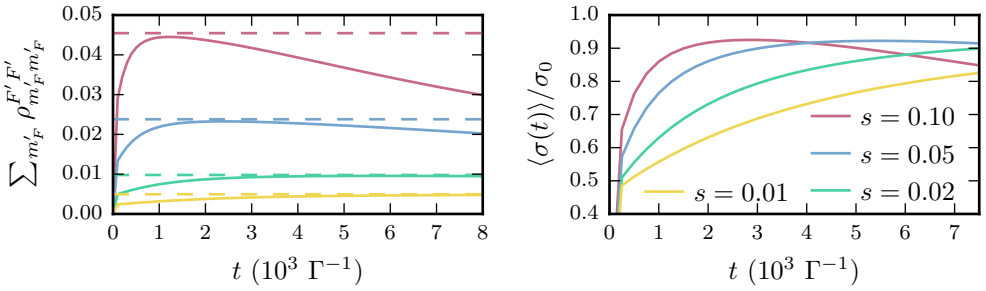

Figure 4.27: Total excited-state populations as a function of time for a number of different saturation parameters. The dashed horizontal lines are the steady-state populations of the excited state in the absence of any Doppler effect. (b) The excited-state populations from (a) averaged over the duration of the exposure time and normalised to the steady state value. This information can be used to estimate the systematic error on an atom-number measurement.

with the exposure time that minimizes the systematic error in the atom number measurement. In all cases the saturation parameter is much less than 1 and so the optical pumping time to the stretched state is approximately proportional to the saturation parameter. Similarly the response of the camera is linear in the exposure time and intensity of the incident light. This implies that, once the exposure time is optimised for the intensity being used, the systematic error becomes independent of that intensity and is close to its minimum value, where the effective cross section is ~0.92 σ_0.

Next the uncertainty due to the optical depth of the atom cloud is considered. If the optical depth is too high two separate effects arise. The first is due to the finite sensitivity of the CCD camera: a certain number of photons are required for a pixel of the camera to record a count in the least-significant bit. If there is so little light transmitted that the LSB of the camera is insensitive to the presence of additional atoms, then it is impossible to determine the actual number of atoms. The second effect is due to the diminished intensity of the probe beam as it propagates through an optically thick cloud. Atoms on the opposite side of the cloud to the source of the probe light see a much reduced intensity, which causes the optical pumping time to become long compared to the exposure time. Consequently, the actual absorption cross section is reduced from its nominal two-level value. This effect is illustrated in Fig. 4.28, where allowing the cloud to expand before imaging results in the number of atoms measured being greater, despite the MOT being loaded for the same duration in all cases. For the largest MOT (i.e. longest load time), the number of visible atoms increases only by about 25% as the free-expansion duration is increased by a factor of 2.5, from $\tau = 4$ ms to $\tau = 10$ ms, which reduces the optical depth by a similar factor. Therefore, at the lowest optical depths observed here, the measured number is close to convergence. In practice, care is taken to ensure that the optical depths are reduced even further, which is achieved automatically in the

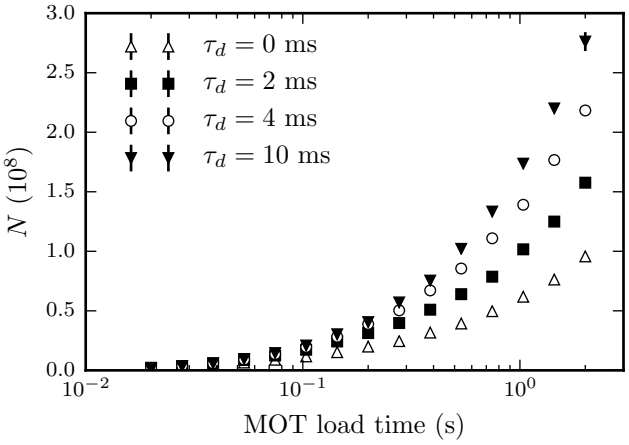

Figure 4.28: Experimental data illustrating the optical thickness problem. Here the atoms are released from a MOT and imaged after a duration of free expansion τ_d. As the cloud expands the optical depth is reduced. For each free expansion duration the number of atoms visible is calculated. The number of atoms is varied by loading the MOT for different durations. When the cloud is allowed to expand for longer there 'appears' to be more atoms as the optical thickness is less. The effect is exacerbated in larger clouds.

type-II MOT by the accumulation of atoms in $F = 1$, where they do not interact with the imaging light. Typically only about 10% of the atoms are found in $F = 2$, so the optical depth problem does not affect the measured atom number. In fact, the optical depths are typically so low that a controlled optical pumping step is used to prepare some fraction of atoms in $F = 2$ prior to imaging.

Finally, systematic uncertainties exist in the precise knowledge of the frequency of the imaging light and of the magnification of the imaging system. The spacing of the lenses in the optical arrangement is set by imaging a 200 µm pinhole, illuminated by a plane-wave, onto the CCD camera. The alignment of the system is adjusted in-situ by bringing a fluorescence image of atoms confined in the MOT into sharp focus on the camera. Finally, absorption images are recorded of atoms falling under gravity. A total of 16 images are taken at 1 ms intervals after atoms are released from a MOT and this is repeated 5 times. When the initial position, initial velocity and acceleration are free parameters a fit to the data yields gives $a = 10.0(1)$ m/s^2, suggesting a magnification of $a/g = 1.02$. This value is not significantly different to the nominal value of 1.0, and such small discrepancies might be accountable to causes other than the magnification. The frequency of the imaging light is known to at least ~0.6 MHz, which is determined by scanning the imaging light over the cycling transition and fitting the resulting lineshape to a Voigt profile. This corresponds to an uncertainty of about 4% in the cross section, in the worst case scenario and for a single experimental shot. However, since all measurements made are averaged over a number of experimental realisations the actual correction to the cross-section is even smaller.

In summary, the largest contribution to the systematic uncertainty is likely to be due to the finite optical-pumping time to the stretched state. This effect is exacerbated when the optical thickness of the cloud is high. A resonant probe beam is used to image the atoms in order to obtain an atom number measurement. For cases where the atom number is large the atom number measurement would be made after a free-expansion time to reduce the optical thickness of the cloud. However, the blue-detuned type-II MOT is optically thin in comparison to the type-I MOT, because atoms are mostly in $F = 1$. Therefore, many of these systematic effects due to the attenuation of the imaging light are alleviated. With all these factors considered the reader should prescribe a systematic uncertainty of about ~10% to the measurements presented in this thesis. This value is based upon the results obtained by numerically solving the optical Bloch equations describing the optical pumping of the atom by the imaging light, which are shown in Fig. 4.27. The transient optical pumping reduces the optical absorption cross section from its nominal two level value, so the actual atom numbers and densities are expected to be about 10% higher than those measured, under optimum conditions.

4.9.2 Model fitting

In the following section a detailed experimental characterisation of the blue-detuned magneto-optical trap is presented. Many of its properties are quantified in terms of various parameters extracted by fitting models to experimental data. Models are fit to sets of data using the *NonlinearModelFit* function provided by Wolfram Mathematica. The function uses the Marquardt-Levenberg minimisation method to find the optimal least-squares fit of a specified model to experimental data. The fit is weighted according to the uncertainty in each of the data points, which is calculated from the variance of a set of repeated measurements obtained using identical experimental parameters. The chi-squared value is defined by

$$\chi^2 = \sum_i \left(\frac{y_i - y(x_i, a, b \dots)}{\alpha_i} \right)^2, \tag{4.13}$$

where y_i is the measured value of the dependent variable for a value x_i of the independent variable, $y(x, a, b \dots)$ is the model describing the data with parameters a, b, etc., and α_i is the measured uncertainty associated with y_i. The best-fit function $y(x)$ is obtained by minimising the chi-squared value, $\chi = \chi_{\min}$. The uncertainty in a best-fit parameter a_0, Δa, can be obtained by solving numerically the equation

$$\chi^2_{\min} + 1 = \sum_i \left(\frac{y_i - y(x_i, a_0 + \Delta a, b_0 \dots)}{\alpha_i} \right)^2, \tag{4.14}$$

for Δa. While not explicitly stated in the documentation, comparisons between direct calculations of χ^2 values and the stated uncertainties returned by *NonlinearModelFit* verify that this is indeed the method used.

5 A blue-detuned Rb MOT

This chapter presents an overview of the observed behaviour and measured characteristics of a blue-detuned type-II MOT of ^{87}Rb.

To begin, a brief description of the preliminary observations of the first blue-detuned MOT are described. In the section that follows measurements are presented of the temperature of atoms cooled using light tuned close to the $F = 1 \rightarrow F' = 1$ and $F = 2 \rightarrow F' = 2$ transitions. The behaviour of the temperature is studied in an optical molasses, in a MOT, and in an optical molasses with a homogeneous magnetic-field applied to it. Then, measurements of the density of atoms confined in the blue-detuned MOT are presented. The variation in the density with magnetic-field field gradient is studied. It is found that the density of atoms can be increased beyond what is typically achieved in a type-I MOT, despite the inherently weak confinement. Next, the spring constant and damping coefficient of the trap are studied. Measurements of the phase-space density in the blue-detuned MOT are presented next. The phase-space density is measured to be many orders of magnitude higher than that reported in other type-II atomic MOTs. The phase-space density is even close to the highest phase-space density reported for any MOT where the laser cooling uses electric-dipole-allowed transitions (as opposed to narrow-linewidth spin-forbidden transitions, where a higher phase-space density has been achieved). In the penultimate section, measurements of the lifetime of atoms in the MOT are presented. The number of atoms trapped in the blue-detuned MOT decays non-exponentially, indicating that intra-trap collisions contribute significantly to the loss-rates. Finally, measurements of the capture velocity of the trap are presented. The data presented in this final section are complementary to the measurements of the loss-rate coefficients, and speculations are made as to the dominant trap-loss mechanisms in the blue-detuned MOT.

5.1 Preliminary observation

The first observations of a magneto-optical confining force using light blue detuned from the type-II transitions were made by measuring the atom-density profile of a cloud of atoms released into the type-II MOT. Absorption images were recorded 10 ms after switching to the type-II configuration. The polarisation of the light in the type-II MOT can be arranged so that the restoring beams drive either $\Delta m_F = +1$ or $\Delta m_F = -1$ transitions from the ground state.

Fig. 5.1 shows the first compelling evidence that a magneto-optical confining

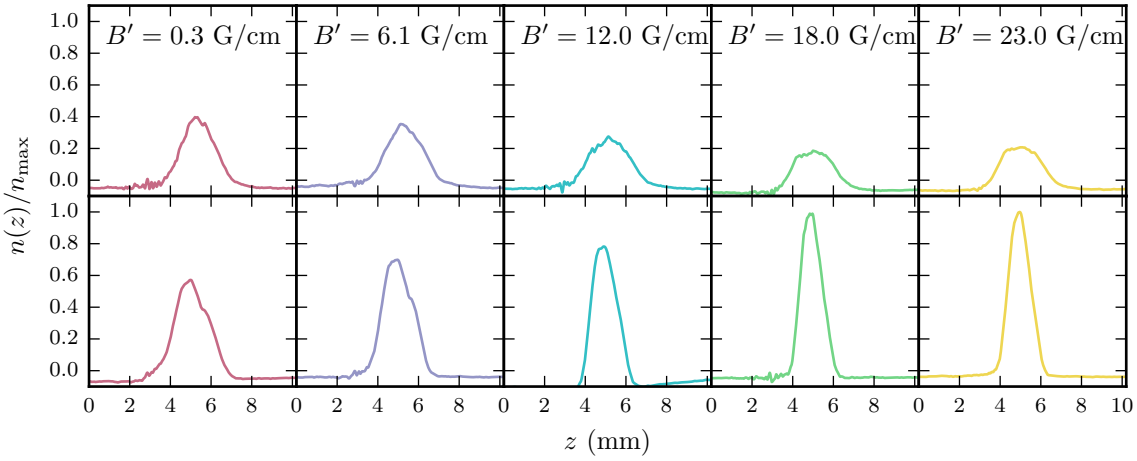

Figure 5.1: First observation of a position-dependent magneto-optical force in the type-II configuration. Axial atom-density profiles of atoms released into a blue-detuned type-II MOT after a 10 ms hold period. The data is coloured according to the magnetic-field gradient. The polarisation of the MOT light used in the top panels is opposite to that used in the bottom panels. As the magnetic field gradient is increased one polarisation of light gives a higher atom number density, whereas the other polarisation leads to a reduction in the atom number density.

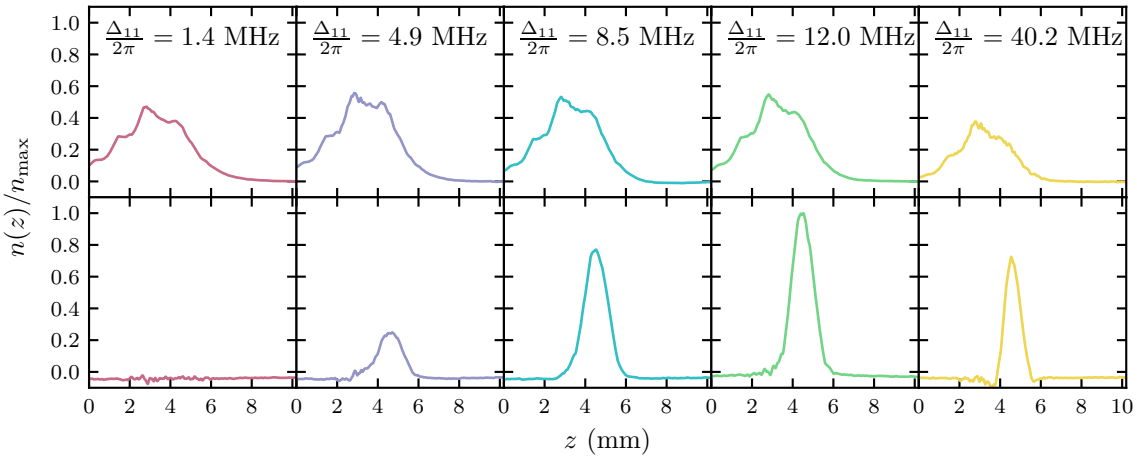

Figure 5.2: Density distribution of atoms for a number of different Δ_{11}. The atoms are imaged after being held for 10 ms in the type-II MOT. The bottom panels have the correct polarisation to give a restoring force for light blue-detuned from $F = 1 \rightarrow F' = 1$, and for this polarisation the number of visible atoms remaining in the trap exhibits a clear peak at $\Delta_{11}/(2\pi) = +12$ MHz. In these early investigations there was no state preparation prior to imaging and so the visibility of the atoms also depends on Δ_{11}. The true value that maximises the number of remaining atoms will be more positive than the data suggests.

force can be obtained in the type-II configuration using blue-detuned light. The data shows the density profile along the axial direction of the MOT, obtained by integrating absorption images along the perpendicular axis of the detector. In the top panels of the figure, the polarisation is such that the restoring beams drive $\Delta m_F = +1$ transitions, and in the bottom panels the restoring beams drive $\Delta m_F = -1$. Crucially, when the light is polarised with the correct handedness increasing the magnetic field gradient leads to higher atom number densities being measured, which is suggestive of a confining force. Conversely, when the polarisation is reversed increasing the magnetic field gradient leads to a reduction in the atom number density, suggesting an anti-confining force. For both cases the values of the detuning were $\Delta_{11}/(2\pi) = +14$ MHz and $\Delta_{22}/(2\pi) = -38$ MHz. As would become apparent, this value of Δ_{11} is quite close to the value for which the maximum lifetime is obtained, whereas the value of Δ_{22} is not. Nonetheless, on these short time scales a magneto-optical confinement is apparent, which is insensitive to the exact value of Δ_{22}. Fig. 5.2 shows a similar set of measurements made as the value of Δ_{11} is varied and the other parameters kept fixed, again the restoring beams are polarised, in turn, with both circular handednesses. The value that maximises the number of visible atoms remaining at the time of the imaging is close to $\Delta_{11}/(2\pi) = +12$ MHz. As Δ_{11} is decreased towards zero from its optimum value, the number of atoms remaining decreases sharply. As Δ_{11} is made larger than its optimum value the number of visible atoms decreases more steadily. The apparent decrease for larger Δ_{11} is at least partly because a greater fraction of the atoms are in $F = 1$, where they are practically invisible to the imaging light. A more sophisticated imaging sequence was later implemented, allowing all atoms to be prepared in the correct state for imaging. A similar set of measurements were made as the intensity and alignment of the laser beams were varied, allowing for a quantitative preliminary optimisation of the blue-detuned type-II MOT. Soon after these observations were made lifetimes of many seconds were observed and more thorough investigations could begin.

5.2 Temperature of atoms cooled by blue-detuned light

Sub-Doppler cooling mechanisms in type-I systems are known to be severely disrupted by magnetic fields. In this thesis it is proposed that by blue detuning the trapping light used in a type-II MOT, the properties of the MOT will be improved. When the light is blue-detuned the only cooling mechanisms are due to polarisation-gradient, sub-Doppler forces. The results of the simulations presented in [73], and

also those in Chap. 3, suggest that the sub-Doppler processes in type-II systems are more robust to magnetic fields than those in type-I systems. Nevertheless, few examples of investigations into three-dimensional grey-molasses cooling exist, and the effect of a magnetic field on the cooling process has not been examined experimentally. Therefore, it is sensible to first address the question of whether cooling will be effective in the blue-detuned MOT. If the cooling mechanism is sufficiently disrupted, atoms will be heated by Doppler processes and could evaporate from the MOT.

Measurements of the temperature of the atoms are also the simplest to perform experimentally. By measuring the temperature as a function of various parameters, the robustness of the polarisation-reversing and laser-relocking procedure can be tested. The results in this section are divided as follows. First, measurements made of the equilibrium temperature of atoms cooled in a type-II molasses are presented and discussed. Then, data obtained for the temperature of atoms cooled in the type-II MOT are presented. Measurements have also been made on the temperature of atoms cooled in a 3D optical molasses in the presence of a homogeneous magnetic field in order to try to elucidate the role of the magnetic field in the cooling process, these are presented last.

5.2.1 Measuring the temperature via ballistic expansion

The temperature of the atoms is measured using a ballistic expansion method. Atoms are allowed to expand freely, in the absence of any light or magnetic fields that would otherwise alter their trajectories. After some duration of free expansion an absorption image of the atom cloud is recorded. By repeating this for a number of free-expansion durations the rate of expansion of the cloud can be measured and used to determine the temperature of the atoms. The distribution of atomic velocities in a MOT is well described by a Maxwell Boltzmann distribution,

$$f(v_x, v_y, v_z) = (2\pi k_{\mathrm{B}} T/m)^{-3/2} \exp\left(-\frac{m(v_x^2 + v_y^2 + v_z^2)}{2k_{\mathrm{B}}T}\right), \tag{5.1}$$

where v_x, v_y, v_z are the components of the atomic velocity along the x, y, z coordinates, T is the temperature of the ensemble, m is the mass of an individual atom and k_{B} is the Boltzmann constant. The probability that the components of the atom's velocity are within the interval $v_x + dv_x$, $v_y + dv_y$, and $v_z + dv_z$ is simply $f(v_x, v_y, v_z)dv_x dv_y dv_z$. The time evolution of the atomic density along one axis, z, during a ballistic expansion depends on the distribution of velocities along that axis,

$$f(v_z) = \int_{-\infty}^{\infty}\int_{-\infty}^{\infty} f(v_x, v_y, v_z)dxdy = (2\pi k_{\mathrm{B}} T/m)^{-1/2} \exp\left(-m\frac{v_x^2}{2k_{\mathrm{B}}T}\right). \tag{5.2}$$

Suppose there are $n_0(z_0)dz$ atoms initially within the region $z_0 \rightarrow z_0 + dz$, where $n_0(z) = n(z, t = t_0)$ is the initial atomic density. During the ballistic expansion these atoms redistribute themselves so that the atom number density at a time t after the start of the expansion, $n(z,t)$ is given by,

$$n(z,t) = n_0(z_0)(2\pi k_{\mathrm{B}}T/m)^{-1/2} \exp\left(-m\frac{(z-z_0)^2}{2k_{\mathrm{B}}Tt^2}\right). \tag{5.3}$$

The number density of atoms at position z_0 when the expansion begins is $n_0(z_0)$. Atoms confined to a harmonic potential adopt a Gaussian density distribution when in thermal equilibrium with a heat bath. For the purposes of this analytical calculation, it is generally assumed that this is the case in a MOT. In reality, experimental imperfections and radiation trapping can result in non-Gaussian density distributions. During the ballistic expansion, however, atoms are allowed to expand to such an extent that any small irregularities in the initial density distribution are irrelevant to the value of the temperature calculated using this method. Therefore, it is assumed the initial distribution is given by $n_0(z_0) = n_0(0)\exp(-z_0^2/2\sigma_0^2)$. The final distribution of atoms is calculated by integrating Eq.5.3 over all z_0,

$$\int_{-\infty}^{\infty} n_0(0)(2\pi k_{\mathrm{B}}Tm)^{-1/2} \exp\left(-m\frac{(z-z_0)^2}{2k_{\mathrm{B}}Tt^2}\right) \exp\left(-\frac{z_0^2}{2\sigma_0^2}\right) dz_0 \tag{5.4}$$

recognising this as a convolution over z_0 of two Gaussian functions we can immediately write down that the density distribution remains Gaussian at all times and has a $1/e^2$ width, $\sigma(t)$, given by

$$\sigma(t)^2 = \sigma_0^2 + \frac{k_{\mathrm{B}}Tt^2}{m}. \tag{5.5}$$

Fig. 5.3 shows a sequence of absorption images recorded of atoms released from a blue-detuned MOT. From images like these the characteristic size of the cloud in the axial, and radial, directions is extracted and the square of this value is plotted against the free-expansion time squared. The data are then fit to a straight line, which gives the temperature of the atoms.

5.2.2 Visibility of atoms to the imaging light

The branching ratios of excited-state decays from $F' = 1$ and $F' = 2$ to the two ground states are not equal. For the typical values of Δ_{11} and Δ_{22} used in the blue-detuned MOT, the majority of atoms are in $F = 1$ at any given time. This reduces the visibility of atoms to the imaging light, which addresses the $F = 2 \rightarrow F' = 3$ transition. For certain combinations of laser detuning, $|\Delta_{22}| \ll |\Delta_{11}|$, close to 100%

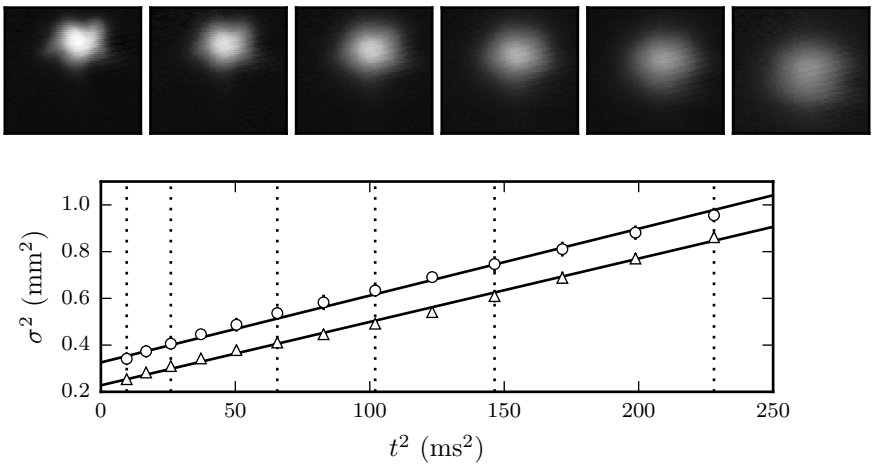

Figure 5.3: Ballistic expansion of atoms cooled in a blue-detuned magneto-optical trap. The images are absorption images of the cloud taken at the times corresponding to the dotted vertical lines in the graph and represent a 5 mm × 5 mm area of the camera's detector. The rms widths of the clouds in the axial (○) and radial (△) directions are extracted from fits to the images. Then, the squared rms widths are plotted as a function of the square of the free-expansion duration, t. Each point is an average of 5 individual runs and the standard deviation of the set of individual measurements gives the error bars. The fitted temperatures are 29(1) µK and 30(1) µK in the axial and radial directions, respectively.

of atoms are in $F = 1$, and when these parameters are used the imaging sequence must be modified to increase the visibility of the atoms. In the earlier stages of the investigation the visibility of the atoms was increased by briefly illuminating atoms with an intense optical molasses that is red detuned from $F = 2 \rightarrow F' = 3$ and $F = 1 \rightarrow F' = 1$. Atoms cooled in the type-II MOT or molasses are released and expand ballistically, during which time the $F = 2$ laser is relocked to the red side of the $F' = 3$ transition using the procedure described in Sec. 4.3.1. Once the laser has settled, the atoms are illuminated in a high intensity optical molasses for a ~100 µs period, which is immediately followed by the imaging exposure. Fig. 5.4 shows a comparison of the temperatures measured using this method, and the temperatures measured in the absence of the optical pumping by the type-I molasses. By using this method the properties of the MOT can be measured even when the atoms predominantly populate the lower ground state, which the imaging light is insensitive to. For example, the data presented in Fig. 5.7(b) are obtained using this method. One drawback of this method is a ~2 ms settling time for the laser relocking process, which is unimportant for the temperature measurements, but prohibits a direct measurement of the density distribution of atoms in the blue-detuned MOT. For this reason, a more sophisticated optical pumping scheme was implemented later in the course of the experiment, described in Sec. 5.7. This allowed atoms to be reliably prepared in the $F = 2$ state in a much shorter time prior to imaging.

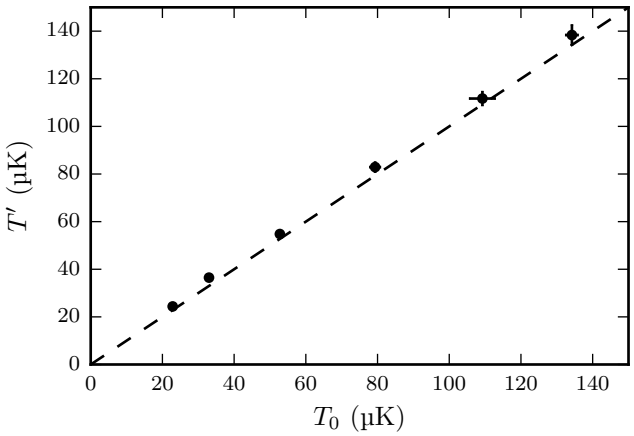

Figure 5.4: Comparison of the measured temperature of atoms both with the optical molasses optical-pumping stage T', and without the optical-pumping stage T_0. The line $y = x$ is plotted for comparison to the data. Data points are obtained by varying the intensity of the blue-detuned MOT and measuring the temperature of the atoms with and without the preparatory optical pumping. For each intensity, the measured temperature using the optical pumping is plotted against the measured temperature without. Fitting the data to a function of the form $T' = aT_0 + b$ gives best estimates for the parameters of $a = 1.02(2)$ and $b = 2(1)$ μK.

5.2.3 Cooling in an optical molasses

In this section data are presented on the equilibrium temperature of Rb atoms cooled using an optical molasses where the lasers are tuned close to the $F = 1 \rightarrow F' = 1$ and $F = 2 \rightarrow F' = 2$ transitions.

Cooling of alkali-metal atoms on transitions with $F' \leq F$ has been studied previously. The technique is commonly referred to as grey molasses, owing to the reduction in the scattering rate of atoms trapped in dark or nearly-dark states, as compared to a type-I molasses. In [53, 54] the authors demonstrate grey molasses cooling on the blue side of the $F = 3 \rightarrow F' = 2$ transition in caesium atoms. Temperatures as low as ~1 μK are obtained, which is below the previous record obtained for caesium atoms in a bright molasses [87]. Indeed, the authors speculate that the method could lead to higher phase-space densities than are possible using a bright molasses, adding credence to the idea that a MOT in which the principal cooling mechanisms lead to a confinement of atoms in nearly-dark states might perform favourably when compared to a traditional MOT. Grey molasses cooling of ^{87}Rb has also been studied experimentally on both the $F = 1 \rightarrow F' = 1$ [57], and $F = 1 \rightarrow F' = 0$ transitions [88], both of which use a 1D optical molasses. Two important conclusions from those studies are as follows. Firstly, an applied magnetic field can facilitate magnetically-assisted steady-state sub-Doppler laser cooling (SDLC) in systems where population can otherwise accumulate in dark states. Secondly, the presence and proximity of additional hyperfine levels in the

excited-state can prevent the velocity-selective coherent dark state on the $F = 1 \rightarrow F' = 1$ transition from being efficiently populated. The lowest temperature measured in those studies is obtained using a 1D linϕlin configuration and is ~4 µK.

The geometry of the magnetic field and polarisation gradients considered here is more complicated. When considering sub-Doppler laser cooling in a type-I system, an applied magnetic field can lead to efficient cooling, but to non-zero velocities, or it can disrupt the sub-Doppler cooling mechanism as has been discussed in Sec. 3.4.2. The outcome depends upon the relative orientation of the dc magnetic field and ac electric-field vectors. In the MOT there is no fixed relationship between the local magnetic-field vector and the electric-field vector of the light due to the complicated gradients in polarisation in the 3D optical molasses. In this section data are first presented on the temperature of atoms cooled in a type-II optical molasses. Then, similar data are presented for atoms cooled in a MOT. Interesting behaviour is observed in the temperature as the magnetic-field gradient is increased. Finally, data are presented on the temperature of atoms cooled in an optical molasses in the presence of an external homogeneous magnetic field. The magnetic-field bias coils are used to vary the strength of the homogeneous magnetic field. The temperature of the atoms is measured in the directions parallel and perpendicular to the magnetic field, and these data used to elucidate the role of the magnetic field in the cooling process.

Fig. 5.5 shows the temperature of atoms cooled in a type-II molasses. In part (a) of the figure, Δ_{22} is held fixed as Δ_{11} is varied. As is expected for the sub-Doppler processes on these transitions, cooling to low temperatures is observed when $\Delta_{11} > 0$. Conversely, a strong heating effect is observed when the laser is red detuned from the transition. The inset figure shows an enlarged section of the data. The optimum detuning for obtaining the lowest temperature occurs at approximately $\Delta_{11}/(2\pi) = +20$ MHz. Fig. 5.5(b) shows how the temperature depends on the detuning of the $F = 2 \rightarrow F' = 2$ laser. The temperature varies much less sensitively with $Delta_{22}$ then with $Delta_{11}$. Perhaps surprisingly, as the $F = 2$ laser is tuned to the red side of the transition the resulting increase in temperature is only a few microkelvins. Later, in Sec. 5.2.4, similar data are obtained in the presence of a magnetic field. For non-zero magnetic field strengths and when $\Delta_{22} < 0$ the cooling process is more severely disrupted and the equilibrium temperature is significantly higher.

The lowest temperature observed in the course of these measurements is about 10 µK, twice the lowest temperature reported for the 1D linϕlin configuration in [57]. This does not seem unreasonable, since the polarisation gradients in the 3D molasses are quite different to those of the 1D molasses used in [57].

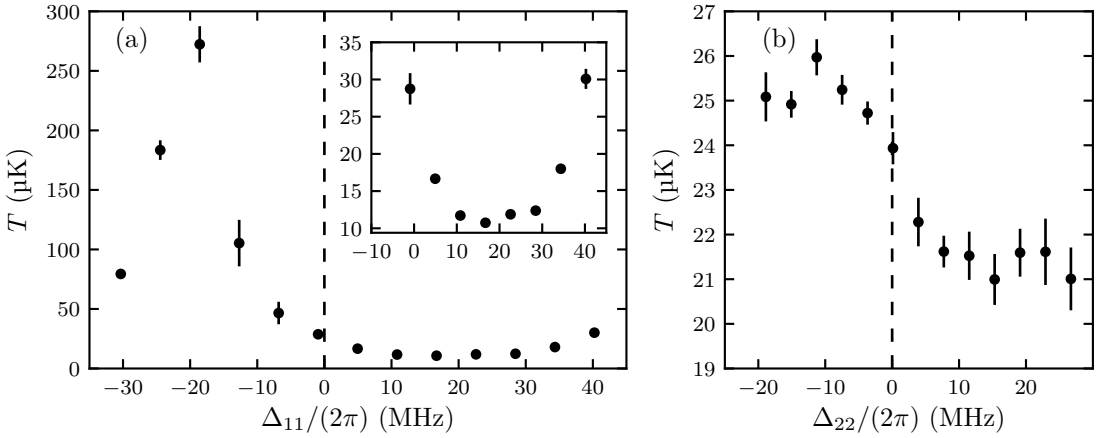

Figure 5.5: Temperature of atoms cooled in a low-intensity molasses. In (a) $\Delta_{22}/(2\pi) = +22$ MHz and Δ_{11} is varied. The inset is a magnified view of a sub-set of points from the main plot. When the $F = 1 \rightarrow F' = 1$ laser is red-detuned from the transition ($\Delta_{11} < 0$) there is a strong heating effect due to sub-Doppler processes. In (b) $\Delta_{11}/(2\pi) = +35$ MHz and Δ_{22} is varied. The temperature obtained is remarkably insensitive to the value of Δ_{22}, even when a red-detuning is used.

5.2.4 Cooling in the blue-detuned MOT

Competition between the Zeeman shifts and light shifts of the ground-state sub-levels can lead to a variety of cooling mechanisms that have previously been studied in 1D, or a suppression of efficient sub-Doppler laser cooling. In Chap. 4 it was demonstrated how the temperature of atoms cooled in a type-I optical molasses can be used as a sensitive probe of the ambient magnetic field. Fig. 4.16 shows how measurements of the molasses temperature were used to cancel out the ambient magnetic field in this experiment, using the chamber's bias coils.

Fig. 5.6(a) shows how the temperature of atoms cooled in a blue-detuned MOT changes as the magnetic field is increased. For these measurements the magnetic field is quickly changed from the value at which the type-II MOT is loaded to the value shown in the figure, for a period of 10 ms. The intensity is reduced during the same period, from the value used to load the type-II MOT to a value of $I_t = 24$ mW/cm^2. The atoms are released and the temperature is measured by ballistic expansion over a period of 20 ms. Initially, as the magnetic-field gradient is increased, the temperature increases roughly in proportion. The lowest temperatures, of about 10 μK, are obtained when the magnetic-field coils are switched off. A maximum temperature of about 38 μK is reached at a field gradient of some 10 G/cm. As the field gradient is increased beyond this point, the temperature once again falls. As the field gradient is increased to even larger values, $B' \gtrsim 30$ G/cm, the temperature becomes insensitive to even very large changes in B', settling at a temperature of about 24 μK. Fig. 5.6(b) shows similar data taken over a smaller range of magnetic-

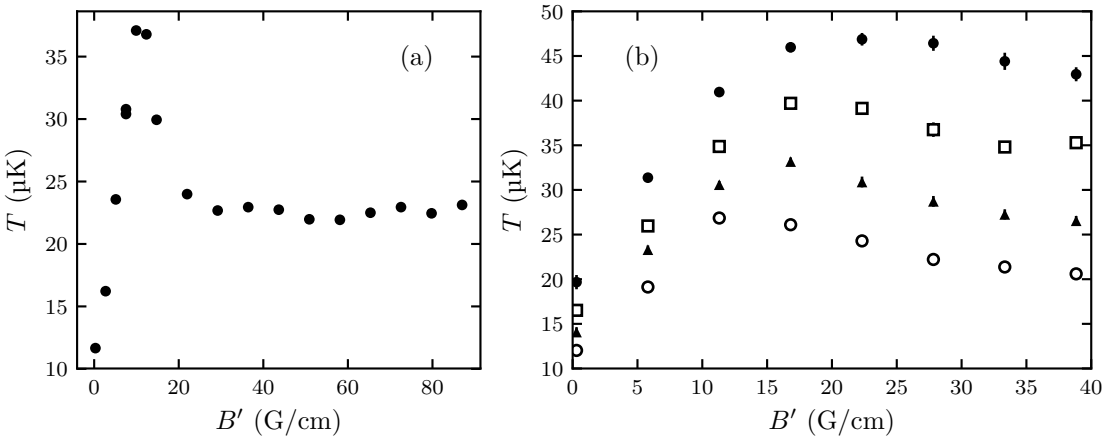

Figure 5.6: The geometric mean temperature $T = (T_z T_r^2)^{1/3}$ of atoms cooled in a MOT as the magnetic field is varied and for a number of different intensities. The field gradient is reduced to the value shown for a period of 10 ms before the atoms are imaged. In (a) the parameters are $\Delta_{11}/(2\pi) = 35$ MHz, $\Delta_{22}/(2\pi) = 11.5$ MHz and $I_t = 28$ mW/cm^2. In (b) the detuning is the same as (a) and the intensities are $I_t = 23$ mW/cm^2 (○), $I_t = 32$ mW/cm^2 (▲), $I_t = 44$ mW/cm^2 (□), $I_t = 61$ mW/cm^2 (●). As the intensity is increased the maximum temperature occurs at higher field gradients and the peak becomes less pronounced.

field gradients, but for a number of different intensities. As the intensity of the MOT light is increased the maximum temperature occurs at higher magnetic-field gradients. The width of the hot peak also increases with intensity. The precise heating and cooling mechanisms are not well understood. The data appears to show that there are at least two cooling mechanisms in the MOT, one effective at low magnetic field, where the Zeeman shifts are smaller than the light shifts, and one effective at high magnetic field, where the opposite is true. As the intensity increases the light shift of the bright states increases in proportion, so the magnetic-field gradient required for the magnetic-field induced cooling to be dominant must also increase. The MOT geometry is not well suited to investigating these cooling mechanisms. Traditionally, clearer interpretations are obtained from experiments in which transverse laser cooling is applied to an atomic beam. Here, the situation is further complicated because atoms can be in either ground state, each of which has a different g-factor.

Fig. 5.7 shows how the temperature of atoms cooled in the blue-detuned MOT varies as a function of laser detuning and for a variety of different intensities. As the detuning of one laser is varied, the detuning of the other is held fixed. Fig. 5.7(a) shows the temperature of the atoms as Δ_{11} is varied. When compared to the data obtained for molasses cooling in Fig. 5.5, the lowest temperatures occur at larger detuning but are not as low as those obtained in the optical molasses. The equilibrium temperature obtained in a red-detuned type-I molasses is proportional to

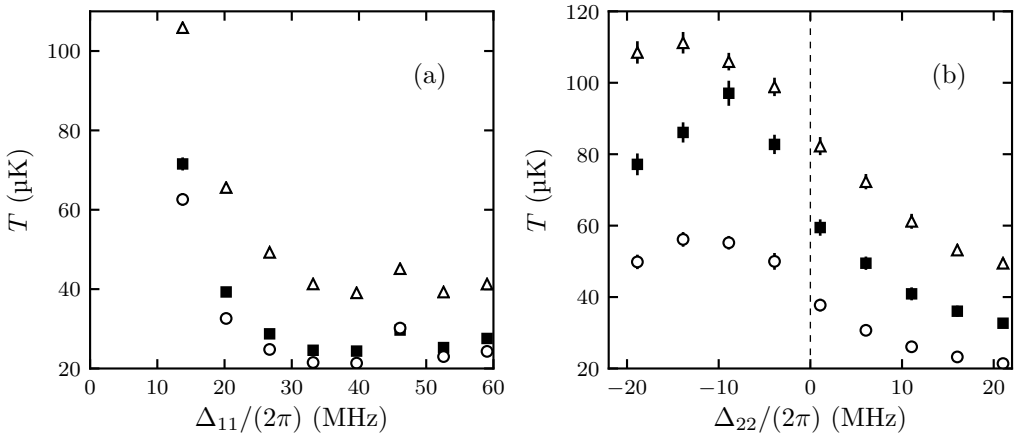

Figure 5.7: The temperature of atoms cooled in a blue-detuned MOT as a function of Δ_{11} (a), and as a function of Δ_{22} (b). The MOT intensity is reduced for a period of 5 ms prior to releasing the atoms and imaging the ballistic expansion. The parameters in (a) are I_t =14 mW/cm^2 (○), 19 mW/cm^2 (■) and 38 mW/cm^2 (△), with $\Delta_{22}/(2\pi) = +11.5$ MHz The parameters in (b) are $I_t = 21$ mW/cm^2 (○), 42 mW/cm^2 (■) and 76 mW/cm^2 (△), with $\Delta_{11}/(2\pi) = +35$ MHz. In all cases the higher intensities give higher temperatures and $B' = 88$ G/cm.

the light-shift parameter $T_{\rm eq} \propto |\Omega|^2/|\Delta|\Gamma$, over a broad range of laser intensity and detuning [89]. Fig. 5.7(a) shows qualitatively similar behaviour, with an inverse relationship between temperature and detuning, and a roughly linear relationship between temperature and intensity. This qualitative agreement is satisfactory, given the relative population of the ground states depends on the intensity and detuning of the two lasers and each ground state has a separate light-shift parameter.

Fig. 5.7(b) shows the temperature of atoms cooled in the MOT as a function of Δ_{22}. In contrast to the data in Fig. 5.5(b), which is a similar experiment performed in the molasses, when the $F = 2$ laser is red-detuned the equilibrium temperature is significantly higher. It is well understood why the temperature is higher for a red detuning. What is less obvious is why the temperature is so much more sensitive to Δ_{22} when a magnetic field is present. Similar observations are made in the next section, where a homogeneous magnetic field is applied to the molasses.

5.2.5 Cooling in a homogeneous magnetic field

The effect of applying a homogeneous magnetic field to an optical molasses has also been investigated. Two pairs of bias-field coils, mounted along the radial axes of the MOT, are configured to be driven by a single current driver. A homogeneous magnetic field, which is aligned perpendicular to the imaging axis, is produced by the coils at the position of the MOT. The temperatures along both the parallel and perpendicular directions to the applied magnetic field are then measured simulta-

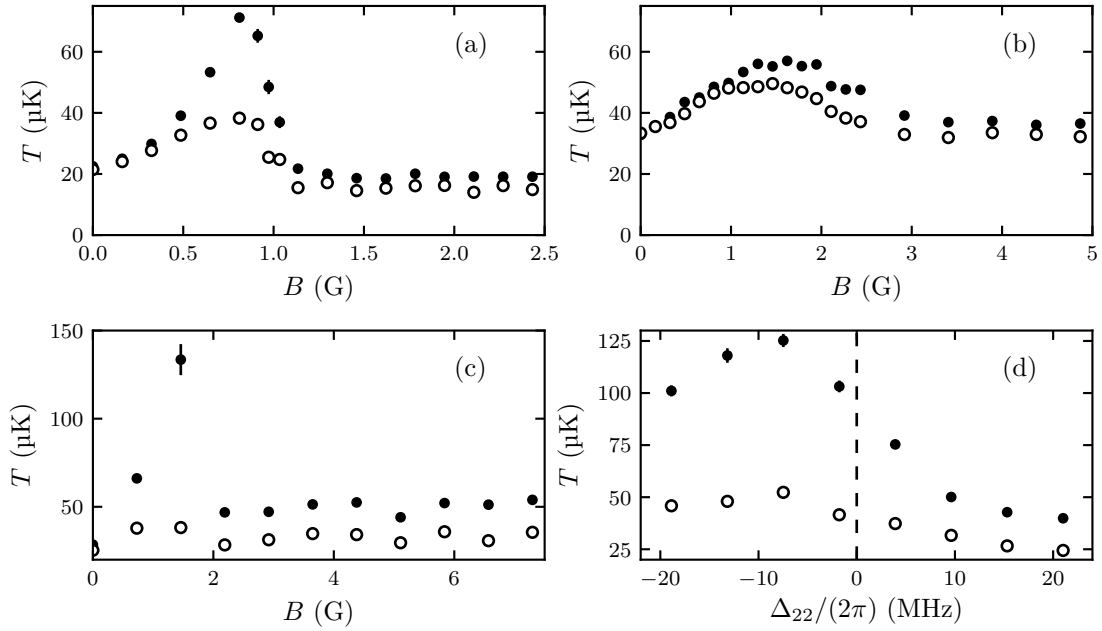

Figure 5.8: Temperature of atoms in a 3D optical molasses in the presence of a homogeneous magnetic field. All graphs show the temperature along the direction of the magnetic field (filled markers) and in the perpendicular direction direction (hollow markers). (a), (b) and (c) show the temperature as a function of magnetic field for different laser parameters. In (a) and (b) $\Delta_{11}/(2\pi) = +35.5$ MHz and $\Delta_{22}/(2\pi) = +38$ MHz. In (a) $I_t = 20$ mW/cm^2 and in (b) $I_t = 70$ mW/cm^2. In (c) $\Delta_{11}/(2\pi) = +35.5$ MHz, $\Delta_{22}/(2\pi) = -13$ MHz and $I_t = 20$ mW/cm^2. (d) shows the temperature as a function of Δ_{22} when $B = 1.0$ G/cm, $I_t = 20$ mW/cm^2 and $\Delta_{11}/(2\pi) = +35.5$ MHz.

neously from a ballistic expansion of the atoms. Atoms are cooled for 5 ms in the type-II molasses before the light is switched off and the atoms are imaged.

In the absence of a magnetic field the temperature of atoms cooled in an optical molasses is insensitive to Δ_{22}. For atoms cooled in the magnetic field of the MOT, however, the temperatures obtained for $\Delta_{22} < 0$ far exceed those obtained when $\Delta_{22} > 0$. When $\Delta_{22} > 0$ the temperature is lowest at zero magnetic field. As the magnetic field gradient is increased, the temperature of the atoms increases before falling again at higher field gradients. Similar behaviour is observed when a homogeneous magnetic field is applied to the optical molasses. Fig. 5.8 shows the effect that varying the strength of the homogeneous magnetic field has on the temperature in the optical molasses. In parts (a), (b) and (c) the laser parameters are fixed and the strength of the magnetic field is varied. In all cases the temperature initially increases with magnetic field, before decreasing and then becoming insensitive to changes in the magnetic field. In all cases the temperature along the direction of the magnetic field is higher than the temperature in the perpendicular direction. The magnetic field at which the difference in the temperatures along the two directions is largest coincides with the magnetic field that gives the highest temperatures.

Comparing parts (a) and (b) of the figure the following observations are made. The largest variation in temperature over the range of magnetic-field strengths investigated is observed at low intensities. At higher intensities the hot peak is broader, less sharply defined, and the increase in temperature is less dramatic. All these observations suggest a competition between processes depending on the Zeeman shifts and light shifts of the atoms. Treating Rb as a two-level atom, the ground-state energy shift due to the AC Stark effect is $\Delta\omega_{\text{Stark}} = |\Omega_{eg}|^2/(4\Delta)$, which evaluates to $\omega_g \simeq 0.3\ \Gamma$ for the parameters in Fig. 5.8(a). At $B = 1$ G, the Zeeman shift of the $|F = 1, m_F = \pm 1\rangle$ state is $\omega_{\text{Zeeman}} = \mp 0.2\ \Gamma$. Competition between the AC Stark effect and Zeeman effect therefore seems like a plausible explanation for the observed behaviours. In Fig. 5.8(b), the intensity is higher by a factor of 3.5, and the magnetic-field at which the temperature becomes insensitive to B is increased by about the same factor. The ratio of $\omega_{\text{Zeeman}}/\omega_{\text{Stark}}$ at the value of B where the temperature becomes insensitive is, therefore, about the same in parts (a) and (b).

5.2.6 Variation of temperature with atom number and intensity

A detailed investigation of the dependence of the temperature on the number of trapped atoms, N, has been undertaken using a caesium MOT in [90]. Heating of the atoms above the molasses temperature is caused by multiple photon scattering in the trap. The MOT temperature T follows the relation $(T - T_0) \propto N^{1/3}$, where T_0 is the temperature in a low density molasses. Further experimental work confirming these observations and a theoretical explanation of the scaling law based on an enhanced diffusion coefficient due to radiation trapping are presented in [91]. Fig. 5.9 shows how the temperature of the atoms varies as a function of intensity in the blue-detuned MOT. The three data sets are obtained by loading different initial numbers of atoms into the MOT. For a fixed detuning, the temperature is seen to increase approximately linearly with the total intensity I_t. The total intensity is divided roughly equally between the two frequencies and the same attenuation is applied to each. The deviation from the linear trend at higher intensities could be due to the onset of saturation in one or both of the transitions. Interestingly, the temperature is largely independent of the number of atoms trapped, over the range investigated here.

5.2.7 Discussion

The behaviour of the temperature as a function of magnetic field is quite complicated. In the MOT there is no simple relationship between the orientation of the magnetic field and the electric-field polarisation, as there has been by design in previous investigations into the effects of magnetic fields on SDLC. For example, the

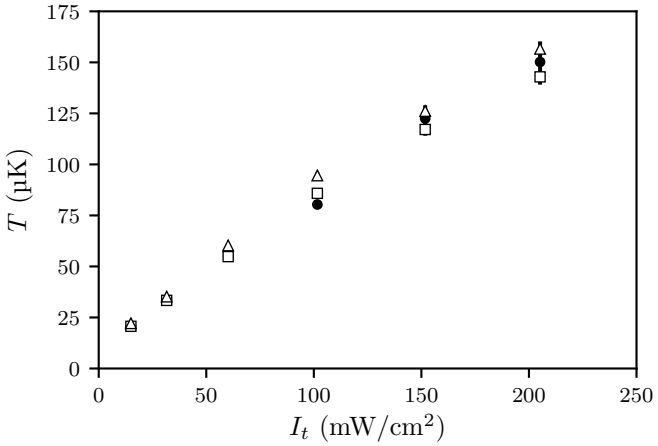

Figure 5.9: The temperature of atoms as a function of total laser intensity I_t. The other parameters are $\Delta_{11}/(2\pi) = +26$ MHz, $\Delta_{22} = +11.5$ MHz and $B' = 89$ G/cm. Three sets of measurements are made, each with a different initial number of atoms loaded into the blue-detuned MOT. Data for the largest number of atoms is represented by the triangle markers and the smallest number of atoms is represented by the filled circles. For the lowest intensity value shown the trapped atom numbers at the time of imaging are $N = 4 \times 10^7, 9 \times 10^7$ and 12×10^7. There is no clear difference between the temperatures obtained for these different numbers of atoms.

magnetic-resonance cooling to non-zero velocities in [49], and the magnetic-field-induced SDLC in [48, 88], both use collimated beams, 1D optical molasses, and 1D magnetic fields. In a type-I molasses magnetic fields are known to disrupt the SDLC processes, as was reported in the first observation of sub-Doppler temperatures [6]. The reason for this, as discussed in [46] and illustrated in Fig. 3.7, is that the locking-velocity to which atoms are cooled due to multi-photon processes translates by a different amount in an applied magnetic field to the locking-velocity due to Doppler processes. It may be due to the weaker Doppler forces in the type-II MOT that sub-Doppler processes persist in magnetic fields that would inhibit efficient sub-Doppler cooling in type-I systems. In the blue-detuned type-II MOT the situation is complicated by the presence of two ground states, each having different g-factors. The geometry of the MOT is not well suited to investigating the nature of the sub-Doppler forces, and so an exact mechanism to explain the observed dependence of the temperature on the magnetic-field gradient remains unclear. Still, numerical simulations can help to provide some insight. Fig. 5.10(a) shows experimental data obtained for the scattering rate of atoms in the type-I molasses as a function of the homogeneous magnetic-field strength. Also shown are the force-velocity curves (part (b)) and excited-state population (part (c)) obtained from the OBEs, for a number of different magnetic field strengths. Part (d) of the figure shows the coefficient of fiction, obtained from the force-velocity curves, and the excited-state population at the locking velocity. As the field strength is increased the excited-state population

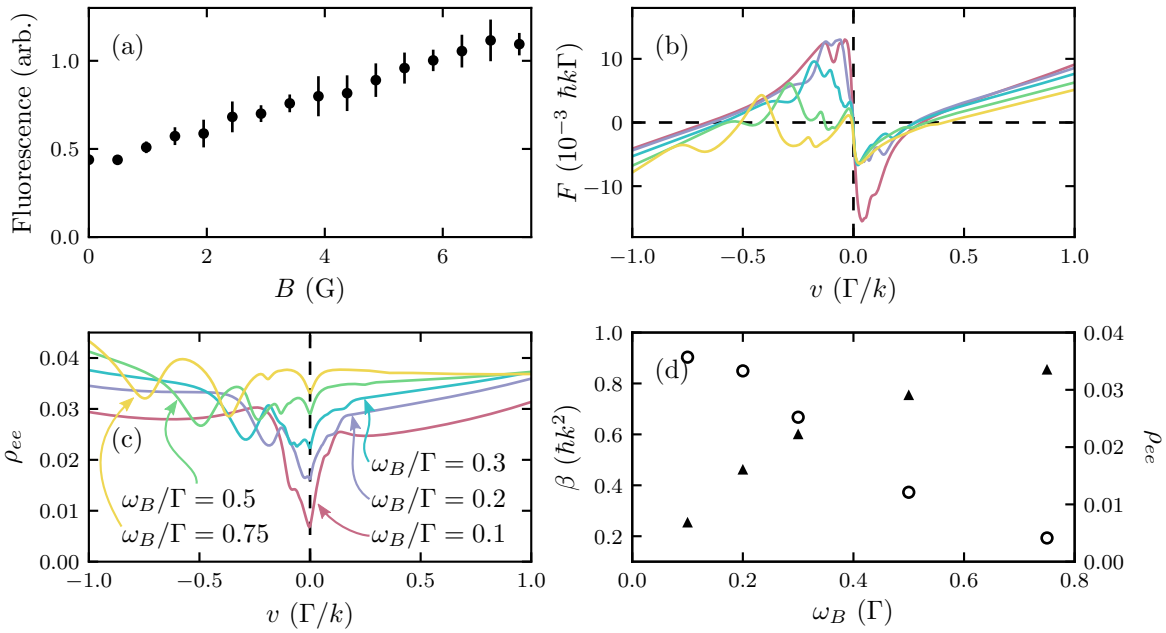

Figure 5.10: Understanding cooling and heating processes in the MOT. (a) Experimental measurements of the fluorescence rate per atom in the type-II optical molasses in the presence of a homogeneous magnetic field. (b), (c) and (d) are the results from a numerical integration of the OBEs for an atom in motion through a 3D molasses. The motion is along one of the optical axes and a magnetic field is applied in the direction of motion. The g-factors are $g_u = 2/3$ and $g_l = -1/2$, as in ^{87}Rb. (b) is the force-velocity curve and (c) is the excited-state population. (b) and (c) share a common colour scheme and the curves correspond to the magnetic field strengths indicated. The other simulation parameters are $\Delta = 2.5\,\Gamma$ and $I/I_{\text{sat}} = 1.0$. (d) shows the coefficient of friction (unfilled circles), and the excited-state population at the locking velocity, where $F(v) = 0$ (filled triangles). $\omega_B = \Gamma$ is equivalent to $B = 4.3$ G.

at low velocities increases, just as is observed experimentally. This is attributable to the same effect as is used to brighten molecular dark states in beam slowing experiments. The dark state is destabilised because the magnetic field introduces a time-dependent phase between ground states with different magnetic quantum numbers. As the magnetic-field strength increases atoms become more likely to make a transition to a bright state away from the intensity minima of the standing wave, where motion-induced couplings remix states. Hence the Sisyphus-like cooling mechanism becomes less efficient and the coefficient of friction decreases. It is not obvious from these simulations why the temperature again decreases at higher field strengths.

The variation in the temperature with atom number is insignificant over the range of atom numbers investigated. For instance, in Fig. 5.9 at the lowest intensities the measured temperature does not change, within error, as the number of atoms is increased by a factor of three. At the highest intensity the change in temperature is only ~4%. This insensitivity to N is probably due to the presence of dark Zeeman

sub-levels, which reduce the effect of radiation trapping in the cloud in two ways. Firstly, the overall scattering rate of an individual atom is reduced, so that the flux of spontaneously emitted photons is less. Secondly, the optical absorption cross section for an atom to re-absorb a spontaneously emitted photon is lower, so photons are less likely to be re-absorbed than for a type-I system.

5.3 Density of atoms in the blue-detuned MOT

The ability to obtain high number densities is almost always of benefit to experiments using laser-cooled atoms and molecules. Studies of cold and ultra-cold collisions require the densities to be sufficiently high that the intra-trap collisional loss rate exceeds the loss rate due to collisions with untrapped atoms. Proposals to sympathetically cool molecules with ultra-cold atoms will benefit from high densities of both atoms and molecules. Efficiently loading laser-cooled molecules into conservative potentials, such as magnetic or optical tweezer traps, will also benefit from cold, dense samples. There are a number of density-limiting effects that are important in atomic MOTs, as well as techniques that have been developed specifically to overcome them. To begin this section a brief review of these density-limiting effects is given. Then, data are presented on the density of atoms in the blue-detuned MOT. Finally, comparisons are made with other type-II MOTs that have been demonstrated to date.

5.3.1 Density-limiting effects in light-force traps

The first density-limiting effect occurs at the very lowest atomic densities, where interactions between atoms can be neglected. This density limit is due to the finite temperature of the atoms [56]. As succinctly expressed via the equipartition theorem (cf. Sec. 5.4.1), atoms confined in a harmonic potential due to a force $F(z) = -\kappa_z z$, and with a temperature T, adopt a Gaussian distribution with a characteristic size σ_z, where $\sigma_z^2 = k_\mathrm{B}T/\kappa_z$. Traps in which the spring constant is very large — such as in type-I atomic MOTs — achieve higher densities of trapped atoms at a given temperature than those with a smaller spring constant. Similarly, if atoms are cooled to a lower temperature in a trap with a given spring-constant, then the number-density of atoms increases. In Sec. 3.5 it is described how, by reversing the polarisations and sign of the detuning of the trapping light, a near-identical force is obtained for an atom with a given velocity confined in a type-II MOT. Sub-Doppler cooling using light blue detuned from type-II transitions leads to temperatures much lower than can be obtained in a conventional red-detuned type-II MOT, where polarisation-gradient forces heat atoms and molecules. Data

has been presented demonstrating that this robust cooling mechanism is effective in the blue-detuned MOT presented here. It follows that the temperature-limited densities obtainable in the blue-detuned MOT are far higher then for its red-detuned counterpart. In Sec. 5.2 it has been shown that atoms are cooled to temperatures of $T \sim 30$ µK in the blue-detuned MOT, 2-3 orders of magnitude below the temperatures T' obtained in comparable red-detuned atomic MOTs. From Eq. 5.11, one might expect a proportional reduction in σ_i^2, and therefore a reduction in the volume by a factor $\propto (T/T')^{3/2}$. If the finite temperature of the atoms were the only density-limiting effect then the atom number density $n = N/V$ could be expected to be increased by $10^3 - 10^{4.5}$. The density in the blue-detuned MOT is higher by about this factor, representing a substantial improvement over red-detuned type-II atomic MOTs. At the highest densities of atoms observed here, other density-limiting effects become important, which prevent the MOT operating in the temperature-limited density regime.

As the number of atoms loaded into a MOT is increased the density of the atoms $n = N/V$, initially increases in proportion. This is the 'temperature-limited' density regime. This behaviour does not continue indefinitely. As more atoms are loaded into the trap the flux of spontaneously-emitted photons can become significant, and is eventually comparable to the flux of photons pushing an atom back towards the trap centre. In addition to this, as the number of atoms becomes large, attenuation of the trapping laser by the atom cloud reduces the confinement of the innermost atoms. At some point these effects bring the inward and outward radiation-pressures into equilibrium, at which point a density limit is reached. In this radiation-pressure-limited density regime a photon emitted by one atom is likely to be absorbed and re-emitted by other atoms in the MOT. This has a number of effects in addition to limiting the density, the most obvious of which is an increase in the temperature, due to the extra steps of an atom's random walk in momentum space.

Lastly, the number of atoms confined in a MOT is governed by the loading-rate and loss-rate of the trap. In some situations collisions between trapped atoms can lead to trap loss. This occurs at a rate proportional to the square of the atom number density, and leads to an additional density-limiting effect.

5.3.2 Experimental results

The volume of the MOT is defined as $V = (2\pi)^{3/2}\sigma_z\sigma_r^2$. Using this definition, and when the atom-density distribution is Gaussian, the peak density at the trap centre n_0 is simply

$$n_0 = \frac{N}{V}. \tag{5.6}$$

In order to calculate n_0 both the total atom number, and dimensions of the atom cloud in the MOT must be measured. In this experiment the imaging process is complicated by the fact that atoms populate both the $F = 1$ and $F = 2$ states. Atoms in $F = 1$ are not visible to the light used for absorption imaging, which uses the $|F = 2,\ m_F = \pm 2\rangle \ \rightarrow \ |F' = 3, m'_F = \pm 3\rangle$ cycling transition. A consequence of this is that the visibility of the trapped atoms is reduced. In order to account for this, two separate measurements are made. First, the atom cloud is imaged immediately after the MOT is switched off. From this image the rms widths of the cloud in the axial and radial directions are obtained, giving the trap volume V. In order to measure the total atom number, N, atoms must be optically pumped into the $F = 2$ state. This is achieved by releasing the atoms from the blue-detuned MOT, relocking the $F = 2$ laser to address the $F = 2 \rightarrow F' = 3$ transition and switching on an intense optical-molasses for a duration of ~10 µs. The molasses is then switched off, the atoms are allowed to expand to reduce the optical thickness of the cloud, and finally the atoms are imaged on the cycling transition. The volume of the trapped atom cloud is found to be well described by an expression of the form $V = V_0 + N/n_{\max}$, where the second term accounts for density-limiting effects in the MOT caused by interactions between trapped atoms, such as radiation trapping. With this definition the peak density is given by,

$$n_0 = \frac{N}{V_0 + \frac{N}{n_{\max}}}. \tag{5.7}$$

As the number of trapped atoms becomes very large, $N \rightarrow \infty$, the peak number density reaches its limiting value, $n_{\max}$. $n_{\max}$ depends on the intensity and detuning of the trap lasers, and the magnetic-field gradient. Fig. 5.11 shows the results obtained for measurements of the peak atom number density, n_0, at the trap centre as the number of trapped atoms is increased. The experimental procedure used to obtain the data in Fig. 5.11 (a) was as follows. As usual, atoms are first loaded into the type-I MOT. The atoms are then briefly cooled in a low-intensity molasses before the laser light is switched off. The $F = 2$ laser is then relocked to the $F = 2 \rightarrow F' = 2$ transition and the type-II MOT trapping beams are switched back on. The magnetic field is increased from the the value used in the loading phase, 14 G/cm, to the final value desired, over a period of 100 µs. The atoms are held in the type-II MOT for 90 ms before being released and imaged. Measurements are taken for a range of magnetic-field gradients. A number of noteworthy features are visible in the data. The onset of saturation in the peak density with atom number suggests the densities of atoms are sufficiently high that radiation trapping within the cloud is the limiting factor. Clearly, the inherently weak confining force of the type-II MOT is not detrimental to the densities obtainable, and can be compensated

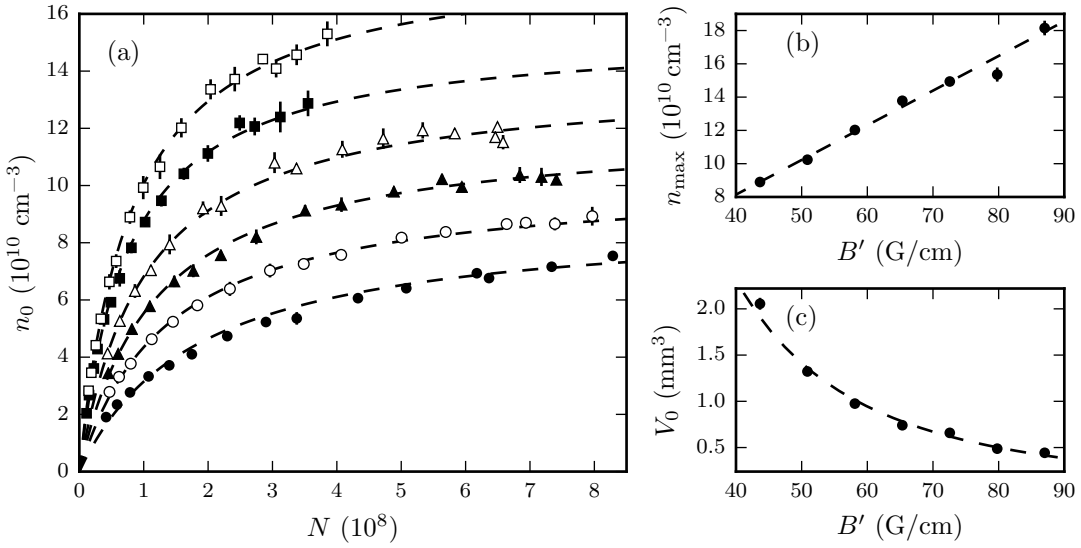

Figure 5.11: (a) The peak number-density of atoms at the trap centre, n_0, as the number of trapped atoms is varied in the presence of different magnetic-field gradients. The gradient are 43 G/cm (●), 50 G/cm (○), 58 G/cm (▲), 65 G/cm (△), 79 G/cm (■), 87 G/cm (□). The data are fit to Eq. 5.7. (b) The limiting density in the limit of large N, extracted from the fits in (a). The fit is to a straight line where both the gradient and the y-intercept can vary. The best-fit has a y-intercept consistent with zero. (c) The low-atom-number volume, V_0, extracted from the fits in (a). The fit is to $V_0 = aB'^p$ and yields $p = -2.21(6)$. The laser parameters are $\Delta_{11}/(2\pi) = +26$ MHz, $\Delta_{22}/(2\pi) = +11.5$ MHz and $I_t = 134$ mW/cm^2.

for by increasing the magnetic-field gradients to the values used here, which are far higher than those in typical type-I atomic MOTs. Perhaps surprisingly, the densities obtained here significantly exceed those in the type-I MOT, which are measured to be up to ~5×10^{10} cm^{-3} in this experiment. The density limit $n_{\max}$, extracted from each of the fits is plotted in Fig. 5.11 (b) as a function of the magnetic-field gradient. A linear function is fit to the data. The best-fit parameters are found to be $dn_{\max}/dB' = 2.08(7) \times 10^9$ cm^{-3}/(G/cm), and $n_0(B' = 0) = -2(4) \times 10^9$ cm^{-3}.

5.3.3 Discussion

Both the spring constant of the trap and the internal radiation pressure depend on the intensity and detuning of the lasers through the scattering rate of the atoms. The equilibrium temperature, and hence density distribution of the atoms, also depends on these parameters. If the scattering rate is high then the confinement is stronger, but atoms are heated to higher temperatures and the outward radiation pressure is increased as well. The laser parameters used to obtain the data in Fig. 5.11 are given in the caption of the figure. Other values for the detuning have also been investigated. When the magnitude of the detuning is reduced, so that the scattering

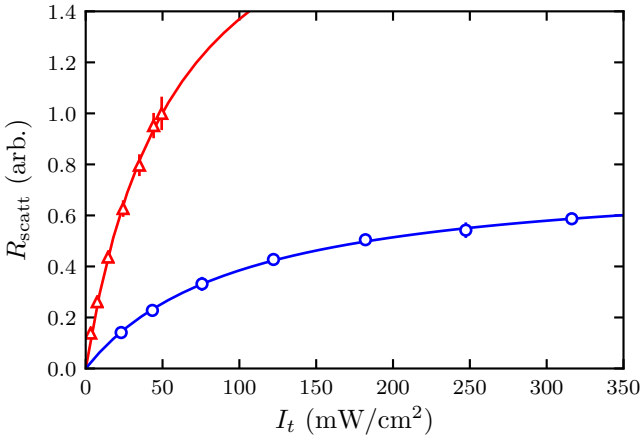

Figure 5.12: Measurements of fluorescence from the type-I MOT, represented by the triangles, and the blue-detuned type-II MOT, represented by the circles. Measurements are made using a CCD detector by the imaging system described in Sec. 4.5. The detector exposure time is short in comparison to the lifetime of the blue-detuned MOT and so the atom number does not change appreciably. An absorption image of the atoms is also recorded in order to calculate a fluorescence rate per atom, R_{scatt}. The absolute scattering rate is not calibrated but the points displayed in the figure are comparable. The scattering rate in the blue-detuned MOT is 20-30% of the corresponding rate in the type-I MOT for the same intensity, which allows high densities of atoms to be obtained.

rate increases, the size of the cloud increases. As the magnitude of the detuning is increased further then the temperature remains low but the confinement becomes weak.

There is no evidence that the limiting value of n_{max} has been reached over the range of field gradients investigated. Even higher densities might be achievable at higher field gradients, which could be straightforwardly achieved with higher-power MOT coils and improved thermal management. The number densities demonstrated here are comparable to those obtained in type-I compressed MOTs (CMOT), which are operated at similarly large magnetic-field gradients and laser detuning [92].

However, at these high densities, trap loss due to intra-trap collisions becomes very significant, as will be discussed in Sec. 5.6. For this reason, the tighter confinement provided by even higher filed gradients may not help to increase the density any further because the intra-trap collisions impose a density limit, much like that observed in a compressed MOT [92].

The atom number density measured in the blue-detuned type-II MOT exceeds that measured in the type-I MOT in the same apparatus, despite the inherently weak confinement. As mentioned previously, the dark Zeeman sub-levels reduce the scattering rate of the atoms, and the absorption cross section for radiation scattered by other atoms is also smaller. Radiation trapping within the cloud is reduced and so the radiation-pressure limited density is higher. Therefore, when the number of trapped atoms is large it may be beneficial to use a blue-detuned type-II

MOT, despite the small spring constant. The sub-Doppler cooling is also robust to high densities of atoms and it seems likely that these benefits will be compounded in experiments where very large numbers of atoms are advantageous. It is the presence of dark ground-state sub-levels that is responsible for the relatively small spring constant but that, seemingly counter-intuitively, permits higher densities to be obtained, due to a reduced radiation-pressure between atoms in the trap. Data collected for the scattering rate per atom in each of the trapping configurations is shown in Fig. 5.12. The scattering rate of the blue-detuned MOT is determined by the scattering rate of bright-state atoms, and the fraction of atoms in the bright state. Even at high intensity, atoms can decay to a dark-state and so the average scattering rate is limited by the rate of remixing of dark and bright states through motion-induced couplings or Larmor precession. This is visible, from Fig. 5.12, in the saturation of the scattering rate at lower values than for the type-I MOT.

5.4 Spring constant and damping coefficient of the blue-detuned MOT

In this section measurements are presented of the spring constant and damping coefficient of the blue-detuned MOT. A number of different methods have previously been used to measure the spring constant of a MOT. The first is via the use of the equipartition theorem, as in [89]. In this method, simultaneous measurements of the temperature and density distribution of atoms in a MOT are used to calculate the spring constant. The advantages of this method are that it is conceptually simple and experimentally straightforward to implement. A major disadvantage is that this method is only valid when the density distribution of atoms is governed by the trapping potential, and interactions between atoms can be neglected. The method is not applicable when the density of atoms is limited by radiation trapping within the cloud. Another method which has been used to probe the trapping potential in a MOT is via the parametric resonance that can occur when the trap stiffness is modulated by changing the intensity of the trap lasers [93]. Under certain conditions instabilities occur at precise modulation frequencies [94], which can be used to infer the trap frequency [95]. In [96] this method is used to probe the sub-Doppler and Doppler contributions to the trapping potential in a MOT. Finally, observation of the transient oscillation and relaxation of a cloud of atoms displaced from the centre of the MOT can be used to calculate the trap frequency and damping coefficient [97].

The spring-constant of type-II traps is inherently small as a result of the dark Zeeman sub-levels in the ground states. In previous sections measurements are presented of the temperature of atoms in the blue-detuned MOT. Sub-Doppler cooling

can proceed efficiently, so the damping coefficient is high. The combination of small restoring forces and high frictional forces conspire to make measurements of the spring constant and damping coefficients difficult. The dynamical methods used to measure the properties of the MOT rely on the motion of the atoms being under-damped. Under-damped motion can be achieved in type-I MOTs by using a low intensity, but in the blue-detuned MOT under-damped motion is never observed. Both the parametric resonance and transient oscillation methods have been applied to the blue-detuned MOT, but neither produced useful results. The only remaining option is to use the equipartition theorem.

5.4.1 The equipartition theorem

The equipartition theorem can be used to determine the spring constant of the trap from measurements of the equilibrium spatial distribution of the atoms [89] and their temperature. The equipartition theorem is most generally stated as,

$$\left\langle x_n \frac{\partial H}{\partial x_n} \right\rangle = k_{\mathrm{B}} T, \tag{5.8}$$

where H is the Hamiltonian of the system and x_n are a set of generalised coordinates with which the system can be described. The angled brackets indicate an average over the ensemble of atoms. The equation holds when the system is coupled to a heat bath with which it can exchange energy and is in thermal equilibrium. In a MOT, atoms are heated by the spontaneous emissions of photons and cooled by the sub-Doppler or Doppler forces. Therefore, the equation is applicable to the ensemble of atoms. For the purpose of calculating a spring constant, it is assumed that the position-dependent force is linear in the displacement. For an atom displaced along the $\hat{z}$ axis by an amount z, the restoring force is $F(z) = -\kappa_z z$. In this case $x_n \equiv z$ and $H \equiv H_z = \frac{1}{2}\kappa_z z^2$. Substituting these expressions into Eq. 5.8, the following expression is obtained,

$$\langle \kappa_z z^2 \rangle = k_{\mathrm{B}} T. \tag{5.9}$$

Similar expressions apply to the other components of the position vector. If the spatial distribution of atoms has a Gaussian form, then this expression is readily evaluated,

$$\langle z^2 \rangle = \frac{\int z^2 n(z) dz}{\int n(z) dz} = \frac{\sqrt{2\pi}\sigma_z^3}{\sqrt{2\pi}\sigma_z} = \sigma_z^2, \tag{5.10}$$

and so one can write,

$$\kappa_i = \frac{k_{\mathrm{B}} T}{\sigma_z^2}. \tag{5.11}$$

In writing the above it is assumed that the atoms experience a harmonic potential due to the confining force of the MOT. This, however, is generally not the case. As discussed in the previous section type-I MOTs typically operate in the radiation-pressure-limited density regime. In such a regime the atom density distribution is modified by radiation trapping in the cloud. In order to accurately calculate the spring constant the density distribution of atoms in the low-atom-number limit must be determined. The low-atom-number volume, V_0, which was used as a parameter in Eq. 5.7, can be used to define a spring constant for the MOT κ_{MOT} in the following way,

$$\kappa_{\mathrm{MOT}} = (\kappa_z \kappa_r^2)^{1/3} = k_{\mathrm{B}} \left(\frac{T_z}{\sigma_z^2} \left(\frac{T_r}{\sigma_r^2} \right)^2 \right)^{1/3} = \frac{2\pi k_{\mathrm{B}} T_{\mathrm{MOT}}}{V_0^{2/3}}, \tag{5.12}$$

where $V_0 = (2\pi)^{3/2} \sigma_z \sigma_r^2$ and $T_{\mathrm{MOT}} = (T_z T_r^2)^{1/3}$. Again it is assumed that $\sigma_x = \sigma_y \equiv \sigma_r$. A theoretical consideration of the scattering force in a MOT gives a spring constant that is proportional to the magnetic-field gradient, $\kappa_i \propto B_i'$. Since the field gradient in the axial direction is twice that in the radial direction $\kappa_z = 2\kappa_r$. From Eq. 5.12 it follows that $\kappa_z = 4^{1/3} \kappa_{\mathrm{MOT}}$. If these assumptions hold, then the characteristic dimensions of a cloud of atoms in thermal equilibrium are related by $\sigma_r = \sqrt{2}\sigma_z$. When the MOT beams are well aligned and the intensities are well-balanced this is generally a good description of the shape of the trapped atom cloud in the MOT.

Knowing the spring constant of the trap allows the damping coefficient to be obtained from the transient relaxation of a displaced cloud of atoms. The equation of motion for the atoms in the MOT is assumed to be given by

$$m\ddot{x} = -\kappa x - \beta \dot{x}, \tag{5.13}$$

where κ is the spring constant of the trap and β is the damping coefficient of the trap. The motion of the trap centre is over-damped when $\beta^2 - 4\kappa m > 0$. Experimental observations suggest this appears to be the relevant case over a wide range of parameters. The solution to the equation is,

$$x(t) = A_1 \exp[-\gamma^+ t] + A_2 \exp[-\gamma^- t], \tag{5.14}$$

with, $\gamma^{\pm} = (-\beta \pm \sqrt{\beta^2 - 4\kappa m})/2m$.

Fig. 5.13 shows the sequence of measurements made in order to determine the spring constant and damping coefficient of the MOT. First, shown in panel (a), the atom number density was measured as a function of the atom number, measurements identical to those presented in Fig. 5.11(a) and described in more detail in Sec. 5.3. A fit to these data allows the characteristic size of the trap to be estimated for small

atom numbers, where the density distribution of atoms is governed solely by the position-dependent force from the MOT. Next, shown in panel (b), the temperature is measured via a ballistic expansion using the method described in Sec. 5.2. The temperature has been observed to be insensitive to the number of atoms in the trap and so a single measurement is made. Eq. 5.12 can then be used to calculate the spring constant from the temperature and distribution of atoms. Once the spring constant has been calculated the damping coefficient can be measured by quickly displacing the atoms in the trap and observing the over-damped transient relaxation to the new equilibrium position. Experimentally this is achieved by applying a homogeneous bias field along the axis of the MOT, which is superimposed with the quadrupole MOT field. The bias field is generated by a pair of coils driven by a high-power op-amp. The switching time for the coils is much smaller than the measured relaxation time for the atoms. Fig. 5.13(c) shows a typical trajectory for a cloud of atoms displaced in such a way. Consider now Eq. 5.14. Expressing the spring constant in terms of the trap frequency, $\omega_0^2 = \kappa/m$, and noting that $\beta/2m = \gamma_0$ is the characteristic damping time of the velocity, then $\gamma^{\pm} = -\gamma_0 \pm \sqrt{\gamma_0^2 - \omega_0^2}$. The velocity-dependent forces, for small velocities, are comparable to those in type-I MOTs, whereas the trap frequencies are far smaller, which implies $\omega_0 \ll \gamma_0$, and hence $|\gamma^+| \ll |\gamma^-|$. This argument is based upon values of ω_0 and γ_0 reported elsewhere in the literature. Therefore, γ^- only contributes to the dynamics of the relaxation at very early times, and the recorded trajectory is governed by the value of γ^+. For this reason, the data is fit to a single exponential, with damping time γ^+, rather than the full form of Eq. 5.14. Indeed, the data are found to be well approximated by this simplified function.

For the data shown in Fig. 5.13 the laser parameters were $\Delta_{11}/(2\pi) = +35$ MHz, $\Delta_{22}/(2\pi) = +11.5$ MHz and $I_t = 134$ mW/cm^2, the magnetic-field gradient in the MOT was 87 G/cm. Using the value of V_0 taken from Fig. 5.13(a), and the temperatures in the axial and radial directions, measured in Fig. 5.13(b), the value of the spring constant in the axial direction is found to be $\kappa_z = 2.7(1)\times10^{-20}$ N/m. The corresponding damping coefficient is found to be $\alpha/m_{\mathrm{Rb}} = 4.6(4) \times 10^3$ s^{-1}.

Fig. 5.14 shows a series of measurements made to obtain the spring constant and damping coefficient as Δ_{11} s varied. As the detuning is increased from $\Delta_{11}/(2\pi) = +12$ MHz to $\Delta_{11}/(2\pi) = +40$ MHz the damping coefficient increases, roughly doubling in value, and the spring constant decreases, roughly halving in value. The behaviour of the damping coefficient is similar to that expected for Sisyphus cooling for a type-I system, where $\alpha \propto \Delta/\Gamma$ [31]. Additionally, 1D MOT theory predicts that the spring constant decreases as the detuning is increased above a certain value, as is the general trend here.

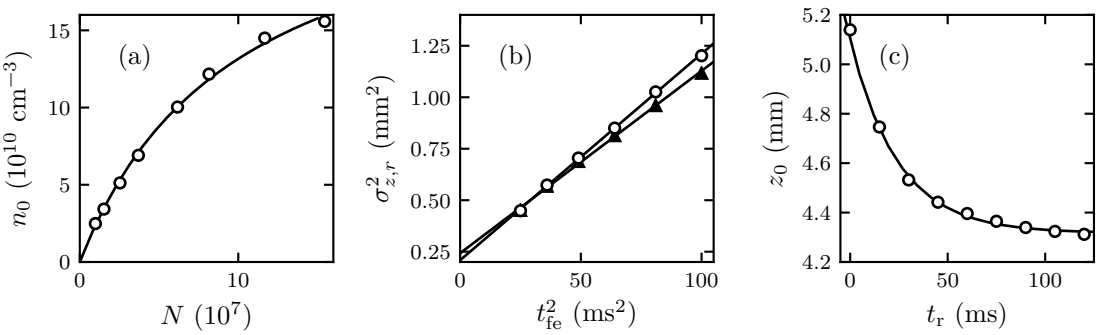

Figure 5.13: Data collected in order to calculate the spring constant and damping coefficient. (a) The peak atom number density, n_0, as a function of the total number of trapped atoms, N. The fit is to the function given in Eq. 5.7 and yields a value for the low-atom-number volume, V_0, of 0.38(1) mm^3. (b) The squared rms widths of the cloud in the axial and radial directions, $\sigma^2_{z,r}$, as a function of the square of the free-expansion duration, $t^2_{\rm fe}$. The fits are to a functions of the form Eq. 5.5, and give 94(2) µK and 106(1) µK in the axial and radial directions, respectively. (c) Lastly, the relaxation of the atoms in the trap is recorded following a rapid displacement of the trap centre. The centre-of-mass of the atom density distribution, z_0, in the axial direction is recorded in the detector coordinates as a function of the relaxation time $t_{\rm r}$. The displacement occurs at $t_{\rm r} = 0$. The fit is to a single exponential-decay and gives a damping time, $\tau = 26(2)$ ms.

Discussion

The calculated value of the spring constant depends sensitively on the alignment of the MOT through the characteristic size of the cloud. The size and shape of the cloud is very sensitive to the precise alignment of the MOT beams, the balance of intensities between them, and the presence of any inhomogeneity in the intensity distribution of the beam. Small imperfections in any of these parameters can lead to large changes in the low-atom-number volume, V_0, because the shape of the cloud is easily distorted. When repeating identical measurements to those presented in this chapter, large variations are found in the calculated value for the spring constant. For instance, the measurements presented in Fig. 5.13 were repeated at a later time, after the beams had been realigned and rebalanced multiple times, using the same trap parameters. The spring constant was calculated to be $\kappa_z = 9(2) \times 10^{-20}$ N/m and the damping coefficient was $\alpha/m_{\rm Rb} = 5(1) \times 10^3$ s^{-1}. The spring constant, as calculated by using the equipartition theorem, seems to be especially sensitive to the trap alignment. It is thus difficult to state with confidence a precise value for the spring constant of the trap. A value of $\kappa_z = 5(2) \times 10^{-20}$ N/m is obtained by averaging a number of measurements using identical trap parameters but made at different times.

Measurements of the spring constants of type-II atomic MOTs have not been reported directly. In [45] a red-detuned type-II MOT of ^{85}Rb is reported. From

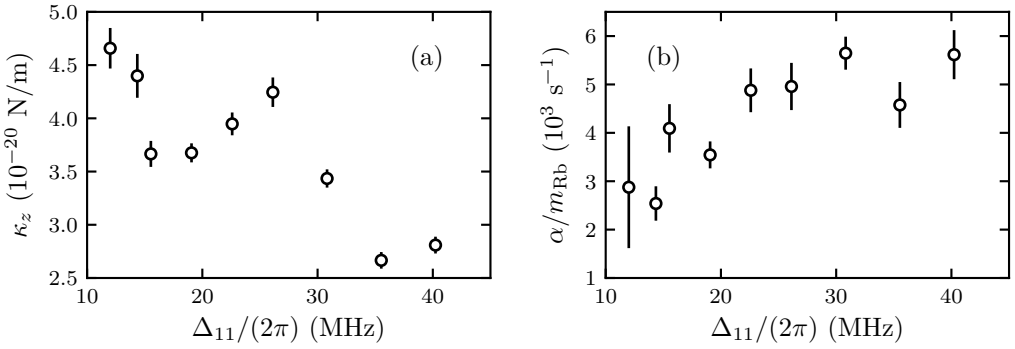

Figure 5.14: Measurements of the spring constant and damping coefficient as a function of the detuning of the $F = 1 \rightarrow F' = 1$ laser. (a) Spring constant in the axial direction of the MOT, obtained from the equipartition theorem. (b) Damping coefficient obtained from the spring constant and the measured motional damping time. The parameters are $I_t = 113$ mW/cm^2, $B' = 87$ G/cm, $\Delta_{22}/(2\pi) = +11.5$ MHz.

the reported temperature and size of the cloud the equipartition theorem gives $\kappa_z = 8 \times 10^{-20}$ N/m at field gradient of 10 G/cm. The radial spring constant of a MOT of SrF has been reported to be 4×10^{-20} N/m for a field gradient of 9 G/cm [71]. Lastly, for CaF, a value of 3.9×10^{-20} N/m has been reported for a field gradient of 30 G/cm [98]. These values are close to those measured for the blue-detuned MOT, although the field gradient used for the blue-detuned MOT is a few times higher than for these other measurements.

There are a number of subtleties to consider when making comparisons between red-detuned and blue-detuned type-II MOTs. First, it is well known from studies of type-I MOTs that the trapping potential due to the restoring force of the MOT has Doppler and sub-Doppler components. Two component atom-density distributions are reported in [92], and the properties of the sub-Doppler trap are investigated in [96]. Analytical expressions for the sub-Doppler MOT force for a type-I system are derived in [99,100]. Close to the trap centre the force is linear in the displacement of the atom. The sub-Doppler contribution to the trapping force is also visible in Fig. 7(e) of [73], where it is simulated numerically for a $F = 1 \rightarrow F' = 2$ system in a three-dimensional MOT configuration.

The sub-Doppler contribution to the position-dependent force in type-II systems is quite different in its form. In earlier chapters it has been discussed how, for a static laser polarisation, type-II systems are optically pumped into a dark-state. In molecular-beam-slowing experiments a static magnetic-field can be used to brighten the dark-state. At the centre of a MOT the magnetic-field is zero, but moving atoms can still make a non-adiabatic transition from a dark-state to a bright-state thanks to the gradients in polarisation and intensity. The likelihood of this type of transition occurring depends on the velocity of the atom. This leads to a non-linear velocity-

dependent and position-dependent force. It also implies that a hotter ensemble of atoms can experience a larger spring-constant at the trap centre because the dark and bright states are more effectively remixed by motion-induced couplings. The temperatures in red-detuned type-II atomic MOTs far exceed those reported here, and so this could be the reason for the larger spring-constant reported for those MOTs for comparable field gradients.

Similarly, the form of the function fit to the transient relaxation of the cloud assumes a linearised velocity-dependent force, characterised in terms of a damping coefficient. Numerical simulations show that this is not actually the expected behaviour, but the data fits the function reasonably well so that the magnitude of the frictional force can still be compared to other MOTs. In these experiments, the damping coefficient has values in the range $\alpha/m_{\mathrm{Rb}} = 2 - 6 \times 10^3$ s^{-1}. In [98] the damping coefficient is measured as a function of trap laser intensity and detuning for a MOT of CaF. The data are well described by a two-level model with an effective saturation parameter. The maximum damping coefficient is $\alpha/m_{\mathrm{CaF}} = 3 \times 10^3$ s^{-1}, which occurs at a detuning of $\Delta = -\Gamma$ and decreases rapidly with more negative detuning, falling to below half its maximum value at $\Delta = -2\ \Gamma$. The detuning used in this experiment is typically much larger and the damping coefficient is observed to increase with the detuning, having values close to 6×10^3 s^{-1} at $\Delta = +5\ \Gamma$. This makes sense because the damping in the blue-detuned MOT is exclusively due to sub-Doppler processes, whereas in the CaF MOT it is due mainly to Doppler processes.

The non-linearity of the position and velocity-dependent forces in the blue-detuned type-II MOT raises the question of whether the approach used to calculate the spring constant in this section is valid. The application of these methods to red-detuned type-II MOTs is less concerning because the size of these clouds is much larger. Most of the atoms experience a trapping potential dominated by one-photon processes, and the force is approximately linear in the displacement when averaged over a large enough extent. This extent can be comparable to the characteristic size of the atom clouds due the the high temperature of the atoms or molecules. Despite these considerations, the atom-density distributions for the blue-detuned MOT do appear to be generally well described by a Gaussian function, so that the equipartition theorem can be used to obtain a value for the spring constant, which can then be compared to other MOTs.

More precise measurements of the density distribution and temperature of the atoms, such as via a time-of-flight measurement, may reveal more information about the structure of the trapping potential and thus help to refine the measurements presented in this section.

5.5 Phase space density of the blue-detuned MOT

The phase-space density obtainable in a MOT is limited by a number of different processes. The temperature atoms can be cooled to is limited by diffusion in momentum space caused by the spontaneous emission of photons and by fluctuations in the numbers of photons absorbed from the trapping beams. When the number of trapped atoms is large the diffusion coefficient is enhanced due to multiple photon scattering between atoms [101]. Thus, the limiting temperature to which atoms can be cooled in a MOT depends on the number of trapped atoms [91]. The efficiency of sub-Doppler cooling processes is also inhibited by multiple photon scattering [55]. In addition to increasing the temperature, radiation trapping in the cloud imposes a density limit on the trap, as discussed in the previous section. Finally, collisions between excited-state and ground-state atoms can lead to high loss-rates in a MOT, reducing both the number and density of trapped atoms.

To increase the phase-space density further, atoms are transferred to a conservative potential, such as a magnetic or dipole-trap. Once here, evaporation of the most energetic atoms and rethermalisation of those remaining increases the phase-space density. This is the means by which atoms are cooled and condensed to the quantum-degenerate regime.

Invariably, a MOT is used to load a conservative trap in preparation for evaporation. The higher the phase-space density of the MOT, the quicker the evaporation can proceed and the larger the condensate obtained. The dimensionless phase-space density of an ensemble of atoms is defined as [102],

$$\rho = n\lambda_{\mathrm{T}}^3, \tag{5.15}$$

where n is the number-density of atoms and λ_{T} is the thermal de Broglie wavelength,

$$\lambda_{\mathrm{T}} = \sqrt{\frac{2\pi\hbar^2}{Mk_{\mathrm{B}}T}}. \tag{5.16}$$

The thermal de Broglie wavelength is closely related to the effective wavelength of a particle of mass M, whose kinetic energy is $k_{\mathrm{B}}T$. Eq. 5.15 can therefore be interpreted as the number of atoms within a box that has a side-length equal to λ_{T}. Quantum-degenerate behaviour manifests itself when $\rho \sim 1$ [103], and particles are separated by less than the de-Broglie wavelength. The phase-space density that can be obtained in a type-I MOT is typically 10^{-6}-10^{-5} and for large numbers of atoms, the value is smaller [102].

While the highest phase-space densities demonstrated in type-I atomic MOTs remain 5-6 orders of magnitude below the BEC threshold, condensates are nowadays

routinely produced [104, 105]. This is possible due to the large numbers of atoms than can be captured by a MOT and loaded into conservative traps at modest densities and temperatures. The possibility of achieving BEC using the previously demonstrated red-detuned type-II systems seems remote. As has been discussed in previous sections, the densities of these traps are typically 2-3 orders of magnitude smaller, and their temperatures 2-3 orders of magnitude higher than is achieved using the type-I MOT. The resulting phase-space densities are prohibitively small to be considered a viable start point for obtaining BEC. For the alkali-metal atoms this is not a problem because type-I MOTs can be used, but molecules are always cooled and trapped using type-II transitions.

In this section measurements are presented of the typical phase-space densities achieved in the blue-detuned type-II MOT. Reassuringly, these are found to be $10^5 - 10^6$ times higher than for comparable red-detuned type-II MOTs, representing a vast improvement over the status quo. The highest phase-space densities are obtained when the blue-detuned MOT is loaded at high magnetic-field gradient and laser intensity. Then, the intensity of the trap is substantially reduced for a brief period of time, which further cools the atoms. During the period of reduced intensity the magnetic field remains at the same value for which the MOT is loaded. As has been demonstrated in earlier chapters, high magnetic-field gradients do limit the temperature that atoms are cooled to, but the atom number density also remains higher after the low-intensity cooling phase. Low temperatures are obtained even for large numbers of atoms and so the phase-space densities obtained here are remarkably high.

Fig. 5.15 shows how each of the number of atoms, their density, their temperature, and the resulting phase-space density varies as a function of the total trap intensity used during the cooling phase. The temperature varies approximately linearly with intensity over the range of intensities measured. For $I_t \gtrsim 100$ mW/cm^2 the peak density does not change much but the temperature is proportional to I_t. As I_t is reduced to lower values the peak density begins to decrease, as does the temperature. Overall, the phase-space density increases monotonically with decreasing I_t over the whole range of intensities measured.

5.5.1 Discussion

The phase-space density in a MOT is limited by the internal radiation pressure between atoms or molecules. One very successful technique that has been demonstrated previously is the dark SPOT (Spontaneous Force Optical Trap) first demonstrated by Ketterle et al. [56]. In a dark-SPOT a region of reduced photon scattering is created, where cold atoms can accumulate at high atomic densities liberated from

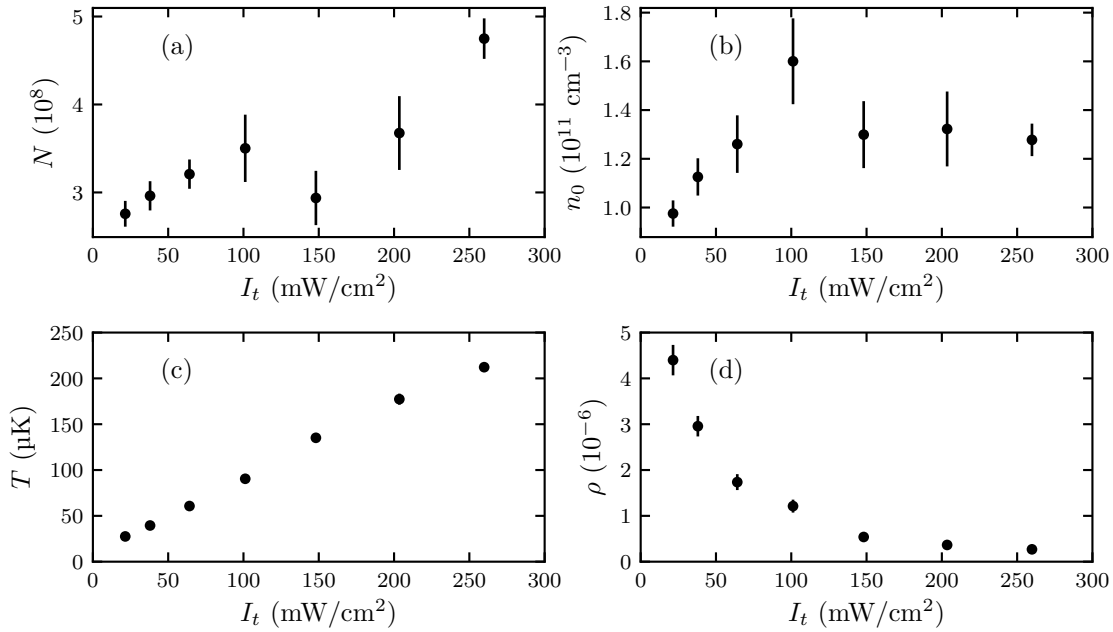

Figure 5.15: (a) Atom number, (b) peak atom density, (c) temperature and (d) phase-space density of atoms in the blue-detuned MOT, as a function of the total trap intensity. The MOT is loaded and held at high intensity for 90 ms. For the final 5 ms the intensity is reduced to the value shown here, reducing the temperature of the atoms. The other parameters are $\Delta_{11}/(2\pi) = 35.5$ MHz, $\Delta_{22}/(2\pi) = 11.5$ MHz and $B' = 87$ G/cm. The variation in atom number and density is relatively small when compared to the change in the temperature. The change in the phase-space density is mostly due to the temperature of the atoms.

the repulsive effects of photon re-scattering. Experimentally this is achieved using a de-pumping beam to deliberately shelve atoms in a state that is de-coupled from the trapping light. In [56] the authors demonstrate a two-orders of magnitude improvement in the number-density of trapped atoms, which occurs when the population of the bright state is reduced to about ~1%. One potential disadvantage of this technique is that the forced depumping into the dark-state can lead to heating above the molasses temperature, since no cooling takes place in the dark-state. Nevertheless, far higher phase space densities have been demonstrated than are otherwise obtainable in a bright MOT. Radwell et al. (2013) report a phase-space density of $8{\times}10^{-6}$, obtained in a dark SPOT using a spatial light modulator to precisely shape the re-pumping and de-pumping beams, which is a record for the phase-space density in a MOT [106]. The highest phase-space density that is observed in the blue-detuned MOT is about 6×10^{-6}, very close to the record set in [106]. The very high phase-space densities that we obtain are due to the efficient cooling mechanisms that are robust to very large magnetic-field gradients in the MOT. The atom number density is higher than in a bright type-I MOT due to the presence of dark Zeeman sub-levels in the ground state, though not as high as has been obtained in a dark

SPOT. The temperatures of atoms in the blue-detuned MOT compare favourably to those obtained in a bright MOT, especially one in which the magnetic-field gradient or the atom number density are as high as are demonstrated here. Many of the proposed applications of laser cooled molecules require, or would benefit from, high phase-space densities. In the type-II atomic MOTs reported to date the phase-space density is about 10^{-12}, using molecules the phase-space density is even lower, at about 10^{-14} [14]. If the technique demonstrated here could be applied to molecules vast improvements in the phase-space density might be obtained and many more of the proposed applications would be made feasible.

5.6 Lifetime of atoms in the blue-detuned MOT

In the very first realisation of a magneto-optical trap [6], the authors reported the observation of a rapid, non-exponential loss rate at short times that limits the maximum density of atoms. At longer times, when the density of the atoms in the trap is much lower, the atom number decays exponentially. The authors note that the loss rate is proportional to the square of the atomic density, and they conclude that the non-exponential loss is due to two-body collisions between trapped atoms. In a follow-up publication the density-dependent loss rate coefficient in a sodium MOT is measured to be $\beta = 4 \times 10^{-11}$ cm^3/s [42]. The exact mechanism is not explained, but an earlier theoretical paper by J. Vigué [107] had pointed out that collisions occurring between cold atoms in the presence of near-resonant laser light can result in kinetic energy being imparted to the atom. The kinetic energy is released by excitation to an attractive molecular potential, which causes a pair of atoms to accelerate towards their common centre of mass, followed by spontaneous emission at shorter inter-atomic separation. The idea that the collisions involved an excited-state molecular potential was further supported by the observation that the collisional loss-rate in the MOT far exceeds that observed in the dipole trap [35], where the excitation rate is much lower. Cross sections can be calculated from these loss rates and the study of these cold collisions quickly emerged as a productive area of research.

The realisation of the first blue-detuned magneto-optical trap presents an exciting opportunity to investigate the cold collisions occurring between atoms in the presence of near-resonant blue-detuned laser light. In this section results are presented from measurements made of the lifetime of atoms confined in the blue-detuned MOT. The loss rate of atoms from the trap is found to be strongly dependent on the atom density and measurements have been made of the loss rate due to two-body collisions occurring in this trap.

This section begins with a review of the various mechanisms that can lead to the

loss of atoms from a magneto-optical trap. Then, data is presented on the density-dependent loss rate of atoms from the blue-detuned MOT. The one and two-body loss-rate coefficients are measured as a function of various laser parameters. Finally, speculations are made as to the dominant mechanism contributing to the two-body loss rate of the atoms. These speculations are supported by direct measurements of the capture velocity of the trap, presented in Sec. 5.7.

5.6.1 Loss mechanisms in the MOT

The MOT is the most commonly used tool to study cold and ultra-cold collisions between atoms. An atom trapped in a MOT can undergo a collision with either an untrapped atom or a second trapped atom. Both types of collision can lead to trap loss. The presence of near-resonance laser light can modify collisions between atoms at ultracold temperatures. Under such conditions the lifetime of the excited state can be comparable to the duration of the collision, and this can give rise to a variety of light-assisted effects. In what follows, a brief overview of these mechanisms is given. The loss rate due to collisions between trapped and untrapped atoms is discussed first. Afterwards, intra-trap collisions are covered.

Collisions with untrapped atoms

Elastic collisions occurring between trapped and untrapped atoms can eject the trapped atom if sufficient kinetic energy is imparted so that its new velocity exceeds the capture velocity of the MOT. The rate at which these collisions occur depends on the collision cross section for the interaction. The collision cross section depends upon the species of atom trapped and the species of the untrapped atom or molecule. Typically, the background-gas composition consists mainly of N_2, CO, H_2 and CO_2. The collision rate for a particular species is proportional to its density n, and hence pressure through the ideal gas law $P = nk_{\mathrm{B}}T$. The total rate of collisions is summed over all the constituents of the background gas. It has previously been observed that the loss rate due to these collisions is highly insensitive to the trap depth of the MOT. This is because the trap depths, which are at most a few kelvin, are far smaller than the temperature of the background gas. A theoretical calculation [108] concludes that the lifetime due to collisions with residual gas, τ_r, depends on the trap depth W_t as $\tau_r \propto W_t^{0.2}$. To a good approximation, the loss rate of trapped atoms due to the background gas is $\frac{dN}{dt} = -\zeta P_{\mathrm{bg}} N$. In addition to the background gasses there is the alkali-metal vapour from which the MOT is loaded. In this experiment the pressure of rubidium vapour P_{Rb} inside the chamber can be changed by adjusting the dispenser current, which is typically kept constant throughout the duration of any set of measurements. The pressure reaches its steady-state value after some

initial transient, which can be characterised by monitoring the loading curve of a MOT. Collisions between trapped atoms and the thermal vapour lead to loss in the usual way. Slow moving atoms are also captured from the vapour, and this loading rate is sensitive to the intensity and detuning of the laser light. The loading rate R of the atoms is given in [41], $R = 0.5nV^{2/3}v_c^4(\frac{m}{2k_BT})^{3/2}$, where V is the capture volume of the trap and v_c is its capture velocity. Alternatively, the loading rate can be expressed in terms of the beam diameter d, where $V \approx d^3$ [85]. The capture velocity is also related to the beam diameter through the stopping distance, so that $R \propto d^4$. In this limit of low density, where intra-trap collisions are negligible, and using the fact that for a fixed temperature $P_{\mathrm{Rb}} \propto n$,

$$\frac{dN}{dt} = \nu P_{\mathrm{Rb}} - N(\xi P_{\mathrm{Rb}} + \zeta P_{\mathrm{bg}}). \tag{5.17}$$

The solution to this equation for $t \geq 0$ is

$$N(t) = \frac{\nu P_{\mathrm{Rb}}}{\xi P_{\mathrm{Rb}} + \zeta P_{\mathrm{bg}}}(1 - e^{-t(\xi P_{\mathrm{Rb}} + \zeta P_{\mathrm{bg}})}). \tag{5.18}$$

The steady-state population N_∞, and the loading time τ are

$$N_\infty = \frac{\nu P_{\mathrm{Rb}}}{\xi P_{\mathrm{Rb}} + \zeta P_{\mathrm{bg}}}, \qquad \tau = \frac{1}{\xi P_{\mathrm{Rb}} + \zeta P_{\mathrm{bg}}}. \tag{5.19}$$

When the pressure of rubidium is small, so that $\zeta P_{\mathrm{bg}} \gg \xi P_{\mathrm{Rb}}$, the steady-state atom number increases with the rubidium partial pressure, $N_\infty \sim (\nu/\zeta)(P_{\mathrm{Rb}}/P_{\mathrm{bg}})$, and the loading rate is insensitive to small changes in P_{Rb}. On the other hand, if $\xi P_{\mathrm{Rb}} \gg \zeta P_{\mathrm{bg}}$, then $N_\infty = \nu/\xi$ and is independent of P_{bg}, whereas the loading time $\tau = 1/(\xi P_{\mathrm{Rb}})$. One important consideration is that if Eq. 5.17 is solved with $\nu \to 0$ and for an initial atom number N_0, then the solution is $N(t) = N_0 \exp(-t/\tau)$, where τ has exactly the same form as in Eq. 5.19. Therefore, the loading rate of the MOT in the vapour cell is the same as the lifetime of the atoms in the absence of any loading. This is an important consideration when making comparisons between the red-detuned type-I MOT and blue-detuned type-II MOT because the blue-detuned MOT does not capture atoms from the vapour.

Simple numerical calculations based upon the equations presented above agree well with experimental observations. In [109] numerical simulations are performed to predict how the number of trapped atoms in a MOT varies with the beam diameter d. The simulations yield a model $N \sim d^b$, with $b = 3.6$. This is close to the experimentally observed scaling law in [85], where $b = 3.65(14)$.

Radiative escape and fine-structure-changing collisions

Collisions can also take place between two trapped atoms. These two-body collisions lead to a loss rate that is proportional to the local density of atoms squared. The loss rate coefficient is denoted by β, and the total loss rate of atoms is obtained by integrating over the trap volume. The rate equation for the number of trapped atoms is then,

$$\frac{dN}{dt} = \nu P_{\mathrm{Rb}} - N(\xi P_{\mathrm{Rb}} + \eta P_{\mathrm{bg}}) - \beta \int n^2(\mathbf{r}, t) d^3r. \tag{5.20}$$

The presence of near-resonant laser light can modify the collisions between trapped atoms in a variety of ways. It was first predicted by J. Vigué [107] that two-body collisions between a ground and excited-state atom could impede laser cooling at high densities. In the first demonstration of the magneto-optical trap a density limit was reached that was due to intra-trap collisions [6]. It was further noted that the intra-trap collisional loss rate was much higher than had previously been observed in the dipole trap [35], so that the collisions in the MOT were likely to be of the kind described by Vigué.

There are two types of trap-loss mechanism that involve excited-state atoms; radiative escape and fine-structure changing collisions. If the density of ground state atoms is denoted by $n(r)$ and the density of excited-state atoms by $n^*(r)$, then fine-structure-changing collisions lead to a loss-rate,

$$\frac{dN}{dt} = -\beta_{\mathrm{fsc}} \int n(\mathbf{r}, t) n^*(\mathbf{r}, t) d^3r, \tag{5.21}$$

and radiative-escape leads to a loss rate,

$$\frac{dN}{dt} = -\beta_{\mathrm{re}} \int n(\mathbf{r}, t) n^*(\mathbf{r}, t) d^3r. \tag{5.22}$$

Fig. 5.16 illustrates the two types of collision that can occur between an excited-state and ground-state atom. The potential curves are plotted in terms of the inter-atomic separation R. In Fig. 5.16(a) there are three long-range fine-structure asymptotes shown, which correspond to 5s $^2\mathrm{S}_{1/2}$ + 5s $^2\mathrm{S}_{1/2}$, 5p $^2\mathrm{P}_{1/2}$ + 5s $^2\mathrm{S}_{1/2}$, and 5p $^2\mathrm{P}_{3/2}$ + 5s $^2\mathrm{S}_{1/2}$. At long range the interaction potentials are described by a power law $V(R) = C_n/r^n$. Two ground-state atoms interact via the van der Waals interaction, where $n = 6$. An excited-state and ground-state atom interact via the resonant dipole-dipole interaction, where $n = 3$. The cross section for collisions between ground and excited state atoms is correspondingly large. There are both attractive and repulsive molecular potentials, the attractive molecular potentials support bound states, whereas the repulsive potentials do not. In a conventional

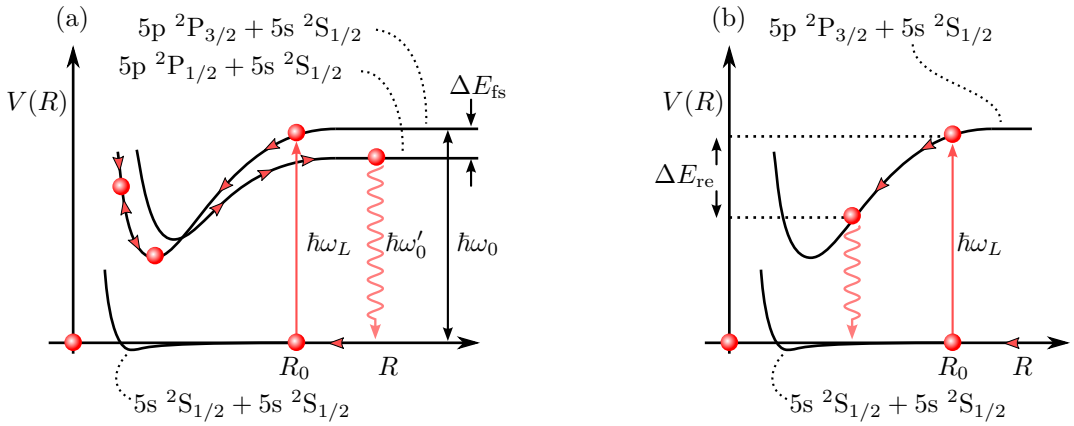

Figure 5.16: Collisions between ground and excited state atoms that can lead to loss from a magneto-optical trap. The figures illustrate the molecular potentials $V(R)$ as a function of atomic separation R. At long range the potentials are described by a power law $V(R) = C_n/r^n$. For two ground state atoms $n = 6$. An excited atom and a ground-state atom interact via the dipole-dipole interaction, where $n = 3$. (a) Illustrates a fine-structure-changing collision. Two ground-state atoms approach each other along the 5s ^{2}S$_{1/2}$ + 5s ^{2}S$_{1/2}$ asymptote. At the Condon point R_0 the laser is resonant with a molecular bound state, $\hbar(\omega_L - \omega_0) = -C_3/R_0^3$, and a 'quasi-molecule' can be excited. The two higher-lying molecular potentials asymptotically correspond to 5p ^{2}P$_{3/2}$ + 5s ^{2}S$_{1/2}$ and 5p ^{2}P$_{1/2}$+5s ^{2}S$_{1/2}$. At short separations mixing can occur between these potentials. An atom can approach along the $J = \frac{3}{2}$ asymptote and exit the collision along the $J = \frac{1}{2}$ asymptote. When spontaneous emission occurs the kinetic energy of the two atoms is increased by the fine-structure splitting of the excited state. For ^{87}Rb this splitting corresponds to a thermal energy of $T = \Delta E_{\rm fs}/k_{\rm B} = 342$ K, and both atoms are ejected from the trap. (b) Illustrates the radiative escape mechanism. Again, two ground state atoms approach along the 5s ^{2}S$_{1/2}$ + 5s ^{2}S$_{1/2}$ asymptote and are excited to a weakly-bound molecular complex at R_0. At low collision energies there is a finite probability of spontaneous emission occurring at short atomic separations. In this case the spontaneously emitted photon is lower in energy than the laser photon by an amount $\Delta E_{\rm re}$ and this excess is shared between the kinetic energy of the two atoms.

MOT the laser light is red-detuned with respect to the frequency of the transition being driven. At the Condon point R_0, the laser, which is detuned by an amount Δ_L from the atomic transition, is resonant with a transition to a molecular bound state $-C_3/R_0^3 = \hbar\Delta_L$, as illustrated in the figure. Once excited to the attractive potential, atoms accelerate towards each other and approach at short inter-atomic separations where two types of exoergic collision can occur.

In a fine-structure changing collision, shown in part (a) of the figure, an atom enters the collision along one of the $J = \frac{3}{2}$ asymptotes but leaves the collision along the $J = \frac{1}{2}$ asymptote. This is facilitated by mixing between the molecular potentials at small inter-atomic separations. Spontaneous emission occurring on the $J = \frac{1}{2}$ asymptote is red-shifted relative to the laser photon absorbed by an amount equal to the fine-structure splitting of the excited state, $\Delta E_{\rm fs}$. Each atom gains a kinetic energy $\frac{1}{2}mv^2 = \Delta E_{\rm fs}/2$. For ^{87}Rb $\Delta E_{\rm fs}/h = 7.1$ THz, which as a temperature corresponds to $T = \Delta E_{\rm fs}/k_{\rm B} = 342$ K. For sodium it is a much more modest 24 K, which is still many times larger then the typical trap depths obtained in a MOT.

In radiative escape, shown in part (b) of the figure, the atoms enter the collision along the same channel as for a fine-structure-changing collision, but spontaneous emission occurs at short inter-atomic separations where the atoms are deep in the molecular potential. This mechanism is illustrated in Fig. 5.16(b). Again the spontaneous emission is red-shifted relative to the photon absorbed so there is a net increase in kinetic energy of the atoms by an amount $\Delta E_{\rm re}$, divided equally between the two.

A quasi-static semi-classical model of the collisions was developed by A. Gallagher and D. Pritchard in [110]. The model is used to derive expressions for the rate coefficients for these two trap-loss mechanisms. The rate coefficients for radiative escape and fine-structure-changing collisions are evaluated for sodium. The dominant trap-loss mechanism is predicted to be due to fine-structure changing collisions, so $\beta \simeq \beta_{\rm fsc}$. The energy released in this process, 12 K per atom for sodium, far exceeds the trap depths obtained in a MOT and a fine-structure-changing collision will always eject an atom, irrespective of the laser intensity. It is therefore expected that β should increase with the intensity, at least in part due to the larger population of the excited state. These predictions contradicted earlier experimental observations that β was insensitive to the intensity used in a sodium MOT [42].

A further experimental investigation into the dependence of β on the intensity and detuning of the laser light was performed in [39]. In that investigation a caesium MOT is used. In contrast to previous observations, the authors did report a strong intensity-dependence of β. There are two notable features. The first is a rapid increase in β, by at least an order of magnitude, occurring at low laser intensity as the intensity of the trap is reduced. This is attributed to hyperfine-state-changing

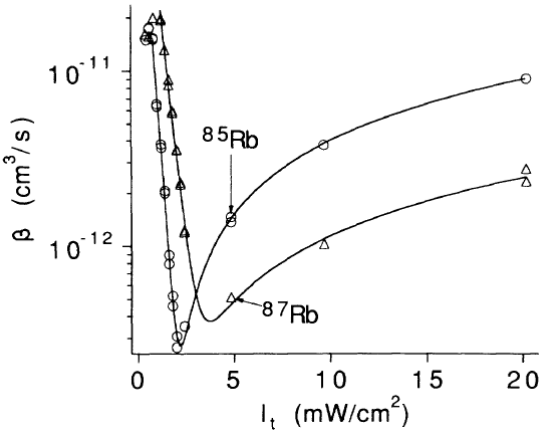

Figure 5.17: Trap loss rate coefficient as a function of total trap intensity in a type-I MOT. The graph is reproduced from [111]. The effect of hyperfine-state-changing collisions between ground-state atoms is clearly visible as a high loss rate at the lowest intensities.

collisions between ground-state atoms. These collisions can lead to significant trap loss if the depth of the trap is small, and are discussed in the next section. The second observation, made at higher laser intensities, is a linear increase of β with intensity. This is in qualitative agreement with the predictions of the Gallagher & Pritchard model [110], though there is a discrepancy of about a factor of five in the quantitative value.

Similar results were obtained in [111] for ^{87}Rb and ^{85}Rb. Both isotopes have qualitatively similar behaviour. Some data obtained in that investigation is reproduced in Fig. 5.17. At the lowest trap laser intensities the loss rate coefficient is measured to be $\sim 2 \times 10^{-11}$ cm^3/s for both isotopes. As the intensity is increased β falls rapidly, reaching a minimum value of $\sim 3 \times 10^{-12}$ cm^3/s at a total trap laser intensity $I_t \simeq 2.5$ mW/cm^2 for ^{85}Rb and $\sim 5 \times 10^{-12}$ cm^3/s for $I_t \simeq 5$ mW/cm^2 for ^{87}Rb. As the intensity is increased beyond this point the loss rate increases approximately linearly with intensity.

Hyperfine-state changing collisions

Investigations into the intensity dependence of the density-dependent loss rate coefficient of atoms confined in a MOT are presented for sodium in [43], lithium in [112], caesium in [39] and rubidium in [113]. A common feature to all these investigations is a sharp increase in the density-dependent loss rate when the intensity is further reduced below some small value, like that visible in Fig. 5.17. Similar behaviour is observed for sodium atoms confined in a type-II MOT operating on the D1 line in [114], though this behaviour is notably absent for the D2 type-II sodium MOT in [43].

The high loss rate at low intensity is the result of hyperfine-state-changing colli-

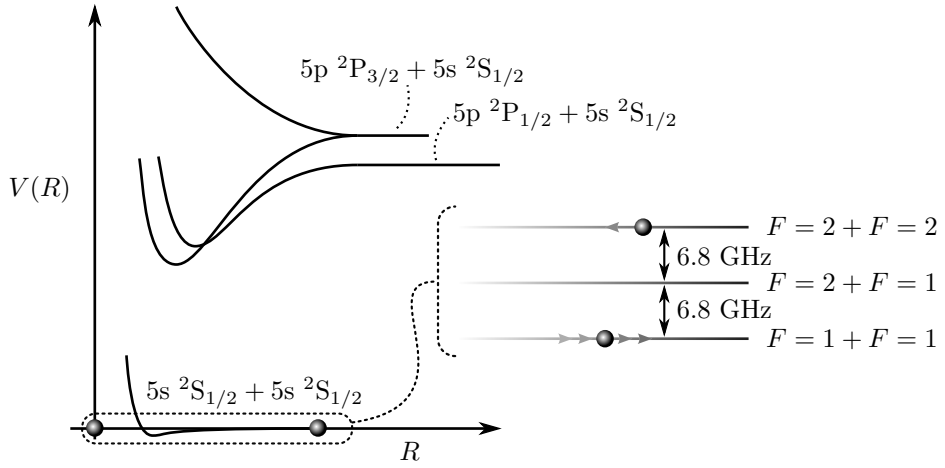

Figure 5.18: Hyperfine-state-changing collisions between ground state atoms. For two atoms in the ground state there are three long-range asymptotes, at intervals of 6.8 GHz. Atoms approaching along either of the upper two asymptotes can undergo a collision at short range and emerge moving along one of the lower-energy asymptotes. The potential energy is shared equally, as kinetic energy, between the two atoms.

sions between ground-state atoms. Fig. 5.18 shows the asymptotic collision channels between pairs of ground-state atoms at large separations. The figure also shows the excited-state molecular potentials, though these need not participate in the collisions[1]. As the atoms approach smaller separations spin-exchange and spin dipole-dipole interactions lead to mixing between states, and the pair can exit the collision along a different channel [116]. The initial and final asymptotic states can differ by $\Delta F = 2$, $\Delta F = 1$ or $\Delta F = 0$ [114, 117]. For ^{87}Rb the ground-state hyperfine splitting is 6.8 GHz. The maximum energy released by a hyperfine-state-changing collision occurs when $\Delta F = 2$, releasing 6.8 GHz of energy per atom. Trap loss due to these collisions is easily suppressed in type-I MOTs [118].

The rate at which these collisions occur does not depend on the trap light intensity, as the collision takes place between two ground-state atoms. Instead, the variation of β with intensity is due to the change in the capture velocity of the MOT. For type-I MOTs the capture velocity increases rapidly with laser intensity and can easily be large enough to recapture the products of exoergic collisions between ground state atoms. In [118] repulsive collisions are deliberately induced in a rubidium MOT in order to measure the capture velocity. Light that is blue-detuned by an amount Δ_L is used to excite colliding atoms to repulsive molecular potentials. The atoms accelerate away from one-another, each gaining $\hbar\Delta_L/2$ of kinetic energy. When $\hbar\Delta_L = mv_c^2$, where v_c is the capture velocity of the MOT, radiative escape can proceed. For a laser detuning smaller than 15 GHz no loss is observed, from

[1]The rate of these collisions can be increased using catalysis lasers that excite ground-state atoms to an attractive potential during the collision, as in [115]. However, the higher loss rate is only due to an increased flux of ground-state atoms at small separations.

which the capture velocity of the trap is determined to be at least $v_c = 8.3$ m/s. This is measured at a total MOT intensity of 2 mW/cm^2, far lower than is typically used. Therefore, these collisions do not normally contribute to trap loss in type-I MOTs. In the blue-detuned MOT the capture-velocity is limited by the sub-Doppler nature of the damping, hence it is important to consider this kind of collision.

Suppressing collisions between trapped atoms

The intra-trap collisions discussed in previous sections often limit the lifetimes, or maximum densities, of atoms confined in a MOT. Techniques have been developed to mitigate some of these effects. One especially successful technique is that of the dark-SPOT (Spontaneous Force Optical Trap) first demonstrated by Ketterle et al. [56]. In this technique atoms are deliberately 'shelved' in the lower hyperfine ground state, where they do not interact with the trapping light. These dark atoms can accumulate at high densities because of the reduction in radiation trapping which limits the densities in bright MOTs. In [56] a region of the repumping light, at the centre of the beam, is obscured by an optical mask. Two such beams are overlapped with a standard retroreflected 3-beam MOT so that a small volume at the centre of the trap has no repumping light. Spectroscopic measurements suggested that approximately 1% of atoms were in the bright hyperfine ground state. Densities of almost 10^{12} cm^{-3} were achieved for numbers of trapped atoms exceeding 10^{10} using this technique.

In the dark region of the SPOT the excited-state population is close to 0%, reducing the rate of fine-structure-changing collisions involving excited-state atoms. Additionally, the absence of near-resonant light reduces the rate at which light-assisted collisions between ground-state atoms occur. Both of these factors contribute to a reduction in the density-dependent loss rates in the trap. The lifetime of atoms in the trap can be thus be extended in a dark-SPOT. In [119] a similar technique is used to improve the properties of a MOT of rubidium loaded from a low-pressure vapour under UHV conditions. When using a bright MOT loaded directly from a vapour, one encounters a trade off between trapped-atom number and lifetime. To avoid this, in [119], a 'forced dark-SPOT' approach is used. This approach uses an additional laser frequency, to actively de-pump atoms into the lower hyperfine ground state in the region of the trap where the repumping light is obscured. Using this technique allowed for a tenfold increase in the steady state trapped atom number as compared to a bright MOT. The lifetime of the atoms was also extended by a similarly impressive factor. The technique allowed for large numbers of atoms to be cooled and captured under UHV conditions. This is ideal to prepare atoms for evaporative cooling in a magnetic trap and the first observation of Bose-Einstein condensation in an atomic vapour used this arrangement [104].

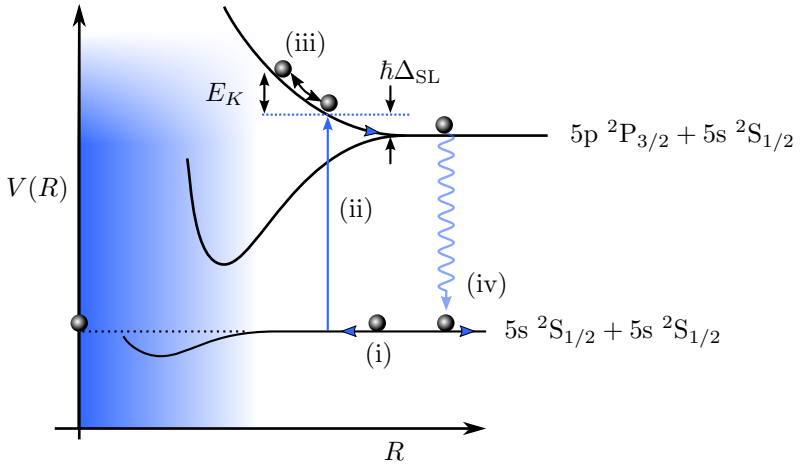

Figure 5.19: Optical shielding. (i) Two ground-state atoms approach along one of the three ground-state asymptotes. Inelastic collisions between ground state atoms occur at short inter-atomic separations, indicated by the shaded blue region. (ii) Blue-detuned laser light excites the pair to a repulsive molecular potential. (iii) Adiabatic motion along the molecular potential reduces the kinetic energy E_K of the colliding pair until a turning point is reached, reversing the direction of relative motion. Spontaneous emission may occur on the outgoing channel, in which case the atoms share a a maximum increase in energy given by $\hbar\Delta_{SL}$, where Δ_{SL} is the detuning of the suppression laser. Providing $\hbar\Delta_{SL} < \Delta E_{hfs}$ the collision is less inelastic than in the absence of the laser.

The dark-SPOT suppresses inelastic collisions between atoms by reducing the excited-state population in a small volume near the trap centre. There is a further possibility for suppressing inelastic collisions, which actually requires laser light. This effect is called optical shielding, and it has been used to reduce the loss rate coefficient for hyperfine ground-state changing collisions in a MOT [120]. The principle is illustrated in Fig. 5.19. A blue-detuned laser is used to excite colliding ground-state atoms to a repulsive molecular-potential, which prevents them from reaching small inter-atomic separations. Spin-exchange interactions between ground state atoms can lead to inelastic collisions and trap loss, but the cross-section for these processes is very small. Adiabatic motion along the repulsive potential reduces the kinetic energy of the colliding pair. At low temperatures the kinetic energy is insufficient for the atoms to approach close enough for an inelastic collision to take place, instead a turning point is reached and the pair then move apart, accelerated by the potential. Spontaneous emission can occur at large inter-atomic separation, imparting at most $\hbar\Delta_{SL}$ energy to the atoms, where Δ_{SL} is the detuning of the suppression laser. In [120] a 50% suppression in the loss rate due to inelastic collisions between ground-state atoms is achieved using a suppression laser detuned by 500 MHz. Since 500 MHz is significantly less than the ground-state hyperfine splitting, fewer atoms are ejected from the trap.

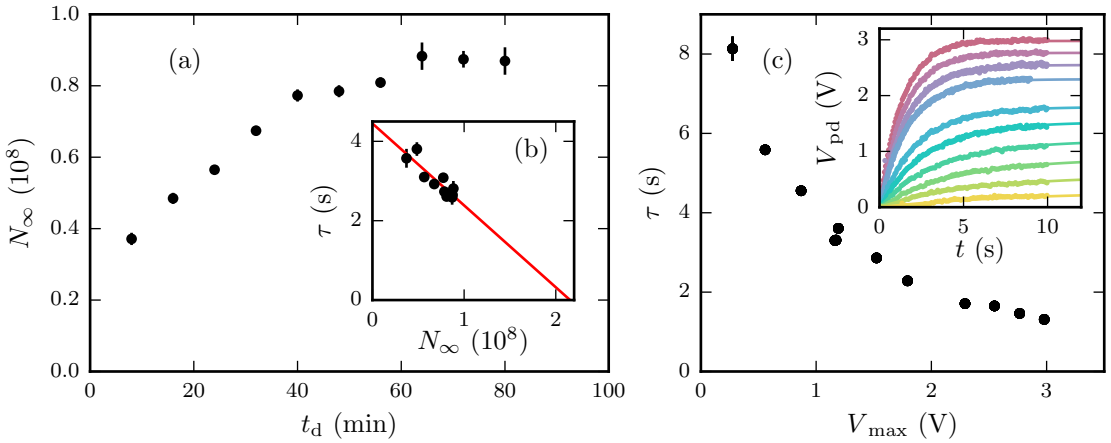

Figure 5.20: Lifetime of the type-I MOT as inferred from the loading rate. In (a) the steady-state number N_∞ of a MOT is recorded periodically as a function of time t_d after the dispensers are switched on. As the pressure increases the steady-state number increases in accordance with Eq. 5.19. At $t_d \approx 60$ minutes the partial-pressure of rubidium vapour in the chamber has reached its equilibrium value. (b) Shows the lifetime plotted against the steady-state atom number, both obtained from the data in (a). The data is fit to a straight line, as per Eq. 5.23. (c) A photodiode monitors the fluorescence from a MOT as it is loaded. The photodiode voltage V_{pd} is proportional to the atom number in the MOT. The loading curves shown in the inset are obtained by varying the trap intensity as the vapour pressure is kept constant. The loading time and steady-state atom number, expressed through the maximum photodiode voltage V_{max}, are obtained from the loading curves shown in the inset. As the intensity increases the loading rate increases, but the trap lifetime is shortened by intra-trap collisions between atoms.

5.6.2 Experimental results - type-I MOT

When the two-body loss rate can be neglected the rate equation for the number of trapped atoms is given by Eq. 5.17. The steady-state value for the trapped-atom number, N_∞ and the loading time for the trap τ are given in Eq. 5.19. Using these expressions to eliminate the dependence on the partial-pressure of rubidium vapour in the chamber, one obtains,

$$\tau = \frac{1}{\zeta P_{bg}}\left(1 - \frac{\xi}{\nu}N_\infty\right) \equiv \frac{1}{\gamma}\left(1 - \frac{\xi}{\nu}N_\infty\right). \tag{5.23}$$

The loss rate due to collisions with nonrubidium species is $\gamma = \xi P_{bg}$. The maximum lifetime obtainable in a particular set up is given by $\tau_{max} = 1/\gamma$. Fig. 5.20 shows some data obtained for the loading rate and steady state number of atoms trapped in the type-I MOT. Fig. 5.20(a) shows how the steady-state number increases during the time after the rubidium dispensers are switched on. Fig. 5.20(b) shows how the loading time for the MOT varies with the steady-state number of trapped atoms, for the data shown in the main panel. The data is taken for a fixed laser intensity and detuning. If two body collisions were neglected the data suggests that the longest

lifetime obtainable for the type-I MOT in this experimental set up is ~4.5 s, which occurs at the lowest partial-pressures of rubidium and is given by the y-intercept in (b). The largest MOT that could be loaded has $N_\infty \simeq 2.2 \times 10^8$. Fig. 5.20(c) shows how N_∞ and τ vary with the intensity of the MOT light. For these measurements the loading curves are recorded by monitoring the fluorescence of the MOT using a photodiode. The photodiode voltage is proportional to the number of atoms in the MOT, $V_{\rm pd} \propto N(t)$. As the intensity is increased N_∞ increases and τ decreases. The number of trapped atoms increases because the rate at which atoms are captured from the vapour increases with intensity. The loading rate, and equivalently the lifetime of the trap, decreases because the density more quickly reaches a point where the two-body loss rate dominates. To see why this is the case consider the following. In the absence of intra-trap collisions, the rate equation for the number of trapped atoms leads to the intensity-independent loading time given in Eqs. 5.19. Consider now the effect of collisions between trapped atoms as a MOT is loaded. These introduce an additional loss rate that depends on the number of trapped atoms. As the trap fills with atoms the total loss rate becomes equal to the loading rate more quickly, and consequently the steady-state atom number is reduced. The higher the intensity, the more quickly the trap fills and the sooner the density-dependent loss-rate exceeds the one-body loss rate. Hence, the effect is more severe at higher intensities. This effect is clearly visible from the data in Fig. 5.20(c). Actually, under these conditions the loading curve is non-exponential [121], instead being governed by the solution to Eq. 5.20. In Fig. 5.20(c), however, the loading rates are extracted from a fit to an exponential growth curve. The loading time of the trap is closest to that set by one-body processes when the intensity is lowest, which is where the best estimate for $\tau_{\rm max} = 1/\gamma$ is made. From Fig. 5.20(c) the pressure-limited lifetime is at least 8 s for the particular rubidium partial pressure present.

5.6.3 Preliminary results - type-II MOT

Fig. 5.21 shows the lifetime of atoms trapped in the blue-detuned MOT. In the figure, two sets of data are shown. The data represented by the filled markers was taken soon after the first blue-detuned MOT was realised in the lab. The type-II MOT is less robust than the type-I MOT and during the course of these early measurements the MOT beams would need frequent realignment and rebalancing of powers. Later, the stability of the set up was improved by using larger beams and additional polarisation optics to minimise variations in the relative powers between beams. Once realigned the set up was much more stable and the lifetime of the MOT was improved. Data taken after these changes were made are represented by

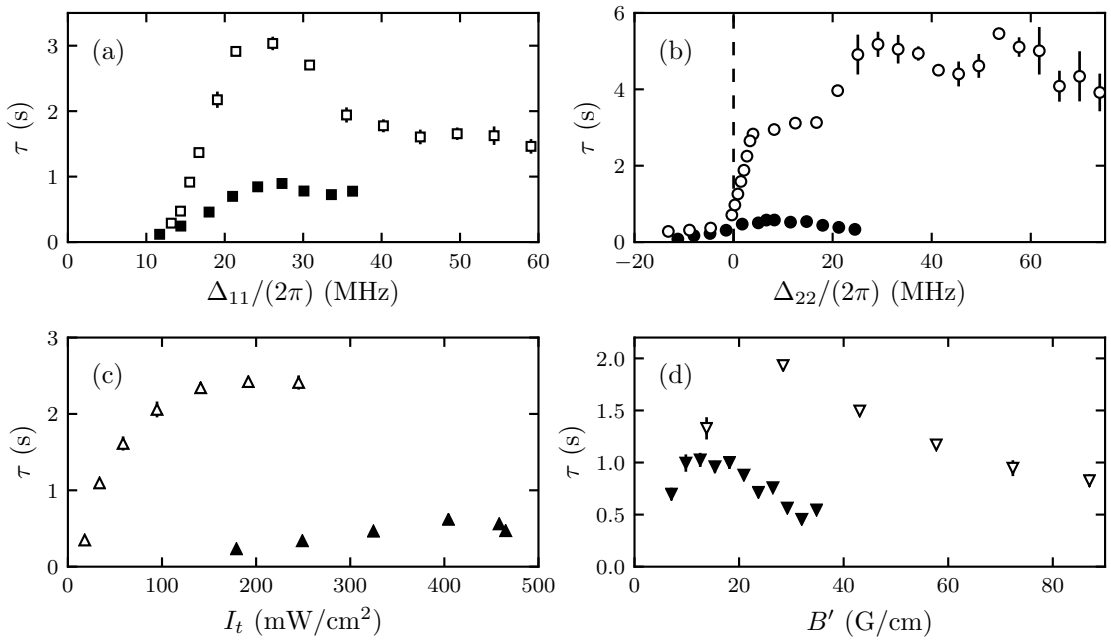

Figure 5.21: Lifetime of atoms confined in the blue-detuned MOT. Absorption imaging is used to measure the number of atoms remaining as a function of hold time. These data are fit to a single exponential decay to extract the lifetime. Two sets of data are shown. The filled markers were taken when the MOT beams had a $1/e^2$ radius of 3.6 mm. Later, the beams were enlarged to give a $1/e^2$ radius of 5.8 mm and the data represented by the unfilled markers was obtained. The other parameters are (a) $I_t = 179,280$ mW/cm^2, $\Delta_{22}/(2\pi) = 21, 11.5$ MHz and $B' = 24, 88$ G/cm. (b) $I_t = 465,280$ mW/cm^2, $\Delta_{11}/(2\pi) = 19, 36$ MHz and $B' = 14, 88$ G/cm. (c) $\Delta_{11}/(2\pi) = 19, 36$ MHz, $\Delta_{22}/(2\pi) = 14, 11.5$ MHz and $B' = 14, 88$ G/cm. (d) $I_t = 465,320$ mW/cm^2, $\Delta_{11}/(2\pi) = 19, 19$ MHz and $\Delta_{22}/(2\pi) = 6, 10$ MHz. The first value in each pair corresponds to the filled markers and the second to the unfilled markers.

the unfilled markers in Fig. 5.21.

To obtain these data absorption images are recorded of the number of atoms remaining in the trap after a variable hold time. A sequence of absorption images is used to extract the decay of the number of atoms remaining as a function of time. These data are fit to an exponential decay to extract the lifetime of the trap. This model is obtained from the solution to equation Eq. 5.17, with the loading rate set to zero. This solution does not capture information about the density-dependent loss rate in the trap, but this is addressed later on. There are a number of interesting features in the figure. Fig. 5.21(a) shows the lifetime as the detuning of the $F = 1 \rightarrow F' = 1$ laser is varied. The longest lifetimes are obtained for $\Delta_{11}/(2\pi) \simeq +25$ MHz, which is significantly larger than the detuning typically used in the type-I MOT. Fig. 5.21(b) shows similar data, obtained as Δ_{22} is varied. A MOT is formed for both positive and negative detuning, but the lifetime is much shorter when $\Delta_{22} < 0$. For positive detuning $\Delta_{22}/(2\pi) \gtrsim +5$ MHz the lifetime is insensitive to the detuning, while for $\Delta_{22}/(2\pi) \gtrsim +20$ MHz the lifetime is long, but

the trapped atoms are observed to form a diffuse, weakly-confined cloud. Fig. 5.21(d) shows the lifetime as a function of the magnetic-field gradient in the MOT. For both sets of data the lifetime first increases, reaches a maximum, and then decreases with increasing field gradient. For the larger MOT beams the maximum lifetime occurs at $B' \simeq 27$ G/cm and decreases to less than half this maximum value by $B' \simeq 80$ G/cm. These data strongly suggest that the density-dependent loss rates are significant in the blue-detuned MOT, especially at higher field gradients.

The blue-detuned MOT is well suited to studying collisions as the loading rate of atoms from the background vapour must be extremely small. This allows the loss rates to be measured directly, rather than being inferred from the steady-state density of atoms as would be the case for the type-I vapour-cell MOT.

Motivated by the desire to measure the intra-trap collisional loss rate, and to better understand the data in Fig. 5.21, improvements were made to the imaging system that increased its sensitivity. This allowed the loss rate of atoms from the trap to be measured as the trapped atom number varied by a factor of 100, during a single sequence. A more complete model, which included atom loss due to intra-trap collisions, could be fit to the data obtained using this improved imaging scheme.

5.6.4 Improving the imaging system

The difficulty in obtaining data of sufficiently high quality to extract the various contributions to the loss rate lies in the large range of trapped atom numbers for which the density must be precisely measured. To extract the one-body loss rate, which gives the maximum lifetime of the trapped atoms imposed by evaporation and collisions with untrapped atoms, the loss rates of very small numbers of trapped atoms must be measured. To extract the two-body loss rate coefficient the loss rate from traps with large numbers of atoms must be measured. Additionally, the density distribution of the trapped atoms must be known. This is more difficult to obtain than just a measurement of the total number of atoms remaining and required the imaging system to be improved.

Fig. 5.22(a) shows the visibility of the atoms in the type-II MOT to the imaging light. The detuning of the $F = 1 \rightarrow F' = 2$ laser is fixed at $\Delta_{11}/(2\pi) = 19$ MHz and Δ_{22} is varied. When $|\Delta_{22}| < |\Delta_{11}|$ the rate of optical pumping from $F = 2$ is higher than from $F = 1$, and atoms accumulate in $F = 1$. Here, they do not interact with the imaging light. For typical values of Δ_{11} and Δ_{22} the population in $F = 2$ can be <10%, which imposes a lower limit on how many atoms can be imaged. This makes the loss rate due to one-body processes difficult to measure because the number of trapped atoms must be small for these to dominate. To counteract the optical pumping into the lower hyperfine ground state, light is taken from the $F = 1$

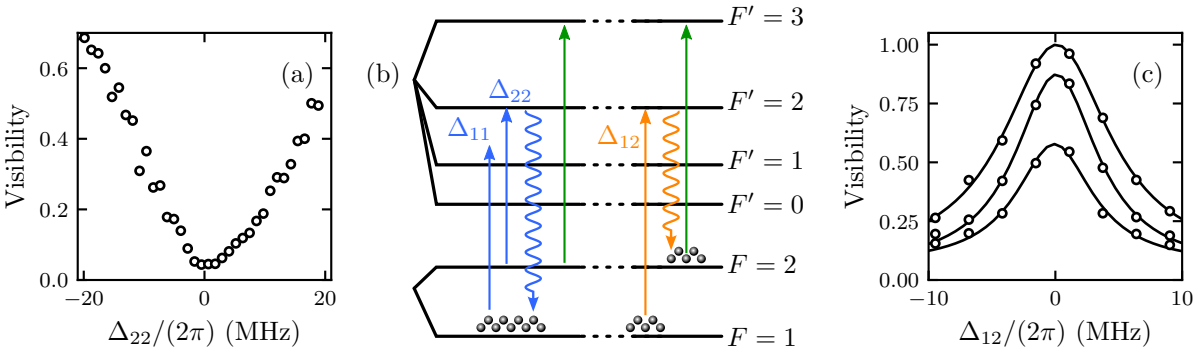

Figure 5.22: Improved imaging scheme. (a) Visibility of the atoms to the imaging light, shown in green in (b), as a function of Δ_{22} used in the MOT. As $|\Delta_{22}| \to 0$ most of the population is in $F = 1$ and the visibility decreases. In (a) $\Delta_{11}/(2\pi) = +19$ MHz. (b) To increase the visibility a brief pulse of light, detuned by Δ_{12} from the $F = 1 \to F' = 2$ transition, optically pumps atoms from $F = 1$ to $F = 2$ prior to imaging. (c) Shows the effect of varying Δ_{12} and the duration of the optical pumping. The three curves correspond to three different optical pumping times: 10 µs, 20 µs and 50 µs.

laser, double passed through an AOM and coupled into the same optical fibre as the imaging light. The light can be tuned to be resonant with the $F = 1 \to F' = 2$ transition. Once released from the MOT atoms are briefly illuminated with this light, which pumps them into $F = 2$. The absorption image is recorded immediately after the optical-pumping light is switched off. Fig. 5.22(c) shows the effect of varying the detuning and exposure duration of the optical pumping light on the visibility of the atoms recorded in the absorption images.

5.6.5 Results - type-II MOT

The improvements to the imaging scheme allow a greater range of atom numbers to be imaged. In turn, this allows for the density-dependent and density-independent loss rate coefficients to be determined more precisely. The rate equation governing the number of atoms in the type-II MOT is

$$\frac{dN}{dt} = -\gamma N - \beta \int n^2(\mathbf{r}, t) d^3r. \tag{5.24}$$

The atom density distribution in the blue-detuned MOT is Gaussian,

$$n(x, y, z) = n_0 \exp\left(-\frac{x^2}{2\sigma_x}\right) \exp\left(-\frac{y^2}{2\sigma_y}\right) \exp\left(-\frac{z^2}{2\sigma_z}\right), \tag{5.25}$$

where n_0 is the peak density at the centre of the trap. Substituting the explicit form for the density distribution given by Eq. 5.25 into Eq. 5.24 and evaluating the

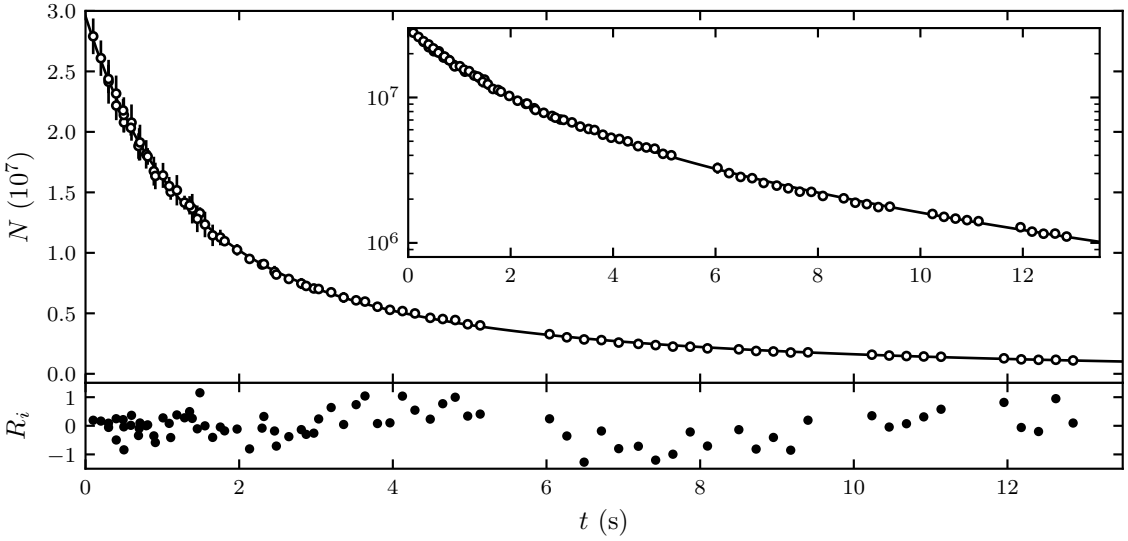

Figure 5.23: Number of atoms remaining in the trap as a function of hold time. The laser parameters are $\Delta_{11}/(2\pi) = +26$ MHz, $\Delta_{22}/(2\pi) = +12$ MHz, $B' = 48$ G/cm and $I_t = 240$ mW. The data is fit numerically to Eq. 5.28. The inset shows the same data on a log scale. At short times the enhanced loss rate due to intra-trap collisions is clearly visible as a steeper gradient. The fit gives $\beta = 1.94(3) \times 10^{-10}$ cm^3 s^{-1} and $\gamma = 0.075(3)$ s^{-1}. This value implies a background-pressure-limited lifetime of $\tau = 1/\gamma = 13.3(5)$ s. The lower panel shows the residuals R_i from the fit to the data, which have been normalised to the error associated with each of the points.

resulting integral gives

$$\frac{dN}{dt} = -\gamma N - \beta n_0^2 \pi^{3/2} \sigma_x \sigma_y \sigma_z. \tag{5.26}$$

In Sec. 5.3 data is presented for the peak density of atoms in the type-II MOT as a function of the atom number. The data are well described by a function,

$$n_0(N) = \frac{N}{V(N)} = \frac{N}{V_0 + \frac{N}{n_{\max}}}, \tag{5.27}$$

where the volume for a given atom number, $V(N) = (2\pi)^{3/2} \sigma_x \sigma_y \sigma_z$. Substituting these into Eq. 5.26, the following expression is obtained,

$$\frac{dN}{dt} = -\gamma N - 2^{-3/2} \beta \frac{N^2}{V_0 + \frac{N}{n_{\max}}}. \tag{5.28}$$

Fig. 5.23 shows data fitted to the solution of Eq. 5.28. The data are obtained in two steps. First, a series of images are taken of the blue-detuned type-II MOT as the number of atoms is varied. Both the atom density distribution in the MOT and total atom number are recorded and the resulting data are fit to Eq. 5.27 to obtain V_0 and $n_{\max}$. Next, the type-II MOT is loaded with the same laser parameters and field

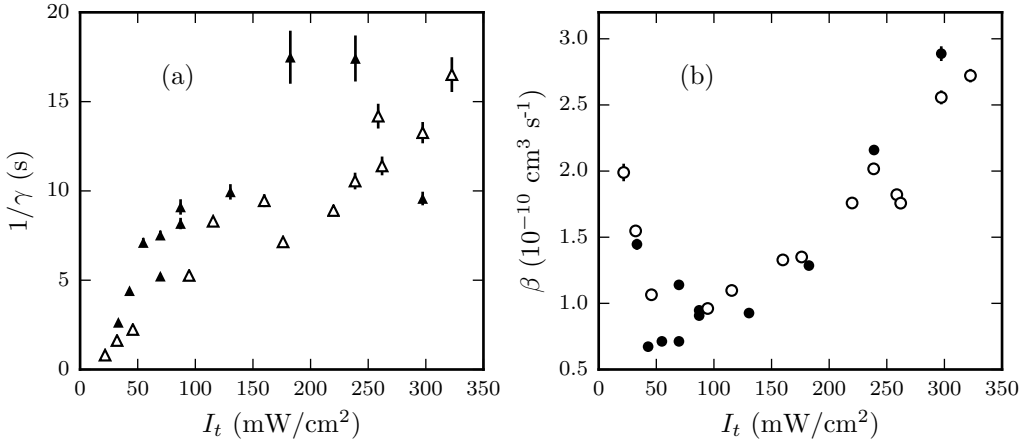

Figure 5.24: Rate coefficients for trap loss due to one body and two body processes as a function of trap laser intensity. (a) Shows the one-body loss rate coefficient expressed as a lifetime $\tau = 1/\gamma$. This is the lifetime at low atom number densities and is due to collisions with untrapped atoms or evaporation from the trap. (b) Shows the density-dependent two-body loss rate coefficient β. The coefficients are obtained by the method outlined in the text and illustrated in Fig. 5.23. The data represented by the solid markers is obtained with $\Delta_{11}/(2\pi) = +26$ MHz and $\Delta_{22}/(2\pi) = +18$ MHz. Data represented by the hollow markers is obtained for $\Delta_{11}/(2\pi) = +26$ MHz and $\Delta_{22}/(2\pi) = +12.5$ MHz.

gradient and the number of atoms remaining as a function of hold time is recorded. The data are fit numerically to the solution of Eq. 5.28 in order to extract β and γ. The inset panel of the figure shows the same data plotted on a logarithmic scale. If the trap loss was due to one-body processes the data would describe a straight line. Instead, at short times the gradient is steeper, which is indicative of an enhanced loss rate due to intra-trap collisions. At the longest times these become negligible and the curve becomes a straight line with gradient $-\gamma$.

Fig. 5.24 shows the loss rate coefficients measured for a variety of total trap laser intensities. Two sets of data are combined, each with a different laser detuning. The laser detuning and magnetic-field gradient remain fixed within each set of data. Fig. 5.24(a) shows the reciprocal of the one-body loss rate γ. This is the limiting lifetime of the trap $\tau = 1/\gamma$, which is due to collisions with untrapped atoms and evaporation. Fig. 5.24(b) shows the loss rate coefficient for two-body processes. As discussed in the preceding sections, there are multiple mechanisms that contribute to β. These include hyperfine-state-changing collisions between ground-state atoms, and light-assisted collisions that can lead, in a conventional MOT, to fine-structure-changing collisions and radiative escape.

There are a number of intriguing features of Fig. 5.24. Fig. 5.24(a) shows the small-n lifetime of the type-II MOT. As the intensity is increased there is a clear increase in τ, with an approximately linear relationship. Previous studies of the one-body loss rate for type-I MOTs have noted that this loss rate has only a very

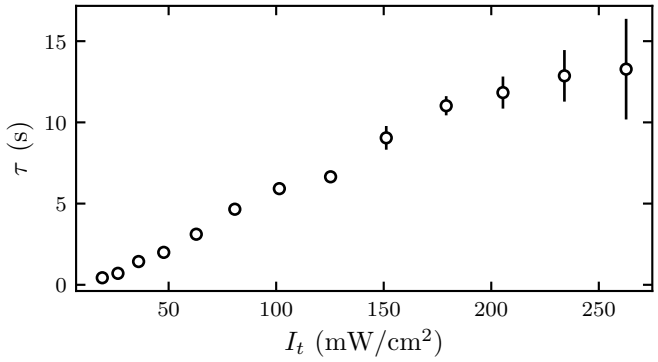

Figure 5.25: Measurements of the trap lifetime made using small numbers of atoms. The blue-detuned MOT is loaded with a small number of atoms, so that the two-body loss rate is minimised. The lifetime is extracted from a fit to a single exponential. The same trend, which is roughly linear, in the limiting lifetime is observed as from the data in Fig. 5.24. The other parameters are $\Delta_{11}/(2\pi) = +26$ MHz, $\Delta_{22}/(2\pi) = +11.5$ MHz and $B' = 87$ G/cm.

weak dependence on the trap laser intensity [108]. The reason for this is that the temperature of the untrapped atoms is so much greater than the trap depth of a MOT that even a glancing collision, in which a small fraction of the incident atom's kinetic energy is imparted to the trapped atom, would be sufficient to lead to trap loss. The trap depth of the type-II trap is known to be far lower and so one could reasonably surmise that the low-density lifetime should be even more insensitive to the intensity of the trap laser. It might be expected that the lifetime is related to the fraction of atoms in the excited state. A previous investigation using a dark-SPOT concluded that the cross section for collisions with untrapped atoms was approximately three times higher for a trapped atom in its excited state, when compared to a trapped ground-state atom [119]. In that case the lifetime should decrease as the fraction of excited-state atoms increases, the exact opposite of what is observed here. One interesting possible explanation of the observed behaviour of the lifetime is that there is a kind of optical shielding effect between trapped and untrapped atoms. This could act to 'soften' the impact parameter of the collision, reducing the energy imparted to the trapped atoms and leading to a reduction in the loss rate. A more comprehensive theoretical consideration is needed to add credibility to such an idea. One clear experimental signature of such an effect is that it would be ineffective when the background gas composition was dominated by species other than Rb. Direct measurements of the loss rates of traps with small numbers of atoms have also been performed to verify the behaviour of the one-body loss rate coefficient presented in Fig. 5.24(a). For these measurements the trapped atom number is sufficiently small that two-body losses contribute negligibly to the total trap-loss rate. These data are presented in Fig. 5.25.

Fig. 5.24(b) shows the density-dependent loss rate coefficient as a function of in-

tensity. Similar measurements to those presented here have been made in numerous type-I atomic MOTs. A few examples also exist of measurements of the loss rate coefficients for type-II traps. The behaviour of β in Fig. 5.24(b) is dissimilar to all the measurements reported for those MOTs.

First consider the magnitude of β across the whole range of trap laser intensities measured. Values for the density-dependent trap-loss rate coefficients measured for a type-I rubidium MOT lie in the range $10^{-13} - 10^{-10}$ cm^3 s^{-1}, depending on the trap laser intensity and detuning [111, 113]. In all type-I atomic MOTs the highest loss rates occur at low trap intensities, where the energy released by a ground-state hyperfine-changing collision is sufficient to eject an atom from the trap. In the blue-detuned MOT the capture velocity is limited to the narrow range of velocities over which sub-Doppler cooling is efficient. It is therefore reasonable to expect that ground-state hyperfine-changing collisions remain effective at ejecting atoms from the trap over a far greater range of trap intensities than in the type-I MOT[1]. Since these processes lead to the highest trap-loss rates in type-I MOTs a significant contribution to the loss rate measured here might be due to collisions between ground-state atoms. Supposing that is the case, the observed variation of β, which is related to the cross section for the collision and the velocity distribution of the atoms by $\beta = \langle \sigma(v)v \rangle$, might be due to the increased temperature of the atoms at higher intensities. The loss-rate coefficient for these collisions in ^{87}Rb has previously been measured to be $\beta = 2 \times 10^{-11}$ cm^3 s^{-1} at low trap intensities and a detuning $\Delta/(2\pi) = -4.9$ MHz in [111]. At low intensity but higher detuning the rate was measured to be $\beta > 10^{-10}$ cm^3 s^{-1} [113]. The minimum value measured here is about five times higher than in [111], but comparable to that reported in [113], where the detuning is larger. In the trapping scheme used in this investigation, however, most of the atoms are in the lower hyperfine-ground state, where inelastic collisions are energetically forbidden. It therefore does not seem likely that these collisions are the sole contribution to the loss rates measured here, unless they are somehow enhanced by the trapping scheme.

A flux-enhancement effect that increases the trap-loss-coefficient has previously been reported in [115]. This effect is facilitated by multiple laser frequencies, which can lead to multiple excitations occurring during a collision. After each excitation to a molecular bound-state, the pair of atoms accelerate towards their common centre of mass. The pair are more likely to approach very small distances, where inelastic collisions can occur, when there are multiple excitations during a collision. The enhancement factor η of the loss rate is observed to increase as the detuning of the

[1] cf. Sec. 5.7, where measurements of the capture velocity are presented. It is concluded that the capture velocity is sufficiently small over the entire range of trap laser intensities that ground-state collisions should lead to trap loss.

probe laser is made more negative and increase with the probe laser intensity. For a probe detuning of $\Delta/(2\pi) = -1$ GHz and intensity of 8 mW/cm^2 the enhancement factor is observed to be $\eta = 3$. Here, there are two high-intensity trapping lasers addressing the two hyperfine ground states. The detuning of the $F' = 2$ laser relative to atoms in $F = 1$ is -6.8 GHz. It could be that the arrangement used in this experiment leads to a flux-enhancement effect of ground-state inelastic collisions, which is why the trap-loss coefficient measured here is significantly higher. A detailed theoretical consideration has not yet been undertaken so this is merely a suggestion.

For total trap laser intensities $I_t \gtrsim 100$ mW/cm^2 β increases with the trap intensity. The increasing value of β with trap laser intensity could implicate excited-state atoms in the collision mechanisms leading to trap loss. Inelastic collisions involving excited state atoms proceed via the radiative escape or fine-structure-changing mechanisms. These collisions can be initiated by excitation to an attractive molecular potential by the MOT light. In this experiment the light is blue-detuned so long-range excitation should occur primarily to repulsive potentials. It has been shown that similar conditions can lead to a suppression of inelastic collisions between ground-state atoms [120]. This is known as optical-shielding and the principle is illustrated in Fig. 5.19. The values measured for β in the blue-detuned MOT seem to preclude an optical shielding effect. Optical shielding may be ineffective in the blue-detuned MOT because the light is not blue-detuned from the entire excited-state manifold. Previous investigations have noted that the hyperfine structure of the excited state can lead to significant modification of the trap-loss spectrum [122, 123] and a rigorous theoretical treatment is formidable [124]. Instead of shielding atoms from inelastic collisions, for some range of inter-atomic separations and laser detuning, excitation may instead occur to attractive potentials that asymptotically correspond to $F' = 3$ or $F' = 2$. In [122] a catalysis laser is used to induce trap loss from a MOT. The resulting spectrum of β shows a sharp peak at a catalysis laser detuning $\Delta/(2\pi) \sim -266$ MHz relative to the $F = 2 \rightarrow F' = 3$ transition in ^{87}Rb, close to the detuning of the $F = 2 \rightarrow F' = 2$ laser typically used in the blue-detuned MOT. This could suggest that inelastic collisions between excited and ground state atoms might be strongly induced, rather than suppressed, by the trap light.

Despite the density and complexity of molecular-state potentials, the long-range interaction between ground and excited-state atoms remains well described by a repulsive dipole-dipole interaction. It is appealing to consider the possibility that by manipulating the trap laser detuning or intensity that inelastic collisions might be suppressed. This would represent a major advantage to the use of a blue-detuned type-II MOT over a conventional trapping arrangement.

In Fig. 5.26 β is measured as a function of trap laser detuning. There is a general

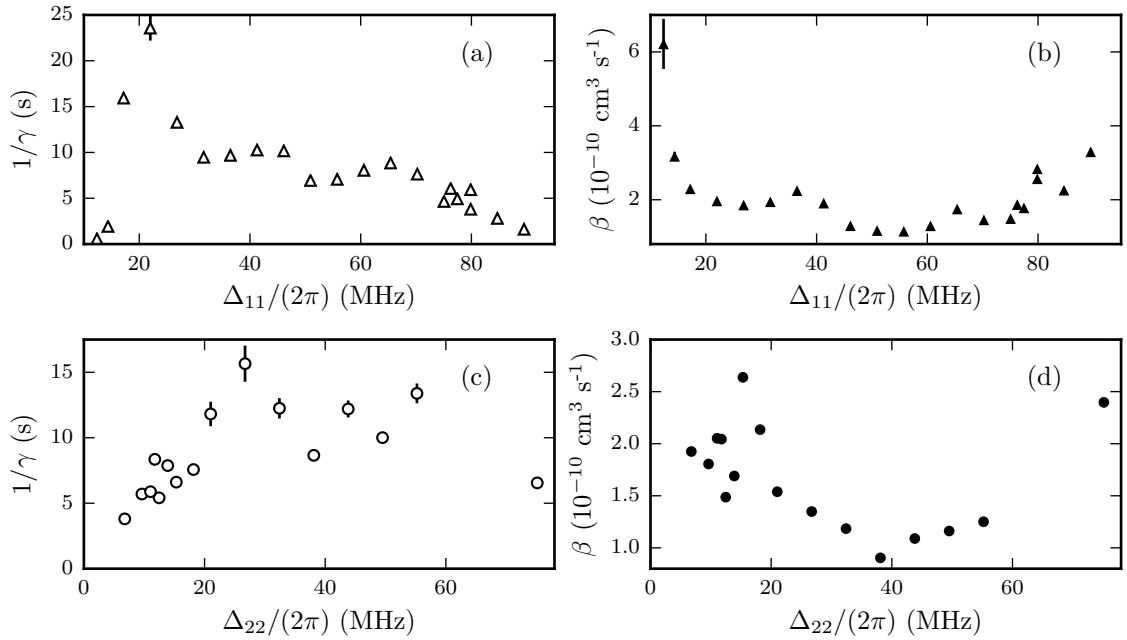

Figure 5.26: Loss-rate coefficients as a function of trap laser detuning. In (a) and (b) $I_t = 215$ mW/cm^2 and $\Delta_{22}/(2\pi) = 11.5$ MHz. In (c) and (d) $I_t = 350$ mW/cm^2 and $\Delta_{11}/(2\pi) = 26$ MHz. (a) and (c) show the one-body loss rate coefficient, expressed as a trap lifetime $\tau = 1/\gamma$. (b) and (d) show the two-body loss-rate coefficient.

trend for β to decrease as the detuning is increased. As many previous investigations have noted these trap-loss spectra are difficult to interpret because the trap depth is also changing. The trap-loss coefficient is the product of the rate at which a particular collision occurs and the probability that, having occurred, the products of the collision will be ejected from the trap. Fig. 5.26 (b) shows β as a function of Δ_{11}, and (d) shows β as a function of Δ_{22}. For both parameters the value of detuning that minimises β is significantly higher than is used to achieve good confinement in the MOT. If the reduction in β is due to optical shielding it may be that further improvements could be made by using multiple frequencies, some of which provide confinement and some of which act as suppression lasers.

5.6.6 Discussion

Throughout this section comparisons have been made to similar measurements reported for type-I atomic MOTs. When compared to existing type-II atomic MOTs the loss rates reported here compare favourably. In [114] a type-II sodium MOT is formed using the $F = 2 \rightarrow F' = 2$ and $F = 1 \rightarrow F' = 2$ transitions of the D1 line. At laser intensities comparable to those investigated here, the trap-loss rate coefficient is as high as 4×10^{-9} cm^3 s^{-1}. In [45] a red-detuned type-II MOT of ^{85}Rb is reported, which operates on the $F = 2 \rightarrow F' = 1$ transition. The density-

dependent loss rate coefficient reported for that trap is $\beta = 9.1(7) \times 10^{-9}$ cm^3 s^{-1}, about 90 times larger than the value measured here. Such high loss rates have never been observed for a type-I MOT, even at the lowest laser intensities where every collision ejects the atoms[1]. This is likely to be due, at least in part, to the high temperature of red-detuned type-II MOTs, which can easily exceed those measured in type-I MOTs by a factor of ~100. The associated increase in $\langle v \rangle$, and hence β, is a factor of 10. The high loss rate could also imply that collisions between ground and excited-state atoms contribute significantly to the values of β reported for the red-detuned type-II MOTs. Since the properties of the trap reported in [45] and [114] are expected to be comparable to the properties of the trap reported here, given the their common type-II nature, this may suggest that some form of optical shielding is indeed occurring in the blue-detuned MOT.

The minimum value of β measured for the blue-detuned MOT is 200 times larger than that reported for type-I MOTs of the same atomic species operating with $\Delta \sim \Gamma$. Comparable loss rates are obtained for type-I traps operating at similar detuning to that used here. These loss rates are attributed to ground-state hyperfine-changing collisions. In the next section, measurements made of the capture velocity of the MOT are presented. These measurements support the proposition that a major contribution to the trap loss could be due to collisions between ground state atoms. In order for the blue-detuned MOT to perform favourably when compared to the type-I MOT these ground-state collisions must be suppressed. This might be achieved by changing the geometry of the beams to increase the capture volume, using a higher laser intensity or by a more exotic method such as optical shielding. A more flexible investigation into the behaviour of β could separate the roles of trap laser and suppression laser, in which case strong confinement might simultaneously be achieved with suppression of inelastic collisions, though this is purely speculative. On the other hand the presence of dark states may actually inhibit any optical shielding effect. The blue-detuned MOT might perform better when applied to ^{85}Rb, where the ground-state hyperfine splitting is about half the value in ^{87}Rb. The capture velocity of the MOT would then be similarly relaxed in order to recapture the energetic products of these inelastic ground-state collisions.

In the final chapter presented in this thesis, observations of MOTs operating in a number of different trapping configurations are presented. One of these configurations uses light tuned to the $F = 1 \rightarrow F' = 1$ and $F = 2 \rightarrow F' = 1$ transitions. Under these conditions, the population is even more concentrated in $F = 1$, where exoergic inelastic ground-state collisions are forbidden. The loss rate for intra-trap collisions has not yet been measured for this configuration, but such a measurement would complement the material presented in this chapter. If the predominant loss

[1] At the lowest intensities β is observed to become constant as the intensity is further reduced.

mechanism is due to these collisions then the lifetime of atoms in this alternative trapping configuration might significantly exceed the values measure to date.

5.7 Measuring the capture velocity of the blue-detuned MOT

In the previous section, measurements of the lifetime of atoms in the blue-detuned MOT were presented. When the density of atoms is high, the loss rate due to intra-trap collisions is many times higher than the loss-rate due to collisions with untrapped atoms or due to evaporation from the trap. The loss-rate coefficient for intra-trap collisions has been measured for a range of trap parameters and is found to have values in the range $0.5 - 3.0 \times 10^{-10}$ cm^3 s^{-1}, which is generally higher than the values measured in type-I MOTs [113], but significantly lower than that previously reported for red-detuned type-II atomic MOTs. Knowledge of the capture velocity of the trap can help to understand the origin of the high intra-trap collisional loss rate. Quantitative measurements of the capture velocity allows the exclusion or admission of various types of inelastic collision between trapped atoms that can lead to trap loss, on the basis of energy considerations.

In this section the methods used to obtain measurements of the capture velocity of the MOT are described. The experimental sequence used for these measurements is the most technically demanding that has been implemented in the course of the investigation. Performing these measurements required the addition of a push beam, used to impart velocity to the atoms, and a state-preparation scheme used to optically pump atoms into the state that interacts most strongly with the push beam. The push beam is resonant with the $F = 2 \rightarrow F' = 3$ transition and circularly polarised to drive the cycling transition, as is the imaging light. The state-preparation beam is required as most of the steady-state population of atoms in the blue-detuned MOT, which is loaded before atoms are launched, are in the $F = 1$ hyperfine ground state and are not sensitive to the push beam.

5.7.1 Methods

The experimental set-up used for these measurements, including the push-beam and state-preparation beam is illustrated in Fig. 4.22 of Chap. 4. The light used for the push beam emerges from an optical fibre, is collimated and then enters the vacuum chamber through the back window, the same as is used to monitor the MOT fluorescence on a CCTV camera. A PBS cube is used to direct the beam into the chamber so that the CCTV camera can be simultaneously used to monitor the fluorescence. Just before entering the chamber the beam is circularly polarised

by a quarter-wave-plate. The two pairs of bias coils along the radial axes of the MOT are driven by a single FET and arranged to produce a magnetic field that is homogeneous near the centre of the trap and aligned along the axis of the push beam. This arrangement of magnetic-field bias coils gives the flexibility to load the blue-detuned MOT at different displacements along the push-beam axis. In turn, this allows for atoms accelerated by different amounts by the push beam to have the same initial displacement when the blue-detuned MOT is switched back on and the number of atoms re-captured measured. As has been mentioned in previous chapters, atoms in the blue-detuned MOT are extremely sensitive to the alignment and relative intensities of the MOT beams. Small imbalances in intensities or slight misalignments can lead to prohibitively short lifetimes. As the MOT is loaded at increasing displacement from the trap centre, the lifetime of the trapped atoms is shortened. Displacements of up to 1 mm or so are possible without adversely affecting the lifetime, which is sufficient to account for the range of positions of atoms accelerated up to about 6.7 m/s at the time when the push beam is switched off and the MOT is switched back on. The experimental set up described here has been illustrated previously in Fig. 4.22.

To begin the experimental sequence, atoms are loaded into the type-I MOT and transferred to the blue-detuned type-II MOT in the usual fashion. Some time is allowed to elapse, typically 100 ms, to allow the atoms to equilibrate. Once the atoms have settled, the MOT light is quickly extinguished using an AOM.

The atoms are then prepared in the $F = 2$ ground state. Some light from the $F = 1$ laser is double-passed through an AOM (AA Optoelectrics MT110-B50A1-IR) using an arrangement identical to that used for the imaging light, depicted in Fig. 4.19 of Sec. 4.5. The alignment of the AOM is adjusted to maximise the amount of light in the +1-order mode and the frequency of the AOM is tuned so that the double-passed light is resonant with the $F = 1 \rightarrow F' = 2$ transition. This light is coupled into the same single-mode fibre as the imaging light and is shown in Fig. 4.19. Prior to being launched by the push beam, atoms are illuminated by light resonant with the $F = 1 \rightarrow F' = 2$ transition, which optically pumps them into $F = 2$.

The light used in the push beam is derived from the reference laser. A double passed AOM setup is used, identical to that used for the imaging light, to obtain light resonant with the $F = 2 \rightarrow F' = 3$ transition. This light is coupled into a polarisation-maintaining, single-mode optical fibre and sent to the vacuum chamber. The light is collimated by a 50 mm focal-length lens. The beam profile at the position of the MOT is approximately Gaussian with a $1/e^2$ radius of 4.4(2) mm, estimated by fitting the data in Fig. 5.28(c) to a Gaussian function. A PBS cube is used to centre the push beam on the MOT. The light is circularly polarised by a

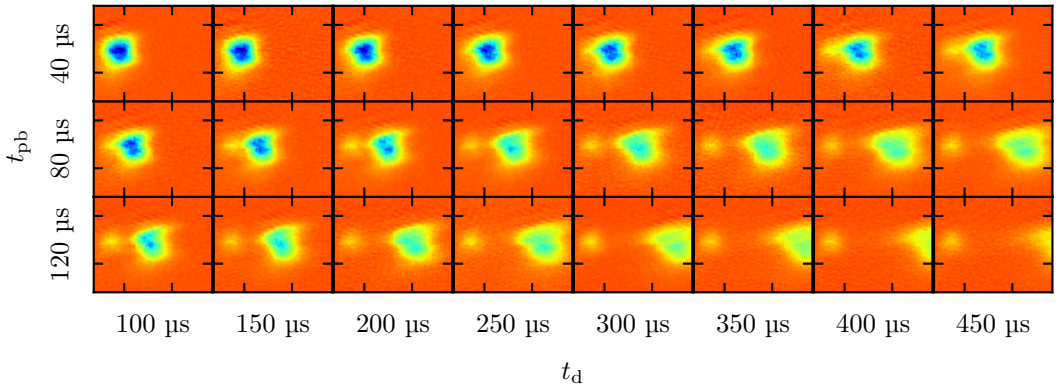

Figure 5.27: Preparing and launching atoms from the MOT. Atoms are released from the blue-detuned magneto-optical trap and illuminated with optical-pumping light resonant with the $F = 1 \rightarrow F' = 2$ transition, causing population to accumulate in $F = 2$. After 100 µs the optical pumping light is switched off and the push-beam light, resonant with the $F = 2 \rightarrow F' = 3$ transition, is switched on for a duration t_{pb}. Atoms are imaged after a delay t_d. A sequence of images recorded at various t_d are used to calibrate the velocity distribution of the atoms. The k-vector of the push beam is in the horizontal direction. Here, the state-preparation is incomplete, and some atoms remain in $F = 1$ when the push-beam is switched on. These atoms are not launched and are visible as a small, stationary cloud that provide a point of reference across the images.

quarter-wave-plate just before entering the chamber through the rear view-port.

Once prepared in the $F = 2$ state the atoms are illuminated by the push beam. The velocity imparted to the atoms can be controlled by varying the duration for which atoms are exposed to the push beam. A sequence of absorption images of the atoms is recorded in flight to measure the velocity imparted along the axis of the push beam. The field of view of the CCD camera is about 8 mm along the axis of the push beam at the position of the MOT and the velocities imparted are up to about 10 m/s, limiting the duration for which the atoms are within the field of view to about 100 µs at the highest velocities. For an accurate calibration of the velocity it is necessary to have a short exposure time, allowing the centre of mass of the atom cloud to be recorded at multiple intervals before leaving the field of view. As the exposure time is reduced the intensity of the imaging light is increased to maintain a good signal on the CCD. At the shortest exposure times, where the intensity of the imaging beam is highest, the intensity remains well below the saturation intensity. It is difficult to simultaneously obtain good fibre-coupling efficiencies for both the imaging light and the state-preparation/optical-pumping light and as a result the intensity of optical pumping light at the position of the MOT is rather small. The optical-pumping time required for a complete population transferral to $F = 2$ is measured to be about 100 µs, when the light is on-resonance.

To calibrate the velocity imparted to the atoms by the push beam a sequence of absorption images are recorded of the atoms in flight after the push beam is

switched off. A set of these images are shown in Fig. 5.27. Three different sequences are shown. For each sequence the push beam is on for a different time, and it is seen that longer exposure times launch the atoms to higher velocities. For the images in the figure the preparation of atoms in $F = 2$ before the launch is incomplete. Atoms remaining in $F = 1$ do not interact with the push beam. These are visible as a small cloud that remains stationary at the position of the MOT as the remaining atoms move away.

The images are integrated along the axis of the detector that is perpendicular to the motion of the atoms, and a Gaussian distribution is fit to the one-dimensional data. Some distributions obtained from absorption images in this way are shown in Fig. 5.28(a). The centre-of-mass of the atoms along the push-beam axis is extracted from the fits to the one-dimensional atom density distributions. The centre-of-mass is then plotted as a function of flight time to obtain a measurement of the velocity of the atoms. Some data illustrating this are given in Fig. 5.28(b). The frequency of the push beam is tuned by adjusting the frequency of the AOM in the double-pass configuration. The velocity imparted to the atoms after being illuminated by the push beam for a fixed duration is recorded as the frequency of the push beam is tuned across the $F = 2 \rightarrow F' = 3$ transition. The AOM frequency is set to maximise the velocity imparted to the atoms. Good alignment of the push beam with the MOT is obtained by adjusting the vertical and horizontal alignments using a translation stage, on which the fibre collimator is mounted, and measuring the velocity imparted to the atoms. Data obtained in the course of this alignment are shown in Fig. 5.28(c). The velocity at which atoms are launched is tuned by varying the exposure duration of the push beam. Data showing the variation in velocity with push-beam exposure duration are shown in Fig. 5.28(d). The data are fit to a simple model which assumes a two-level atom. The acceleration is due to the scattering force and takes into account the Doppler shift as the velocity of the atom increases. Atoms can be launched with velocities of up to almost 10 m/s. Obtaining higher velocities requires the atoms to be accelerated for longer durations by the push beam, which increases the displacement of the atoms at the end of the launch. At a velocity of about 7 m/s the initial displacement of the atoms is ~1 mm. The displacement accumulated during the launch can be compensated for by adjusting the initial position of the MOT using the bias coils, but for displacements $\gtrsim 1$ mm the MOT becomes unstable. The measured capture velocity of the blue-detuned MOT is always lower than this value, so this effect is unimportant.

Once prepared in the $F = 2$ state and launched by the push beam the MOT light is quickly switched back on, and atoms that are travelling slower than the capture velocity of the MOT are recaptured. The atoms that are recaptured are allowed to settle for a brief period, the MOT is switched off, and the remaining

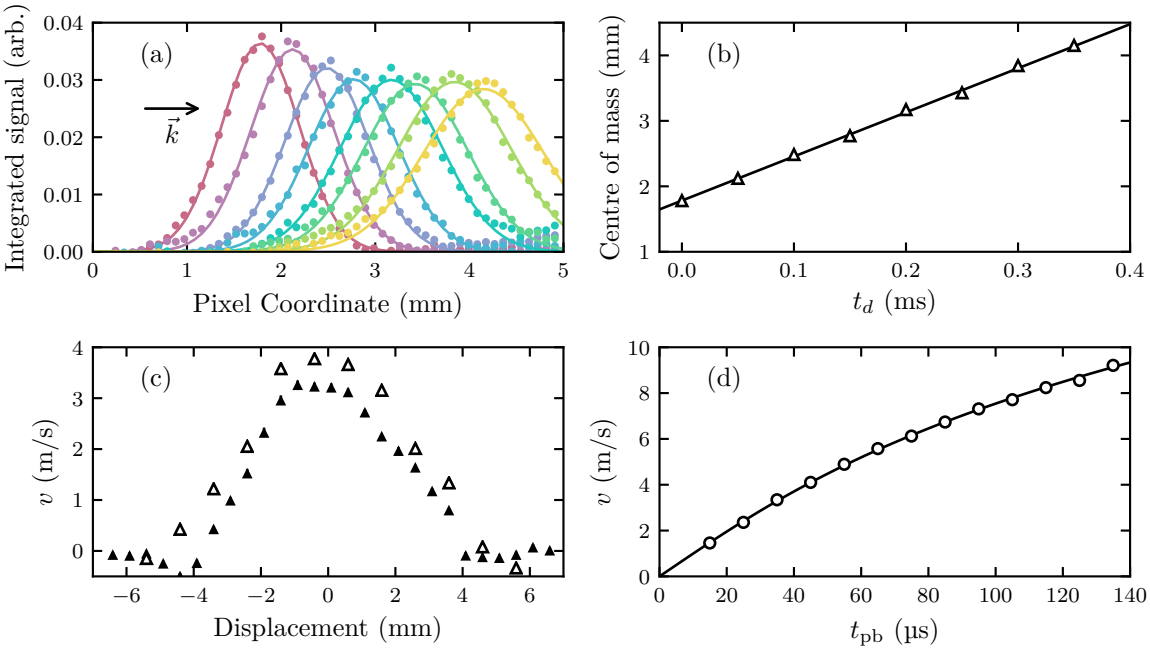

Figure 5.28: Calibrating the centre-of-mass velocity of the atoms. (a) Absorption images are recorded and integrated along the axis perpendicular to the direction of motion of the atoms to give the coloured distributions. Each distribution corresponds to a different delay time and the interval between each is 50 µs. The resulting profile is fit to a Gaussian function and the centre of mass of the distribution is extracted. (b) The centre of mass as a function of delay time t_d after the atoms have been launched. The points are extracted from the fits in (a). These data are fit to extract a velocity. Here the resulting fit gives $v = 6.74(2)$ m/s. The atoms were exposed to the push beam for $t_{\mathrm{pb}} = 90$ µs. This method is used to precisely align the push beam with the MOT. In (c) the optical fibre and collimator are translated along the two axes perpendicular to the k-vector of the light. Atoms are exposed to the push beam for a fixed duration. When the push-beam is well overlapped with the centre of the MOT the velocity imparted to the atoms is highest. (d) Velocity of the centre of mass of the atoms as a function of push beam exposure duration. The data is fit to the numerical solution of the differential equation for the atoms' velocity, assuming a two-level atom. The saturation parameter s is a free parameter in the model and the fit gives $s = 9.6(1)$.

atoms are then imaged. The number of atoms recaptured by the MOT falls sharply as the centre-of-mass velocity approaches the capture velocity of the MOT. In the absence of velocity-broadening effects, the number of atoms recaptured as a function of centre-of-mass velocity, v_0, can be described by,

$$N(v_0) = \frac{N_0}{\sqrt{\pi}\sigma_v} \int_{-v_c}^{v_c} \exp\left[-\left(\frac{v - v_0}{\sigma_v}\right)^2\right] dv, \tag{5.29}$$

where v_c is the capture velocity of the MOT and σ_v characterises the width of the velocity distribution after the atoms have been launched by the push beam. As $v_c \to \infty$, $N(v_0) \to N_0$. Additionally, the function is allowed to have an offset, which accounts for the fact that only atoms in $F = 2$ are launched by the push beams.

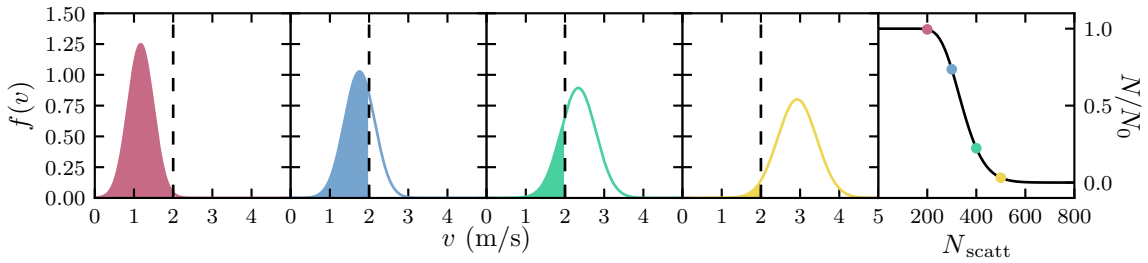

Figure 5.29: The resulting velocity distribution for $N_{\mathrm{scatt}} = 200$ (a), 300 (b), 400 (c) and 500 (d). The width of the initial velocity distribution is characterised by a temperature of 50 µK. The fraction of atoms with $v < v_c$, where $v_c = 2$ m/s is indicated by the dashed black line, is highlighted. (e) The fraction of atoms with $v < v_c$ as a function of the number of photons scattered. The points corresponding to (a)-(d) are shown.

Atoms that are in $F = 1$ when the push beam is switched on are not accelerated and are all recaptured when the MOT is switched back on. The velocity distribution of the atoms is altered by the push beam in two ways. Firstly, the centre-of-mass velocity of the atoms increases to a value v_0, which is related to the number of photons scattered, N_{scatt}, by

$$v_0 = \frac{\hbar k N_{\mathrm{scatt}}}{m_{\mathrm{Rb}}}. \tag{5.30}$$

Secondly, the velocity is also broadened as a result of the spontaneous emission. The width of the distribution is characterised by the temperature of the atoms, which increases by an amount,

$$\Delta T = \frac{\hbar^2 k^2 N_{\mathrm{scatt}}}{3 m_{\mathrm{Rb}} k_{\mathrm{B}}}, \tag{5.31}$$

where k_{B} is the Boltzmann constant, $k = 2\pi/\lambda$ and m_{Rb} is the mass of a ^{87}Rb atom. Fig. 5.29 shows a simple illustration of how the velocity distribution of atoms is expected to change as the atoms are accelerated by a push beam. In each of the panels the portion of the distribution with $v < v_c$, where $v_c = 2$ m/s, is highlighted. Fig. 5.29(e) shows the fraction of atoms recaptured as a function of the number of photons scattered by the push beam. The simulated data are fit to an error function. The sharpness of the roll off is set by the width of the velocity distribution. Ideally, the velocity distribution would be narrow, $|\sigma_v|/v_0 \ll 1$, so that the capture velocity can be precisely determined. In practice, there are a number of contributing factors which cause the roll off to become more shallow. First, there is the increase in the width of the velocity distribution due to spontaneous emission given by Eq. 5.31. This is not so severe, since for $v_0 = 10$ m/s the increase in the temperature of the distribution is ~200 µK. The standard deviation of the associated velocity distribution is only $\sigma_v = 0.14$ m/s. More significant are the effects of the intensity profile of the push-beam. This leads to a broadening of the velocity distribution because atoms closest to the intensity maximum are accelerated to a higher velocity. This effect is

more severe with longer exposure times, which are used to impart higher velocities. The result of these effects is that roll off in the number of atoms recaptured $N(v_0)$ becomes asymmetric about the capture-velocity, acquiring a high-velocity tail. The extra spread in velocity can be described by an additional contribution to the increase in temperature of the atoms, $\Delta T = (\hbar^2 k^2 / 3 m_{\mathrm{Rb}} k_{\mathrm{B}}) N_{\mathrm{scatt}} + a N_{\mathrm{scatt}}$. Thus the final model, which is used to extract the capture velocity is

$$N(v_0) = \frac{N_0(F=2)}{\sqrt{\pi}\sigma_v} \int_{-v_c}^{v_c} \exp\left[-\frac{(v-v_0)^2}{\sigma_0^2 + \sigma_v^2(v_0)}\right] dv + N_0(F=1). \tag{5.32}$$

Here, $N_0(F = 1, 2)$ is the number of atoms in the $F = 1, 2$ ground states as the push-beam is switched on, σ_0 is the width of the velocity distribution due to the initial temperature of the atoms, and $\sigma_v(v_0)$ accounts for the broadening of the distribution due to spontaneous emission and systematic effects.

5.7.2 Results

Fig. 5.30 shows how the number of atoms recaptured by the MOT varies as a function of centre-of-mass velocity v_0, for a range of different MOT intensities. The maximum height of each curve is different as a result of the variation in the lifetime of the trap with intensity and detuning. Modest numbers of atoms are used and the trap is run at lower field gradients to reduce the density. This ensures the loss of atoms from the trap is dominated by one-body processes and the whole curve is simply scaled in the vertical direction, rather than being distorted. For each intensity the capture velocity is extracted by fitting the data to Eq. 5.32. At the highest intensity the capture velocity is $v_c = 3.8(1)$ m/s. The inset of the figure shows how the measured capture velocity varies with the total MOT intensity. The extracted capture velocities are fit to a power law $v_c = a I_t^b$, which gives a best estimate $b = 0.73(2)$. The value of the capture velocity measured here is about half of the critical velocity suggested by the simulation results in Fig. 3.9(b). This critical velocity represents a maximum upper bound for the actual value of the capture velocity in the blue-detuned MOT, because atoms above this velocity are accelerated, rather than decelerated by the molasses. One might therefore expect the measured capture velocity to approach the critical velocity in situations where the MOT beams are very large and intense.

At the highest intensities, the capture velocity is still small compared to that measured elsewhere, both for type-I and type-II MOTs. In a recent study the capture velocity of a red-detuned MOT of CaF was measured to be about 11 m/s [98], almost three times the value measured here. Small capture velocities are expected for a blue-detuned MOT, since it is only the sub-Doppler contribution to the velocity-

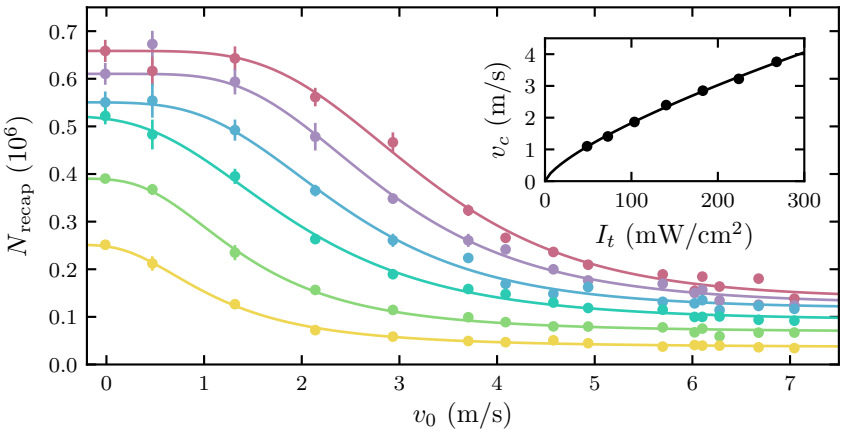

Figure 5.30: Number of atoms recaptured by the blue-detuned MOT as a function of centre-of-mass velocity, for a number of different intensities. Atoms are launched into the MOT using the technique described in the text. The inset shows the values of the capture velocity, extracted from the fits in the main figure, as a function of the total intensity in the MOT. The fit is to a polynomial $v_c = aI_t^b$ and gives $b = 0.73(2)$. The other MOT parameters are $\Delta_{11}/(2\pi) = +26$ MHz, $\Delta_{22}/(2\pi) = +11.5$ MHz and $B' = 39$ G/cm.

dependent forces that slow and cool atoms. Atoms moving faster than some critical velocity $v > v_{\mathrm{crit}}$ are instead heated by the Doppler forces. In a conventional MOT the capture velocity can be estimated using the trapping volume and damping coefficient, obtained from the velocity-dependent force. In the blue-detuned MOT, atoms moving with $v > v_{\mathrm{crit}}$ are not slowed, and therefore can not be captured by the MOT, irrespective of the trap volume. In [73], the force-velocity curves are calculated for some type-II systems. The critical velocity is predicted to vary with the square-root of the intensity. Here, the critical velocity is not measured directly, but imposes an upper limit on the velocity of atoms that can be recaptured. Additionally, the level structure used in the blue-detuned MOT is more complicated than that considered in [73].

In the previous section, measurements of the trap-loss coefficients were presented. The density-dependent coefficient was shown to have values in the range $\beta = 0.5 - 3.0 \times 10^{-10}$ cm^3 s^{-1}, and it was suggested that hyperfine-state changing collisions between ground-state atoms might contribute significantly to this. Following a collision resulting in $\Delta F = 2$, a pair of initially stationary atoms each move with $v = 7.9$ m/s, while for $\Delta F = 1$ the speed of each atom is $v = 5.6$ m/s. Therefore, any inelastic collision occurring between ground state atoms will certainly result in both atoms being ejected from the trap, over the whole range of trap laser intensities investigated here. This implies that variation in the intensity dependence of β due to hyperfine-changing collisions is due to the increased temperature of the atoms.

The variation of capture velocity with trap volume has not been investigated ex-

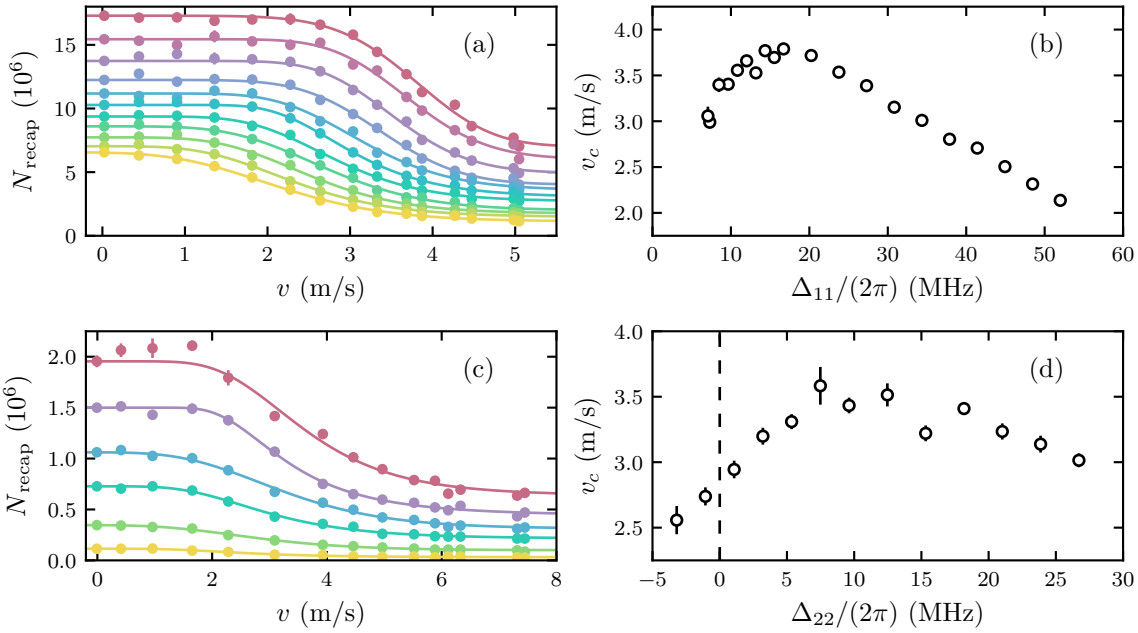

Figure 5.31: Measuring the capture velocity as a function of trap-laser detuning. (a) and (c) show the number of atoms captured from a moving cloud, as a function of its centre-of-mass velocity for a variety of different detunings. The capture velocity is extracted from these fits and plot as a function of detuning in (b) and (d). In (a) and (b) the detuning of the $F = 1 \rightarrow F' = 1$ laser is varied, while the other parameters are $\Delta_{22}/(2\pi) = +11.5$ MHz, $I_t = 260$ mW/cm^2, $B' = 39$ G/cm. In (c) and (d) the detuning of the $F = 2 \rightarrow F' = 2$ laser is varied, while the other parameters are $\Delta_{11}/(2\pi)$=+26 MHz, $I_t = 270$ mW/cm^2, $B' = 39$ G/cm.

perimentally. Assuming that the capture velocity continues to increase with intensity as shown in the inset of Fig. 5.30, then a total trap intensity of $I_t = 752$ mW/cm^2 would be required to recapture the products of ground-state hyperfine changing collisions with $\Delta F = 2$. Experimentally, this is prohibitively high and it does not seem desirable to attempt to suppress these inelastic collisions simply by increasing the intensity.

Fig. 5.31 shows how the capture velocity of the trap varies as a function of trap laser detuning. Each of the two lasers is varied in turn. Parts (a) and (b) of Fig. 5.31 show how the capture velocity varies with the detuning of the $F = 1$ laser. The capture velocity is largest when $\Delta_{11}/(2\pi) = +16$ MHz and decreases gradually as the detuning is increased. The capture velocity decreases more sharply as the magnitude of the detuning is reduced. For $\Delta_{11} \lesssim 7$ MHz, the lifetime of the trap becomes prohibitively short to perform these measurements. Parts (c) and (d) of Fig. 5.31 show how the capture velocity varies with the detuning of the $F = 2$ laser. The maximum capture velocity is obtained for $\Delta_{22}/(2\pi) \sim +10$ MHz. When the $F = 2$ laser is on resonance the capture velocity is 80% of its maximum value, and the trap can still recapture moving atoms reasonably well. This illustrates that most

of the cooling occurs when atoms are in $F = 1$.

It is interesting to note that the variation in the measured capture velocity of the MOT is much less extreme than the variation in the lifetime of the trapped atoms over the same parameter space. For example, at the smallest value of Δ_{11} measured, the capture velocity is still 80% of its maximum value. The lifetime of the trap, however, is dramatically reduced from its maximum value.

5.8 Summary of experimental observations

In this chapter data has been presented from a comprehensive investigation of the properties of a blue-detuned magneto-optical trap. By using light that is blue-detuned from type-II transitions sub-Doppler temperatures are achieved. The lowest temperatures are achieved when there are no magnetic fields present, in which case the temperature is comparable to that obtained in a conventional type-I optical molasses. Small magnetic fields are observed to disrupt the cooling and increase the temperature of the atoms, but increasing the magnetic field to even higher values causes the temperature to decrease again and eventually become insensitive to the magnetic-field gradient. The exact cooling mechanism, specifically the interplay between magnetic and optical fields, remains elusive and could be investigated further.

Atoms are tightly confined in the type-II MOT by using a high magnetic-field gradient, which counteracts the inherently weak confinement. The spring constant of the MOT is estimated to be $5(2) \times 10^{-20}$ N/m for typical trap parameters. Considering the size of the magnetic-field gradient, this value is relatively small compared to those reported for other type-II MOTs. This could be because in the blue-detuned MOT the temperature is smaller. As described in Chap. 3 the dark-state is velocity-selective, atoms moving with higher velocities are brightened by non-adiabatic transitions. By brightening the dark state the spring constant of the trap is increased. The damping coefficient, which here is measured to have values in the range $\alpha/m_{\mathrm{Rb}} = 2 - 6 \times 10^3$ s^{-1}, is substantially larger than that reported for other type-II MOTs. Elsewhere values of $\alpha/m_{\mathrm{CaF}} = 400$ s^{-1} for CaF [98], and $\alpha/m_{\mathrm{SrF}} = 310$ s^{-1} for SrF [71] have been reported. The large value measured in this experiment can be attributed to the efficient sub-Doppler polarisation-gradient cooling, which occurs in type-II systems when the light is blue-detuned.

The insensitivity of the sub-Doppler cooling to strong magnetic fields allows low temperatures to be achieved simultaneously with high densities, which are higher even than for a typical type-I MOT. Consequently, the phase-space density is a million times higher than has been achieved in conventional type-II MOTs and is also impressive when compared to that achieved in type-I atomic MOTs.

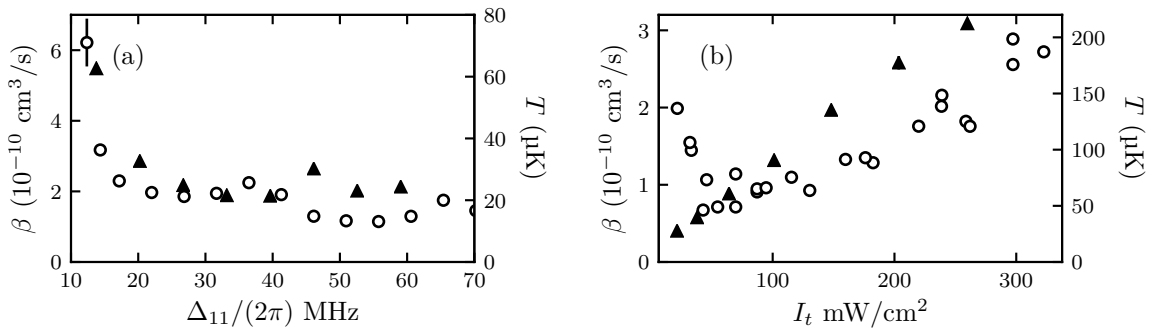

Figure 5.32: A comparison between the temperature (filled triangles) and density-dependent loss-rate coefficient β (hollow circles). β is proportional to the rate at which collisions occur, which in turn is related to the velocity distribution of the atoms, $\beta \propto \langle \sigma(v)v \rangle$. For inelastic collisions between ground-state atoms β only depends on the trap intensity through the velocity distribution of the atoms. Over the whole range of intensities the capture velocity is small enough that hyperfine-state-changing collisions can eject atoms from the trap.

The loss rate of atoms from the trap at high atom number densities is dominated by intra-trap collisions. The value of the loss-rate coefficient measured for this trap is similar to that reported for a type-I Rb MOT operated at a larger-than-typical detuning and modest intensity. Direct measurements of the capture velocity of the trap have been performed and confirm that hyperfine-state-changing collisions between ground-state atoms can result in trap loss over the whole range of intensities and laser detuning investigated.

It is more difficult to comment on the role of collisions between ground and excited-state atoms. This is straightforward to do in a type-I MOT because inelastic hyperfine-state-changing collisions can be suppressed. The loss-rate coefficients measured at higher intensity can then be attributed to collisions involving excited-state atoms. It is particularly frustrating that trap loss due to ground-state collisions cannot be suppressed in this particular system because light-assisted collisions have never been studied in the presence of near-resonant blue-detuned light. Such a setting is expected to modify the cross section for inelastic collisions occurring within the trap in desirable ways. The ratio of to the capture velocity of a blue-detuned MOT may be more favourable for other species of atoms or molecules. In such cases, where losses due to inelastic collisions between ground-state particles are suppressed, optical shielding of ground-state excited-state collisions would be additional persuasive reason for using a blue-detuned MOT over a conventional MOT.

Fig. 5.32 shows some data obtained for the density-dependent loss-rate coefficient plotted along with measurements of the temperature of the atoms as the same parameters are varied. There is a clear correspondence between the two: the parameters that give higher temperatures also are those where the loss-rate coefficient is highest. Again this implicates ground-state collisions as the dominant trap-loss

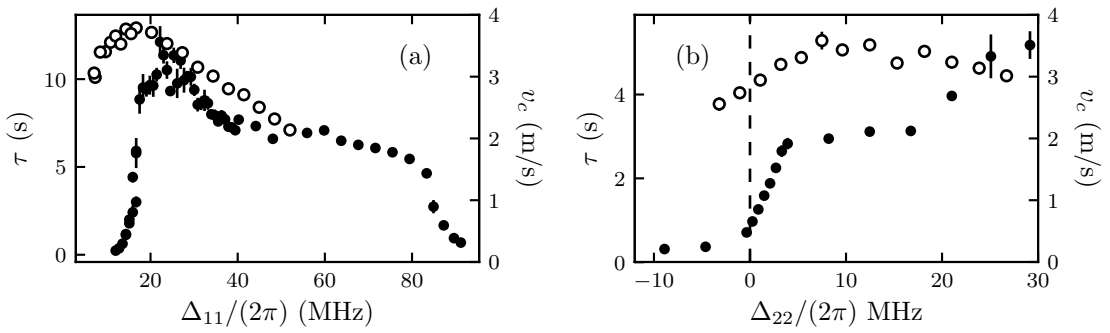

Figure 5.33: Measurements of the trap lifetime, made by measuring the loss-rate from traps with small numbers of atoms. Measurements of the trap lifetime are represented by the filled markers. The lifetime data was obtained with $I_t = 300$ mW/cm^2, $\Delta_{22}/(2\pi) = +11.5$ MHz and $B' = 89$ G/cm. Measurements of the capture velocity are also shown, which are the same data as in Fig. 5.31(a). As the detuning is reduced below $\Delta_{11}/(2\pi) = +20$ MHz the lifetime decreases much more rapidly than the capture velocity.

mechanism, since these depend on the trap parameters only through the resulting velocity distribution of the atoms. As the intensity is reduced below $I_t \simeq 50$ mW/cm^2 the value of β increases. Such a feature could suggest that the capture velocity of the MOT has been reduced below some threshold, which permits an additional inelastic collision mechanism to eject atoms from the trap. The capture velocity at this intensity is less than 1 m/s, which could implicate $\Delta F'$ collisions between excited-state atoms. At these low intensities, however, the excited-state population is smallest.

The one-body loss-rate coefficient for the trap is measured to have an approximately linear dependence on the trap intensity. This behaviour is extracted from fits to the nonexponential decay of the atom number from the trap and verified through direct measurements of the loss rate for small numbers of trapped atoms. Experimental observations of the one-body loss rate due to collisions with untrapped atoms made for type-I MOTs reveal an insensitivity to the trap intensity. This is because even a glancing collision transfers sufficient energy to eject an atom from the trap. The capture velocity in the type-II MOT is smaller, and so one might expect the loss rate to be even less sensitive to the total intensity of the trap. The loss rate due to collisions between trapped and untrapped atoms can be modified by the trap light through the excited-state fraction, for which the cross section for collisions with untrapped ground-state atoms is larger. This reduces the trap lifetime, in contrast to what is observed here. An interesting idea is that the blue-detuned light is shielding the trapped atoms from collisions with untrapped atoms, an effect which has not been observed or studied anywhere else.

Fig. 5.33(a) shows data for the capture velocity and the limiting lifetime of the trap, inferred by measuring the loss rates of small numbers of trapped atoms. It

is interesting to compare the data for $0 < \Delta_{11}/(2\pi) < +20$ MHz. As the detuning is reduced from 20 MHz the capture velocity begins to decrease gradually. The lifetime, however, decreases much more rapidly. Part (b) of the figure shows the same data as a function of Δ_{22}. Similar behaviour is observed when the detuning of the $F = 2$ laser is reduced below $\Delta_{22}/(2\pi) \lesssim +5$ MHz, though the decrease in lifetime is less abrupt. One-body losses are due to either evaporation or collisions with untrapped atoms. If the velocity distribution is truly Gaussian, evaporation does not seem likely. This is because the capture velocity remains above 3 m/s, which is the most-probable velocity of ^{87}Rb at 47 mK. The measured temperature of the atoms is orders of magnitude lower than this value. It also does not seem likely that the atom could be pumped into a dark state and drift out of the trapping region because the magnetic field in the MOT should prevent atoms from doing so. The capture volume of the MOT has also been verified to be significantly larger than the trapped atom clouds. One alternative is a modification to the collision cross section for collisions with untrapped atoms. Further measurements of the lifetime as a function of laser detuning for a variety of intensities might help to clarify the matter. The lifetime falls rapidly as Δ_{11} is reduced towards the value for which $\Delta_{11}/\Delta_{22} \sim 1$. The loss rate could thus be related to the fraction of atoms in $F = 2$. Losses due to inelastic collisions between atoms in $F = 2$ appear as a density-dependent loss rate but this could be misinterpreted as a one-body loss rate if the loss-rate coefficient is very large.

More detailed simulations might reveal that the velocity distribution of atoms in this setting is not expected to be Gaussian. A high-velocity tail in the velocity-distribution could lead to evaporation even at these low temperatures. In that case increasing the intensity, and thus the critical velocity for which cooling occurs in these type-II systems, could reduce the evaporation rate and explain the observations made here.

6 A menagerie of MOTs

The experiment that has been built to investigate the blue-detuned MOT allows atoms to be captured and cooled in a type-I MOT before being released and recaptured using a different set of laser detunings and polarisation. The trapping scheme used to demonstrate the first blue-detuned MOT uses light tuned close to the $F = 1 \rightarrow F' = 1$ and $F = 2 \rightarrow F' = 2$ transitions. The unusually high flexibility of the apparatus enables a range of other potential MOT configurations to be investigated, and a number of additional stable trapping configurations have indeed been observed. Some of these use red-detuned light and some use blue-detuned light. Some of the new traps differ substantially in their appearance, both from one another and in comparison to the blue-detuned MOT described in previous chapters. In this section, preliminary observations of a number of these traps are described. Some of these trapping configurations may present interesting avenues for further research. Measurements performed using these traps, of the loss-rate coefficients for example, will complement measurements described in previous sections. The majority of the traps do not have a steady-state trapped atom number. That is, once loaded from atoms cooled in the type-I MOT, the atom number decays until the fluorescence from the MOT is undetectable. There is one exception, which does load atoms from the vapour. None of these trapping configurations have been reported previously in ^{87}Rb.

The first trapping configuration that will be discussed is very similar to that already studied in previous chapters. The two lasers are tuned close to $F = 1 \rightarrow F' = 1$ and $F = 2 \rightarrow F' = 1$. The polarisations of both lasers are such that $\Delta m_F = +1$ transitions are driven by the restoring beams, opposite to the type-I rubidium MOT, and the light is blue detuned. Initially, it was thought this trapping configuration would perform worse than the blue-detuned MOT discussed in previous chapters. This is because, following the rules for choosing MOT polarisations presented in [72], the two transitions require opposite polarisations to give a confining force. Such an arrangement can not be implemented using the existing experiment. Despite the fact the $F = 2 \rightarrow F' = 1$ laser has the 'incorrect'[1] polarisation, a stable trap is produced.

The next trapping configuration is obtained when the lasers are polarised in the same way as for the type-I MOT. The $F = 1$ laser is red-detuned from $F' = 2$. A stable MOT is obtained when the $F = 2$ laser is red-detuned from $F' = 1$ or tuned

[1] Actually, when the OBEs are used, as in [73], there is a reversal of the sign in the position-dependent force for small magnetic fields such as near the centre of the MOT. Only for larger fields does the OBE approach agree with the rate-equation model.

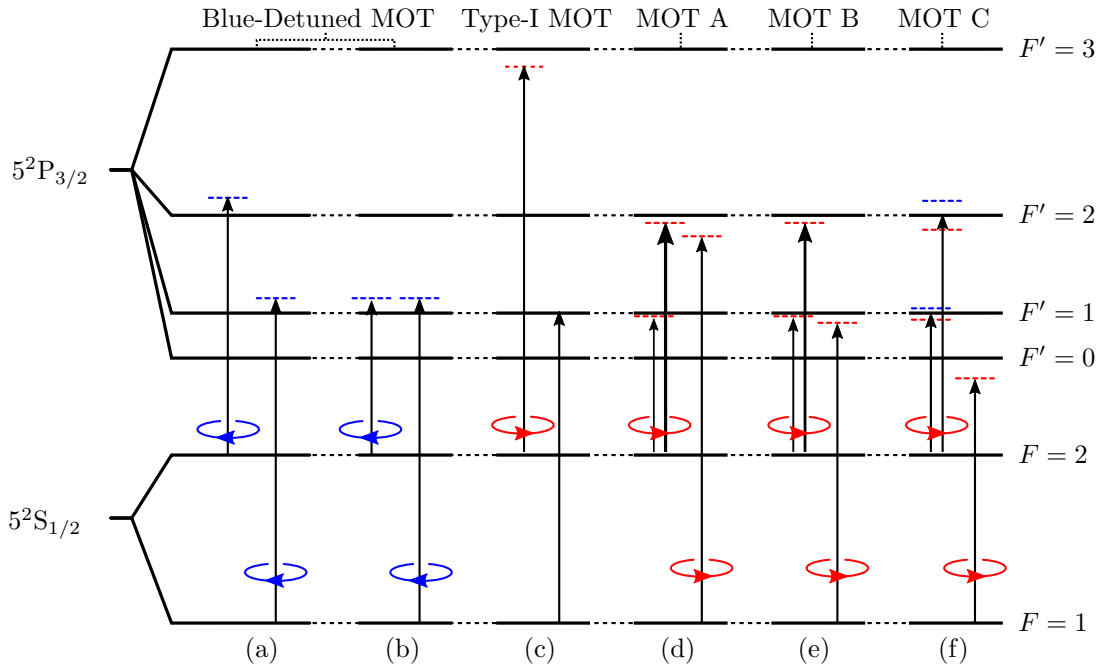

Figure 6.1: Stable trapping configurations in ^{87}Rb. The coloured arrows represent the polarisation of the MOT light. When the arrow is red the polarisation is the same as for the type-I MOT, when the arrow is blue it is the opposite. (a) is the blue-detuned MOT studied in detail in previous chapters. (b) is similar to (a) but the $F = 2$ laser also couples atoms to $F' = 1$. (c) is the standard type-I MOT. (d) shows 'MOT A', which has a hybrid type-I/type-II nature. The $F = 2$ laser can be red-detuned from $F' = 2$ or $F' = 1$, but the former gives a longer lifetime. This MOT is able to capture atoms from the background vapour. (e) shows 'MOT B', the red-detuned counterpart to the MOT studied in previous chapters. (f) Shows 'MOT C', which is obtained when the $F = 1$ laser is red-detuned from $F' = 0$. The MOT is stable when $F = 2$ is tuned to either $F' = 2$ or $F' = 1$ and the detuning in both cases can be positive or negative.

around $F' = 2$. For some combinations of parameters this MOT can actually capture atoms from the vapour, and so has a steady-state atom number. This configuration is referred to as 'MOT A'.

Another trapping configuration is obtained when the lasers are red-detuned from $F = 1 \rightarrow F' = 1$ and $F = 2 \rightarrow F' = 2$. This is the red-detuned counterpart to the blue-detuned scheme discussed in the earlier chapters of this thesis. As expected, the polarisation must be opposite to that used in the blue-detuned MOT. The behaviour and characteristics of this MOT are quite striking, and very different to its blue-detuned equivalent. This configuration is referred to as 'MOT B'.

The final trapping configuration that has been observed is obtained when the $F = 1$ laser is red-detuned from $F' = 0$. A stable, long-lived trap is produced. This is quite surprising because there is no trapping force for a $F = 1 \rightarrow F' = 0$ system. This configuration is referred to as 'MOT C'.

6.1 Blue-detuned MOTs

There are two stable trapping configurations where the light is blue detuned. The first is (a) in Fig. 6.1, which is the configuration that has been studied throughout this thesis. This is obtained when the $F = 1$ laser is blue-detuned from $F' = 1$ and $F = 2$ is blue-detuned from $F' = 2$. Both lasers have the same polarisation, which is opposite to the type-I MOT.

When $F = 2$ is blue-detuned from $F' = 1$, a stable trap is also produced. This is labelled (b) in Fig. 6.1. According to the studies in [72, 73], in this configuration the position-dependent force for atoms in $F = 2$ is anti-confining when the atoms are more than a certain distance from the trap centre. Preliminary measurements of the lifetime of atoms in this trap have been made and do appear to be shorter than for when the laser is blue-detuned from $F' = 2$. However, detailed measurements in which the one and two-body loss-rate coefficients are measured have not yet been performed. Measurements have been made of the temperature of atoms confined in this MOT: with $I_t = 400$ mW/cm^2, $\Delta_{11}/(2\pi) = 35$ MHz, and $B' = 48$ G/cm the temperature varies between 180 µK and 215 µK as the $F = 2$ laser is detuned between $27 - 37$ MHz relative to $F' = 1$. At a lower intensity, $I_t = 30$ mW/cm^2, the temperature varies between $32 - 38$ µK as the $F = 2$ laser is detuned between $35 - 47$ MHz relative to $F' = 1$. In this configuration, both ground states are coupled to a single excited state. Similar configurations have been observed to produce interesting effects as a result of Raman couplings between ground states. One such example, recently reported in [125], is a Λ-enhanced grey molasses cooling scheme for ^{87}Rb. The phase-space density of this molasses is nearly 10-times higher than that achieved with a conventional, bright molasses. It would be interesting to investigate whether such a cooling scheme could remain effective in the trapping configuration reported here. However, the best results presented in [125] require the two lasers to have a coherent phase, which is not currently the case in this experiment. Fig. 6.2 shows data obtained for the lifetime of atoms trapped in this MOT. The measurements are made by monitoring the decay of fluorescence from the trap using a photodiode. The resulting signal is fit to a single exponential decay to extract the trap lifetime. The lifetime varies rapidly and in a complicated way, changing by more than a factor of two as the detuning is changed by less than Γ. This could suggest interesting behaviour in the density-dependent trap-loss-rate coefficient, as such rapid variations are unlikely to be the result of changes in the trap depth due to the magneto-optical force.

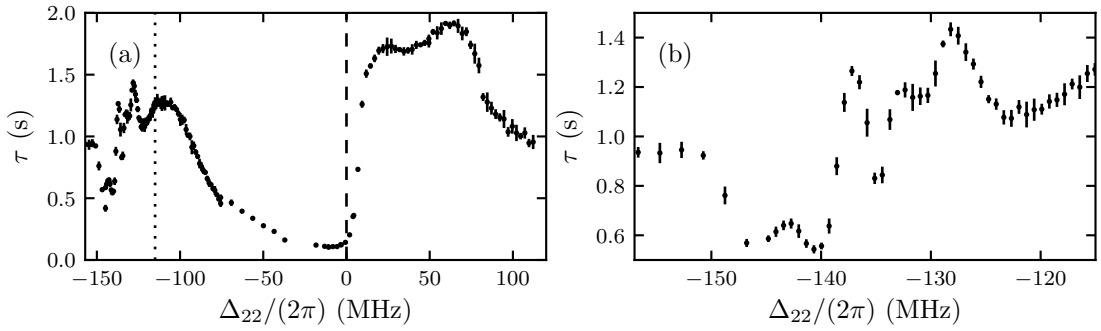

Figure 6.2: The lifetime of atoms confined in the blue-detuned MOTs as Δ_{22} is varied. When $\Delta_{22} = 0$ the laser is tuned to the $F = 2 \rightarrow F' = 2$ resonance. The $F = 2 \rightarrow F' = 1$ transition is indicated by the dashed line at -157 MHz. In (a) there are two broad regions visible where a MOT forms. When the laser is blue-detuned from $F' = 2$, the MOT is the blue-detuned MOT studied previously (labelled (a) in Fig. 6.1). The new blue-detuned MOT is obtained when the $F = 2$ laser is blue-detuned from $F' = 1$, corresponding to (b) in Fig. 6.1. For small-values of red-detuning close to the $F = 2 \rightarrow F' = 2$ transition the MOT is very short-lived. Part (b) of the figure is an enlarged section from part (a), which shows the complicated behaviour of the lifetime more clearly. Similar behaviour is reproduced day-to-day and also as the other parameters are varied.

6.2 Red-detuned MOTs

In the following sections, the trapping configurations that use red-detuned light are discussed.

6.2.1 MOT A

MOT A has a hybrid type-I/type-II nature and is depicted by (d) in Fig. 6.1. The laser polarisation is the same as for the type-I MOT. The $F = 1$ laser is red-detuned from $F' = 2$, and the $F = 2$ laser is tuned close to either the $F = 2 \rightarrow F' = 2$ or $F = 2 \rightarrow F' = 1$ transitions. Both transitions give stable MOTs. When the $F = 2$ laser is tuned close to $F' = 2$ the populations of both ground states should be equal, because $F' = 2$ decays with equal probability to the two ground-states. There are no dark-states in the lower hyperfine ground-state and, when the light is red detuned, atoms in the lower ground-state are cooled by sub-Doppler processes. When the $F = 2$ laser drives transitions to $F' = 2$ the MOT actually captures atoms from the background vapour. However, the steady-state number of atoms is smaller than for the type-I MOT. When atoms are loaded into this trap there is an initial decay of fluorescence, which is used to measure a trap lifetime.

Fig. 6.3 shows the lifetime of atoms in the MOT as a function of the laser detunings. When the $F = 2$ laser is tuned close to $F' = 1$ the lifetime of the MOT is shorter and the trap does not capture atoms from the vapour. When the $F = 2$

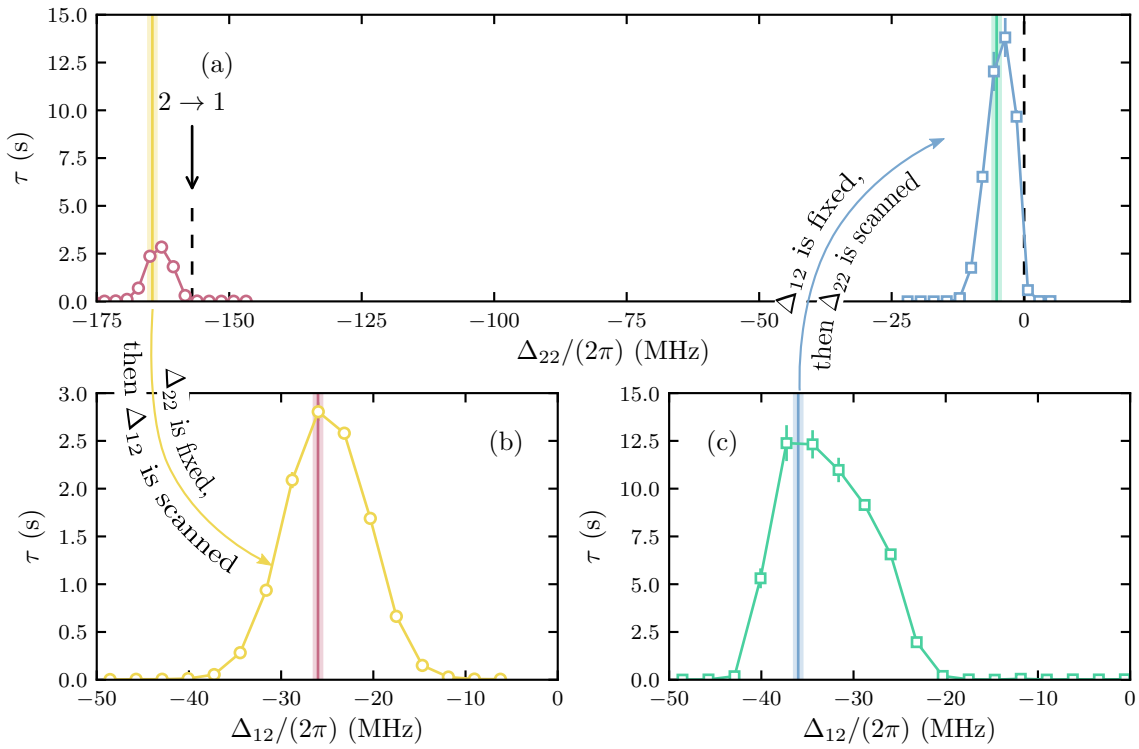

Figure 6.3: Lifetime of MOT A as a function of laser detuning. In (a) the detuning of the $F = 2$ laser is varied. There are two separate sets of data. The first, represented by the blue squares, was obtained with $\Delta_{12}/(2\pi) = -36$ MHz, which is the blue vertical line in (c). The second, represented by the pink circles, was obtained with $\Delta_{12}/(2\pi) = -26$ MHz, which is the pink vertical line in (b). For the data in (b) the detuning of the $F = 1$ laser is varied and the $F = 2$ laser is red-detuned from $F' = 1$, as shown by the vertical yellow line in (a). For the data in (c) the detuning of the $F = 1$ laser is varied and the $F = 2$ laser is red-detuned from $F' = 2$, as shown by the vertical green line in (a). For all sets of data the other parameters are $I_t = 260$ mW/cm^2 and $B' = 44$ G/cm.

laser is tuned close to $F' = 2$, a red detuning is required. Under such conditions there is sub-Doppler heating, but the polarisation of the light is correct to realise a confining force. When the $F = 2$ laser is tuned close to $F' = 1$, a red-detuning is also required. Now there is sub-Doppler heating and the rate-equation model predicts and anti-confining force for the laser polarisation used here. Therefore, one might expect that a blue-detuning would be preferable, but no MOT is observed. However, an important deviation exists between the predictions of the rate equation model presented in [72] and the OBE method in [73]. The rate equation model predicts that for a $F = 2 \rightarrow F' = 1$ system the sign of the g-factor in the ground state does not alter the sign of the position-dependent force in a MOT. The OBE model, however, predicts that when the sign of the g-factor in the ground state is reversed then the sign of the position-dependent force also changes in the innermost regions, closest to the trap centre. To realise a trapping force at the centre the polarisation should be reversed or sign of the detuning changed. For the relevant g-factors, the OBE model predicts a confining force for red-detuned light. This probably explains

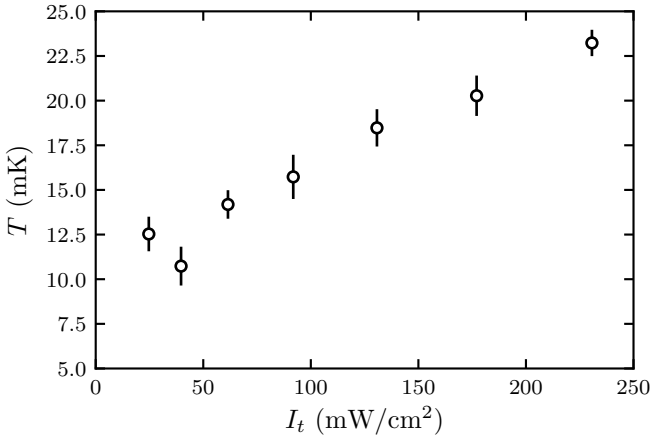

Figure 6.4: Temperature of MOT A as a function of total trap intensity. The other trap parameters are $\Delta_{12}/(2\pi) = -27$ MHz, $\Delta_{22}/(2\pi) = -4$ MHz and $B' = 44$ G/cm.

why the trap only works when the $F = 2 \rightarrow F' = 1$ laser is red-detuned. The extra heating due to the red-detuning of the $F = 2 \rightarrow F' = 1$ could contribute to the reduced lifetime of the MOT for this choice of transition. Similarly, when the laser is tuned to the blue side of $F' = 2$, there is sub-Doppler cooling, but an anti-confining force and no MOT is observed.

Fig. 6.4 shows the temperature of atoms captured by MOT A as a function of laser intensity. The temperature increases approximately linearly with the total trap intensity. The temperatures measured are nearly three orders of magnitude higher than those measured in the type-I MOT, or the blue-detuned type-II MOTs. The temperatures are comparable to the CaF MOT reported in [14]. The populations of the two ground states are roughly equal. While atoms in the lower hyperfine ground state experience sub-Doppler and Doppler cooling, those in $F = 2$ experience sub-Doppler heating, which probably causes the high temperatures observed here.

That atoms are mainly in the lower hyperfine-ground-state in this red-detuned magneto-optical trapping configuration is in itself a novelty. Although a type-II MOT of ^{85}Rb has been demonstrated where the ground-state population is predominantly in the lower hyperfine level [45], the equivalent has not been demonstrated before in ^{87}Rb. Moreover, for the right choice of detuning and magnetic field gradient, this configuration can capture atoms from the vapour. This trapping scheme is more robust than the blue-detuned MOT and could be used to make complementary measurements of the trap-loss rate coefficients in the study of cold collisions.

6.2.2 MOT B

MOT B is the red-detuned counterpart to the blue-detuned MOT described in earlier chapters. The lasers couple each of the ground states to the same upper-states as for

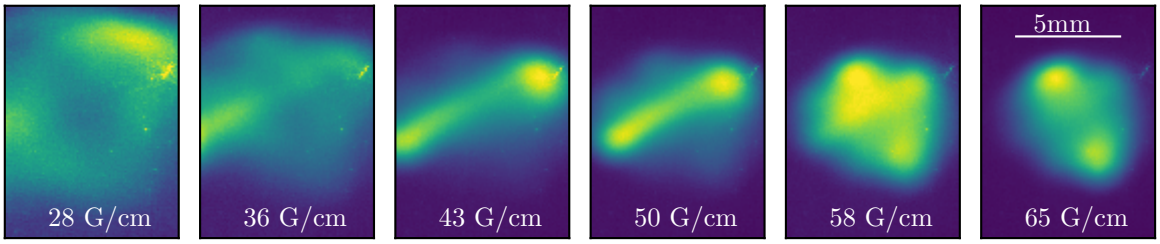

Figure 6.5: Fluorescence images of MOT B ((d) in Fig. 6.1) for different magnetic field gradients. For each image the histogram of pixel values is expanded to use the full scale of colours, revealing the relative atom density distribution. Higher field gradients lead to tighter confinement. The orientation of the ring structure changes with the magnetic field gradient. The centre of the trap is hollow. The field gradients used are indicated by the annotations. The other trap parameters are $\Delta_{11}/(2\pi) = -25$ MHz, $\Delta_{22}/(2\pi) = -12$ MHz, $I_t = 103$ mW/cm^2.

the blue-detuned MOT but the polarisations are reversed so that a confining force is obtained for this negative detuning. The sub-Doppler processes lead to strong heating effects for the level-structure and detuning used in this configuration. Long lived magneto-optical traps are only obtained when the $F' = 2$ laser is tuned to the red of the $F' = 2$ transition, a maximum lifetime being obtained for $\Delta_{22}/(2\pi) \sim -12$ MHz. The magnetic-field gradient must also be high, with the longest lifetimes being obtained for $60 \leq B' \leq 90$ G/cm. The atom density distribution in this MOT is quite different to that of the other trapping configurations. Atoms confined in this MOT form stable, ring-like structures. The geometry of these rings responds to changes in the intensity, magnetic-field gradient, and detuning. Fig. 6.5 shows a sequence of fluorescence images of the MOT as the magnetic-field gradient is increased. Fluorescence images are recorded on the CCD camera using the arrangement illustrated in Fig. 4.18. Fig. 6.6 shows a second sequence of fluorescence images in which the trap laser intensity is varied. At the lowest intensities, atoms form a single ring structure. As the intensity is increased the diameter of the ring decreases slightly. Then, as the intensity is increased further, a second ring structure appears. The axes of the two rings of the double-ring structure are approximately perpendicular to each other.

Similarly intriguing atom density distributions have been reported in type-I MOTs. For instance, abrupt transitions from a spherical cloud to a 'clumped' orbital mode and to a ring-like orbital mode are reported in [40]. The authors describe a central ball-like cloud of atoms orbited by atoms forming either a small clump or continuous ring. Similar observations are reported and studied in [126], where a bifurcation to a concentric double-ring structure is observed. Theoretical investigations have also been carried out [127, 128]. These instabilities are explained as

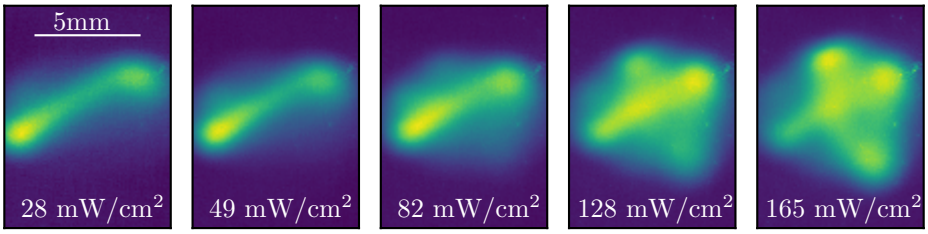

Figure 6.6: Fluorescence images of MOT B ((d) in Fig. 6.1) for different intensities of trapping light. For each image the histogram of pixel values is expanded to use the full scale of colours, revealing the relative atom density distribution. At lower intensities, a single-ring structure is observed and at higher-intensities a double-ringed structure forms. In all cases atoms are absent from the centre of the trap. The intensities used are indicated by the annotations. The other parameters are $\Delta_{11}/(2\pi) = -25$ MHz, $\Delta_{22}/(2\pi) = -12$ MHz and $B' = 53$ G/cm.

resulting from the repulsive radiation force between atoms due to multiple-photon-scattering. Additionally, the orbital modes are induced by a misalignment of the radial beams in order to produce a net torque on the cloud. Here, a bifurcation to an orthogonal double-ring structure occurs at high intensity, where the scattering rate is high and repulsive interactions between atoms are stronger. Unlike the instabilities reported in type-I MOTs, here there is no central ball. This could be a consequence of the high temperatures in the MOT, which produce a diffuse temperature-limited density distribution. Atoms are thus likely to be found relatively far from the centre of the trap, where small misalignments in the trap beams can impart a net torque to the atom, and could produce the kind of orbital trajectories observed here.

Fig. 6.7 shows how the lifetime of MOT B varies as a function of trap laser detuning and magnetic field gradient. The optimum detuning of the $F = 1$ laser is $\Delta_{11}/(2\pi) \sim -30$ MHz and for the $F = 2$ laser it is $\Delta_{22}/(2\pi) \sim -12$ MHz. The magnitude of the detuning that optimises the trap lifetime for the case of blue-detuning and red-detuning is therefore very similar, for both of the lasers. The trap does not form for field gradients below about 45 G/cm. As the magnetic-field gradient is increased to higher values the lifetime increases. A maximum lifetime is obtained for $B' = 70$ G/cm, and the lifetime then decreases again for higher field gradients. This could be due to intra-trap collisions between atoms. It would be interesting to measure the loss rate coefficients in this trap in order to compare them to the blue-detuned MOT. To do so, however, requires measurements of the density of the atoms, which would be complicated by the unusual structure of the MOT.

Understanding the atom-density distributions observed in MOT B

Sub-Doppler polarisation-gradient forces heat atoms to non-zero equilibrium velocities in a red-detuned type-II MOT. The velocity-dependent and position-dependent force curves obtained by numerically solving the optical Bloch equations for these

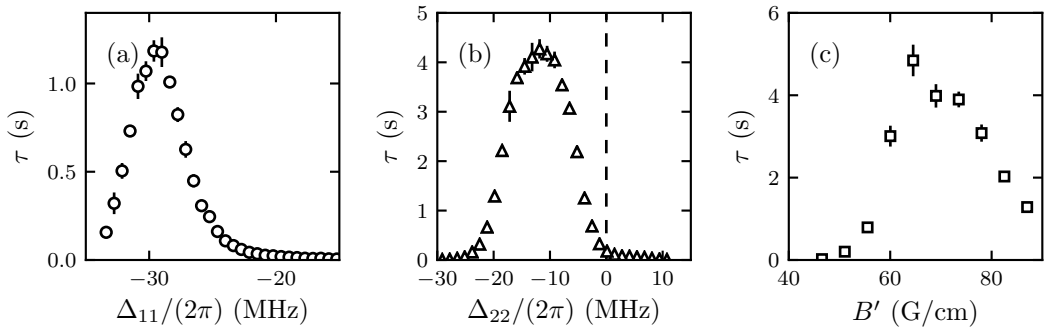

Figure 6.7: Lifetime of atoms loaded into MOT B, as a function of various parameters. (a) Lifetime as a function of Δ_{11}, the other parameters are $\Delta_{22}/(2\pi) = -13$ MHz, $B' = 58$ G/cm and $I_t = 264$ mW/cm^2. (b) Lifetime as a function of Δ_{22}, when $\Delta_{11}/(2\pi) = -31$ MHz, $B' = 68$ G/cm and $I_t = 264$ mW/cm^2. (c) Lifetime as a function of magnetic field gradient when the other parameters are $\Delta_{11}/(2\pi) = -31$ MHz, $\Delta_{22}/(2\pi) = -13$ MHz and $I_t = 264$ mW/cm^2.

MOTs have been presented and discussed in Chap. 3. In particular, the force curves shown in Fig. 3.9 are calculated using the full hyperfine level structure of ^{87}Rb and similar experimental parameters to those used to record the fluorescence images in Fig. 6.6 and Fig. 6.5. To investigate the atom density distributions observed in MOT B, trajectory simulations are performed using the force curves of Fig. 3.9. The motions of the atoms are treated classically, and there are no interactions between particles. The position-dependent forces along each of the axes are assumed to be independent of one-another, and the force in the radial directions is scaled by a factor of 0.5, i.e. the total position-dependent force is $\vec{F}(x,y,z) = 0.5f(x)\hat{x}+0.5f(y)\hat{y}+f(z)\hat{z}$, where $f(x)$ is the red force curve in Fig. 3.9(a). The atoms also experience a velocity-dependent force $\vec{F}_v(v_x,v_y,v_z) = g(v)\vec{v}/|\vec{v}|$. $g(v)$ is related to the red velocity-dependent force curve in Fig. 3.9(b), which is now labelled $f_v(v)$. In reality, the position-dependent and velocity-dependent forces are not decoupled in this way, and so this simplified model may not capture all of the physics of the system. Indeed, it is found to be necessary to modify the velocity-dependent force to prevent the simulated atoms from escaping the trap. The function used in the trajectory simulations is given by $g(v) = \frac{1}{10} f_v(v/4) \exp\left(-\frac{x^2+y^2+z^2}{2\sigma_r^2}\right)$. The purpose of the Gaussian envelope is to account for the weakened velocity-dependent forces in regions of low intensity away from the trap centre. The characteristic length scale for the Gaussian envelope is $\sigma_r = 5.8 \times 10^{-3}$ mm, which is the $1/e^2$ radius of the MOT beams in the experiment. Fig. 6.8 shows the positions of a collection of 40 atoms at various times. At $t = 0$ the atoms are located at the origin of the trap. For $t > 0$ the atoms' positions evolve according to $\vec{a} = \frac{1}{m}\left(\vec{F}(x,y,z) + \vec{F}_v(v_x,v_y,v_z)\right)$. From the figure it can be seen that atoms form a ring-like distribution, where the axis of the ring is aligned with the direction of tightest confinement of the MOT, similar

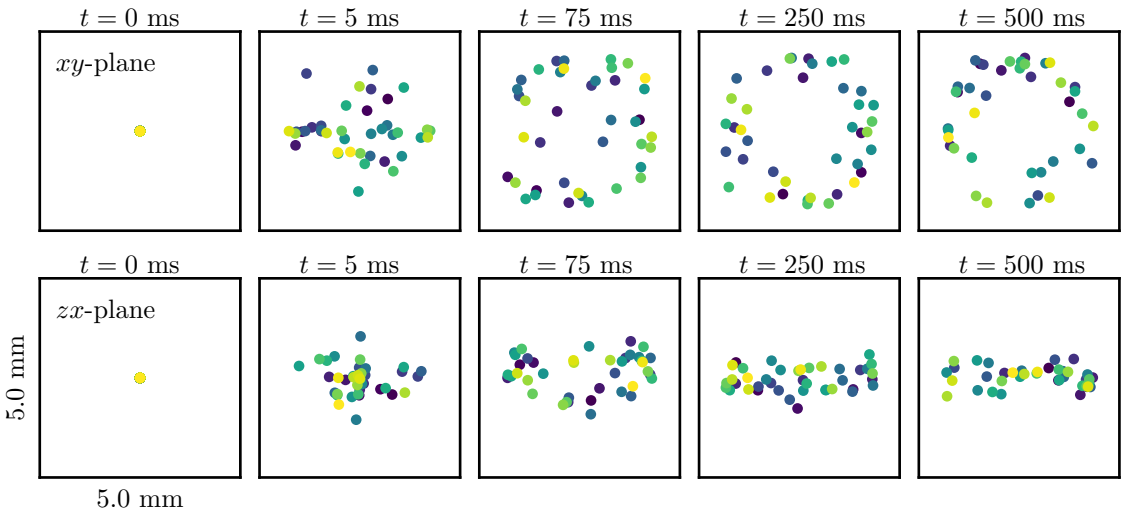

Figure 6.8: Trajectory simulations of atoms confined in the red-detuned type-II MOT labelled 'MOT B'. At $t = 0$ atoms are located at the origin of the MOT. For $t > 0$ the atoms' positions and velocities evolve according to the model described in the text. Atoms quickly form ring-like density distributions, similar to those observed experimentally.

to what is observed experimentally. The simple model does not take into account interactions between atoms, which may be necessary to understand the bifurcation to a double-ring structure.

6.2.3 MOT C

The final trapping configuration is MOT C, which is (f) in Fig. 6.1. This trapping configuration was discovered unintentionally when mapping out the laser-detuning parameter space for which MOT B was stable. The regions of laser detuning where this MOT forms have been labelled in Fig. 6.9, and the following discussion should be read in conjunction with a scrutiny of the figure.

There are features in Fig. 6.9 that suggest trapping can occur when the $F = 1$ laser is either red-detuned or blue-detuned from $F' = 0$, although the lifetime is significantly higher for the red detuning. The longest lifetime for this MOT is obtained when the $F = 1$ laser is red detuned from $F' = 0$ by an amount $\Delta_{10}/(2\pi) \sim -26$ MHz. The $F = 2$ laser can be tuned to either $F' = 2$ or $F' = 1$, as shown in Fig. 6.9(c). The frequency can be either red detuned or blue detuned from either of these transitions, so the confinement must be due to transitions from the lower hyperfine ground state. The confinement can not be due to the conventional MOT force because the $F' = 0$ excited-state has no structure. A similar observation has been made previously for a sodium MOT, as reported in [129]. The confinement is explained in terms of a level-mixing effect between the closely spaced $F' = 0$ and $F' = 1$ states, induced by the magnetic field in the MOT. Such an effect, if proceed-

ing here, is diluted by the larger spacing of 72 MHz between $F' = 0$ and $F' = 1$ in ^{87}Rb, compared to the equivalent 16 MHz spacing in Na. Indeed, the extent of the atom cloud in this MOT is much larger than for the other trapping configurations. This could also be the reason why the MOT requires a high field gradient to function, since the mechanism described in [129] relies on the perturbation of the zero-field states by the magnetic field.

Since the $F = 1 \rightarrow F' = 0$ transition is a cycling transition, virtually all of the population should be in the lower hyperfine ground-state, where exoergic collisions between ground-state atoms are energetically forbidden. It would therefore be interesting to measure the trap-loss rate coefficient for this trapping configuration. On the other hand, the rate coefficient might be unremarkable, and the long-lifetime be the result of the very small density in the trap.

There is evidence of confinement when the $F = 1$ laser is tuned to about $\Delta_{10}/(2\pi) = +12$ MHz. This feature is visible in parts (b) and (d) of Fig. 6.9. The model developed to explain the origin of confinement in the $F = 1 \rightarrow F' = 0$ MOT in [129], predicts that confinement should arise in multiple ranges of detuning. However, in [129] only one of these is observed experimentally. This is attributed to the fact that the MOT is loaded from a vapour cell, and the capture velocity in these other regions is diminished. In this investigation the trap can still be loaded because atoms are cooled to low temperatures in the type-I MOT. As discussed in [129], the force from this level-mixing effect does not change sign with the detuning. Since the features observed here exist for both red and blue-detuning close to $F = 1 \rightarrow F' = 0$, and also do not depend on the sign of the detuning of the $F = 2$ laser, it seems likely that both are due to the mixing force.

6.3 Summary

In this section a number of new trapping configurations have been presented. None of these have previously been reported. Some of these traps, such as the $F = 1 \rightarrow F' = 0$ MOT, offer new opportunities for measurements to be made that could complement the body of literature concerning cold and ultracold collisions. Certainly, these measurements would complement the work presented in this thesis, and that presented in [80]. This is also an ideal experimental platform for theories of laser cooling and trapping in complex systems to be investigated more thoroughly.

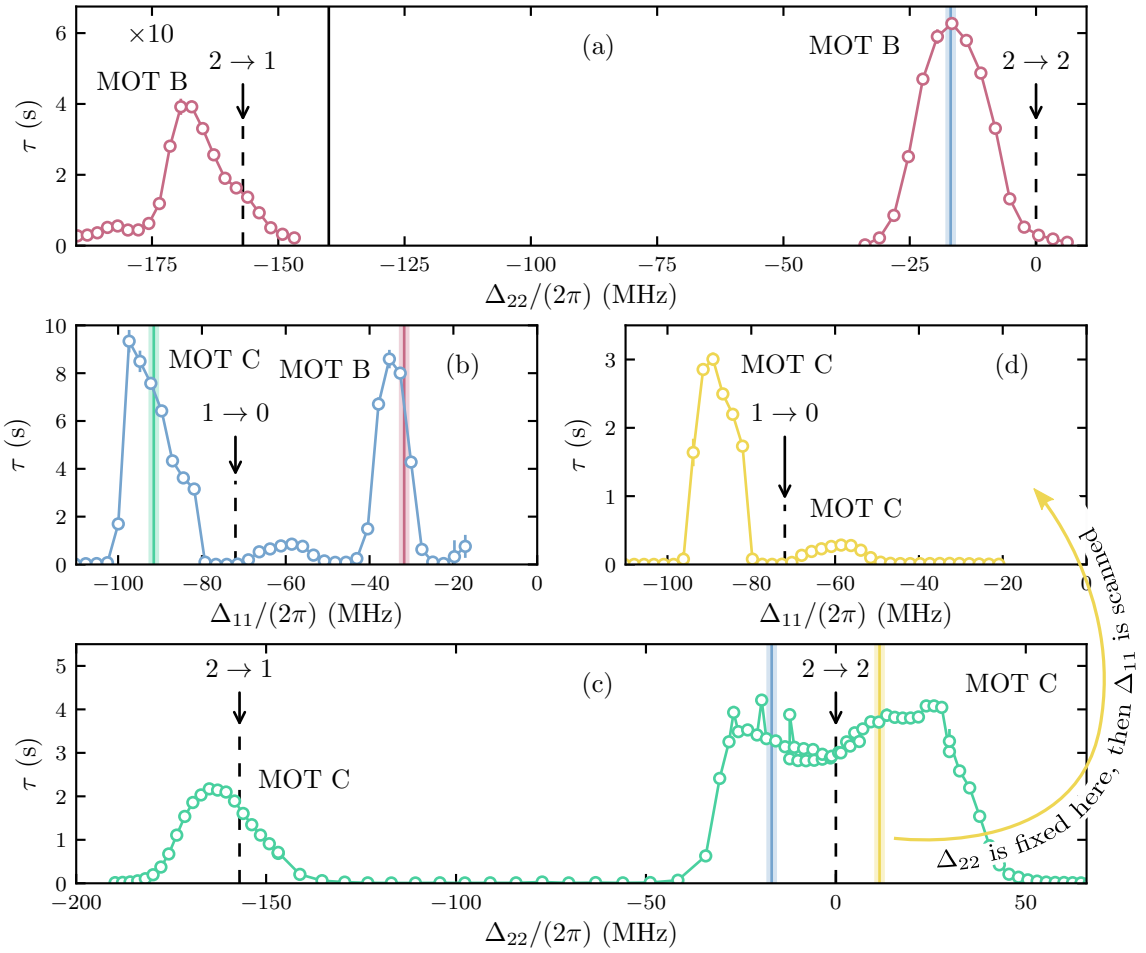

Figure 6.9: Lifetime of MOT B and MOT C as a function of laser detuning. Here the stability of the MOT is mapped out over a 2-dimensional parameter space defined by the detuning of the two lasers. In each panel the frequency of one laser is varied and the other is held fixed. In (a) the $F = 2$ laser is scanned as the $F = 1$ laser is held fixed at $\Delta_{11}/(2\pi) = -31$ MHz, which is the vertical pink line in (b). There is a stable MOT for $-25 < \Delta_{22}/(2\pi) < -5$ MHz, which is 'MOT B', the same as is imaged by fluorescence in Fig. 6.5 and Fig. 6.6. A MOT is also formed when the $F = 2$ laser is tuned to the red of $F' = 1$, but it is shorter lived and in the plot the lifetime has been magnified by a factor of ten. The $F = 2$ laser is then fixed at $\Delta_{22}/(2\pi) = -17$ MHz, indicated by the blue vertical line, and the $F = 1$ laser is scanned to obtain the data in (b). MOT B is stable in the region $-40 < \Delta_{11}/(2\pi) < -30$ MHz and there are two further stable traps. The longer-lived of these occurs when the $F = 1$ laser is red-detuned from $F' = 0$, which is quite surprising because a $1 \to 0$ transition in isolation cannot provide confinement. To investigate this MOT further the $F = 1$ laser is fixed at $\Delta_{11}/(2\pi) = -91$ MHz, which is -19 MHz from $F' = 0$. This detuning is indicated by the green line. Then, the $F = 2$ laser is scanned again to obtain the data in (c). The lifetime of the MOT is largest when the $F = 2$ laser is tuned close to $F' = 2$, and the detuning can be positive or negative. Thus the confinement is certainly due to the $F = 1 \to F' = 0$ transition. The MOT also functions when the $F = 2$ laser is tuned to $F' = 1$, though not as well. Finally, the $F = 2$ laser is locked at $\Delta_{22}/(2\pi) = +11.5$ MHz, as shown by the vertical yellow line and the $F = 1$ laser is scanned to obtain the data in (d). MOT B does not function with the $F = 2$ laser blue-detuned but the $1 \to 0$ MOT still does.

7 Outlook

7.1 Conclusions

This thesis has described the experimental realisation of a novel kind of magneto-optical trap, where blue-detuned light is used to cool and confine atoms. Conventional type-II MOTs, which are characterised by the presence of dark ground-state sub-levels, use red-detuned light. This leads to strong heating effects due to the nature of the polarisation-gradient forces in these systems. In turn, this leads to low number densities, which may prohibit the realisation of many of the proposed applications of cold molecules, where laser cooling and trapping always uses type-II transitions. The blue-detuned MOT performs exceptionally well in comparison. Strong magnetic-field gradients can be used to compensate for the small spring constant of the trap, which is inherent to all type-II MOTs. Number densities exceeding 1.5×10^{11} cm^{-3} have been obtained by increasing the magnetic-field gradient of the MOT to 90 G/cm. The sub-Doppler cooling mechanisms have been demonstrated to be robust to these magnetic-field gradients and cool atoms to low temperatures. At the highest field gradients used, the temperatures remain below 30 µK. Finally, because the cross-section for multiple photon scattering is reduced by the presence of dark ground-state sub-levels, the radiation-pressure-limited number density is higher. The result is an impressively high phase-space density of up to 6×10^{-6}, which is comparable to the best dark SPOTs, where type-I transitions are used.

The presence of dark ground-state sub-levels in type-II systems profoundly alters the light-matter interactions. The dark states reduce the scattering rate and hence confinement in the MOT, but also facilitate efficient sub-Doppler cooling, and reduce the detrimental effects of radiation trapping in the MOT. The dark state is destabilised by the magnetic field in the MOT, and is therefore most efficiently populated at the trap centre, which is a similar effect to that obtained using a dark-SPOT.

One potentially severe limitation of the blue-detuned MOT is the geometry-independent limit to the capture velocity imposed by the critical-velocity v_c of the cooling force. An atom with velocity $v > v_c$ cannot be recaptured by the MOT, irrespective of the capture volume. If $\frac{1}{2} m_{\mathrm{Rb}} v_c^2 < \Delta E_{\mathrm{hfs}}/2$, where ΔE_{hfs} is the hyperfine splitting of the ground state, then any hyperfine-state changing collisions result in atom loss. Previously, it has been demonstrated that optical shielding can reduce the rate at which this type of collision occurs. The suppression factor depends on the Rabi frequency of the transition driven by the laser [120], and here, because the laser is tuned close to resonance, the Rabi frequency is high. Nevertheless, collisions

between ground-state atoms appear to be the dominant trap loss mechanism. The prospects for optical shielding could be investigated further if a separate suppression laser could be varied independently from the MOT light.

Recently, impressive increases in the phase-space density of laser-cooled molecules have been made using conventional techniques, such as a compressed MOT, and grey-molasses cooling. Molecules have even been loaded into a magnetic trap, an impressive feat when considering the shallow trap depth. However, it remains desirable to improve the properties of molecules confined in the MOT, where the dissipation of energy in the presence of a restoring force could lead to higher phase-space densities. At this time, the technique has not yet been successfully applied to molecules.

More generally, the outcomes of this investigation help to consolidate the conclusions of recent theoretical work and previous experimental observations of type-II MOTs. A comprehensive understanding of the properties of arbitrary magneto-optical trapping schemes is now possible. Additionally, the purpose-built experimental set up has been used to investigate a number of additional configurations that are predicted to give confinement according to [72, 73]. These were presented in Chap. 6. This further demonstrates the progress made by recent theoretical work focussed on understanding unconventional MOTs.

7.2 Avenues for further research

There are a number of tangible avenues of further research motivated by this thesis. In Sec. 5.6 data obtained for the loss-rate-coefficient due to intra-trap collisions was presented. A better understanding of the trap loss mechanisms could be obtained by further investigation. A first experiment might involve measuring the density-dependent trap loss rate coefficient for the blue detuned MOT using the $F = 1 \rightarrow F' = 1$ and $F = 2 \rightarrow F' = 1$ transitions. In this configuration, more of the population is concentrated in the lower hyperfine ground-state, where inelastic collisions between ground-state are energetically forbidden. For ^{87}Rb the capture velocity of the blue-detuned MOT is insufficient to recapture the products of inelastic ground-state collisions. In ^{85}Rb, however, the ground-state hyperfine splitting is only 3 GHz. The capture velocity in a blue-detuned MOT of ^{85}Rb might therefore be high enough to suppress trap loss due to inelastic collisions between ground-state atoms.

Preliminary measurements of the properties of a number of additional magneto-optical trapping configurations have been made. Further characterisation of those traps would allow a direct comparison between the properties of red-detuned and blue-detuned type-II MOTs in ^{87}Rb. These characterisations would also complement

the existing body of literature concerning magneto-optical traps.

7.3 Concluding remarks

Despite having been demonstrated for the first time over 30 years ago, it is only recently that a thorough, generally applicable understanding of magneto-optical traps has been achieved. This has been motivated by the rapid progress recently made in the application of these techniques to molecules. However, given the ubiquity of the MOT in atomic physics research, it seems unsatisfactory that questions regarding the early observations of type-II MOTs should have pervaded the field for so long. The data presented in this thesis demonstrates that a satisfactory theory of magneto optical trapping, applicable beyond the 'simple' type-I structure, and to both atoms and molecules, now exists.

A Additional information

A.1 Acronyms and abbreviations

Table A.1 gives a list of the acronyms and abbreviations used throughout this thesis. Here, they are collected together for convenience.

Acronym/Abbreviation	Meaning
MOT	Magneto-Optical Trap
QWP	Quarter-Wave Plate
HWP	Half-Wave Plate
PBS	Polarising Beam-Splitter(ing)
SDLC	Sub-Doppler Laser Cooling
SPOT	Spontaneous-Force Optical Trap
OBEs	Optical Bloch Equations

Table A.1: Acronyms used throughout this thesis, collected for the reader's convenience.

A.2 ^{87}Rb level structure

Fig. A.1 shows the hyperfine level structure of ^{87}Rb.

A.3 List of components used in the frequency-offset locks

The tables below list the components used in each of the two frequency discriminator circuits used to generate the error signals for the frequency-offset locks described in Chap. 4.

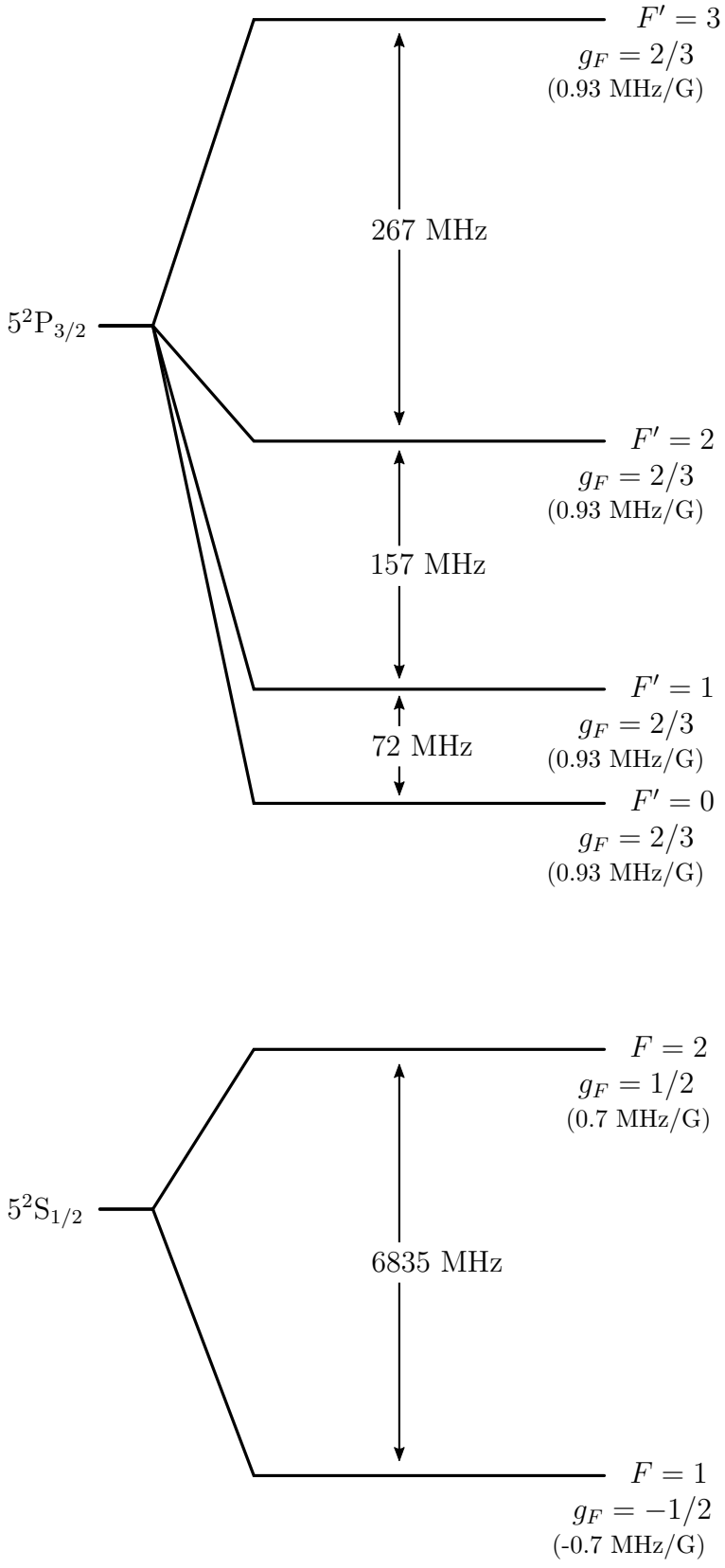

Figure A.1: The hyperfine level structure of ^{87}Rb including g-factors, level spacings, and hyperfine angular momentum quantum numbers.

Component	Model Number	Manufacturer	Notes
Bias Tee	ZX85-12G-S+	MiniCircuits	
PD Amplifier	ZKL-2R5+	MiniCircuits	×2
Mixer	ZFM-1W-S+	MiniCircuits	
Amplifier	ZX60-P105LN+	MiniCircuits	
VCO	ZX95-625-S+	MiniCircuits	
Low Pass Filter	SLP-550+	MiniCircuits	(a)
High Pass Filter	SHP-250+	MiniCircuits	

Table A.2: Components used in the frequency discriminator for the $F = 2$ frequency-offset lock described in Sec. 4.2.2. (a) This filter is optional, its purpose is to attenuate higher orders of the fundamental tone of the VCO, which can complicate the error signal.

Component	Model Number	Manufacturer	Notes
Bias Tee	ZX85-12G-S+	MiniCircuits	
PD Amplifier	ZX60-24-S+	MiniCircuits	×2
Mixer	ZX05-153-S+	MiniCircuits	
Post-mixer amplifier	ZX60-P105LN+	MiniCircuits	
VCO	ZX95-3450A-S+	MiniCircuits	
VCO amplifier	ZJL-5G+	MiniCircuits	
Doubler	ZX90-2-36-S+	MiniCircuits	
Doubler amplifier	ZX60-8008E-S+	MiniCircuits	

Table A.3: Components used in the frequency discriminator for the $F = 1$ frequency-offset lock described in Sec. 4.2.2.

A.4 Permissions

Included in the following pages are the permissions obtained for the reproduction of Fig. 5.17 in Sec. 5.6.

American Physical Society
Reuse and Permissions License

26-Apr-2018

This license agreement between the American Physical Society ("APS") and Kyle Jarvis ("You") consists of your license details and the terms and conditions provided by the American Physical Society and SciPris.

Licensed Content Information

License Number:	**RNP/18/APR/003758**
License date:	26-Apr-2018
DOI:	10.1103/PhysRevLett.69.897
Title:	Isotopic difference in trap loss collisions of laser cooled rubidium atoms
Author:	Christopher D. Wallace et al.
Publication:	Physical Review Letters
Publisher:	American Physical Society
Cost:	USD $ 0.00

Request Details

Does your reuse require significant modifications: No

Specify intended distribution locations:	UK & Commonwealth (excluding Canada)
Reuse Category:	Reuse in a thesis/dissertation
Requestor Type:	Student
Items for Reuse:	Figures/Tables
Number of Figure/Tables:	1
Figure/Tables Details:	FIG. 3. Dependence of P on total intensity I, for the two isotopes. The solid lines are curves to guide the eye.
Format for Reuse:	Print and Electronic
Total number of print copies:	Up to 1000

Information about New Publication:

University/Publisher:	Imperial College London
Title of dissertation/thesis:	The blue-detuned magneto-optical trap
Author(s):	Mr K N Jarvis
Expected completion date:	Apr. 2018

License Requestor Information

Name:	Kyle Jarvis
Affiliation:	Individual
Email Id:	k.jarvis14@imperial.ac.uk
Country:	United Kingdom

American Physical Society
Reuse and Permissions License

TERMS AND CONDITIONS

The American Physical Society (APS) is pleased to grant the Requestor of this license a non-exclusive, non-transferable permission, limited to Print and Electronic format, provided all criteria outlined below are followed.

1. You must also obtain permission from at least one of the lead authors for each separate work, if you haven't done so already. The author's name and affiliation can be found on the first page of the published Article.
2. For electronic format permissions, Requestor agrees to provide a hyperlink from the reprinted APS material using the source material's DOI on the web page where the work appears. The hyperlink should use the standard DOI resolution URL, http://dx.doi.org/{DOI}. The hyperlink may be embedded in the copyright credit line.
3. For print format permissions, Requestor agrees to print the required copyright credit line on the first page where the material appears: "Reprinted (abstract/excerpt/figure) with permission from [(FULL REFERENCE CITATION) as follows: Author's Names, APS Journal Title, Volume Number, Page Number and Year of Publication.] Copyright (YEAR) by the American Physical Society."
4. Permission granted in this license is for a one-time use and does not include permission for any future editions, updates, databases, formats or other matters. Permission must be sought for any additional use.
5. Use of the material does not and must not imply any endorsement by APS.
6. APS does not imply, purport or intend to grant permission to reuse materials to which it does not hold copyright. It is the requestor's sole responsibility to ensure the licensed material is original to APS and does not contain the copyright of another entity, and that the copyright notice of the figure, photograph, cover or table does not indicate it was reprinted by APS with permission from another source.
7. The permission granted herein is personal to the Requestor for the use specified and is not transferable or assignable without express written permission of APS. This license may not be amended except in writing by APS.
8. You may not alter, edit or modify the material in any manner.
9. You may translate the materials only when translation rights have been granted.
10. APS is not responsible for any errors or omissions due to translation.
11. You may not use the material for promotional, sales, advertising or marketing purposes.
12. The foregoing license shall not take effect unless and until APS or its agent, Aptara, receives payment in full in accordance with Aptara Billing and Payment Terms and Conditions, which are incorporated herein by reference.
13. Should the terms of this license be violated at any time, APS or Aptara may revoke the license with no refund to you and seek relief to the fullest extent of the laws of the USA. Official written notice will be made using the contact information provided with the permission request. Failure to receive such notice will not nullify revocation of the permission.
14. APS reserves all rights not specifically granted herein.
15. This document, including the Aptara Billing and Payment Terms and Conditions, shall be the entire agreement between the parties relating to the subject matter hereof.

Bibliography

[1] E. F. Nichols and G. F. Hull. A preliminary communication on the pressure of heat and light radiation. *Physical Review*, 13(5):307–320, 1901.

[2] E. F. Nichols and G. F. Hull. The pressure due to radiation. *Physical Review (Series I)*, 17(2):91–104, 1903.

[3] R. Frisch. Experimenteller Nachweis des Einsteinschen Strahlungsrückstoßes. *Zeitschrift für Physik*, 86(1):42–48, 1933.

[4] J. E. Bjorkholm, R. R. Freeman, A. Ashkin, and D. B. Pearson. Observation of focusing of neutral atoms by the dipole forces of resonance-radiation pressure. *Physical Review Letters*, 41(20):1361–1364, 1978.

[5] J. E. Bjorkholm, R. R. Freeman, and D. B. Pearson. Efficient transverse deflection of neutral atomic beams using spontaneous resonance-radiation pressure. *Physical Review A*, 23(2):491–497, 1981.

[6] E. L. Raab, M. Prentiss, A. Cable, S. Chu, and D. E. Pritchard. Trapping of neutral sodium atoms with radiation pressure. *Physical Review Letters*, 59(23):2631–2634, 1987.

[7] H. Müller, A. Peters, and S. Chu. A precision measurement of the gravitational redshift by the interference of matter waves. *Nature*, 463(7283):926–929, 2010.

[8] N. Huntemann, B. Lipphardt, C. Tamm, V. Gerginov, S. Weyers, and E. Peik. Improved limit on a temporal variation of mp/me from comparisons of Yb^+ and Cs atomic clocks. *Physical Review Letters*, 113(21):1–5, 2014.

[9] M. A. Lombardi, T. P. Heavner, and S. R. Jefferts. NIST primary frequency standards and the realization of the SI second. *NCSL International Measure*, 2(4):74, 2007.

[10] S. Y. Lan, P. C. Kuan, B. Estey, P. Haslinger, and H. Müller. Influence of the Coriolis force in atom interferometry. *Physical Review Letters*, 108(9):1–5, 2012.

[11] J. G. Wacker. Using atom interferometry to search for new forces. *Physics Letters, Section B: Nuclear, Elementary Particle and High-Energy Physics*, 690(1):38–41, 2010.

[12] B. Elder, J. Khoury, P. Haslinger, M. Jaffe, H. Müller, and P. Hamilton. Chameleon dark energy and atom interferometry. *Physical Review D*, 94(4):1–15, 2016.

[13] J. F. Barry, D. J. McCarron, E. B. Norrgard, M. H. Steinecker, and D. DeMille. Magneto-optical trapping of a diatomic moleucle. *Nature*, 512:286–289, 2014.

[14] S. Truppe, H. J. Williams, M. Hambach, L. Caldwell, N. J. Fitch, E. A. Hinds, B. E. Sauer, and M. R. Tarbutt. Molecules cooled below the Doppler limit. *Nature Physics*, 13(12):1173–1176, 2017.

[15] T. Grünzweig, A. Hilliard, M. McGovern, and M. F. Andersen. Near-deterministic preparation of a single atom in an optical microtrap. *Nature Physics*, 6(12):951–954, 2010.

[16] D. DeMille. Quantum computation with trapped polar molecules. *Physical Review Letters*, 88(6):067901, 2002.

[17] T. Wilk, A. Gaëtan, C. Evellin, J. Wolters, Y. Miroshnychenko, P. Grangier, and A. Browaeys. Entanglement of two individual neutral atoms using Rydberg blockade. *Physical Review Letters*, 104(1):2–5, 2010.

[18] L. Isenhower, E. Urban, X. L. Zhang, A. T. Gill, T. Henage, T. A. Johnson, T. G. Walker, and M. Saffman. Demonstration of a neutral atom controlled-not quantum gate. *Physical Review Letters*, 104(1):8–11, 2010.

[19] O. S. of America. *Handbook of Optics Third Edition, 5 Volume Set*.

[20] A. Ashkin. Atomic-beam deflection by resonance-radiation pressure. *Physical Review Letters*, 25(19):1321–1324, 1970.

[21] W. D. Phillips. Laser cooling and trapping of neutral atoms. *Reviews of Modern Physics*, 70(3):721–741, 1998.

[22] W. D. Phillips, J. V. Prodan, and H. J. Metcalf. Laser cooling and electromagnetic trapping of neutral atoms. *Journal of the Optical Society of America B*, 2(11):1751, 1985.

[23] J. V. Prodan, W. D. Phillips, and H. Metcalf. Laser production of a very slow monoenergetic atomic beam. *Physical Review Letters*, 49(16):1149–1153, 1982.

[24] W. D. Phillips and H. Metcalf. Laser deceleration of an atomic beam. *Physical Review Letters*, 48(9):596–599, 1982.

[25] J. Prodan. Stopping atoms with laser light. *Physical Review Letters*, 54(10):992–995, 1985.

[26] A. L. Migdall, J. V. Prodan, W. D. Phillips, T. H. Bergeman, and H. J. Metcalf. First observation of magnetically trapped neutral atoms. *Physical Review Letters*, 54(24):2596–2599, 1985.

[27] S. Chu, L. Hollberg, J. E. Bjorkholm, A. Cable, and A. Ashkin. Three-dimensional viscous confinement and cooling of atoms by resonance radiation pressure. *Physical Review Letters*, 55(1):48–51, 1985.

[28] J. P. Gordon and A. Ashkin. Motion of atoms in a radiation trap. *Physical Review A*, 21(5):1606–1617, 1980.

[29] D. J. Wineland and W. M. Itano. Laser cooling of atoms. *Physical Review A*, 20(4):1521–1540, 1979.

[30] P. Lett, R. Watts, and C. Westbrook. Observation of atoms laser cooled below the Doppler limit. *Physical Review Letters*, 61(2):169–173, 1988.

[31] J. Dalibard and C. Cohen-Tannoudji. Laser cooling below the Doppler limit by polarization gradients: simple theoretical models. *Journal of the Optical Society of America B*, 6(11):2023, 1989.

[32] P. J. Ungar, D. S. Weiss, E. Riis, and S. Chu. Optical molasses and multilevel atoms: theory. *Journal of the Optical Society of America B*, 6(11):2058, 1989.

[33] A. Ashkin. Trapping of atoms by resonance radiation pressure. *Physical Review Letters*, 40(12):729–732, 1978.

[34] A. Ashkin and J. P. Gordon. Cooling and trapping of atoms by resonanace radiation pressure. *Optics Letters*, 4(6):161–163, 1979.

[35] S. Chu, J. E. Bjorkholm, A. Ashkin, and A. Cable. Experimental observation of optically trapped atoms. *Physical Review Letters*, 57:314, 1986.

[36] V. G. Minogin and J. Javanainen. A tetrahedral light pressure trap for atoms. *Optics Communications*, 43(2):119–122, 1982.

[37] A. Ashkin and J. P. Gordon. Stability of radiation-pressure particle traps: an optical Earnshaw theorem. *Optics Letters*, 8(10):511, 1983.

[38] D. E. Pritchard, E. L. Raab, V. Bagnato, C. E. Wieman, and R. N. Watts. Light traps using spontaneous forces. *Physical Review Letters*, 57(3):310–313, 1986.

[39] D. Sesko, T. Walker, C. Monroe, a. Gallagher, and C. Wieman. Collisional losses from a light-force atom trap. *Physical Review Letters*, 63(9):961–964, 1989.

[40] T. Walker, D. Sesko, and C. Wieman. Collective behavior of optically trapped neutral atoms. *Physical Review Letters*, 64(4):408–411, 1990.

[41] C. Monroe, W. Swann, H. Robinson, and C. Wieman. Very cold trapped atoms in a vapour cell. *Physical Review Letters*, 65(13):1571–1574, 1990.

[42] M. Prentiss, A. Cable, J. E. Bjorkholm, S. Chu, E. L. Raab, and D. E. Pritchard. Atomic-density-dependent losses in an optical trap. *Optics Letters*, 13(6):452, 1988.

[43] S. Q. Shang, Z. T. Lu, and S. J. Freedman. Comparison of the cold-collision losses for laser-trapped sodium in different ground-state hyperfine sublevels. *Physical Review A*, 50(6):4449–4452, 1994.

[44] J. Flemming, A. Tuboy, and D. Milori. Magneto-optical trap for sodium atoms operating on the D1 line. *Optics Communications*, 135:269–272, 1997.

[45] V. B. Tiwari, S. Singh, H. S. Rawat, and S. C. Mehendale. Cooling and trapping of ^{85}Rb atoms in the ground hyperfine F=2 state. *Physical Review A*, 78(6):063421, 2008.

[46] M. Walhout, J. Dalibard, S. L. Rolston, and W. D. Phillips. $\sigma^+\sigma^-$ Optical molasses in a longitudinal magnetic field. *Journal of the Optical Society of America B*, 9(11):1997, 1992.

[47] S. Q. Shang, B. Sheehy, P. Van Der Straten, and H. Metcalf. Velocity-selective magnetic-resonance laser cooling. *Physical Review Letters*, 65(3):317–320, 1990.

[48] B. Sheehy, S. Q. Shang, P. Van Der Straten, S. Hatamian, and H. Metcalf. Magnetic-field-induced laser cooling below the doppler limit. *Physical Review Letters*, 64(8):858–861, 1990.

[49] S. Q. Shang, B. Sheehy, H. Metcalf, P. Van Der Straten, and G. Nienhuis. Velocity-selective resonances and sub-Doppler laser cooling. *Physical Review Letters*, 67(9):1094–1097, 1991.

[50] C. Valentin, M. C. Gagné, J. Yu, and P. Pillet. One-dimension sub-Doppler molasses in the presence of static magnetic field. *Europhysics Letters*, 17(2):133–138, 1992.

[51] O. Emile, R. Kaiser, C. Gerz, H. Wallis, and A. Aspect. Magnetically assisted Sisyphus effect. *Journal de Physique II, EDP Sciences*, 3(12):1709–1733, 1993.

[52] M. Weidemüller, T. Esslinger, M. A. Ol'shanii, A. Hemmerich, and T. W. Hänsch. A novel scheme for efficient cooling below the photon recoil limit. *Europhysics Letters*, 27(2):109–114, 1994.

[53] D. Boiron, C. Triché, and D. Meacher. Three-dimensional cooling of cesium atoms in four-beam gray optical molasses. *Physical Review A*, 52(5):3425–3428, 1995.

[54] D. Boiron, A. Michaud, P. Lemonde, Y. Castin, C. Salomon, S. Weyers, K. Szymaniec, L. Cognet, et al. Laser cooling of cesium atoms in gray optical molasses down to 1.1 μk. *Physical Review A*, 53(6):R3734–R3737, 1996.

[55] G. Hillenbrand, K. Burnett, and C. J. Foot. Effect of scattered radiation on sub-Doppler cooling. *Physical Review A*, 52(6):4763–4786, 1995.

[56] W. Ketterle, K. B. Davis, M. A. Joffe, A. Martin, and D. E. Pritchard. High densities of cold atoms in a dark spontaneous-force optical trap. *Physical Review Letters*, 70(15):2253–2256, 1993.

[57] D. Lucas, P. Horak, and G. Grynberg. Sisyphus cooling of rubidium atoms on the D2 ($F = 1 \rightarrow F' = 1$) line: The role of the neighbouring transitions. *The European Physical Journal D*, 7(3):261–267, 1999.

[58] D. Rio Fernandes, F. Sievers, N. Kretzschmar, S. Wu, C. Salomon, and F. Chevy. Sub-Doppler laser cooling of fermionic ^{40}K atoms in three-dimensional gray optical molasses. *Europhysics Letters*, 100(6):63001, 2012.

[59] G. D. Bruce, E. Haller, B. Peaudecerf, D. A. Cotta, M. Andia, S. Wu, M. Y. Johnson, B. W. Lovett, et al. Sub-Doppler laser cooling of ^{40}K with Raman gray molasses on the D2 line. *Journal of Physics B*, 50(9):1–6, 2017.

[60] A. T. Grier, I. Ferrier-Barbut, B. S. Rem, M. Delehaye, L. Khaykovich, F. Chevy, and C. Salomon. Λ-enhanced sub-Doppler cooling of lithium atoms in D1 gray molasses. *Physical Review A*, 87(6):063411, 2013.

[61] J. J. Hudson, D. M. Kara, I. J. Smallman, B. E. Sauer, M. R. Tarbutt, and E. A. Hinds. Improved measurement of the shape of the electron. *Nature*, 473(7348):493–6, 2011.

[62] K. A. B. Soderberg, N. Gemelke, and C. Chin. Ultracold molecules: Vehicles to scalable quantum information processing. *New Journal of Physics*, 11, 2009.

[63] L. D. Carr, D. DeMille, R. V. Krems, and J. Ye. Cold and ultracold molecules: Science, technology and applications. *New Journal of Physics*, 11, 2009.

[64] P. K. Molony, P. D. Gregory, Z. Ji, B. Lu, M. P. Köppinger, C. R. Le Sueur, C. L. Blackley, J. M. Hutson, et al. Creation of ultracold $^{87}Rb^{133}Cs$ molecules in the rovibrational ground state. *Physical Review Letters*, 113(25):1–5, 2014.

[65] E. S. Shuman, J. F. Barry, D. R. Glenn, and D. DeMille. Radiative force from optical cycling on a diatomic molecule. *Physical Review Letters*, 103(22):1–4, 2009.

[66] E. S. Shuman, J. F. Barry, and D. Demille. Laser cooling of a diatomic molecule. *Nature*, 467(7317):820–3, 2010.

[67] B. K. Stuhl, B. C. Sawyer, D. Wang, and J. Ye. Magneto-optical trap for polar molecules. *Physical Review Letters*, 101(24):243002, 2008.

[68] M. Hummon, M. Yeo, B. Stuhl, A. Collopy, Y. Xia, and J. Ye. 2d magneto-optical trapping of diatomic molecules. *Physical Review Letters*, 110(14):143001, 2013.

[69] V. Zhelyazkova, A. Cournol, T. E. Wall, A. Matsushima, J. J. Hudson, E. A. Hinds, M. R. Tarbutt, and B. E. Sauer. Laser cooling and slowing of CaF molecules. *Physical Review A*, 89(5):053416, 2014.

[70] D. J. Berkeland. Destabilization of dark states and optical spectroscopy in Zeeman-degenerate atomic systems. *Physical Review A*, 65(3):033413, 2002.

[71] D. J. McCarron, E. B. Norrgard, M. H. Steinecker, and D. DeMille. Improved magneto-optical trapping of a diatomic molecule. *New Journal of Physics*, 17:1–12, 2015.

[72] M. R. Tarbutt. Magneto-optical trapping forces for atoms and molecules with complex level structures. *New Journal of Physics*, 17, 2015.

[73] J. A. Devlin and M. R. Tarbutt. Three-dimensional Doppler, polarization-gradient, and magneto-optical forces for atoms and molecules with dark states. *New Journal of Physics*, 18(12):123017, 2016.

[74] E. B. Norrgard, D. J. McCarron, M. H. Steinecker, M. R. Tarbutt, and D. DeMille. Submillikelvin dipolar molecules in a radio-frequency magneto-optical trap. *Physical Review Letters*, 116(6):1–6, 2016.

[75] C. Foot. *Atomic Physics*, pages 142–143. Oxford Master Series in Physics. Oxford University Press, 2005.

[76] P. Pearle. Simple derivation of the Lindblad equation. *European Journal of Physics*, 33(4):805–822, 2012.

[77] S. Chang and V. Minogin. Density-matrix approach to dynamics of multilevel atoms in laser fields. *Physics Report*, 365(2):65–143, 2002.

[78] A. Aspect, E. Arimondo, R. Kaiser, N. Vansteenkiste, and C. Cohen-tannoudji. Laser cooling below the one-photon recoil energy by velocity-selective coherent population trapping. *Physical Review Letters*, 61(7):826–829, 1988.

[79] B. H. Bransden. *Quantum Mechanics*. Pearson Education Ltd, 2000.

[80] K. N. Jarvis, J. A. Devlin, T. E. Wall, B. E. Sauer, and M. R. Tarbutt. Blue-detuned magneto-optical trap. *Physical Review Letters*, 120(8):083201, 2018.

[81] A. Millett-Sikking, I. G. Hughes, P. Tierney, and S. L. Cornish. DAVLL lineshapes in atomic rubidium. *Journal of Physics B*, 40(1):187–198, 2007.

[82] R. Giannini. Sub-Doppler diode laser frequency stabilization with the DAVLL scheme on the D1 line of a ^{87}Rb vapor-cell. *14th Internati onal School on Quantum Electronics: Laser Physics and Applications.*, (66040):1–5, 2007.

[83] M. L. Harris, S. L. Cornish, A. Tripathi, and I. G. Hughes. Optimization of sub-Doppler DAVLL on the rubidium D2 line. *Journal of Physics B*, 41(8):085401, 2008.

[84] G. Ritt, G. Cennini, C. Geckeler, and M. Weitz. Laser frequency offset locking using a side of filter technique. *Applied Physics B*, 79(3):363–365, 2004.

[85] K. E. Gibble, S. Kasapi, and S. Chu. Improved magneto-optic trapping in a vapor cell. *Optics Letters*, 17(7):526, 1992.

[86] E. A. Donley, T. P. Heavner, F. Levi, M. O. Tataw, and S. R. Jefferts. Double-pass acousto-optic modulator system. *Review of Scientific Instruments*, 76(6):3–8, 2005.

[87] C. Salomon, J. Dalibard, W. D. Phillips, A. Clairon, and S. Guellati. Laser cooling of cesium atoms below 3 micro-kelvin. *Europhysics Letters*, 12(8):683, 1990.

[88] R. Gupta, S. Padua, C. Xie, H. Batelaan, and H. Metcalf. Simplest atomic system for sub-doppler laser cooling. *J. Opt. Soc. Am. B*, 11(4):537–541, 1994.

[89] C. D. Wallace, T. P. Dinneen, K. Y. N. Tan, A. Kumarakrishnan, P. L. Gould, and J. Javanainen. Measurements of temperature and spring constant in a magneto-optical trap. *Journal of the Optical Society of America B*, 11(5):703, 1994.

[90] M. Drewsen, P. Laurent, A. Nadir, G. Santarelli, A. Clairon, Y. Castin, D. Grison, and C. Salomon. Investigation of sub-Doppler cooling effects in a cesium magneto-optical trap. *Applied Physics B Lasers and Optics*, 59(3):283–298, 1994.

[91] C. J. Cooper, G. Hillenbrand, J. Rink, C. G. Townsend, K. Zetie, and C. J. Foot. The temperature of atoms in a magneto-optical trap. *Europhysics Letters*, 28(6):397–402, 1994.

[92] W. Petrich, M. H. Anderson, J. R. Ensher, and E. a. Cornell. Behavior of atoms in a compressed magneto-optical trap. *Journal of the Optical Society of America B*, 11(8):1332, 1994.

[93] Y. Deng, J. Bechhoefer, and N. R. Forde. Brownian motion in a modulated optical trap. *Journal of Optics A: Pure and Applied Optics*, 9(8):S256–S263, 2007.

[94] K. Kim, H. R. Noh, Y. H. Yeon, and W. Jhe. Observation of the Hopf bifurcation in parametrically driven trapped atoms. *Physical Review A*, 68(3):31403, 2003.

[95] K. Kim, H. R. Noh, and W. Jhe. Measurements of trap parameters of a magneto-optical trap by parametric resonance. *Physical Review A*, 71(3):1–5, 2005.

[96] K. Kim, H. R. Noh, H. J. Ha, and W. Jhe. Direct observation of the sub-Doppler trap in a parametrically driven magneto-optical trap. *Physical Review A*, 69(3):5–9, 2004.

[97] K. Kim, K. H. Lee, M. Heo, H. R. Noh, and W. Jhe. Measurement of the trap properties of a magneto-optical trap by a transient oscillation method. *Physical Review A*, 71(5):1–5, 2005.

[98] H. J. Williams, S. Truppe, M. Hambach, L. Caldwell, N. J. Fitch, E. A. Hinds, B. E. Sauer, and M. R. Tarbutt. Characteristics of a magneto-optical trap of molecules. *New Journal of Physics*, 19(11):113035, 2017.

[99] J. Jun, S. Chang, H. Lee, V. Minogin, and W. Jhe. Double-structure potential due to multiphoton processes in a magneto-optical trap. *Physical Review A*, 60(6):4738–4742, 1999.

[100] J. W. Jun, S. Chang, T. Y. Kwon, H. S. Lee, and V. G. Minogin. Kinetic theory of the magneto-optical trap for multilevel atoms. *Physical Review A*, 60(5):3960–3972, 1999.

[101] G. Hillenbrand, C. J. Foot, and K. Burnett. Heating due to long-range photon exchange interactions between cold atoms. *Physical Review A*, 50(2):1479–1489, 1994.

[102] C. G. Townsend, N. H. Edwards, C. J. Cooper, K. P. Zetie, C. J. Foot, A. M. Steane, P. Szriftgiser, H. Perrin, et al. Phase-space density in the magneto-optical trap. *Physical Review A*, 52(2):1423–1440, 1995.

[103] V. Bagnato, D. E. Pritchard, and D. Kleppner. Bose-Einstein condensation in an external potential. *Physical Review A*, 35(10):4354–4358, 1987.

[104] M. H. Anderson, J. R. Ensher, M. R. Matthews, C. E. Wieman, and E. A. Cornell. Observation of Bose-Einstein condensation in a dilute atomic vapor. *Science*, 269(5221):198–201, 1995.

[105] K. B. Davis, M. O. Mewes, M. R. Andrews, N. J. Van Druten, D. S. Durfee, D. M. Kurn, and W. Ketterle. Bose-Einstein condensation in a gas of sodium atoms. *Physical Review Letters*, 75(22):3969–3973, 1995.

[106] N. Radwell, G. Walker, and S. Franke-Arnold. Cold-atom densities of more than 10^{12} cm^{-3} in a holographically shaped dark spontaneous-force optical trap. *Physical Review A*, 88(4):043409, 2013.

[107] J. Vigué. Possibility of applying laser-cooling techniques to the observation of collective quantum effects. *Physical Review A*, 34(5):4476–4479, 1986.

[108] J. E. Bjorkholm. Collision-limited lifetimes of atom traps. *Physical Review A*, 38(3):1599–1600, 1988.

[109] K. Lindquist, M. Stephens, and C. Wieman. Experimental and theoretical study of the vapor-cell Zeeman optical trap. *Physical Review A*, 46(7):4082–4090, 1992.

[110] A. Gallagher and D. E. Pritchard. Exoergic collisions of cold Na*-Na. *Physical Review Letters*, 63(9):957–960, 1989.

[111] C. D. Wallace, T. P. Dinneen, K. Y. N. Tan, T. T. Grove, and P. L. Gould. Isotopic difference in trap loss collisions of laser cooled rubidium atoms. *Physical Review Letters*, 69(6):897–900, 1992.

[112] N. W. Ritchie, E. R. Abraham, Y. Y. Xiao, C. C. Bradley, R. G. Hulet, and P. S. Julienne. Trap-loss collisions of ultracold lithium atoms. *Physical Review A*, 51(2):890–893, 1995.

[113] S. Gensemer, V. Sanchez-Villicana, K. Tan, T. Grove, and P. Gould. Trap-loss collisions of ^{85}Rb and ^{87}Rb: Dependence on trap parameters. *Physical Review A*, 56(5):4055–4063, 1997.

[114] L. G. Marcassa, K. Helmerson, A. M. Tuboy, D. M. Milori, S. R. Muniz, J. Flemming, S. C. Zílio, and V. S. Bagnato. Collisional loss rate of sodium atoms in a magneto-optical trap operating on the D1 line. *Journal of Physics B*, 29(14):3051–3057, 1996.

[115] V. Sanchez-Villicana, S. D. Gensemer, and P. L. Gould. Observation of flux enhancement in collisions between ultracold atoms. *Physical Review A*, 54(5):R3730–R3733, 1996.

[116] J. Weiner, V. S. Bagnato, S. Zilio, and P. S. Julienne. Experiments and theory in cold and ultracold collisions. *Reviews of Modern Physics*, 71(1):1–85, 1999.

[117] B. Verhaar, J. Koelman, H. Stoof, O. Luiten, and S. Crampton. Hyperfine contribution to spin-exchange frequency shifts in the hydrogen maser. *Physical Review A*, 35(9):3825–3831, 1987.

[118] D. Hoffmann, S. Bali, and T. Walker. Trap-depth measurements using ultracold collisions. *Physical Review A*, 54(2):R1030–R1033, 1996.

[119] M. H. Anderson, W. Petrich, J. R. Ensher, and E. A. Cornell. Reduction of light-assisted collisional loss rate from a low-pressure vapor-cell trap. *Physical Review A*, 50(5):3597–3600, 1994.

[120] V. Sanchez-Villicana, S. D. Gensemer, K. Y. Tan, A. Kumarakrishnan, T. P. Dinneen, W. Süptitz, and P. L. Gould. Suppression of ultracold ground-state hyperfine-changing collisions with laser light. *Physical Review Letters*, 74(23):4619–4622, 1995.

[121] T. Arpornthip, C. A. Sackett, and K. J. Hughes. Vacuum-pressure measurement using a magneto-optical trap. *Physical Review A*, 85(3):1–7, 2012.

[122] D. Hoffmann, P. Feng, and T. Walker. Measurements of rb trap-loss collision spectra. *Journal of the Optical Society of America B*, 11(5):712–720, 1994.

[123] P. Feng, H. Dominikus, and T. Walker. Comparison of trap-loss collision spectra for ^{85}Rb and ^{87}Rb. *Physical Review A*, 47(5):3495–3498, 1993.

[124] P. D. Lett, K. Molmer, S. D. Gensemer, K. Y. Tan, A. Kumarakrishnan, C. D. Wallaceg, and P. L. Gouldg. Hyperfine structure modifications of collisional losses from light-force atom traps. *Journal of Physics B*, 28(1):65–81, 1995.

[125] S. Rosi, A. Burchianti, S. Conclave, D. S. Naik, G. Roati, C. Fort, and F. Minardi. Λ-enhanced grey molasses on the D2 transition of Rubidium-87 atoms. *Scientific Reports*, 8(1):1–9, 2018.

[126] D. Felinto, L. G. Marcassa, V. S. Bagnato, and S. S. Vianna. Influence of the number of atoms in a ring-shaped magneto-optical trap: Observation of bifurcation. *Physical Review A*, 60(3):2591–2594, 1999.

[127] D. Felinto and S. S. Vianna. Orbital modes in low-density magneto-optical traps. *Journal of the Optical Society of America B*, 17 5(5):681–689, 2000.

[128] D. Felinto, H. Regehr, J. W. R. Tabosa, and S. S. Vianna. Fluctuations in ball and ring-shaped magneto-optical traps at low densities. *Journal of the Optical Society of America B*, 18(10):1410, 2001.

[129] K. Nasyrov, V. Biancalana, A. Burchianti, R. Calabrese, C. Marinelli, E. Mariotti, and L. Moi. Magneto-optical trap operating on a magnetically induced level-mixing effect. *Physical Review A*, 64(2):023412, 2001.